Analysis of pressure-induced contractility in cerebral vessels via multi-physics modelling approach

Ioannis Polydoros

Submitted to Swansea University in fulfilment of the requirements for the Degree of Doctor of Philosophy

Swansea University
2024

This thesis is dedicated to the loving memory of Alexandros Rontogiannis who is no longer with us and will never be forgotten. Only the good die young.

Acknowledgements

Firstly I would like to thank my family for their encouragement and support throughout my education. Their love and encouragement during the many stressful times throughout the doctorate degree are not to be underestimated.

To my supervisors Dr. Alberto Coccarelli and Prof. Perumal Nithiarasu, whose expertise, guidance, and continued support throughout my doctorate have been exceptionally valuable. In addition, I thank my friend Dr. Jason Carson for his support and insight.

Peer-reviewed papers during PhD candidature

A. Coccarelli, S. Pant, **I. Polydoros**, and O. F. Harraz. A new model for evaluating pressure-induced vascular tone in small cerebral arteries. *Biomechanics and Modeling in Mechanobiology*, 11 2023.

I. Polydoros, J. Carson, P. Nithiarasu, A. Coccarelli. A new computational framework for blood flow control. Under preparation

Conference papers during the PhD Candidature

I. Polydoros, P. Nithiarasu, A. Coccarelli. Multiscale Modelling of Arterial Contractility. *UK Association for Computational Mechanics (UKACM) 2022*, 20–22 April 2022, Nottingham, UK.

I. Polydoros, P. Nithiarasu, A. Coccarelli. Towards a Comprehensive Modelling of Mechanically-Induced Tone Regulation in Blood Vessels. *7th International Conference on Computational and Mathematical Biomedical Engineering (CMBE22)*, 27–29 June 2022, Milan, Italy.

I. Polydoros, P. Nithiarasu, A. Coccarelli. On the multiscale chemo-mechanical modelling of pressure-induced tone in cerebral vessels. *Biomedical Engineering 2023 Conference (BioMedEnd23)*, 14–15 September 2023, Swansea, UK.

Abstract

The human brain requires substantial energy for its complex functions, necessitating consistent blood flow. The myogenic response regulates this flow despite changes in intraluminal pressure. This adaptive capacity of cerebral arteries is crucial for normal function and is often impaired in pathological conditions. This research develops a computational framework to understand how pressure-induced tone during the myogenic response affects blood flow in cerebral arteries, using a multi-physics approach that integrates the chemical processes within smooth muscle cells with structural and fluid mechanics at the continuum level. At the cellular level, a new chemical model was developed to study the effects of pressure on smooth muscle cell (SMC) signalling. The developed model was fitted against experimental data found in literature regarding different intracellular concentration/phosphorylation levels under different pressure loads and was able to reach to a very good agreement with those data. It was able to accurately simulate the influence of luminal pressure on the various cytoplasmic elements involved in myogenic signalling, both in the control case and when combined with pharmacological interventions. It was then combined with a chemo-mechanical counterpart to simulate the generation and transduction of vascular tone at the tissue level. The active tone part is integrated to a 3D derived hyperelastic material model. The integrated model was capable of accurately capturing experimental measurements for vessels under control conditions, in a calcium-free bath, or under drug intervention cases. The tissue model was also tested on its prediction ability, showing a very good agreement with the experimental findings for the control case, and less but still acceptable for the other two, indicating that the parameter setup chosen is sufficient to accurately reproduce the myogenic response, and that more experimental data are needed for the cellular model for a further improvement. Furthermore, the analysis of the dynamic behaviour of the vessel wall model showed that a combination of the temporal parameters of the two models would be able to reproduce any given dynamic behaviour. To evaluate the effect of the pressure-induced tone on blood flow, a fluid-structure interaction (FSI) model is proposed, combining the structural part with a 1D fluid solver. Under both static and transient conditions, it was shown that the vessels including the active response were able to demonstrate the effects of flow regulation as reported in literature, showing the ability to maintain low fluctuations of blood flow with sudden changes in pressure. It was also shown that the vessel size in terms of both length and diameter highly affects the blood flow development. Taking into account the downstream circulation proved that more data would be needed for its identification and accurate representation through a lumped model. The analysis shed a light on the key components which affect the most this mechano-biological process.

Declarations

This work has not previously been accepted in substance for any degree and is not being concurrently submitted in candidature for any degree.

Signed: Ioannis Polydoros. Date: 31/12/2023

This thesis is the result of my own investigations, except where otherwise stated. Other sources are acknowledged by footnotes giving explicit references. A bibliography is appended.

Signed: Ioannis Polydoros. Date: 31/12/2023

I hereby give consent for my thesis, if accepted, to be available for electronic sharing

Signed: Ioannis Polydoros. Date: 31/12/2023

The University's ethical procedures have been followed and, where appropriate, that ethical approval has been granted.

Signed: Ioannis Polydoros. Date: 31/12/2023

Contents

List of Figures

List of Tables

Nomenclature

All units are in SI unless otherwise stated

Abbreviations

CaCaM	Calcium-calmodulin
CB	Cross-bridge
CF	Contractile fibre
CoW	Circle of Willis
CS	Cell signalling
CU	Contractile unit
FSI	Fluid-structure interaction
LF	Load-free
MCA	Middle cerebral artery
MLCK	Myosin light-chain kinase
MLCP	Myosin-light-chain phosphatase
PKC	Protein kinase C
pSE	Passive surrounding element
ROK	Rho-kinase
SEF	Strain-energy function
SF	Stress-free
SMC	Smooth muscle cell
VOCC	Voltage operated calcium channels
WLR	Wall-to-lumen ratio

List of symbols

$[Ca^{2+}]_i$	Intracellular calcium concentration
β	Temporal parameter of the chemo-mechanical model
χ_i	Cell signalling activation functions
δ_m	Distance between two myosin heads
λ_{r}	Radial stretch
$\lambda_{\mathrm{z,ext}}$	Axial stretch due to external loading
$\lambda_{\mathrm{z,res}}$	Residual axial stretch
λ_{z}	Axial stretch
λ_θ	Circumferential stretch
ED_{50}^n	Half activation constant of calcium to MLCK under constant CaM
μ	Viscosity
ω	Opening angle
ϕ	Fibre angle
Ψ, Ψ_p, Ψ_a	Total/active/passive component of strain-energy function
ρ	Density
τ_i	Temporal parameters of the cell signalling model
ξ_i	Cell signalling model state variables (represent concentration or phosphorylation of substances)
A	Area
A_0	Reference area
C	Compliance
c	Pressure-like material parameter related to isotropic part of the material model
c_0	Reference wave speed
C_A	Arterial compliance
F_a	Force due to cross-bridge power stroke

F_c	Driving force within the contractile unit caused by the cycling cross-bridges
F_z	Axial force
H, h, η	Vascular wall thickness at stress-free/load-free/loaded configuration
h_w	Thickness-medium ratio
K, n	Fitted parameters of the cell signalling model
k_1	Pressure-like material parameter related to anisotropic part of the material model
k_2	Dimensionless material parameter related to anisotropic part of the material model
k_i	Hai-Muprhy model rates of transition between states
K_{CaCaM}	Fitted parameter related to calcium calmodulin
K_{AC}, n_{AC}	Fitted parameters related to the Hill function that defines the passive surrounding element stiffness
k_{pSE}	Passive surrounding element total stiffness
k_{tCB}	Total stiffness of the cross bridge
k_{tCU}	Total stiffness of the contractile units
L, ξ, l	Vessel length at stress-free/load-free/loaded configuration
L_0	Filament overlap
L_m	Length of myosin
L_{SMC}, l_{SMC}	Length of the smooth muscle cell at reference/Current configuration
$n_M, n_{Mp}, n_{AMp}, n_{AM}$	Hai-Murphy model states of the myosin heads
N_{CF}	Number of contractile fibres per unit of area
N_{CU}	Number of contractile units
P	Pressure
P_0	Reference pressure
P_{cap}	Capillary pressure

P_{collapse}	Collapse pressure
P_{tm}	Transmural pressure
P_a	First Piola-Kirchhoff stress
Q	Flow rate
Q_P	Flow rate according to Poiseuille law
R_f	Resistance to flow
R_{VB}	Vascular bed resistance
$R_{i,o}, R'_{i,o}, r_{i,o}$	Inner/outer radius at stress-free/load-free/loaded configuration
s_{f0}	Filament overlap scaling factor
u	velocity
u_{CB}	Elongation of a cross-bridge
u_{fs}	Relative filament sliding
u_{fs}^{chem}	Chemical part of relative filament sliding
u_{fs}^{mech}	Mechanical part of relative filament sliding
u_{fs}^{opt}	Optimal relative filament sliding (value at which the filament overlap is maximised)
u_{pSE}	Deformation of the passive surrounding element
u_{ps}	Average elongation caused by power-stroke
Z_{art}	Arterial characteristic impedance

Chapter 1

Introduction

This thesis focuses on the development of a multi-physics framework for studying the mechanics of pressure-induced tone within cerebral arteries and its effect on flow development. This requires the coupling of several sub-models to assess the most important factors that contribute to active tone development. This introductory chapter reports on all the physiological background involved in this topic, to define the motivation behind this study. An overview of the literature on the contributions of numerical modelling to the fields of interest is presented to shape the picture of the current state of the topic. Finally, the aim and scope of this thesis are discussed.

1.1 Physiological background

The cardiovascular system, also known as the circulatory system, is responsible for delivering oxygen and nutrients to the entire body. Furthermore, it removes waste products generated by cell metabolism. The arterial tree receives blood from the two heart ventricles (left and right). These two ventricles provide with blood two distinctive systems, the systemic and the pulmonary. The right ventricle takes the deoxygenated blood and redirects it to the pulmonary system to oxygenate it again, while the left ventricle provides the systemic circulation with oxygen-rich blood.

Blood circulation occurs through a complex system of vessels that includes arteries, arterioles, capillaries, venules, and veins. Arteries are essential for distributing blood to all body regions, while arterioles are responsible for carrying blood to capillary beds, where oxygen and other essential substances are able to diffuse to cells. Venules collect oxygen-depleted blood from capillaries and transport it back to the heart via veins.

Blood vessels are generally classified according to their size, type, and function.

Those with a diameter greater than $10\,mm$ are known as large arteries and have a thick wall containing a considerable amount of elastic tissue. This elasticity allows them to transport a large amount of blood from the core to the main organs and peripheral areas. Generally, the larger systemic arteries have a binary tree structure, with some exceptions such as the circle of Willis (CoW).

Towards the periphery, the arteries become smaller and stiffer due to the presence of fewer elastic tissues and more layers of smooth muscle cells. This allows the arteries to control the flow of blood by narrowing or widening their lumen, thus making necessary adjustments to the flow. The diameter of the smaller arteries and arterioles is usually around $50 - 100\,\mu m$, and even narrower, reaching $15\,\mu m$, when they enter the tissues.

Arterioles, capillaries, and venules create a dense network with numerous interconnections. The distribution of small systemic vessels is organised to ensure uniform coverage of tissues. This organisation minimises the volume occupied by these vessels while maximising their surface area, facilitating the efficient diffusion of oxygen and nutrients to cells [1]. Microvessels play a crucial role in maintaining the homeostasis of the cellular environment. The venous system withdraws blood from tissues and returns it to the beating heart, establishing a closed loop for the circulation of blood.

Pressure and flow waves arise from the ejection of blood from the ventricles and its interaction with the flexible arterial wall. As a result, the aorta and other elastic arteries need to expand to handle the sudden increase in arterial blood volume triggered by the contraction of the left ventricle during systole. This leads to the arteries showing a rhythmic pulsation, commonly known as the pulse, which follows the heartbeat and results in the transmission of downstream pressure and velocity changes.

The behaviour of blood varies with respect to the diameter of the vessel through which it flows. Depending on the size of the vessel and the Reynolds number of the blood flow, it can be assumed that it is homogeneous, and behaves as a Newtonian fluid with constant viscosity [2]. Furthermore, in most of the arteries and arterioles, blood flow is laminar. Although turbulence can develop in specific regions within large arteries, this can occur only near bifurcations or under pathological conditions [3].

1.1.1 Arterial wall histology

Arteries in the circulatory system can be classified into two main types according to their structural characteristics, the composition of their walls and their functional roles within the circulatory system: *elastic* and *resistance* arteries. How-

ever, there can be vessels that are intermediate between those two types, which are defined as *muscular*. Elastic arteries, such as the aorta and the main pulmonary arteries, focus primarily on maintaining continuous blood flow, stretching, and recoiling to accommodate changes in blood pressure during the cardiac cycle. However, resistance arteries regulate blood flow by constricting or dilating, directing blood to specific organs and tissues according to local needs. They contribute to the overall flow resistance in the circulatory system, determine blood distribution and influence blood pressure [4].

Histology of arterial walls reveals that they are composed of three layers: the intima, the media, and the adventitia. Each layer includes various elements, such as endothelium, smooth muscle, elastin, collagen, and connective tissue. The way these components are arranged within each layer influences the overall mechanical behaviour of the arterial wall at macroscopic level. The structural organisation of these components within the wall can be observed through polarised light microscopy [5, 6].

In many body tissues and organs, the microstructure is significantly influenced by the extracellular matrix (ECM). The ECM serves various functions, imparting strength and resilience to tissues to maintain their shape, and creating a watery environment that facilitates the exchange of nutrients, ions, hormones, and metabolites between cells and the capillary network. The ECM is predominantly composed of proteins, such as collagen, elastin, fibronectin, and laminin [7].

Collagen is one of the major proteins within the human body, which constitutes 25–30 % of the total proteins. It exists in various forms (I–VIII). In arteries, types I and III play a crucial role as the primary load-bearing structural elements. The distribution of collagen I and III varies in different sections of the vascular tree [8]. Elastin, on the other hand, is a key protein responsible for providing elasticity to tissues such as skin and blood vessels. It forms the main structure of elastic fibers and significantly influences the mechanical properties of the tissue. The elastic properties of the elastin meshes allow the tissues to flex and sustain high levels of deformation and stress [8].

These two proteins are combined with smooth muscle cells (SMCs), which constitute a layer of cells responsible for the contractile behaviour of the arterial wall. While the SMCs layer does not contribute to the structural tone of the wall when fully relaxed, it becomes a significant load-bearing component upon activation. This activation may be triggered by different stimuli that can be either mechanical, electrical, or (bio)chemical. Examples of wall regulation include the myogenic response which is initiated by changes in intraluminal pressure that elongate the SMCs, and the metabolic mechanism, which involves the accumula-

tion of vasoactive molecules leading to the relaxation or contraction of the SMC [9]. The contribution of the SMCs occurs in the circumferential direction, due to their alignment within the vascular wall layer [10, 11]. The contraction of blood vessels is orchestrated by a series of smooth muscle cells, and their contractile machinery is based on the phosphorylation of myosin motors, regulated by complex intracellular calcium dynamics. Endothelial cells modulate these processes by releasing factors that can inhibit or activate specific ionic pathways within the smooth muscle [12].

Multi-layered structure

As already mentioned, the arterial wall is structured with three distinctive layers: the intima, the media, and the adventitia, from inner to outer. The structural characteristics of each layer, as well as their functional aspects are discussed next.

The intima layer. The innermost layer of an artery is called the intima and consists of a single layer of endothelial cells lining the arterial wall. This layer rests on a thin basal membrane and a subendothelial layer. While the endothelial layer does not play a significant role in supporting the luminal loading, the subendothelial layer can, as it contains some SMCs and collagen proteins. However, in healthy young resistance arteries, the subendothelial layer is almost absent, making a negligible contribution to the solid mechanical properties of the arterial wall. Consequently, the intima layer as a whole does not contribute significantly to the structural characteristics of the wall [8, 13].

The media layer. This is the middle part of the arterial wall and contains primarily collagen types I and III, elastin, and smooth muscle cells (SMCs). It is the thickest among the three layers and is separated by fenestrated elastic layers that divide the media into multiple concentric fibre-reinforced compartments. The number of layers decreases towards the outer part [13]. Elastin, collagen bundles, and SMCs create a continuous fibrous helix with a small pitch, almost aligning in a circular direction within the media [14]. This organised structure enables the media to withstand significant loads in the circumferential direction.

The adventitia layer. The outermost layer of the arterial wall is called adventitia. It is made up of thick layers of collagen fibres, creating fibrous tissue. The thickness of the adventitia depends on the type of artery and its location in the body. Within adventitia, collagen fibres are organised into two helically aligned bundles, the alignment angle varying widely between vessels [6]. At lower pressure levels, the adventitial layer does not play a significant role in the structural properties of the vessel. However, at higher pressure levels, it becomes a rigid tube, which greatly contributes to preventing the vessel from being overstretched or ruptured [15].

Figure 1.1 shows the aforementioned layers within the arterial wall, along with their structural components.

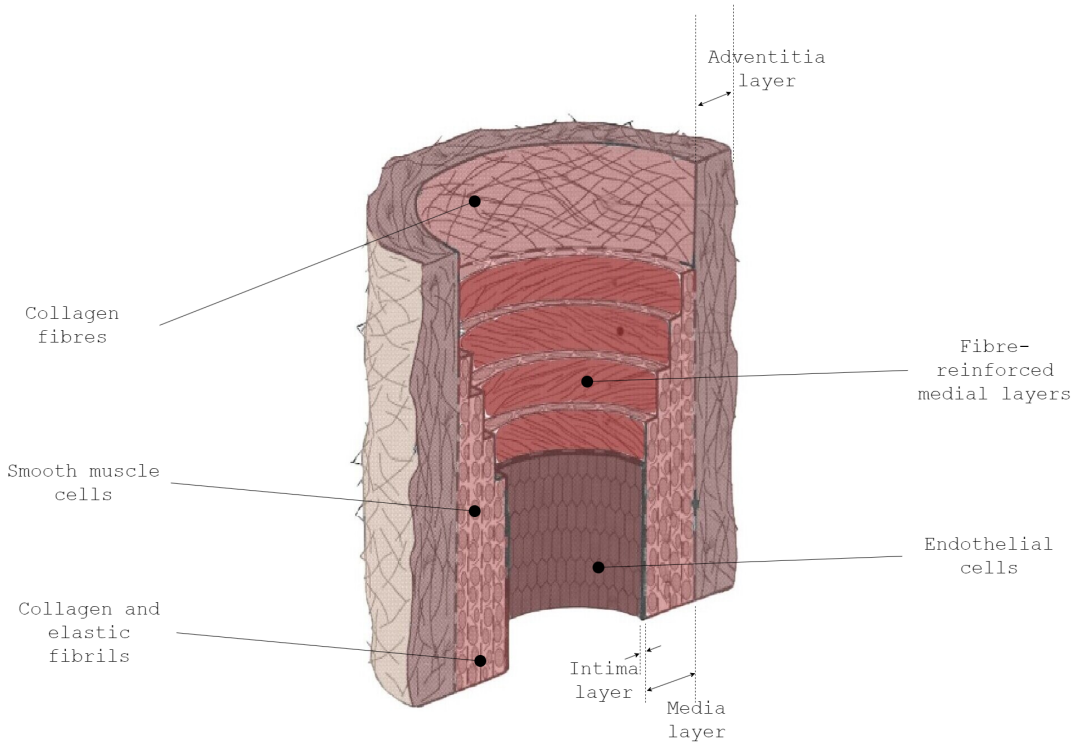

Figure 1.1: Arterial wall layers and their structural aspects (image based on [13])

Material behaviour

The key components that contribute to defining the material wall behaviour are elastin and collagen fibres and SMCs. Macroscopically, the mechanical behaviour of the vascular wall is defined by a nonlinear relationship between stress and strain, anisotropy, incompressibility, and the presence of viscous effects. The way arteries respond to mechanical loading is influenced by environmental factors such as temperature, osmotic pressure, pH, carbon dioxide and oxygen levels, ionic concentrations, and monosaccharide concentration. Under ex vivo conditions, biological degradation leads to alterations in mechanical properties [16].

On examination of histology, one finds that the mechanical properties of the arteries undergo changes along the arterial tree. Although there is noticeable variation and the shape of the stress-strain curve appears to depend on the anatomical location [17], the overall mechanical characteristics of the arterial walls remain consistent. Depending on the type of artery, the materials may exhibit primarily elastic behaviour in the case of proximal elastic arteries, or viscoelastic behavior in distal resistance arteries.

If healthy, arteries exhibit remarkable flexibility as composite structures. When

subjected to mechanical stress, its response follows a nonlinear pattern, characterised by exponential stiffening at elevated pressure levels, a phenomenon common to all biological tissues. Experimental evidence indicates that, under lower stress conditions, the primary contributor to this response is elastin, with collagen playing a minimal role. However, as tension increases, the stiffening effect becomes predominantly driven by collagen [18]. As discussed in previous sections about the properties of the wall of different vessels, larger arteries, characterised by a higher elastin content, tend to exhibit a more elastic behaviour, while smaller vessels demonstrate a stiffer response.

Furthermore, as previously indicated, the collagen fibres within the media and adventitia layers have different alignments, but both in a highly organised structural configuration. This unique arrangement imparts anisotropy to the arterial wall material. Scientific investigations have focused on the meticulous quantification of material symmetry. Although uniaxial tests offer valuable insight into material properties, they do not give a detailed description of the anisotropic characteristics [19]. From a microscopic point of view, arteries can also be seen as a combination of solid and fluid components. However, the stress-induced movement of fluid within the wall can be ignored, leading to the conceptualisation of the arterial wall as a uniform solid material. In this scenario, the assumption of incompressibility becomes applicable [20, 21].

Hysteresis phenomena manifest during cyclic loading, particularly in the absence of muscle tone. As stress softening occurs after a few cycles, the artery undergoes preconditioning, leading to a stress-strain curve exhibiting repeatable cyclic behaviour [22]. Toward the periphery, the viscous effects intensify, signifying a shift towards increased stiffness in the arteries. This suggests a predominant role for dissipative mechanisms related to smooth muscle cell deformation in shaping the dynamic response of blood vessels. Throughout the life of the artery, the arterial wall undergoes continuous adaptations in response to its environment, involving various irreversible processes such as growth, remodelling, ageing, and diseases. These alterations highlight the absence of a singular stress-free configuration, making the unloaded state of a examined vessel likely to encompass residual stresses. Furthermore, the layers of the arterial wall experience different stress conditions in this unloaded configuration [23].

1.1.2 Cerebral vasculature

This thesis focuses on blood flow across the cerebral vasculature and its function. In this section, a concise overview of the structure and function of blood vessels within the brain is given.

Network morphology

The basilar and internal carotid arteries enter the cranial cavity and connect to encircle the optic chiasma, forming the circle of Willis. From this circle, the anterior, middle, and posterior cerebral arteries originate, which then branch into smaller vessels and arterioles to form the cerebral vasculature. This circular connectivity serves the purpose of maintaining cerebral blood flow in the event of carotid artery obstruction. Figure 1.2 illustrates the main vessels constituting the cerebral vasculature. The graph illustrates the vessels that provide blood to the brain on the left side, which are the internal carotid artery and the vertebral arteries that combine to form the basilar artery. Additionally, the right side of the graph shows the main intracranial branches. In terms the main cerebral arteries size reported in literature [24, 25, 26], the internal carotid arteries have a typical length of $18\,cm$ with a diameter of $\sim 5\,mm$, while the basilar diameter is $\sim 4\,mm$ and with a length of about $2\,cm$. The middle cerebral artery (MCA) is $\sim 1\,cm$ long with a diameter of $3\,mm$ and its branch, the superior middle cerebral, has a length of $\sim 7\,cm$ and a diameter of about $2\,mm$, while the anterior cerebral has a similar diameter, but it is shorter with a length of $\sim 2.5\,cm$. Finally, the ophthalmic artery, which is a smaller vessel that branches from the internal carotid is $\sim 1\,cm$ long and has a diameter of about $1\,mm$.

The major cerebral arteries further branch into the pial arteries, which run along the brain surface. In particular, the pressure of the pial artery is relatively low, approximately 50% of systemic pressure, attributed to a low distal/proximal resistance ratio. These pial arteries give rise to smaller arteries that penetrate brain tissue and eventually branch into short arterioles.

Arterial wall function

The cerebral arteries are unique vessels that are responsible for supplying the brain with oxygen and nutrients through blood circulation. They are composed of the intima, media, and adventitia layers [10], with the adventitia being mainly composed of collagen type I and some fibroblasts, as already mentioned. What is important to note is that the endothelial cells in the intima layer are part of the Blood-Brain Barrier (BBB). The media layer, containing collagen type I and III [27], elastin fragments, and smooth muscle cells (SMCs), is also essential for cerebral autoregulation [28]. Cerebral arteries differ from other systemic arteries for three different aspects: the BBB, their elastic lamina, and autoregulation [29].

The blood-brain barrier (BBB) is a vital feature of the cerebral capillaries, which ensures selective permeability. Positioned in the intima, the BBB serves three key functions: regulating ion balance, facilitating nutrient transport, and preventing

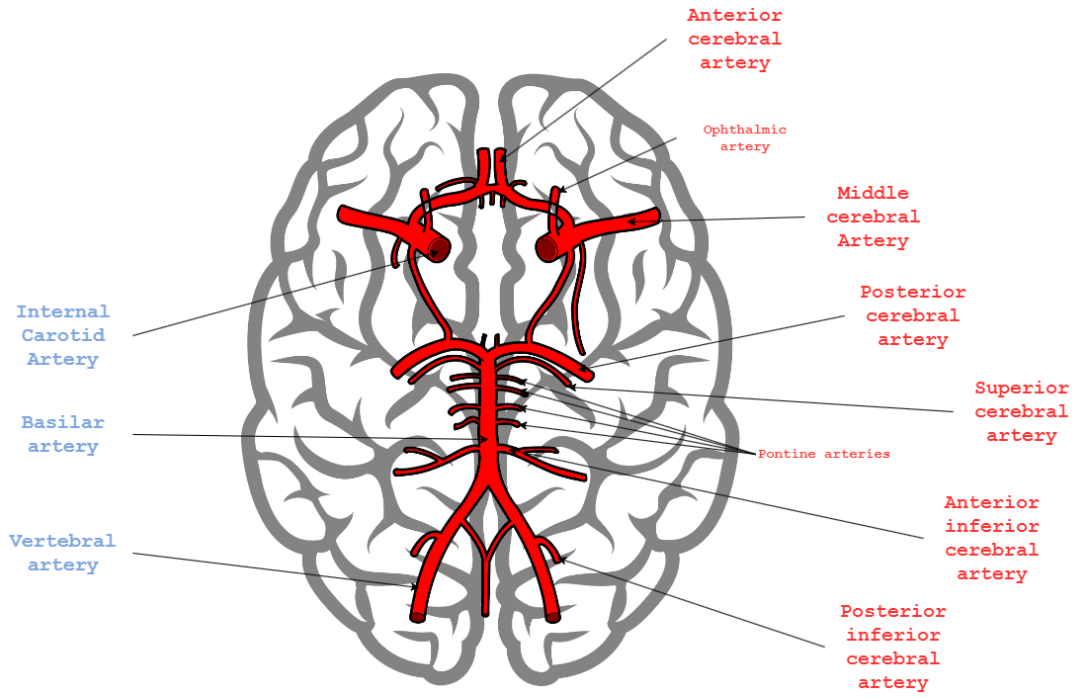

Figure 1.2: The Circle of Willis

harmful substances from entering the parenchyma. Comprising endothelial cells embedded in the basement membrane, the BBB is highly permeable to lipid-soluble substances such as O_2 and CO_2 while effectively restricting lipophobic solutes. This protective mechanism protects the brain from external interference and maintains precise control of the chemical environment of the brain. In addition, the BBB acts as a metabolic barrier, capable of metabolising drugs and nutrients. It is important to note that although crucial, the BBB does not contribute any load-bearing components to the cerebral arteries [30].

Elastic arteries have multiple layers of elastin in the media layer, extending from the internal elastic lamina to the external elastic lamina, which is the boundary between the media and adventitia layers. In contrast, cerebral vessels only have the internal elastic lamina and at the end of the media layer there is a layer of smooth muscle cells (SMCs) [31]. Furthermore, cerebral vessels have fewer elastin layers [32], which leads to a much higher collagen-to-elastin ratio than vessels in other parts of the body [33].

Cerebral blood flow regulation

The human brain is the most important and central part of the body, making up approximately 2% of total body mass, yet it receives $\sim$ 15% of cardiac output and $\sim$ 20% of the oxygen and nutrients due to its high demand [34]. The oxygen and nutrients delivery, as well as the waste product removal is achieved by the

amount of blood reaching the brain through the cerebral blood flow.

There are several factors that affect the blood flow within the brain such as changes in perfusion pressure (the difference between mean arterial pressure and cerebrospinal fluid), changes in the vascular radius, changes in blood viscosity. Alterations in perfusion pressure can arise under normal circumstances, such as shifts in posture or exercise, or they may be induced by drug administration or pathological conditions. The viscosity of blood is directly linked to both hematocrit and the concentration of hemoglobin in the blood and can be altered. The impact of the vascular radius on cerebral blood flow, however, is the most interesting as it plays a crucial role in modulating and regulating CBF. This sensitivity of blood flow to vessel radius is highlighted by the fourth power relationship according to the Poiseuille equation. Changes in arterial radius is modulated by changes within the vascular SMCs through vasoconstriction or vasodilation. There are a number of factors that drive vasoconstriction/vasodilation within the SMCs of the arteries, for example one powerful vasodilator is CO_2, which is able to decrease the blood flow under hypocapnic conditions, and vice versa [35]. However, the most physiologically relevant mechanisms regulating cerebral haemodynamics, are the brain metabolism through neurovascular coupling and autoregulation.

Neurovascular coupling ensures an adequate blood supply to meet the increased metabolic demands of active brain regions. When certain parts of the brain become more active, such as during cognitive tasks or sensory processing, there is a need for more oxygen and nutrients to support the heightened neuronal activity. This increase in cerebral blood flow is driven by various vasoactive mediators, which are substances that can influence blood vessel diameter [36].

Cerebral autoregulation is a physiological mechanism that helps maintaining a relatively constant blood flow to the brain despite fluctuations in systemic blood pressure. Autoregulation of cerebral blood flow involves the ability of cerebral arteries and arterioles to actively adjust their diameter in response to changes in blood pressure. The primary goal is to ensure a stable and adequate supply of oxygen and nutrients to brain cells while preventing damage related to excessive pressure. In situations where systemic blood pressure increases, the cerebral vessels constrict to prevent excessive blood flow that could potentially damage the capillaries and neurones of the brain. On the contrary, when systemic blood pressure decreases, cerebral vessels dilate to maintain sufficient blood flow and oxygen delivery to the brain. This autoregulatory process is crucial to protect the brain from hypoperfusion or hyperperfusion, which could lead to ischemia or hemorrhage, respectively. Cerebral autoregulation is a dynamic and continuous process that occurs in response to changes in metabolic demand and perfusion pressure, helping to ensure the optimal functioning of the brain under varying

physiological conditions. Although the basic mechanisms of autoregulation and neurovascular coupling are not fully understood, there are probably some shared pathways between the two [37, 34].

The physiological foundation of cerebral autoregulation is not fully understood and comprises different mechanisms such as metabolic, neurogenic, and myogenic[38, 39]. The metabolic mechanism involves changes in blood pressure that influence the concentration of vasoactive metabolites [40], thus adjusting blood flow, while the neurogenic mechanism suggests that perivascular neurones play a regulatory role in vessel function [41]. Given its importance, the main focus of this thesis is on the myogenic mechanism, which will be discussed in the following section.

Myogenic mechanism Resistance vessels and large arteries in the homeostatic state are partly contracted. This state of partial contraction is called the basal tone. Basal tone is essential for maintaining the readiness of muscles and organs to respond to stimuli. Vascular tone refers to the degree of constriction or dilation of blood vessels, primarily arteries and arterioles, and controlled by the SMCs in the walls of blood vessels. When blood vessels constrict, the vascular tone increases, leading to a decrease in the diameter of the vessels. This constriction raises blood pressure and reduces blood flow to the tissues. Conversely, when blood vessels dilate, vascular tone decreases, resulting in an increase in vessel diameter, lower blood pressure, and increased blood flow to the tissues. Those two tones, though conceptually separate, collaborate to maintain the balance of physiological processes.

During the myogenic response, when blood pressure is increased suddenly, the vessel is dilated following the pressure increase. Within seconds, however, the vessel develops a vascular tone that causes them to constrict. On the contrary, when blood pressure suddenly decreases, the vascular tone falls, causing a dilation to the vessel. The myogenic response is a mechanism that is very well developed, especially in the cerebral circulation [42].

When the intraluminal pressure increases within an artery or arteriole, the wall is stretched. This stretch causes a depolarisation of the SMC with a consequent elevation in intracellular calcium. The applied mechanical stress is sensed either within the SMC or the endothelium within the vascular wall, and several ionic channels are activated, whose composition depends on the physiological function of the vessel [43, 44, 45]. These channels in turn, dominating the contribution of the L-type calcium ones, are causing ionic exchange within the SMC and cations move from the extracellular to the intracellular space. Increased intracellular calcium concentration, in particular, promotes the synthesis of myosin

light chain kinase (MLCK), which, through the phosphorylation of myosin light chains (LC20), stimulates the interaction between actin and myosin, leading to the formation of cross-bridges between the two proteins. These cross-bridges are responsible for the development of active vascular tone and, hence, cause vasoconstriction [46, 47].

These pathways described above are a widely accepted mechanism of intracellular interactions that lead to the development of the vascular tone. However, there is experimental evidence that indicates that calcium signalling is not the only pathway through which pressure modulates the contractile machinery of the SMC. Research has shown that beyond specific pressure thresholds (approximately 40–60 mmHg), cellular tone is influenced by pathways that do not directly alter intracellular Ca^{2+} levels. Instead, these pathways function as parallel mechanisms, capable of modifying the sensitivity of the contractile machinery to fluctuations in Ca^{2+}, and rearranging the cytoskeleton of the cell through different signalling pathway [48, 49]. These concepts are discussed in more detail in Chapter 3 as it is one of the main motivations for the development of the cell signalling model presented in this thesis.

As the myogenic response causes a blood vessel to narrow, the increased shear stress on the endothelium prompts the endothelial cells to generate certain vasodilators which prevent excessive constriction [42].

1.2 Numerical modelling

In this section a literature overview of the developments in numerical modelling on vascular mechanics is presented. The fields of particular interest lies on the modelling of the arterial wall, the cellular dynamics and the vascular haemodynamics.

1.2.1 Passive mechanical response models

One of the first numerical models of the arterial wall was the highly influential model by Fung *et al.* [50] who introduced the nonlinearities of the continuum through a strain energy function formulation. This model was generalised to the three-dimensional regime [20, 51], while other models were derived from this formulation that included shear deformations [52, 53].

Holzapfel *et al.* [13, 54] incorporated an isotropic Neo-Hookean component and modified the exponential expression of Fung by using tensor invariants. In their study, structural anisotropy is introduced through the reinforcement of collagen fibres, and the model successfully reproduced the distinctive stress-strain rela-

tionship. Since then, this model has been extensively used in the literature and is acknowledged to offer a foundational framework for constructing more advanced models. The models that were derived from [13, 54] were used to model soft tissues in general and specific cases but, more interestingly for this thesis, for numerous applications in the mechanics of arterial wall tissue. In the following, those applications are briefly reported.

Fibre-reinforced models have been the basis for the study of several biological soft tissues. Applications referring to specific soft tissues include studies on the ovine infrarenal vena cava [55], the fibrous tissue of the intestinal wall [56], fibrosus annulus of the lumbar spine [57], and myocardium [58]. Moreover, in soft tissue modelling there were developments in constitutive frameworks that studied several general aspects of soft tissue, such as fibre reorientation [59] or viscoelasticity of tissues [60, 61, 62].

Furthermore, it was widely used in applications regarding the modelling of healthy arteries, which is in line with the scope of this thesis. Holzapfel *et al.* extended their arterial wall model to include viscoelastic effects [15], and the determination of model parameters to include clinical data was determined by Staalhand [63] and Masson *et al.* [64]. There were also advancements that incorporated four families of fibres instead of two [65, 66, 67], and the model was used for the analysis of the wall behaviour during arterial clamping [68]. Applications concerning arteries under pathological conditions also used these formulations as a baseline. Modifications of the model [69, 70] were developed to study atherosclerosis and balloon angioplasty [71], and Rodriguez [72] described the mechanical behaviour of the balloon in a coronary artery using the model by [54]. Furthermore, the multi-layered model by Kroon and Holzapfel [73] was used to study cerebral aneurysm tissue by inverse finite element analysis (FEA). Inverse analysis was also used to study fusiform aneurysms [74], while abdominal aortic aneurysms [75] were studied with the model by [13]. The field of tissue remodelling and tissue growth has also drawn considerable attention. In this context, models were developed or derived that studied collagen fibre remodelling within the arterial wall [76, 77], or arteries growth and remodelling [78, 79].

1.2.2 Vascular wall models including vascular tone

The number of models developed that include the development of active vascular tone is significantly lower than those that describe solely the passive mechanical response of the arterial wall.

The baseline modelling of active contraction was based on the three-element muscle model of Hill [80], which was the first model representation of the mechanical response of the muscle. As can be seen in Figure 1.3, the model contains a con-

tractile element (CE) in parallel with a nonlinear spring element (PE), and in series with another nonlinear spring element (SE). The active tone developed in the CE is the force produced by the cross-bridges of the actomyosin filaments, as described in Section 1.1.2. The passive response is represented by the PE, while the SE represents the elasticity of the filaments. The overall force-length characteristics of a muscle are the result of the combined effects of active and passive elements.

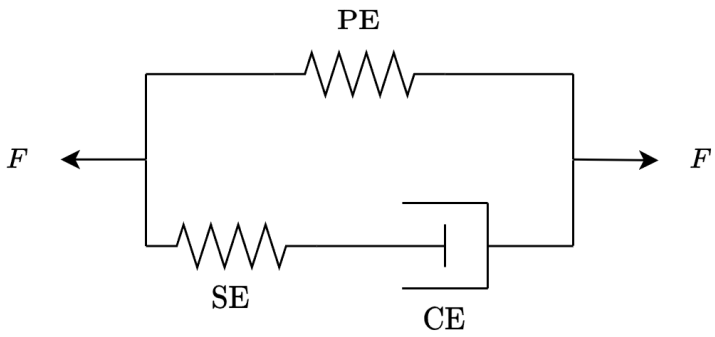

Figure 1.3: The three-element Hill muscle model model

Several models were developed based on the Hill model. One of the first models was the one developed by Gastrelius and Borgstrom [81] where they represented the active contraction with the one-dimensional Hill model, also considering experimental findings that could not be taken into account in the classical Hill model. The model of Carlson *et al.* [82] modelled the myogenic response based on measured length-tension characteristics of smooth muscle, making the assumption that vascular tone has a sigmoidal dependence on circumferential stress. Rachev and Hayashi [83] introduced a three-dimensional continuum mechanics phenomenological model for the passive response, introducing the vascular tone through circumferential stress. The model was extended by Zulliger *et al.* [84] who added the fibre contribution to the material properties with a pseudo-SEF along with a Hill model.

Another modelling approach for incorporating active tone requires the use of more than one sub-model to represent distinct elements participating in the total arterial wall response. One of the most popular approaches is the dynamic modelling of the cross-bridge formation within the SMC. The most widely used method to account for this is through the model developed by Hai and Murphy [85]. Yang *et al.* [86] combined an electrochemical model, which accounted for the dynamic formation of the cross bridge and other intracellular processes, with a Hill-based chemo-mechanical to fully describe the response of a rat cerebrovascular vessel. Schmitz and Bol [87] decoupled the SEF into active and passive parts, where the active part depends on the cross-bridge formation through a calcium-driven representation. Murtada *et al.* [47] developed a framework which

uses the Hai-Murphy model coupled with a Hill-based mechanical model as the active component of a decoupled SEF. Subsequently, this model was extended [88] to include the remodelling of the SMC cytoskeleton.

The final model presented [88] is the basis for the development of the chemo-mechanical model used in this thesis and is described in more detail in Chapter 4.

1.2.3 Computational haemodynamics

Undoubtedly computational haemodynamics can provide efficient quantification of blood flow phenomena, providing insight that is very hard to obtain via direct measurement. Fluid-structure interaction (FSI) modelling are the most accurate approach since it combines the contributions of both the blood flow and the vessel wall within the vascular network.

Reduced order fluid models

Three-dimensional FSI models provide the most accurate solution as they are able to account for all the geometrical details of the problem [89, 90]. However, they come with a very high computational cost and very complex computational domains, hence they are generally only applied at local circulations [91, 92, 93]. Moreover, they require a large amount of input data which in many cases are not easily accessible.

The detailed vessel geometry required is often obtained from 3D/4D radiographic imaging such as computed tomography (CT) scans or magnetic resonance imaging (MRI). Hemodynamic parameters often necessitate assuming the velocity profile at the inlet, whereas pressure measurements typically require the invasive surgical procedures. Furthermore, the material properties required to accurately compute the wall motion are neither easily nor ethically measured. It would require a sample of the patient artery since an ex-vivo sample would have significant differences from the in-vivo environment. This difficulty has led to either making the assumption of isotropic properties in FSI models, although that is not valid as explained in Section 1.1.1, or utilising data from expensive imaging data for the wall dynamics [94, 95]. Wall motion can be utilised to either estimate the wall properties, or to be imposed as a boundary condition, which does not require the wall model. The compliance of the vessel is inferred from time differences in pressure waveforms.

One way to overcome all the aforementioned difficulties rising from the three-dimensional FSI approach is the use of reduced order modelling (ROM), which can provide extremely competitive computational efficiency with an acceptable

reduction in accuracy [96]. Derivations of one-dimensional formulations from three-dimensional models in the fluid domain, and potentially in the solid one, can be a very good compromise. Such methods have improved the fundamental understanding in haemodynamics, providing accurate predictions for cases where the flow is predominantly uni-directional. There are numerous problems that have been gained very useful insights through 1D modelling, such as coronary circulation [97, 98], systemic heat transfer [99], cerebral artery flow regulation [55], and the entire human cardiovascular system [100, 26, 101]. While the concept of ROM for haemodynamics application existed from the 1970s [102], it has been used extensively the last two decades, with most important contributions being the works of Stergiopoulos *et al.* [103], Reymond *et al.* [104], Formaggia *et al.* [105], Sherwin et al. [106], Mynard and Nithiarasu [97], and Alastruey *et al.* [107]. Different numerical methods have been employed to solve the one-dimensional FSI problem, such as finite differences [108], finite elements [97, 109, 105], and finite volumes [110]. For the validation of 1D flow models, in-vivo, in-vitro, or in-silico data are generally used [111, 104, 112]. These averaged models have the option to be integrated with 3D models. This is particularly useful in scenarios where hemodynamic quantities are evaluated under the effect of localised phenomena [113, 114].

Advanced arterial wall models

In hemodynamic models, it is common practice to simplify by neglecting viscosity effects and assuming an elastic tube law for the vascular wall response to pressure [106, 97, 105]. However, smooth muscle cells (SMCs) in the arterial wall give it a viscoelastic behavior [115]. To better represent the vascular wall, it is necessary to add viscoelastic effects. Bessems et al. [116] showed that considering wall viscoelasticity is crucial for accurately predicting how pressure and flow waves propagate and attenuate. Reymond et al. [117] assessed a 1-D distributed viscoelastic model of the human arterial tree, comparing its predictions with measured pressure and flow waveforms. The results suggest significant viscoelastic effects, especially in peripheral branches, seen in both qualitative and quantitative waveform and pressure-flow parameter comparisons. Studies have utilized Voigt-type viscoelastic models to replicate these effects [118, 105, 26, 107], reducing discrepancies between observed and simulated pulse waveforms. Alastruey et al. [107] reported comparable findings when evaluating 1D viscoelastic simulations against data obtained from a 37-branch network in silicone material.

Because of these considerations, several recent efforts have focused on enhancing the understanding of vessel walls, employing linear, quasilinear viscoelasticity, or more advanced nonlinear models [119, 120, 121, 122]. In the work of Coccarelli et

al. [123] the 1D fluid equations are coupled with a 3D derived hyperelastic model that includes the effects of residual stresses based on [13], introducing anisotropy. This work is the basis for the framework described in this thesis.

1.3 Motivation and aim of the thesis

The arterial flow within cerebral vessels is essential for brain health. To ensure that the brain receives a continuous and well-regulated supply of blood, cerebral autoregulation is responsible for maintaining a steady blood flow, regardless of fluctuations in systemic blood pressure. This helps to prevent inadequate or excessive perfusion, which could lead to neurological problems such as ischemia or haemorrhage. Malfunction of cerebral autoregulation can contribute to a variety of brain diseases and conditions including stroke, traumatic brain injury, vascular dementia, and Alzheimer's disease. It is, therefore, essential to understand this intricate reaction, and its impact on tissue perfusion. One of the most influential factors is the myogenic tone that is generated in response to changes in pressure within the blood vessels.

Although a lot of research has been conducted on modelling pressure-induced vascular adaptations [124], this fundamental process still requires a full elucidation and quantification. To the knowledge of the author, there is no model that includes all the procedures that occur on different scales to assess the effect the myogenic response has on blood flow within the cerebral vessels. With this work, the aim is to develop a multi-physics framework that model the myogenic mechanism at both cellular and vascular wall scale and evaluate its effect on blood flow and pressure. This is carried out through a multi-physics approach that integrates the coupled vascular wall and blood flow domains, with the chemical processes within the SMC.

Figure 1.4 shows the structure of the model developed within the thesis. The framework consists of three models: a chemical one that accounts for the intracellular signalling pathways occurring within the SMCs; a chemo-mechanical one that translates these intracellular processes to active vascular tone development; and an FSI solver that integrates the active tone within the material properties of the vascular wall and finally computes the blood flow within the vessel. The specific function of each distinctive sub-model is discussed briefly next. The cell signalling model developed is a representation of all the intracellular signalling pathways that lead to the formation of actomyosin cross-bridges and for the level of F-actin which promotes the cytoskeleton polymerisation, both affecting the level of vascular tone development. The model is accounting for these processes as a response to intraluminal level of pressure. The active tone is generated with

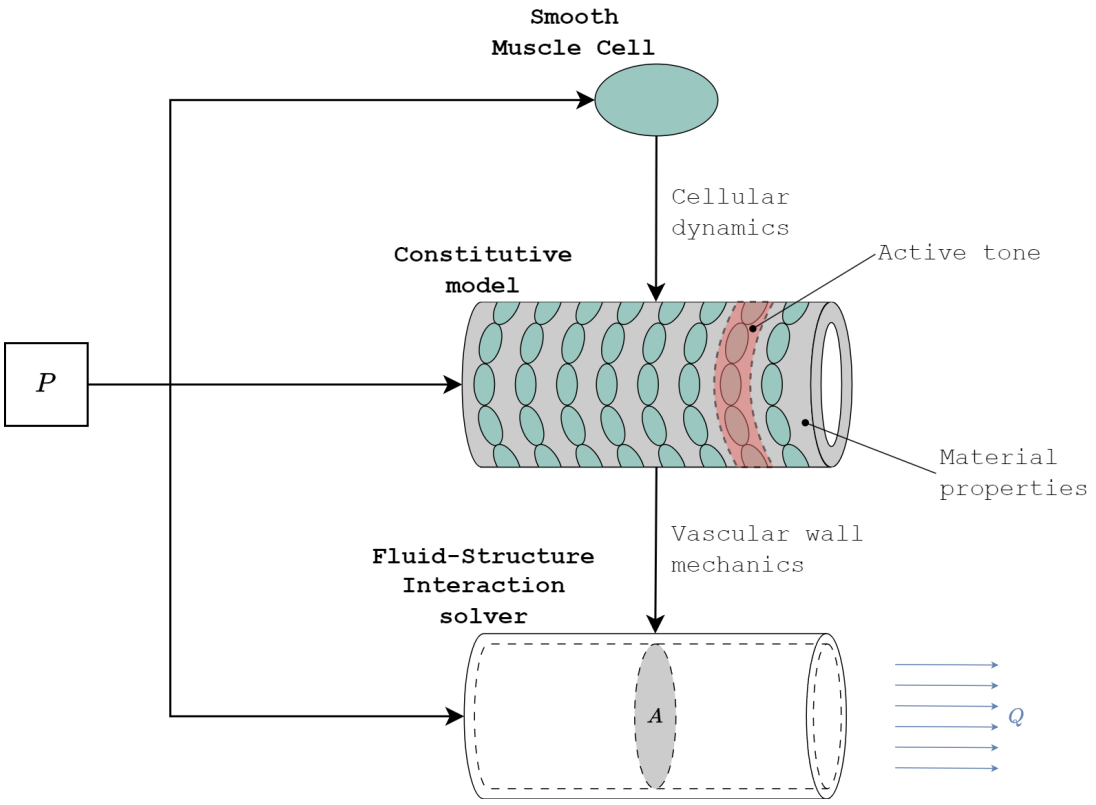

Figure 1.4: Schematic of integrated framework

a chemo-mechanical model which translates the active tone information from the cellular to the tissue level. In the model, passive surrounding elements (mainly F-actin), constituting the actin cortex, are connected with contractile units arranged in series to form the tissue contractile fibres. The developed active stress is incorporated into the vascular wall model as the active component of a decoupled SEF, where its passive part represents the material properties. The constitutive relationship provides the pressure–area relationship of the vascular wall including the active and passive components. Finally, the FSI framework couples the aforementioned structural model of the vascular wall with a one-dimensional fluid dynamics solver, to ultimately provide the flow development within the vessel. Pressure boundary conditions are imposed since the interest of the study is to assess the effect of pressure fluctuations to flow development.

1.4 Thesis outline

Concluding this introductory chapter, this section presents the structure of the thesis with a brief description of each chapter included.

Chapter 2: In this chapter, the mathematical background of the FSI solver is presented. All the necessary background including the fluid and structural

models used are outlined along with their respective formulations. These include the derivation of the 1D flow model, as well as the 3D derived structural model for the vascular wall material. Finally, a framework is presented that identifies the structural model parameter space for different experimental data found in literature. The experimental data were collected to include both uni-axial and bi-axial tests.

Chapter 3: This chapter explores the cellular level of the contractility mechanisms. At first, an overview of the models that have been developed on the field of cellular dynamics of SMCs which govern the arterial contractility is presented. This overview aims to identify the key features that have a significant role in the response, and two models are presented in more detail. Next, the chemical model that was developed in the context of this thesis is presented. The proposed model is based on a logic-based approach that includes all the major intracellular pathways found in literature. The simulated behaviour of five different intracellular components well matches experimental measurements across a large pressure range, for physiological and drug intervention scenarios.

Chapter 4: In this chapter, the chemical model of the previous chapter is incorporated into a 3D hyperelastic material model to account for the the vascular wall mechanics. This serves as a bridge between the cellular dynamics and the tissue response during myogenic response. The active response is modelled as an extra term in the strain energy function of the structural model, and it integrates the output of the chemical model. All the formulation for this integration are presented and explained, as well as the fitting of the model parameters to experimental data. Finally, the model is assessed regarding its steady state and transient output for several cases.

Chapter 5: In this chapter, the structural model is coupled with a reduced order (1D) fluid solver to form the fluid-structure interaction framework that models the blood flow development within cerebral vessels under myogenic response. All the numerical formulations of the coupling between the two models is described as well as the boundary condition setups and the solution procedure. Next, the steady state solution of the FSI framework is presented and discussed, followed by the transient study of the vessel. Finally, the vessel is attached to a Windkessel model to account for the downstream circulation and assess the interaction of the system.

Chapter 6: In this final chapter, a brief summary of all the models that constitute the framework developed for the thesis is made. The advancements and limitations of the framework is discussed, and possible future directions are proposed.

Chapter 2

Vascular Haemodynamics

In this chapter, the mathematical foundation for the solution of the coupled vascular wall with the blood flow problem is reported. The formulations for computing the one-dimensional Navier-Stokes equations for the flow within compliant vessel are presented, as well as the zero-dimensional models for representing the flow at the downstream circulation. Furthermore, the chosen vascular wall model is reported and discussed, along with the extraction of its constitutive relation. The numerical schemes employed and the discretisation they produce are also presented. Finally, a fitting procedure was performed to identify the parameters that reproduce the behaviour of several cerebral vessels. The methodology followed for this fitting procedure, along with the produced results, is presented in the final section of the chapter.

2.1 Derivation of 1D blood flow model

In this section, all the mathematical formulations for deriving the one-dimensional Navier-Stokes equations are presented. Moreover, a description of the one-dimensional velocity profile choice is reported. The formulations are reported in the Doctoral thesis of Carson [125] and are repeated here for completeness.

2.1.1 Governing equations

The incompressible Navier-Stokes equations in three dimensions describe the motion of a viscous fluid under constant density. The governing continuity equation is

$$\nabla \cdot \mathbf{u} = \frac{\partial u_x}{\partial x} + \frac{\partial u_y}{\partial y} + \frac{\partial u_z}{\partial z} = 0, \tag{2.1}$$

where $\mathbf{u} = (u_x, u_y, u_z)$ is the fluid velocity in the three dimensions respectively.

The governing momentum equations in three dimensions are

$$\frac{\partial u_x}{\partial t} + \left(u_x \frac{\partial u_x}{\partial x} + u_x \frac{\partial u_y}{\partial y} + u_x \frac{\partial u_z}{\partial z} \right) + \frac{1}{\rho} \left(\frac{\partial P}{\partial x} \right) + \left(\frac{\partial \tau_{xx}}{\partial x} + \frac{\partial \tau_{xy}}{\partial y} + \frac{\partial \tau_{xz}}{\partial z} \right) = f_x, \tag{2.2}$$

$$\frac{\partial u_y}{\partial t} + \left(u_y \frac{\partial u_x}{\partial x} + u_y \frac{\partial u_y}{\partial y} + u_y \frac{\partial u_z}{\partial z} \right) + \frac{1}{\rho} \left(\frac{\partial P}{\partial y} \right) + \left(\frac{\partial \tau_{yx}}{\partial x} + \frac{\partial \tau_{yy}}{\partial y} + \frac{\partial \tau_{yz}}{\partial z} \right) = f_y, \tag{2.3}$$

$$\frac{\partial u_z}{\partial t} + \left(u_z \frac{\partial u_x}{\partial x} + u_z \frac{\partial u_y}{\partial y} + u_z \frac{\partial u_z}{\partial z} \right) + \frac{1}{\rho} \left(\frac{\partial P}{\partial z} \right) + \left(\frac{\partial \tau_{zx}}{\partial x} + \frac{\partial \tau_{zy}}{\partial y} + \frac{\partial \tau_{zz}}{\partial z} \right) = f_z. \tag{2.4}$$

For x, y, z Cartesian coordinates, respectively. Here, τ is the Cauchy stress tensor and P is the hydro-static pressure. The source terms f_x, f_y, f_z may represent external load terms, such as gravity. Their inclusion (or not) depends on the nature of the problem.

The system consisting of the Navier-Stokes equations (2.1) – (2.4) is closed with the energy conservation, and the equation of state, which interconnects pressure, temperature, and density. In the context of this thesis, none of those two is needed in 1D formulations.

The derivation of the one-dimensional formulation of the Navier-Stokes equations from the above three-dimensional one is achieved through several assumptions, such as axially symmetric flow which is much higher in this direction than any other. The assumptions are presented in more detail later in the text.

The first step for reducing the system to one dimension is applying a change in the coordinate system to the governing equations

$$(x, y, z) \to (x, r, \theta). \tag{2.5}$$

Transformation (2.5) implies a transition from Cartesian to cylindrical coordinate system. Under this transformation, the coordinate mapping would be

$$x = x, \tag{2.6}$$

$$y = r \sin \theta, \tag{2.7}$$

$$z = r \cos \theta. \tag{2.8}$$

Blood can be assumed to be homogeneous and behaves as a Newtonian fluid

with constant viscosity for vessels larger than $200\,\mu m$ in diameter [2, 126]. With the assumption of Newtonian fluid, the 3D continuity equation on the cylindrical coordinate system is

$$\frac{1}{r}\frac{\partial(ru_r)}{\partial r} + \frac{1}{r}\frac{\partial(u_\theta)}{\partial \theta} + \frac{\partial(u_x)}{\partial x} = 0. \tag{2.9}$$

After the coordinate transformation, the expression of the momentum equation in the cylindrical directions will become

$$\begin{aligned}\rho\left[\frac{\partial u_r}{\partial t} + u_r\frac{\partial u_r}{\partial r} + \frac{u_\theta}{r}\frac{\partial u_r}{\partial \theta} - \frac{u_\theta^2}{r} + u_x\frac{\partial u_r}{\partial x}\right] + \frac{\partial P}{\partial r} \\ - \mu\left[\frac{1}{r}\frac{\partial}{\partial r}\left(r\frac{\partial u_r}{\partial r}\right) - \frac{u_r}{r^2} + \frac{1}{r^2}\frac{\partial^2 u_r}{\partial \theta^2} - \frac{2}{r^2}\frac{\partial u_\theta}{\partial \theta} + \frac{\partial^2 u_r}{\partial x^2}\right] = \rho f_r,\end{aligned} \tag{2.10}$$

$$\begin{aligned}\rho\left[\frac{\partial u_\theta}{\partial t} + u_r\frac{\partial u_\theta}{\partial r} + \frac{u_\theta}{r}\frac{\partial u_\theta}{\partial \theta} - \frac{u_\theta u_r}{r} + u_x\frac{\partial u_\theta}{\partial x}\right] + \frac{\partial P}{\partial \theta} \\ - \mu\left[\frac{1}{r}\frac{\partial}{\partial r}\left(r\frac{\partial u_\theta}{\partial r}\right) - \frac{u_\theta}{r^2} + \frac{1}{r^2}\frac{\partial^2 u_\theta}{\partial \theta^2} - \frac{2}{r^2}\frac{\partial u_r}{\partial \theta} + \frac{\partial^2 u_\theta}{\partial x^2}\right] = \rho f_\theta,\end{aligned} \tag{2.11}$$

$$\begin{aligned}\rho\left[\frac{\partial u_x}{\partial t} + u_r\frac{\partial u_x}{\partial r} + \frac{u_\theta}{r}\frac{\partial u_x}{\partial \theta} + u_x\frac{\partial u_x}{\partial x}\right] + \frac{\partial P}{\partial x} \\ - \mu\left[\frac{1}{r}\frac{\partial}{\partial r}\left(r\frac{\partial u_x}{\partial r}\right) + \frac{1}{r^2}\frac{\partial^2 u_x}{\partial \theta^2} + \frac{\partial^2 u_x}{\partial x^2}\right] = \rho f_x.\end{aligned} \tag{2.12}$$

After obtaining the expressions of the continuity and momentum equation in the cylindrical coordinates, the derivation of the one dimensional formulation takes place. This is achieved by making some necessary assumptions. At first, axial symmetry is assumed. Next, it is assumed that the vascular wall can only be displaced in the radial direction r. Moreover, the pressure is assumed constant in each cross section and there is no pressure gradient in the radial and circumferential direction. Finally, as already mentioned, the axial velocity is assumed to be much higher than any of the other two, which allows the omission of the other two components. With these assumptions, the momentum equation along the axial direction takes the following form

$$\frac{\partial u_x}{\partial t} + u_x\frac{\partial u_x}{\partial x} + \frac{1}{\rho}\frac{\partial P}{\partial x} - \frac{\mu}{\rho}\left[\frac{1}{r}\frac{\partial}{\partial r}\left(r\frac{\partial u_x}{\partial r}\right) + \frac{\partial^2 u_x}{\partial x^2}\right] = f_x. \tag{2.13}$$

If the momentum equation is integrated over a section, the expression will be

$$\frac{\partial Q}{\partial t} + \frac{\partial\left(\alpha\frac{Q^2}{A}\right)}{\partial x} + \frac{A}{\rho}\frac{\partial P}{\partial x} - \int_{CS}\frac{\mu}{\rho}\left(\frac{1}{r}\frac{\partial}{\partial r}\left(r\frac{\partial u_x}{\partial r}\right)\right)d\sigma + \frac{\partial^2 Q}{\partial x^2} = Af_x. \tag{2.14}$$

Here, $Q = Au$ is the volumetric flow rate within a cross-section A, u is the

averaged axial velocity, r is the radial component coordinate, while x the axial one. The term α appearing in the Equation (2.14) is called the momentum flux correction term, and it depends on the choice of the velocity profile, which is discussed in Section 2.1.2. Through this term, the non-uniform distribution of velocity is taken into account, and it is given by

$$\alpha = \frac{\int_{CS} u_x^2 \, d\sigma}{Au^2}. \tag{2.15}$$

Similarly to the momentum formulation, the continuity equation in its one-dimensional expression will be

$$\frac{\partial A}{\partial t} + \frac{\partial Q}{\partial x} = \Phi, \tag{2.16}$$

where Φ is a source/sink term.

This system involves three variables: area A; flow rate Q (or velocity u); and hydrostatic pressure P, as shown in Figure 2.1. The constitutive law serves is the extra equation that closes the system, establishing a connection between the pressure and the cross-sectional area. Section 2.2 looks at the constitutive law applied in one-dimensional blood flow models.

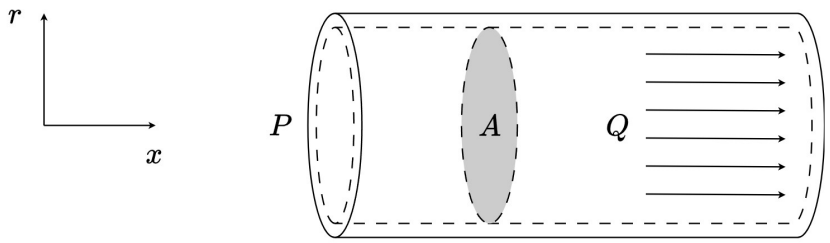

Figure 2.1: Overview of the flow within a blood vessel and the variables P, Q, A

By manipulating equations (2.16) and (2.14) in different ways, one can derive various formulations of the one-dimensional blood flow equations. The three most used variants include the AU [106, 97], AQ [105, 127, 128], and PQ [129, 130] formulations, depending on which variables are included in the momentum and continuity equations.

If in the continuity equation (2.16) the chain rule is applied, this will produce

$$\frac{\partial A}{\partial t} = \frac{\partial A}{\partial P}\frac{\partial P}{\partial t} = C\frac{\partial P}{\partial t}. \tag{2.17}$$

Applying the chain rule, the PQ formulation is obtained. In equation (2.17), the term C represents the compliance of the vessel, which is defined as the area gradient with respect to pressure, and is a key variable in one dimensional haemo-

dynamics. The formulation PQ is the one used in [125] and the present work. In this variation the continuity and momentum equations take the form

$$\frac{\partial A}{\partial P}\frac{\partial P}{\partial t} + \frac{\partial Q}{\partial x} = 0 \tag{2.18}$$

$$\frac{\rho}{A}\frac{\partial Q}{\partial t} + \frac{\rho}{A}\frac{\partial\left(\alpha\frac{Q^2}{A}\right)}{\partial x} + \frac{\partial P}{\partial x} - \frac{f}{A} = 0. \tag{2.19}$$

2.1.2 Velocity profile

The selection of velocity profile will have an effect on two terms in the momentum equation, the friction term and the momentum flux correction factor α. The velocity profile used in this work is the one used in [131, 132], and given by

$$u(x,r) = U\frac{\zeta+2}{\zeta}\left[1-\left(\frac{r}{R}\right)^{\zeta}\right], \tag{2.20}$$

where R is the vessel radius, r the radial coordinate, and $\zeta = \frac{2-\alpha}{\alpha-1}$. The friction term is found by integration of the profile equation (2.20) within a cross section

$$f = \int_{\mathrm{CS}} \frac{\mu}{\rho}\left(\frac{1}{r}\frac{\partial}{\partial r}\left(r\frac{\partial u_x}{\partial r}\right)\right) d\sigma = \frac{-2(\zeta+2)\mu\pi Q}{A}. \tag{2.21}$$

Figure 2.2 illustrates the velocity profiles using Equation (2.20). In the figure the flat profile is obtained with a value of $\alpha = 1$. That profile is imposed in the momentum flux term. For the friction term, the fixed value of $\zeta = 2$ is chosen, which gives the Poiseuille velocity profile, and the friction term is becomes

$$\frac{f}{A} = -8\pi\mu\frac{Q}{A^2}. \tag{2.22}$$

So far, the axial direction was referred to as x. From this point forward, the axial direction will be noted with the letter z. It was not changed through the derivation of the governing equations because the reader might confuse z of the axial direction with the z component in the Cartesian coordinate system.

2.2 Vascular wall model

To solve the system of equations (2.18) – (2.19), a constitutive law is necessary to establish a relationship between a section's cross-sectional area and the transmural pressure

$$P_{\mathrm{tm}}(A) = P - P_{\mathrm{ext}}, \tag{2.23}$$

where P_{ext} is the external pressure outside the vessel.

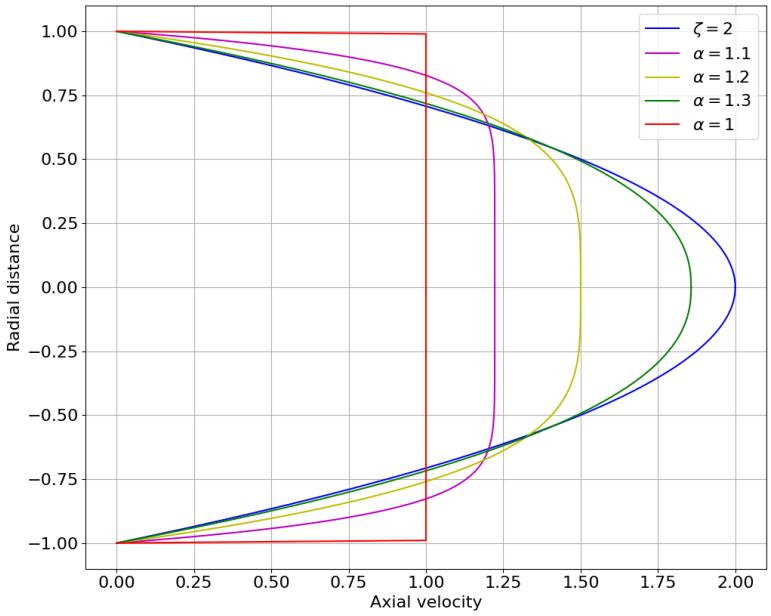

Figure 2.2: Different velocity profiles generated for various values of α

Various constitutive laws are used in one-dimensional models, and one of the most widely used is the nonlinear elastic tube law [106, 105, 97, 109] given by

$$P_{\text{tm}} = 2\rho c_0^2 \left(\frac{\sqrt{A}}{\sqrt{A_0}} - 1 \right) + P_0 = \frac{\beta}{A_0} \left(\sqrt{A} - \sqrt{A_0} \right) + P_0. \tag{2.24}$$

Here P_0 and A_0 is the reference pressure, and the respective area for that pressure level, while c_0 is the reference wave speed at P_0.

Another often used constitutive law is the power law [133, 134, 26] which reads

$$P_{\text{tm}} = \frac{2\rho c_0^2}{b} \left[\left(\frac{A}{A_0} \right)^{b/2} - 1 \right] + P_0, \quad b = \frac{2\rho c_0^2}{P_0 - P_{\text{collapse}}}, \tag{2.25}$$

where P_{collapse} is the pressure level where the vessel completely collapses. The viscoelastic properties of the vascular wall are introduced with an extra term in the constitutive law [105, 26, 107].

From the constitutive law, one can determine the compliance of the vessel at a given pressure. Compliance defines the association between the change in area and the change in pressure. Generally, the constitutive law is formulated as $P = f(A)$. Due to the non-linear relationship between pressure and area, especially in the case of nonlinear constitutive laws, it might not be possible (or straightforward) to rearrange the function to the form $A = f^{-1}(P)$. Consequently, calculating the derivative $\partial A/\partial P$ may not be simple. However, as mentioned in [125], per

the inverse function theorem, for a continuously differentiable function f with a non-zero derivative at a point in its domain, f is invertible in a neighborhood of this point. Its inverse f^{-1} is also continuously differentiable, and the derivative of the inverse function in this neighborhood is the reciprocal of the derivative of f. This implies that the derivative of $P = y(A)$ with respect to A can be expressed as

$$\frac{\partial P}{\partial A} = \frac{1}{\frac{\partial A}{\partial P}}. \tag{2.26}$$

In this thesis, the constitutive relation between lumen area and blood pressure is established by deriving a three-dimensional hyperelastic model describing the properties of the vascular wall. The next section will describe the structural model used in this thesis.

2.2.1 Structural kinematics

The original wall model was proposed by Coccarelli *et al.* [123]. Again, the derivation of the model is described in [123] and is repeated here for completeness.

In accordance with the flow model, axisymmetric deformation is assumed for the vascular wall. Given that residual strains in large arteries have a significant influence on mechanical characteristics [135], these strains are introduced by considering three configurations for the vessel: the *stress-free*; the *load-free*; and the *loaded* configuration, as shown in Figure 2.3.

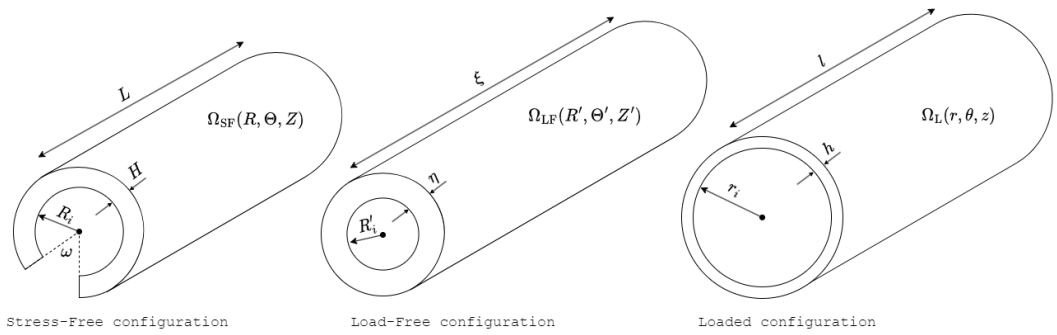

Figure 2.3: Configurations of the vascular wall. From left to right: *stress-free* (Ω_{SF}), *load-free* (Ω_{LF}), and *loaded* (Ω_L) configuration

In the *stress-free* configuration, the vessel does not experience stresses along the radial and axial directions. On the contrary, in the *load-free* configuration, residual stresses exist within the wall of the vessel, while the vessel is not loaded. In laboratory settings, to release these residual stresses, samples are typically cut along both axial and circumferential directions. The assessment of residual stresses commonly involves evaluating the opening angle and axial shortening

observed in the sample after cutting [136, 137, 138, 139]. It is noted that the employment of the different configurations is a suitable way to include all the residual stresses (and stretches) to the structural model. In cylindrical coordinates, the three configurations are described by

$$\Omega_{\mathrm{SF}} : R \in [R_i, R_i + H]\,, \quad \Theta \in [0, 2\pi - \omega]\,, \quad Z \in [0, L]\,, \tag{2.27}$$

$$\Omega_{\mathrm{LF}} : R' \in [R'_i, R'_i + \eta]\,, \quad \Theta' \in [0, 2\pi]\,, \quad Z' \in [0, \xi]\,, \tag{2.28}$$

$$\Omega_{\mathrm{L}} : r \in [r_i, r_i + h]\,, \quad \theta \in [0, 2\pi]\,, \quad z \in [0, l]\,. \tag{2.29}$$

where R_i, R'_i, r_i are the inner radii, L, ξ, l the vessel lengths, H, η, h the wall thickness in the $\Omega_{\mathrm{SF}}, \Omega_{\mathrm{LF}}, \Omega_{\mathrm{L}}$ respectively, while, ω is the opening angle that accounts for the residual stresses, as can also be seen in Figure 2.3.

The axial length of the vessel is assumed to remain constant regardless of the loading exerted by the fluid. Therefore, from the *stress-free* to the *loaded* configuration, the axial stretch would be

$$l = \lambda_{\mathrm{z,res}} \lambda_{\mathrm{z,ext}} L. \tag{2.30}$$

Here, $\lambda_{\mathrm{z,res}}$ is the residual axial stretch, while $\lambda_{\mathrm{z,ext}}$ is the axial stretch due to external loading. The mapping from the *stress-free* to the *loaded* configuration is achieved through the incompressibility constraint

$$\Omega_{\mathrm{SF}} \to \Omega_{\mathrm{L}} : \quad r = \sqrt{\frac{R^2 - R_i^2}{\kappa \lambda_z} + r_i^2}, \tag{2.31}$$

where κ is a parameter representing the residual stress, and it is defined as $\kappa = 2\pi/(2\pi - \omega)$, while $\lambda_z = \lambda_{\mathrm{z,res}} \lambda_{\mathrm{z,ext}}$. Without torsion, the deformation gradient for $\Omega_{\mathrm{SF}} \to \Omega_{\mathrm{L}}$ is diagonal and and can be written in the form [13]

$$\mathbf{F} = \mathbf{I} \left[\frac{\partial r}{\partial R}, \frac{r}{R} \frac{\partial \theta}{\partial \Theta}, \frac{l}{L} \right]^{\mathrm{T}} = \mathbf{I} \left[\frac{R}{r \kappa \lambda_{\mathrm{z}}}, \frac{\kappa r}{R}, \lambda_z \right]^{\mathrm{T}}. \tag{2.32}$$

From equations (2.31) and (2.32) it is seen that the complete description of kinematics across the artery is determined solely by the internal radius r_i and fixed parameters that characterise the opening angle ω and the axial stretch λ_z. The three primary stretches occur along the coordinates

$$\lambda_r = \frac{R}{r \kappa \lambda_z}, \tag{2.33}$$

$$\lambda_\theta = \frac{\kappa r}{R}, \tag{2.34}$$

$$\lambda_z = \lambda_{\mathrm{z,res}} \lambda_{\mathrm{z,ext}}, \tag{2.35}$$

while the right Cauchy-Green strain tensor $\mathbf{C}$ and the first strain invariant I_1 will be

$$\mathbf{C} = \mathbf{F}^{\mathrm{T}}\mathbf{F}, \tag{2.36}$$

$$I_1 = \mathrm{tr}(\mathbf{C}) = \lambda_r^2 + \lambda_\theta^2 + \lambda_z^2. \tag{2.37}$$

There is evidence that arteries are reinforced with collagen fibres, which are helically aligned across the circumferential direction [139, 140]. The implementation of a number of fibres throughout the circumference would be through the fourth strain invariant [13]. If a collagen fibre is placed with a helical angle ϕ, the unit vector along the fibre direction would be $\mathbf{n} = [0, \cos\phi, \sin\phi]$, and therefore the fourth invariant would be

$$I_4 = \mathbf{n} \cdot \mathbf{C}\mathbf{n} = \lambda_\theta^2 \cos\phi^2 + \lambda_z^2 \sin\phi^2, \tag{2.38}$$

which can be extended for any number of fibres [67, 141].

2.2.2 Equilibrium equations

The vascular wall is treated as a hyperelastic material. If its strain energy density is $\Psi(I_1, I_4)$, then the Cauchy stress tensor will be derived as

$$\boldsymbol{\sigma} = 2\mathbf{F}\frac{\partial \Psi}{\partial \mathbf{C}}\mathbf{F}^{\mathrm{T}} - p\mathbf{I}, \tag{2.39}$$

where p is a Lagrange multiplier that enforces incompressibility [142, 143]. Therefore, the normal stress components would be

$$\sigma_{rr} = \lambda_r \frac{\partial \Psi}{\partial \lambda_r} - p, \tag{2.40}$$

$$\sigma_{\theta\theta} = \lambda_\theta \frac{\partial \Psi}{\partial \lambda_\theta} - p, \tag{2.41}$$

$$\sigma_{zz} = \lambda_z \frac{\partial \Psi}{\partial \lambda_z} - p. \tag{2.42}$$

The circumferential momentum equilibrium equation is satisfied, whereas the axial direction does not require consideration due to the assumption of fixed axial stretch. As a result, only the radial component remains, which can be formulated as follows

$$d\sigma_{rr} = \frac{\sigma_{\theta\theta} - \sigma_{rr}}{r} dr. \tag{2.43}$$

Here, the pressures at the internal and external surfaces will equal σ_{rr}. Therefore, by integrating equation (2.43) across the thickness (from the inner to the outer surface of the vascular wall), the pressures acting on the inner and outer surfaces

of the wall will be produced

$$P_{\text{in}} - P_{\text{ext}} = \int_{r_i}^{r_i+h} \frac{\sigma_{\theta\theta} - \sigma_{rr}}{r}\, dr. \tag{2.44}$$

The assumptions made with this derivation are: that the external pressure is constant along the length of the vessel; and that the intraluminal pressure P_{in} is equal to the average blood pressure. Switching the stress terms in equation (2.44) with the expression of the components, and changing the integration variables from *loaded* to the *stress-free* configuration, yields

$$P - P_{\text{ext}} = \int_{R_i}^{R_i+H} \left(\lambda_\theta \frac{\partial \Psi}{\partial \lambda_\theta} - \lambda_r \frac{\partial \Psi}{\partial \lambda_r}\right) \frac{1}{\lambda_\theta \lambda_z r}\, dR, \tag{2.45}$$

And following the same rationale, the integration of the axial stress over the cross section yields the respective expression for the axial force

$$F_z = \pi \int_{R_i}^{R_i+H} \left(2\lambda_z \frac{\partial \Psi}{\partial \lambda_z} - \lambda_\theta \frac{\partial \Psi}{\partial \lambda_\theta} - \lambda_r \frac{\partial \Psi}{\partial \lambda_r}\right) \frac{1}{\lambda_\theta \lambda_z}\, dR. \tag{2.46}$$

2.2.3 Constitutive model

The arterial wall is considered a single layer material, consisting only of the medial layer. This assumption was made for two reasons. At first, considering multiple layers would significantly increase the computational time required for the simulation since it adds an extra complexity to the model. Next, in the majority of the experimental works found in literature regarding the study of active response of vessels, the adventitial layer is removed so the media layer is isolated, and hence only the media layer contributes to the structural behaviour of the vessel. Since the scope of this study is to reproduce and make predictions based on experimental evidence, a single (media) layer model is a suitable assumption. As explained in previous sections, the material of the vascular wall is considered a hyperelastic, fibre-reinforced material. The fibres are placed with a fibre angle ϕ^i with $\phi^{i=1} = -\phi^{i=2}$. The Strain Energy Function (SEF) used is the one proposed by Holzapfel *et al.* [54]

$$\Psi = c(I_1 - 3) + \frac{k_1}{2k_2} \sum_{i=1,2} \left\{ \exp\left[k_2 \left((1-\alpha)(I_1-3)^2 + \alpha(I_4^i - 1)^2\right)\right] - 1 \right\}. \tag{2.47}$$

Here, c, k_1, k_2 are material parameters, with c and k_1 are pressure-like, while k_2 is dimensionless. Moreover, c is the parameter associated with the isotropic part

of the deformation [144]. α is a linear interpolation parameter associated with the contribution of the fibres to the overall response, and I_1, I_4 are the first and fourth strain invariants as already discussed.

In the chosen constitutive model, it is assumed that collagen fibres lack the ability to endure compression loads. Consequently, the anisotropic contribution $I_4^i - 1$ is nullified when $I_4^i < 0$.

If, now, the expression of the SEF in equation (2.45) is replaced with the expression of equation (2.47) the pressure can be expressed as a function of multiple parameters

$$P - P_{\text{ext}} = f(A, H, R_i, \lambda_z, \omega, c, k_1, k_2, \alpha, \phi) = \bar{P}(A, \bar{\psi}). \tag{2.48}$$

Here the dependency on A instead of r_i (which is given by equation (2.45)) is due to the fact that $r_i = \sqrt{A/\pi}$. Furthermore, the vector $\bar{\psi}$ is a vector containing all the parameters except the area.

Figure 2.4 shows a comparison of three different constitutive laws. The 3D derived hyperelastic refers to the law presented in this section, while the other two, i.e. the nonlinear elastic and the power law, were described in the beginning of the section.

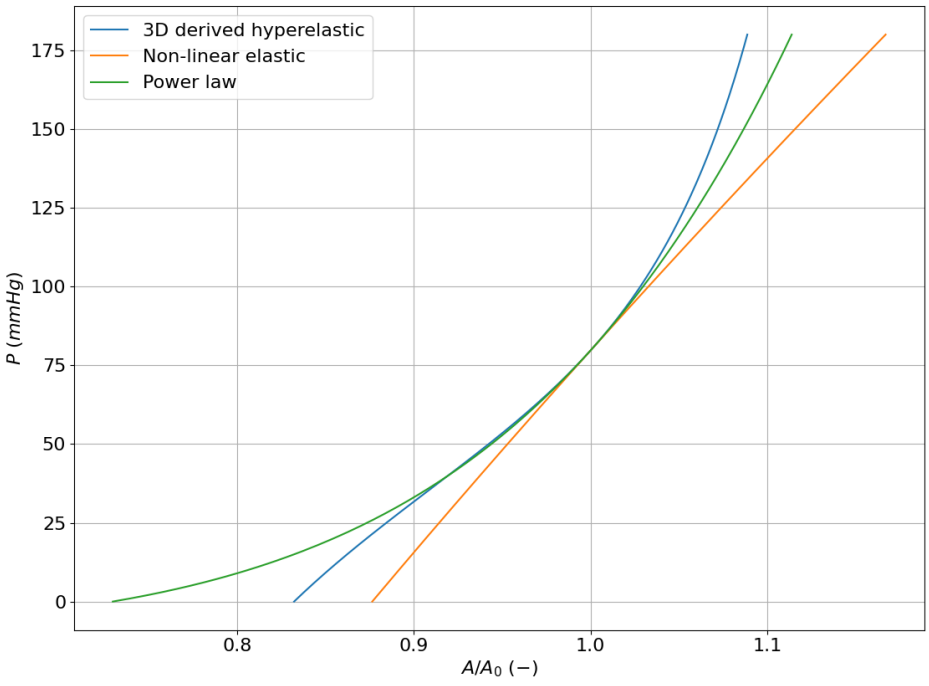

Figure 2.4: Comparison of different constitutive laws

The incorporation of the constitutive law within the blood flow equations, as well as the solution procedure followed for the calculation of the compliance are discussed in the next sections.

2.3 Lumped parameter models for downstream circulation

In 1D modelling, 0D models can be used for representing groups of vascular beds which do not need a detailed representation in space. This is a common practice in many haemodynamics models of the whole body circulation where vascular beds across the whole body are represented through lumped parameter models [104, 26, 100]. There are also works that focus on specific parts of the body, such as the cerebral circulation [25, 145, 146]. Lumped parameter models can be employed to represent the remainder of the circulation downstream a specific point that the 1D model is chosen to be cut off.

The application of 0D models in fluid dynamics involves reducing the complex physics of a system into three essential elements, each representing a primary physical response of fluid flow within a tube. These elements, namely resistance, compliance, and inertance, play crucial roles in capturing the dynamic behavior of the fluidic system.

Resistance, in the context of fluid dynamics, is an element representing the opposition to the flow within a tube. It quantifies the impedance of the fluid in its movement reflecting. For a Poiseuille velocity profile, the resistance of a section Δx and area A is described through

$$R = \frac{8\mu\pi}{A_0^2}\Delta x. \tag{2.49}$$

Compliance plays a significant role in describing the ability of the vessel to undergo changes in volume in response to alterations in pressure. This element represents the elastic properties of the vessel wall, and it is expressed as

$$C = \frac{\partial A_0}{\partial P}\Delta x. \tag{2.50}$$

Inertance characterises fluid inertia and its resistance to changes in flow velocity. It reflects the tendency of the fluid to maintain its current state, and is expressed as

$$L = \frac{\rho}{A_0}\Delta x. \tag{2.51}$$

The flow equations can be described by a set of those elements in a system. This

system reads

$$\Delta P = RQ, \quad \text{Resistance}, \tag{2.52}$$

$$\Delta P = L\frac{\partial Q}{\partial t}, \quad \text{Inductance}, \tag{2.53}$$

$$C\frac{\partial P_{\text{tm}}}{\partial t} = Q_{\text{net}} = Q_{\text{in}} - Q_{\text{out}}. \quad \text{Compliance.} \tag{2.54}$$

The most common representation of 0D models are the Windkessel models. The simplest is the two-element Windkessel model, introduced by Otto Frank in 1899, consisting of peripheral resistance R_{p} and total arterial compliance C_{T}. In the context of this thesis, a three-element Windkessel is used, which was first introduced by Westerhof [147]. In this model, a resistance is places in series with a resistance and a compliance in parallel, as can be seen in Figure 2.5.

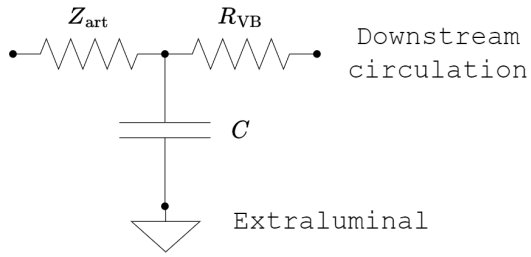

Figure 2.5: Three-element Windkessel model

The initial resistance Z_{art}, identified as the characteristic impedance of the connecting vessel [148], is an intermediate element connecting the simplified lumped model, which is incapable of representing wave propagation phenomena, and the 1D representation of the vessel associated with wave propagation in vascular systems. R_{VB} represents the resistance to the blood flow in the smaller peripheral vessels or the vascular bed. It accounts for the viscous resistance in the circulation, representing the impedance by the smaller arteries and arterioles. Moreover, the compliance C represents the elasticity of the arteries prticipating in the downstream circulation. It reflects the ability of these arteries and arterioles to expand and store blood.

The implementation of the Windkessel model and the connection to the 1D formulations is discussed in later sections.

2.4 Numerical schemes

In this section, an overview of the numerical methods employed for solving the one-dimensional blood flow equations is presented. The numerical schemes utilized are reported, as well as the linearisation and discretisation procedures ap-

plied to the blood flow equations across the framework components. These components are the 1D vessels, 0D models representing the downstream circulation, and the interconnection between 1D and 0D models. Again, all schemes and formulations are reported in detail in the Doctoral thesis of Carson [125], and repeated here for completeness.

In this thesis, the Enhanced Trapezoidal rule Method (ETM) is used, which is proposed by Carson and Van Loon [149]. The ETM scheme is essentially an expansion of the Simplified Trapezoid Method (STM), introduced by Kroon *et al.* [129].

The PQ system from equations (2.18) – (2.19) is considered, with the Poiseuille velocity profile. Furthermore, if the compliance is assumed which by definition is $C_A = \partial A/\partial P$, the governing equations are

$$C_A \frac{\partial P}{\partial t} + \frac{\partial Q}{\partial z} = 0, \tag{2.55}$$

$$\frac{\rho}{A}\frac{\partial Q}{\partial t} + \frac{\rho}{A}\frac{\partial}{\partial z}\left(\frac{Q^2}{A}\right) + \frac{\partial P}{\partial z} + 8\pi\mu\frac{Q}{A^2} = 0. \tag{2.56}$$

2.4.1 Linearisation of the 1D system

In order to discretise the nonlinear system, it has to be linearised. To that end, the following linearisation takes place

$$C_A^{n+1} \approx C_A^{n+1,k}, \quad Q^{n+1} \approx Q^{n+1,k}, \quad P^{n+1} \approx P^{n+1,k},$$
$$\frac{Q^2}{A}^{n+1} \approx \frac{Q^2}{A}^{n+1,k}, \quad \frac{\rho}{A}^{n+1} \approx \frac{\rho}{A}^{n+1,k}, \quad \frac{8\mu\pi Q}{A^2}^{n+1} \approx \frac{8\mu\pi Q}{A^2}^{n+1,k},$$

where k refers to the iteration level and n to the temporal step. To start the iterations, the assumption $k = 1 \approx n$ is made. Here, it is assumed that for all variables, the value at the first iterative step of the next time step would be equal to the value at the previous time step, i.e. $n+1, k \approx n$. For simplicity and to limit the computational time of the solution procedure, only one iterative step is executed [125], as it has shown that it produces accurate results [149]. This means that $n+1, k+1 \approx n+1$. Finally, the linearised continuity and momentum equations have the form

$$C_A^n \frac{\partial P}{\partial t} + \frac{\partial Q^{n+1}}{\partial z} = 0, \tag{2.57}$$

$$\frac{\rho}{A^n}\frac{\partial Q}{\partial t} + \frac{\partial P^{n+1}}{\partial z} = -\left[\frac{\rho}{A}\frac{\partial}{\partial z}\left(\frac{Q^2}{A}\right) + 8\pi\mu\frac{Q}{A^2}\right]^n. \tag{2.58}$$

2.4.2 Discretisation of the blood flow equations

The domain is divided into smaller elements, each with two nodes. The spatial integration of this system is achieved using the trapezoidal rule. Examining each term separately, integrating the mass equation within an element e, for the nodes 1 and 2 (subscript) the following expressions are obtained

$$\int_e \left(C_A^n \frac{\partial P}{\partial t} \right) dz = \frac{\Delta z}{2} \left(C_{A,1}^n \frac{\partial P_1}{\partial t} + C_{A,2}^n \frac{\partial P_2}{\partial t} \right), \tag{2.59}$$

$$\int_e \left(\frac{\partial Q^{n+1}}{\partial z} \right) dz = \left(Q_2^{n+1} - Q_1^{n+1} \right). \tag{2.60}$$

Similarly, for the terms within the momentum equation, following the same annotation, the following is obtained

$$\int_e \left(\frac{\rho}{A^n} \frac{\partial Q}{\partial t} \right) dz = \frac{\Delta z}{2} \left(\frac{\rho}{A_1^n} \frac{\partial Q_1}{\partial t} + \frac{\rho}{A_2^n} \frac{\partial Q_2}{\partial t} \right), \tag{2.61}$$

$$\int_e \left(\frac{\partial P^{n+1}}{\partial z} \right) dz = \left(P_2^{n+1} - P_1^{n+1} \right). \tag{2.62}$$

Let the right hand side of equation (2.58) be h, integrating it in space, similar to the above, yields

$$h = -\left[\frac{\rho}{A} \frac{\partial}{\partial z} \left(\frac{Q^2}{A} \right) + 8\pi\mu \frac{Q}{A^2} \right]^n \Rightarrow \int_e (h)^n \, dz = \frac{\Delta z}{2} \left(h_1 + h_2 \right)^n. \tag{2.63}$$

The discretisation indicates that the mass and momentum are conserved at the centre of each element. For the temporal discretisation of the time derivatives, a second-order backward difference scheme is used, which, given a variable U is

$$\frac{\partial U}{\partial t} \approx \frac{3}{2\Delta t} U^{n+1} - \frac{2}{\Delta t} U^n + \frac{1}{2\Delta t} U^{n-1} \tag{2.64}$$

Using the temporal and spatial discretisation that were presented, the full system reads

$$\begin{bmatrix} \frac{3}{2\Delta t} \frac{\Delta z}{2} C_{A,1}^n & \frac{3}{2\Delta t} \frac{\Delta z}{2} C_{A,2}^n \\ -1 & 1 \end{bmatrix} \begin{bmatrix} P_1 \\ P_2 \end{bmatrix}_e^{n+1} + \begin{bmatrix} -1 & 1 \\ \frac{3}{2\Delta t} \frac{\Delta z}{2} \frac{\rho}{A_1^n} & \frac{3}{2\Delta t} \frac{\Delta z}{2} \frac{\rho}{A_2^n} \end{bmatrix} \begin{bmatrix} Q_1 \\ Q_2 \end{bmatrix}_e^{n+1} = \begin{bmatrix} 0 \\ \frac{\Delta z}{2} \left(h_1^n + h_2^n \right) \end{bmatrix}_e + \begin{bmatrix} \frac{\Delta z}{2} \left(C_A^n \frac{2}{\Delta t} P^n - C_A^n \frac{1}{2\Delta t} P^{n-1} \right)_1 \\ \frac{\Delta z}{2} \left(\frac{\rho}{A^n} \frac{2}{\Delta t} Q^n - \frac{\rho}{A^n} \frac{1}{2\Delta t} Q^{n-1} \right)_1 \end{bmatrix}_e + \begin{bmatrix} \frac{\Delta z}{2} \left(C_A^n \frac{2}{\Delta t} P^n - C_A^n \frac{1}{2\Delta t} P^{n-1} \right)_2 \\ \frac{\Delta z}{2} \left(\frac{\rho}{A^n} \frac{2}{\Delta t} Q^n - \frac{\rho}{A^n} \frac{1}{2\Delta t} Q^{n-1} \right)_2 \end{bmatrix}_e, \tag{2.65}$$

which can be written in the generalised form

$$\mathbf{F}_e\mathbf{P}_e^{n+1} + \mathbf{G}_e^c\mathbf{Q}_e^{c,n+1} = \mathbf{h}_e^n. \tag{2.66}$$

Here, $\mathbf{G}_e^c$ and $\mathbf{Q}_e^{c,n+1}$ arrays are reported in the *conventional* discretisation. However, the flows of the ending nodes of the elements will be reversed to face the centre of the element.

Figure 2.6 shows the arrangement and flow of two neighbouring elements, which share a node (i). The discretisation of the right hand side of the h term, following the nodal annotation of Figure 2.6 is

$$\frac{\partial}{\partial z}\left(\frac{Q^2}{A}\right) \approx \left\{ \begin{array}{ll} \left[\left(\frac{Q^2}{A}\right)_i - \left(\frac{Q^2}{A}\right)_{i-1}\right]\frac{1}{\Delta z} & \text{if } Q_i^n > 0 \\ \left[\left(\frac{Q^2}{A}\right)_{i+1} - \left(\frac{Q^2}{A}\right)_i\right]\frac{1}{\Delta z} & \text{if } Q_i^n < 0 \end{array} \right\} \tag{2.67}$$

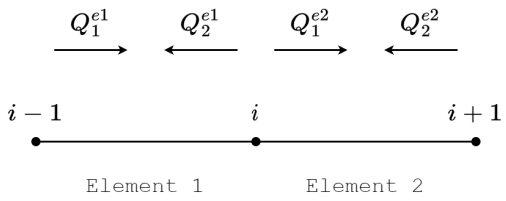

Figure 2.6: Nodal flows and annotation for two neighbouring elements with a shared node (i)

Now, the direction of the flow is changed, from the *conventional* one to the one shown in Figure 2.6. That is, they are enforced to face towards the centre of the element. This conventional change, alters matrix $\mathbf{G}_e^c$ and the flow vector $\mathbf{Q}_e^{c,n+1}$ to

$$\mathbf{G}_e^c = \begin{bmatrix} G_{11} & G_{12} \\ G_{21} & G_{22} \end{bmatrix} \rightarrow \mathbf{G}_e = \begin{bmatrix} G_{11} & -G_{12} \\ G_{21} & -G_{22} \end{bmatrix} \tag{2.68}$$

$$\mathbf{Q}_e^c = \begin{bmatrix} Q_1 \\ Q_2 \end{bmatrix} \rightarrow \mathbf{Q}_e = \begin{bmatrix} Q_1 \\ -Q_2 \end{bmatrix}. \tag{2.69}$$

For the solution, the matrix $\mathbf{G}_e$ is inverted, and ultimately, the final elemental system writes

$$\left[-\mathbf{G}_e^{-1}\mathbf{F}_e\right]\mathbf{P}_e^{n+1} = \left[-\mathbf{G}_e^{-1}\mathbf{h}_e^n\right] + \mathbf{Q}_e^{n+1}. \tag{2.70}$$

Once these individual elemental systems are combined into the matrix of the overall system, it becomes evident that the flow column Q_g^{n+1} corresponds to the conservation of mass between connected elements, resulting in a value of 0 for all internal nodes. The flow column, therefore, only contains non-zero

values at the boundaries, representing external flows. In other words, $Q^g_{n+1} = [Q_{\text{inflow}}, 0, \ldots, 0, Q_{\text{outflow}}]$. This has significant implications for the implementation at junctions, such as bifurcations, as it automatically ensures the continuity of mass [149]. The ETM extends the STM to allow conservation of total pressure to be applied between vessel segments, while within a vessel segment, the ETM and STM are identical.

After assembling the global matrix, the implicit system is solved to determine pressures, and subsequently the flows can be updated using the elemental system described in equation (2.70).

2.4.3 Connection of 1D vessel to Windkessel model

As already mentioned, it is common practice to connect a 1D vessel or network to a 0D model, and specifically a Windkessel model. Figure 2.7 shows the 1D vessel attached to the three-element Windkessel model, and the associated nodal discretisation.

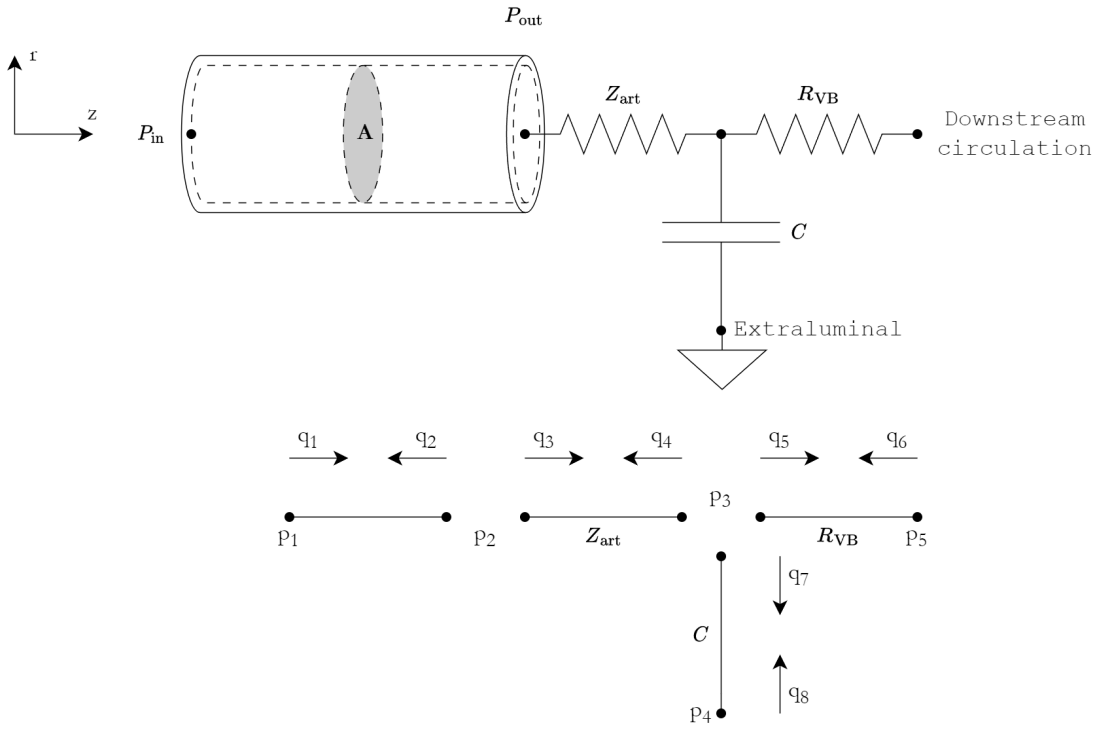

Figure 2.7: 1D vessel attached to a three-element Windkessel model

The Windkessel model can be treated using the elemental equations (2.52) – (2.54), with two pressure and two flow nodes. For the setup of Figure 2.7 the

Windkessel equations would be

$$\frac{1}{Z_{\text{art}}}\left(p_2^{n+1} - p_3^{n+1}\right) = q_3^{n+1} = -q_4^{n+1}, \tag{2.71}$$

$$\frac{1}{R_{\text{VB}}}\left(p_3^{n+1} - p_5^{n+1}\right) = q_5^{n+1} = -q_6^{n+1}, \tag{2.72}$$

$$C\left(\frac{\partial p_3^{n+1}}{\partial t} - \frac{\partial p_4^{n+1}}{\partial t}\right) = q_7^{n+1} = -q_8^{n+1}, \tag{2.73}$$

where the time derivative of equation (2.73) is discretised using a second-order backward difference scheme.

The elemental Windkessel equations exhibit a structure similar to the 1D blood flow equations, with pressure being the only unknown of the system

$$\mathbf{K}_e\mathbf{P}_e^{n+1} = \mathbf{f}_e + \mathbf{Q}_e^{n+1}. \tag{2.74}$$

Similar to the 1D equations, the flow rate column is again set to 0 (ensuring conservation of mass) in internal nodes, with only boundary flows having nonzero values. Once again, the conservation of mass is present in the flow rate column. The outlet boundary conditions for the Windkessel are the external and the downstream circulation pressures, which are generally set constant.

2.4.4 Coupling fluid flow with wall deformation

As described in Section 2.2, the mechanics of the vascular wall is dictated by the constitutive relation described. The specific constitutive relation that connects the pressure with the displacement of the wall defines the compliance of the vessel, and coupled the wall mechanics with the blood flow model.

Since equation (2.47) is a highly nonlinear relationship that links intraluminal pressure with the vascular deformation, a simple central finite difference scheme is employed to calculate the compliance

$$C_A = \frac{\partial A}{\partial P} = \frac{1}{\frac{\partial P}{\partial A}} \approx \frac{2\epsilon}{\bar{P}(A+\epsilon, \bar{\Psi}) - \bar{P}(A-\epsilon, \bar{\Psi})}, \tag{2.75}$$

where ϵ is a sufficiently small number (10^{-8}), and $\bar{P}$ is the pressure difference $P - P_{\text{ext}}$ from equation (2.48), which is numerically integrated by means of the integration rule of Simpson.

At each time step, the pressure distribution is acquired by solving the 1D equations. Given this pressure field at time step $n+1$, the area at each vessel node is also given by equation (2.48). To acquire the area at each node, the equation (2.48) must be solved iteratively. That is, with a given pressure, the area

that produces this pressure according to the equation needs to be found. That is achieved with the nonlinear solver `root` of the library `sciPy` in Python language.

After solving the FSI problem with the solution process explained, the resulting pressures, areas, and flow rates can be acquired in all the nodes of the 1D mesh (vessel or network).

Figure 2.8 presents the solution provided by the FSI model for the common carotid artery (CCA). The FSI solver used included the cerebral arterial network, attached to Windkessel models for the microcirculation. The model solves per cardiac cycle, and as boundary conditions the volumetric flow waveform was imposed at the input, while a venous pressure of 5 mmHg was set at the outlet of the Windkessel models. The FSI model computed the pressure field for the vessel, as well as the volumetric flow and area produced across the length. Since the vessels are considered having a circular cross-section, the velocity at each point would be given by the relationship $u = Q/A$. The area waveform of the vessel presents an oscillatory behaviour due to its elasticity, which is quantified by the compliance. These indicative results present the ability of the model to compute the variables of interest in a cardiovascular vessel or network.

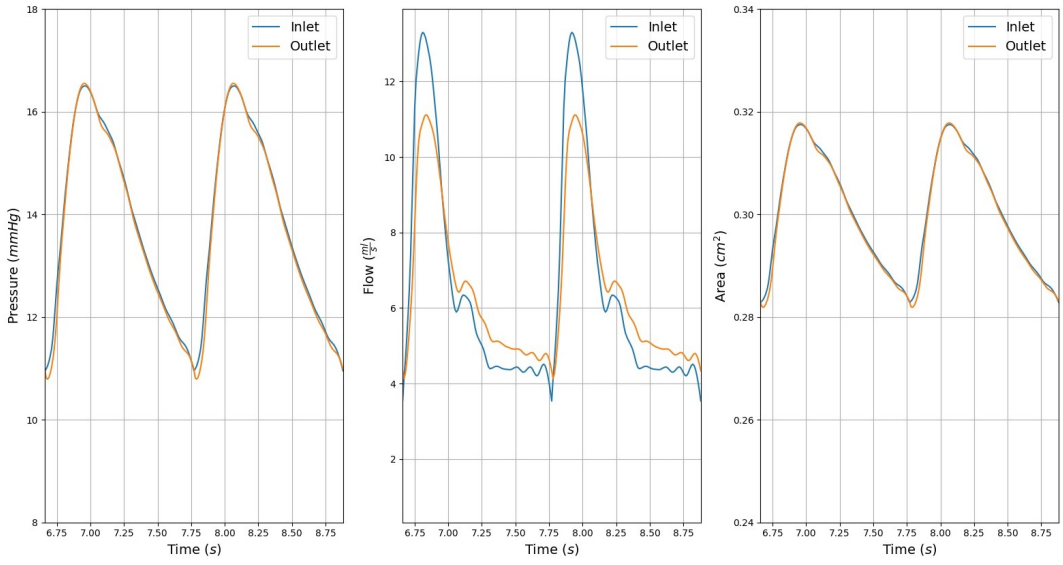

Figure 2.8: Indicative results of the FSI model. Pressure, volumetric flow rate and area waveforms within the CCA

2.5 Identification of passive wall properties

In this section, the parameters characterising the previously reported constitutive law are identified for vessels of different regions and species of the cerebral

cortex. In this way, the capacity of the model to capture the passive behaviour (experimentally recorded) of different vessels is assessed.

As reported in Section 2.2, the constitutive model used in this thesis includes a number of material parameters that define its behaviour. In the work of Coccarelli *et al.* [123], the model parameters were set to reproduce the behaviour of a CCA. Since the interest of this thesis lies on the study of cerebrovascular flow, the model parameters need to be refitted by considering experimental studies on cerebral arteries. The aim of the fitting procedure is to replicate different experimental vascular mechanical tests. The considered experiments were conducted with slightly different approaches, which resulted in a different amount of reported information.

Characterisations carried out for this study include the basilar artery of New Zealand white rabbits [67], human pial arteries [150], and human cerebral arteries [138]. With this choice of vessels the intention was to investigate a wide range of vessel sizes.

2.5.1 Methodology

In this part, the general methodology is presented. Specific details for slight alterations of each examined experiment case will be discussed on the relative section.

At first, the most basic variables are the inner radius R_i and the thickness H of the vessel at the reference configuration. As reported before in section 2.2.1, there are three configurations considered: *stress-free* (SF); *load-free* (LF); and *loaded* (L). The loaded configuration is the state at which the inner and outer pressure loads have been applied.

As mentioned already, residual stresses are modelled through an opening angle ω for each layer considered [23], which in experimental works is measured by cutting the vessel across the axial direction and measuring the angle produced. However, few works actually measure the opening angle [138, 67]. As far as this study is concerned, when data for the opening angle are available, they are used as measured. However, the experimental characterisation of the opening angle presents a very high variability even for the same arteries [138, 64]. To that end, when opening data is not available, a value is used arbitrarily that is within the range found in literature.

In experiments, where measurements are obtained through microscopy or other optical equipment, the measurement takes place before any cutting occurs and the radii (inner or outer) are reported at the LF configuration. The same is valid for the thicknesses reported, however there are fewer works that actually measure

the thickness of the vessel [138, 67] while other do not [151, 152, 150]. Since the thickness of the vessel is one of the most essential measurements for the vessel geometry definition, and the scope of this study is to idenitfy the consitutive parameters, statistical data are employed to assume a thickness level when the value is not trivial. At first, following the work of Bevan *et al.* [153], it is seen that for human pial arteries as the intraluminal vessel diameter increases, its thickness follows a linear increase, which means that the ratio of radius and thickness can be assumed to be within a small range. Furthermore, the Wall-to-Lumen Ratio (WLR) is introduced, which is ratio of vascular wall thickness to luminal diameter [154], and it is given by the following relationship:

$$\mathrm{WLR} = \frac{D_o - D_i}{2D_i}, \tag{2.76}$$

with D_o being the outer diameter and D_i the luminal. Obviously, the thickness is the difference between those diameters halved by two, or equivalently, the difference between outer and inner radii $H = R_o - R_i = \mathrm{WLR} \cdot D_i$. It is finally assumed, that the thickness of the vessel does not change between the LF and SF configuration [67].

The final quantity that needs to be defined is the value of the axial stretch. The total axial stretch value is $\lambda_z = \lambda_{z,\mathrm{res}} \cdot \lambda_{z,\mathrm{ext}}$, where $\lambda_{z,\mathrm{res}}$ is the axial stretch due to the residual stresses from SF to LF, and $\lambda_{z,\mathrm{ext}}$ is the axial stretch due to external loading. Hence, in order to define the transition from LF to SF configuration, the residual axial stretch is needed. Here this effect is either ignored ($\lambda_{z,\mathrm{res}} = 1.0$), or low residual stretch is assumed ($\lambda_{z,\mathrm{res}} = 1.05$). Since the framework in general assumes constant total axial stretch value, the crucial value is the *in-vivo* stretch. In all experiments considered for medium and small cerebral vessels, the value of the *in-vivo* stretch is low compared to the value for larger arteries such as the common carotid. Thus, it is assumed that the *in-vivo* stretch is the result of the loading of the vessel and not associated with residual stresses.

In Figure 2.9 only the LF and SF configurations of Figure 2.3 are shown. Note that unlike the definition of Fung for the opening angle [155], in this work the definition of Coccarelli *et al.* [123] is followed, which computes it from the centre of the vessel, and for a full circular plane. When moving from the LF to the SF configuration, the incompressibility of the vascular wall is considered between the two states.

$$\left(\pi - \frac{\omega}{2}\right)\left(R_o^2 - R_i^2\right) L = \pi \left(R_o'^2 - R_i'^2\right) \xi, \tag{2.77}$$

which, by the assumptions made for the thickness $H = \eta$, it is $R_o = R_i + H$ and $R_o' = R_i' + H$. Moreover, the constant κ is introduced, which is defined as $\kappa = 2\pi/(2\pi - \omega)$, and the residual axial stretch is defined as $\lambda_{z,\mathrm{res}} = \xi/L$. By swapping these in the incompressibility equation, and solving for the SF radius,

it is

$$R_i = \frac{\kappa\lambda_{z,\text{res}}}{2}\left(H + 2R_i'\right) - \frac{H}{2}. \tag{2.78}$$

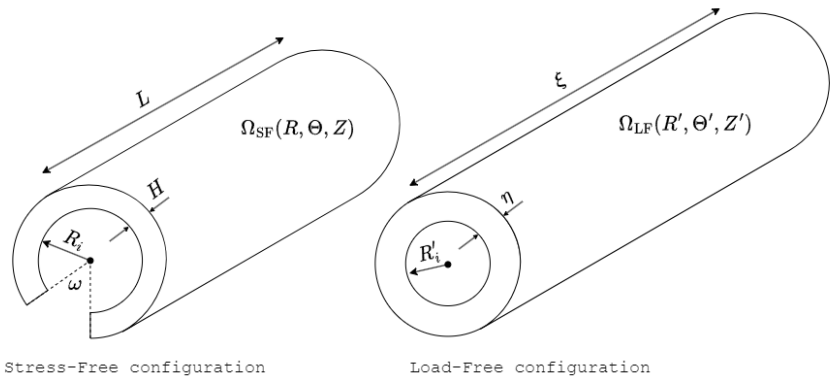

Figure 2.9: The reference configurations, *stress-free* on the left and *load-free* on the right

Through this mapping and the assumptions made, it is feasible to consider the experimental measurements from the works referenced as the LF state and define the SF configuration. Considering now the SEF described in Section 2.2.3 that is used for describing the passive behaviour

$$\Psi_p = c(\mathrm{I}_1 - 3) + \frac{k_1}{2k_2}\sum_{i=1,2}\left\{\exp\left[k_2\left((1-\alpha)(\mathrm{I}_1-3)^2 + \alpha(\mathrm{I}_4^i - 1)^2\right)\right] - 1.\right\} \tag{2.79}$$

With the formulations for the first and fourth strain invariants repeated here: $\mathrm{I}_1 = \lambda_r^2 + \lambda_\theta^2 + \lambda_z^2$; and $\mathrm{I}_4^i = \lambda_\theta^2\cos^2\phi^i + \lambda_z\sin^2\phi^i$. Furthermore, since collagen fibres are helically aligned [140], it is $\phi^1 = -\phi^2$. The characterisation of the vessels depends on finding the values for: c, k_1, k_2, α and ϕ^i.

The wall model is assumed to be single-layered with two circumferential-symmetric fibres at a helical arrangement around the wall. In reality, three layers consist the vessel wall with different fibre orientation in each one of them [140]. There are models developed, based on the one employed here, that use multiple layers and more fibres around the wall for each layer [15, 141]. However, the aim of characterisation and model is not to provide a framework that maximises the accuracy by a very detailed representation of the wall. Instead, the idea is to have a universal wall model that can accurately represent various cerebral vessels with a minimum number of parameters that need identification.

There is plenty of experimental work conducted that examined the passive (and active to some extent) response of vessels in order to assess its correlation to different aspects, such as gravitation [156], ageing [157, 158, 159], distensibility [150] and biochemical mechanisms [152] among others. All of the aforementioned studies are interested in the properties along the radial direction at a uni-axial

analysis of the pressure-diameter relationship. There are also studies, fewer in number, that are interested in the bi-axial response of the vessel, as they examine vascular behaviour along the radial and the axial directions [67, 138, 160].

For this study, the parameters are identified through a model parameter optimisation procedure that is also be employed in the next chapters. The covariance matrix adaptation (CMA) stochastic algorithm was employed through the library `cma` within Python environment. The final target was the minimisation of an error function, which minimised the difference between the model predictions and the experimental pressure-diameter diagrams.

With $d_{o,k}^{\text{exp}}$ being the diameter of each pressure point of the N points chosen, the respective pressure values were input to the solver. Given this pressure field the area at each vessel node is also given by equation (2.48) and the outer diameter d_o is obtained. Finally, the error function that is minimised is

$$e_d = \sqrt{\sum_{k=1}^{N} \left(\frac{d_{o,k}^{\text{exp}} - d_{o,k}}{d_{o,k}^{\text{exp}}} \right)^2}. \tag{2.80}$$

For the case of bi-axial tests, since more data were available, another term is added to the error function that is minimised. The interest of bi-axial experiment lie in identifying the force development in the axial direction. In the wall model implemented, the axial force is calculated through

$$F_z = \pi \int_{R_i}^{R_i+H} \left(2\lambda_z \frac{\partial \Psi}{\partial \lambda_z} - \lambda_\theta \frac{\partial \Psi}{\partial \lambda_\theta} - \lambda_r \frac{\partial \Psi}{\partial \lambda_r} \right) \frac{r}{\lambda_\theta \lambda_z} dR. \tag{2.81}$$

In all these studies, the constant axial stretch considered is the *in-vivo* one. To that end, in terms of solution procedure, a system of equations is set to simultaneously solve the two equations

$$P(A) - P_{in} = 0, \tag{2.82}$$

$$F(\lambda_z) - F_{in} = 0. \tag{2.83}$$

Here, Equation (2.83) is solved similar to the pressure-area equation, with the nonlinear solver described in Section 2.4.4. This way, the in-vivo stretch is computed, which corresponds to the F_{in} axial force value. Hence, the second error calculation refers to the axial force development deviation from the experimental

measurements, through the expression

$$e_F = \sqrt{\sum_{k=1}^{N} \left(\frac{F_{z,k}^{\exp} - F_{z,k}}{F_{z,k}^{\exp}} \right)^2}. \tag{2.84}$$

Depending on the experiment targeted, the above errors can be minimised and produce the wall model parameters. For the uni-axial tests, Equation (2.80) computes the error, while for bi-axial tests cases the error is calculated from a summation of Equations (2.80) and (2.84). Since the optimisation procedure uses a stochastic algorithm, the error functions may converge into local minima. To overcome this difficulty, each optimisation was conducted several times and a statistical analysis provided the vascular wall model parameters for each case.

2.5.2 Results and discussion

Here, the results of the optimisation procedure described previously is presented. The three experimental studies chosen are separately shown. The differences regarding the data that could be extracted from each experiment are discussed in their respective part.

Rabbit basilar artery

The first vessel is based on the work of Wagner and Humphrey [67] on a rabbit basilar artery. The work conducted by the authors employ a similar model with four fibres. This work was chosen as a baseline, to test if a simpler model can provide accurate results. Moreover, this is one of the few works that conducted a bi-axial test.

The parameter setup that is reported from the authors as well as the derived values for the LF configuration can be summarised in the Table 2.1.

Table 2.1: Summary of parameters from the work of Wagner and Humphrey [67] regarding the rabbit basilar artery

Parameter	Description	Value
$\lambda_{z,\text{res}}$ $(-)$	Residual axial stretch	1.0
R_i' (cm)	Inner radius	0.028
H (cm)	Thickness	0.006
ω (deg)	Opening angle	170
κ $(-)$	Constant related to the opening angle	1.89

To pass from the LF to the SF definition, Equation (2.78) is employed and the inner radius for the SF configuration is $R_i = 0.056cm$. The lowest pressure point

reported in this work is $P \approx 6mmHg$, and for such a low value the assumption was made that this is the LF state. Now that the vessel parameters have been set, and the SF state can be acquired, by reverse solving the system of Equations (2.82) and (2.83), provides the model predicted values for diameter and axial stretch that ensure that the pressure and axial force equal to the input values.

Since the work includes a bi-axial experimental test, the errors regarding the difference of the experimental and model-predicted diameter e_d and the axial force e_D are minimised. The total error e_t is calculated as the average between the two errors

$$e_t = \frac{1}{2}(e_d + e_F) = \frac{1}{2}\sqrt{\sum_{k=1}^{N}\left(\frac{d_{o,k}^{\text{exp}} - d_{o,k}}{d_{o,k}^{\text{exp}}}\right)^2} + \frac{1}{2}\sqrt{\sum_{k=1}^{N}\left(\frac{F_{z,k}^{\text{exp}} - F_{z,k}}{F_{z,k}^{\text{exp}}}\right)^2}. \quad (2.85)$$

Ten pressure points were chosen, i.e. $N = 10$, that divide the pressure space in equal increments. The pressure space of the respective experiment is between 6 and 80 $mmHg$. The optimisation procedure was repeated 50 times and the statistical results are presented below for the wall model parameters.

The results presented in Figure 2.10 show the results for all 50 runs of the optimisation procedure. They are presented in their parametric space where pairs of two parameters are compared in each plot to show their relative variation. In more detail, each of the subplots shows the range of each model parameter against the respective range of another. The heatmap shows the frequency that each set (for those two parameters) has been identified. With this plot it is easy to observe the spread of each parameter. If one parameter has a lot of spread against another one it means that it varies a lot. It is clear that the optimisation procedure leads to very good results, and the high density of points for each parameter indicate that the global minimum of the function has been reached. Table 2.2 shows the statistical analysis of the results illustrated.

Table 2.2: Statistical results of the optimisation procedure runs for the rabbit basilar artery

Parameter	Mean	Std dev	Geo. mean	Geo. std dev
c (dyn/cm^2)	1164	± 1364	138.6	20.7
k_1 (dyn/cm^2)	247919	± 3011	247901	1.012
k_2 $(-)$	0.598	± 0.065	0.595	1.101
ϕ^1 (deg)	51	± 0.103	51	1.002
α $(-)$	0.735	± 0.012	0.735	1.016

The statistical findings of the fitting results show a very good convergence in all parameters. The only parameter that presents a high standard deviation is the one related to the elasticity of the wall c. It even shows a high variance in terms of mean versus geometric mean. This is explained because the stiffness of the vessel

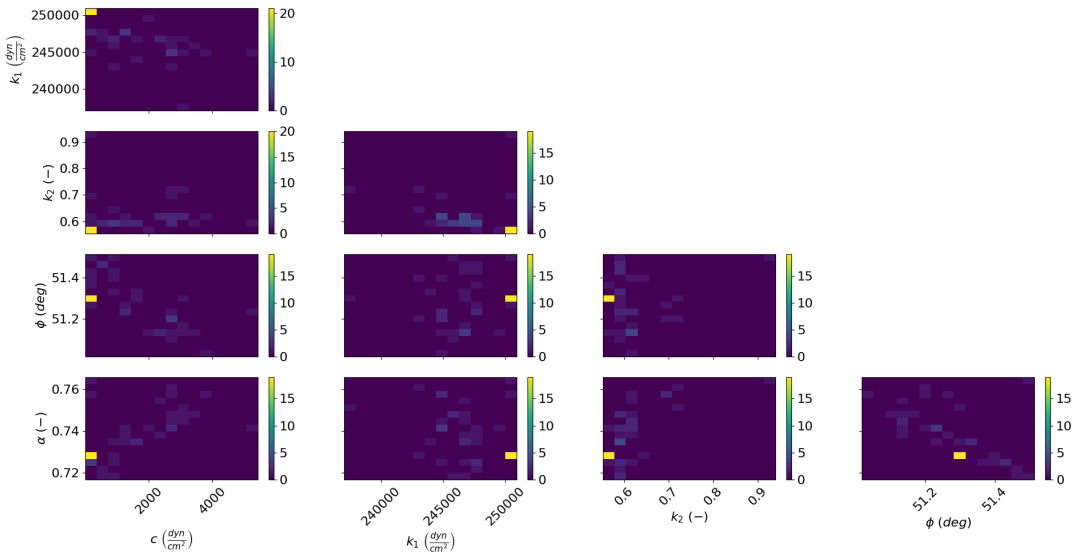

Figure 2.10: Parameter space for rabbit basilar artery. Number of runs: 50

and the resistance to inflation have a much higher effect due to the fibres wrapped around it. Since the elastic part of the SEF does not significantly contribute to the structural behaviour, it is very reasonable to expect a high variation in the parameter related to elasticity.

Finally, the validation of the parameters obtained follows. The wall model was imported with both the mean and geometric mean of the optimised parameters and the system of Equations (2.82) – (2.83) was solved.

From the results presented in Figure 2.11 it is seen that the optimised parameters have a very good agreement with the experimental results regarding the pressure-diameter plot. In the experimental work, the axial stretch is fixed and the experiment was conducted for values of 1.1, 1.15 and 1.2, which are expected to be close to the *in-vivo* values. Note here that the *in-vivo* stretch is a stretch which is not standard for a vessel with high variation from vessel to vessel. This homeostatic state is the stretch for which the axial force does not change during inflation of the vessel [161, 162]. Thus, due to the bi-axial testing and the varying axial force of this experiment, it is not exactly the case. However, it can be assumed to be close to the *in-vivo* homeostatic state. The results for the axial stretch produced by the wall model, due to Equation (2.83) are very close to those results, without showing much fluctuations across the pressure range. This is an indication that it is close to the *in-vivo* value. It can be seen that both statistical results, averaged and geometrically averaged, present results of the same quality without any differences. This is expected since both averaged values do not differ much, except for the elastic parameter c.

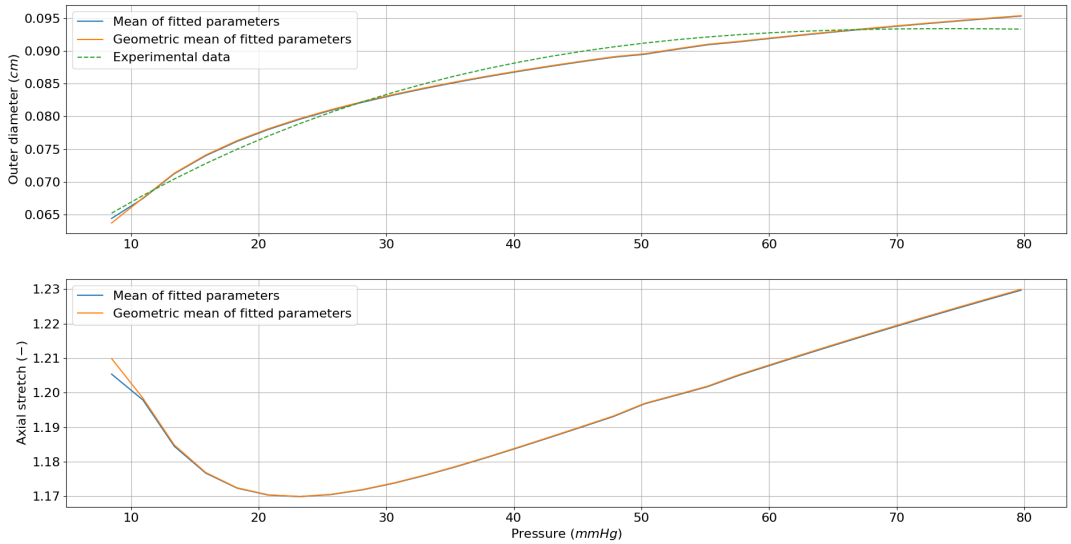

Figure 2.11: Results for diameter and axial stretch for rabbit basilar artery using the mean and geometric mean of the optimisation results

Human cerebral arteries

Next, the experimental work of Monson *et al.* [138] is characterised. This work examines the behaviour of three human cerebral arteries for their bi-axial properties, similar to the previous one. In terms of size of the vessels, the ones examined in this study start from slightly smaller than the rabbit basilar artery, i.e. $0.1cm$, and cover a wide range, reaching to the scale of $0.05cm$ with respect to the maximally distended state. In this work also, the pressure range is wider than the rabbit basilar bi-axial tests, reaching to the levels of $120mmHg$. The three vessels were examined separately, and one case is shown and discussed next. Results for the other two can be found in the Appendix A.1.

This study provides more data, and particularly, a very useful measurement is the LF circumferential stretch of the vessels. This enables the more detailed description of the SF state. More specifically, the circumferential stretch between two configurations is defined as the stretch in the middle point of the thickness. For the reference and current configuration it can be written as:

$$\lambda_\theta = \kappa \frac{r_i + r_o}{R_i + R_o}, \tag{2.86}$$

where r_i and r_o refer to the inner and outer radius of the current configuration, while R_i and R_o refer to these radii on the reference configuration. If applied between the LF and SF with a circumferential stretch $\lambda_{\theta,0}$, and by re-arrangement of the terms, the following relationship can be obtained

$$R_i + R_o = \frac{\kappa}{\lambda_{\theta,0}} \left(R'_i + R'_o\right). \tag{2.87}$$

Here, the known notation is followed for prime and capital variables representing the LF and SF configurations respectively. With this extra equation, it is feasible to solve a system of equations to acquire the inner and outer radius, and hence, the thickness of the SF state can be computed. The incompressibility condition, which is the second equation of the system, can be now written as seen below.

$$R_o^2 - R_i^2 = \kappa \lambda_{z,\text{res}} \left(R_o'^2 - R_i'^2 \right). \tag{2.88}$$

Since the thickness is the difference between the outer and inner radius, i.e. $H = R_o - R_i$ for the SF and $\eta = R_o' - R_i'$ for the LF, the system of Equations (2.87) and (2.88) finally produces the inner and outer radius of the SF configuration, and thus the thickness in this state.

For all three vessels of this study, the optimisation procedure, as described in the previous section, is followed since it also refers to bi-axial testings. Again, the errors of outer diameter and axial force are weighted equally with Equation (2.85).

The first vessel, which is named A2 and this abbreviation is kept, is the largest of the three vessels. It has a similar size to the one examined in the previous section. Similar to the basilar artery, in this work the pressure begins from a point nearly zero and thus can be assumed that is the LF configuration. A table that summarises the vessel LF measured values and assumptions is presented in Table 2.3.

Table 2.3: Summary of parameters from the work of Monson *et al.* [138] regarding the A2 vessel

Parameter	Description	Value
$\lambda_{z,\text{res}}$ $(-)$	Residual axial stretch	1.05
$\lambda_{\theta,0}$ $(-)$	LF-SF circumferential stretch	1.05
R_i' (cm)	Inner radius	0.032
η (cm)	Thickness	0.014
ω (deg)	Opening angle	80
κ $(-)$	Constant related to the opening angle	1.28

With these values for the LF configuration and by solving the system to pass to the SF configuration, the acquired values are $R_i = 0.04cm$ and $H = 0.015cm$. Similarly to the previous study, $N = 10$ points were considered for the pressure range, and the optimisation procedure was carried out 50 times.

The histogram of Figure 2.12 illustrates the parameter space of the optimisation procedure and how close the fittings are for all 50 repetitions. For this vessel it is seen that the optimisation shows a bigger spread of the parameters compared to the previous vessel, which is indicating that there are multiple sets of parameters that can produce the desired behaviour.

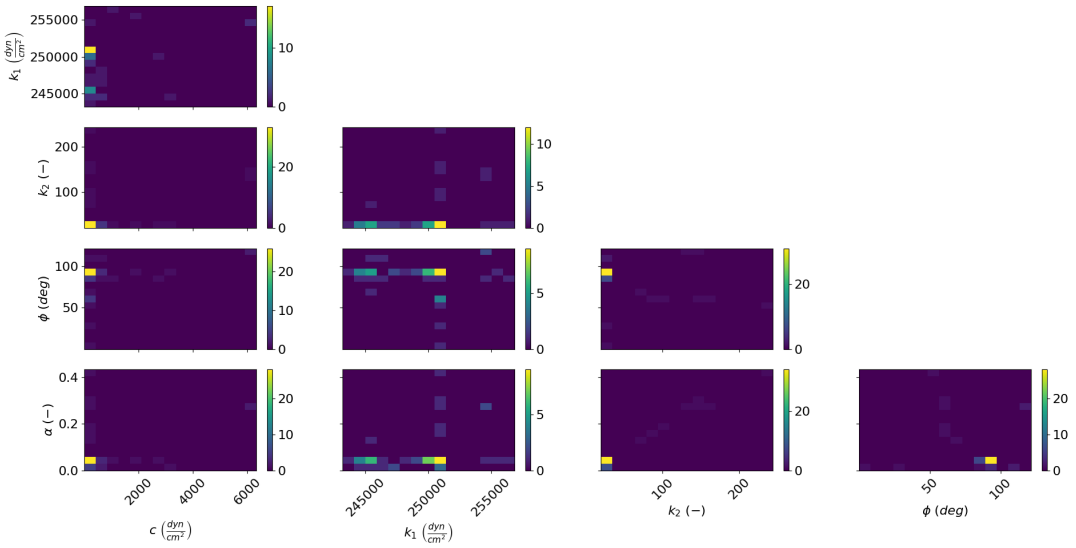

Figure 2.12: Parameter space for A2 human cerebral artery. Number of runs: 50

The statistical findings of the optimisations are presented in Table 2.4. From the histogram and the statistical analysis it is observed that similar to the previous fitting process, the elastic parameter c shows the biggest fluctuation again. It is also seen, that the parameter k_2 that is associated with the fibres also has some deviation, which is not that high in geometric terms. The opposite is seen for the interpolating factor α. Finally, the angle of the fibre may vary relative to the previous study. By comparing the statistical results with the histogram for all parameters except k_1, these fluctuations are associated with some fitted parameters that are much higher or lower in magnitude. This leads to a high value of standard deviation or geometric standard deviation. Furthermore, the parameter k_2 works as a ratio with k_1, which means that they are coupled, and the fluctuation of the one affects the other.

Table 2.4: Statistical results of the optimisation procedure runs for the A2 human cerebral artery

Parameter	Mean	Std dev	Geo. mean	Geo. std dev
c (dyn/cm^2)	527.25	± 1346	12.52	118.56
k_1 (dyn/cm^2)	249106	± 3243	249084	1.013
k_2 $(-)$	45.002	± 45.323	34.758	1.843
ϕ^1 (deg)	85.552	± 19.429	71.155	3.753
α $(-)$	0.07	± 0.09	0.018	67.395

Next, the statistical results of the optimised parameters were imported to the wall model to assess the ability of the model to replicate the experimentally measured behaviour.

As can be seen in Figure 2.13, the two parameter sets of averaged and geometrically averaged fitted parameters have both a very good behaviour. They both

produce a response very close to the experimental values for both outer diameter and total axial stretch. Specifically, the averaged parameters present a relatively better approach to the experimental values, while the geometric averaged have a bigger discrepancy. This behaviour though, vanishes as the pressure increases, which shows that the two parameter sets behave more accurately for a larger inflation of the vessel. As for the axial stretch, they are both within the range of the measured axial stretch. It is seen that unlike the diameter comparison, the axial stretch behaviour is more accurately approached with the geometrically averaged values. However, the difference of the two sets in stretch is very low in absolute value. Moreover, in the experimental axial stretch plots it was hard to distinguish the pressure values to which they referred to, and thus a linear distribution that connects the higher and the lower value was drawn.

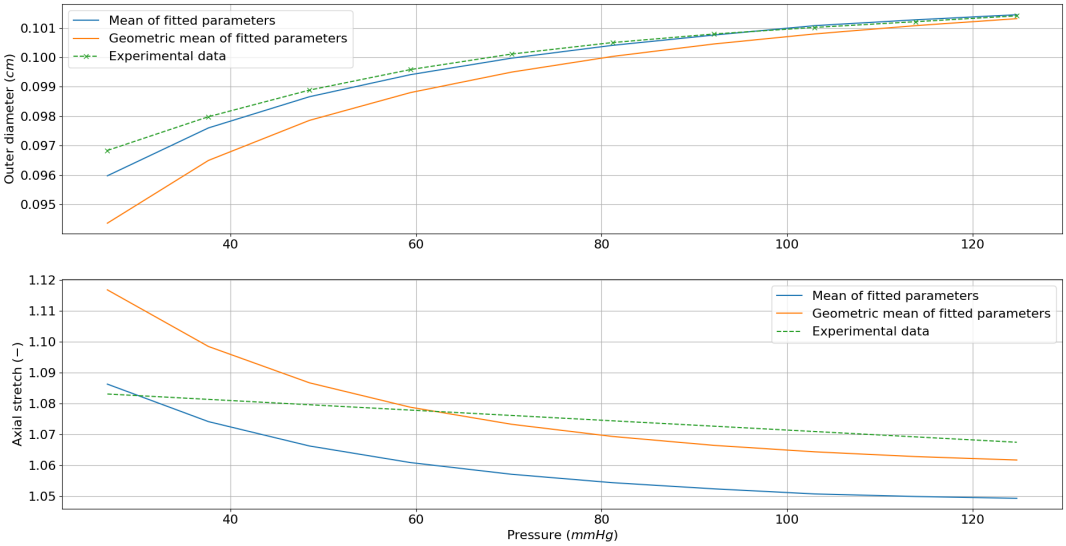

Figure 2.13: Results for diameter and axial stretch for A2 human cerebral artery using the mean and geometric mean of the optimisation results

The behaviour of this vessel in both pressure-diameter and pressure – axial stretch development is accurately reproducing the experiment. The difference for the first pressure points in diameter is $\sim 1\%$ for the averaged parameters, and $\sim 3\%$ for the geometrically averaged ones. Regarding the axial stretch, the maximum difference between measured and model predicted values is $\sim 2\%$ for the averaged parameters, and $\sim 3\%$ for the geometrical one. It is then concluded that for this vessel, the averaged fitted parameters provide better results as an overall.

Human pial arteries

The final vessel that is characterised is based on the work of Thorin [150]. In this work, three human pial arteries are subjected to inflation tests and extract their behaviour in terms of pressure-diameter relationships. In this work, three

families of vessels are examined, which differ in terms of size, and are categorised as *small*, *medium* or *large*. The vessels examined started from a size similar to the one of the basilar artery presented, and gradually got to lower sizes. Specifically the sizes are: 0.1 cm in diameter for the *large*; the *medium* are in the scale of 0.07 cm; and finally the *small* in the scale of 0.025 cm. The vessels were inflated and the maximum pressure varied for each case, starting from 100 mmHg for the small, 120 mmHg for the medium, and 140 mmHg for the large.

For these pial arteries of the study, unlike the previously reported works, no data are reported that could be used for characterisation, apart from the relation of pressure to the diameter. Furthermore, this is a uni-axial study. The only data used from the study is the aforementioned pressure-diameter plots. Of course, with these limited data, some assumptions were essential to characterise the material properties of the vessel.

In specific, there is no data about the residual stretches and stresses. Therefore, the residual stretches are treated as seen so far, by assuming them to be $\lambda_{z,\text{res}} = \lambda_{\theta,0} = 1.05$. For residual stresses, two cases were considered, $\omega = 80^{\text{o}}$ and $\omega = 120^{\text{o}}$ due to lack of data. These values were taken from the previous studies, as residual stresses may vary a lot [139, 138]. The setup and results obtained are following.

The methodology followed and results obtained regarding the characterisation of the *small* pial artery is presented. Results for the other two arteries can be found in A.1. At first, the LF diameter is identified from the given pressure-diameter plot as the value of the diameter for the lowest pressure, which is very close to zero. This value refers to the external diameter and was found to be $D_o^{\text{LF}} = 0.016cm$. With the assumption of WLR = 0.2, the thickness of the vessel can be obtained. For the wall-to-lumen ratio, from [154] it was found that the human intracranial vessels WLR ranges from 0.05 to 0.12, but as the diameter tends to smaller values, the ratio increases [163]. Also, MRI scans have also reported higher values on the ratio [164] for the major vessels of the Circle of Willis, though. Since there is no data regarding the thickness of *small* pial artery employed for the study, a conservative assumption was made regarding its thickness from the combination of the aforementioned studies. All values used for this study are summarised in Table 2.5.

Furthermore, due to the uni-axial nature of the study, only Equation (2.82) could be solved. And with this setup, the axial stretch of the vessel was put in the parameters to be optimised. For simplicity, a single value of the axial stretch was considered for the whole pressure range. The axial stretch was restricted to not exceed the value of 1.6, which is a high value for the axial stretch for these vessels. As an indicative case, the *small* vessel will be presented.

Again, the optimisation was run for 10 pressure points within the given range. The optimisation process now minimised the error given by Equation (2.80). The procedure was repeated 60 times, and its results are presented in the histogram of Figure 2.14.

Table 2.5: Summary of parameters from the work of Thorin *et al.* [150] regarding the *small* vessel

Parameter	Description	Value
$\lambda_{z,\text{res}}$ $(-)$	Residual axial stretch	1.05
$\lambda_{\theta,0}$ $(-)$	LF-SF circumferential stretch	1.05
R_i' (cm)	Inner radius	0.0078
η (cm)	Thickness	0.0023
ω (deg)	Opening angle	80
κ $(-)$	Constant related to opening angle	1.28

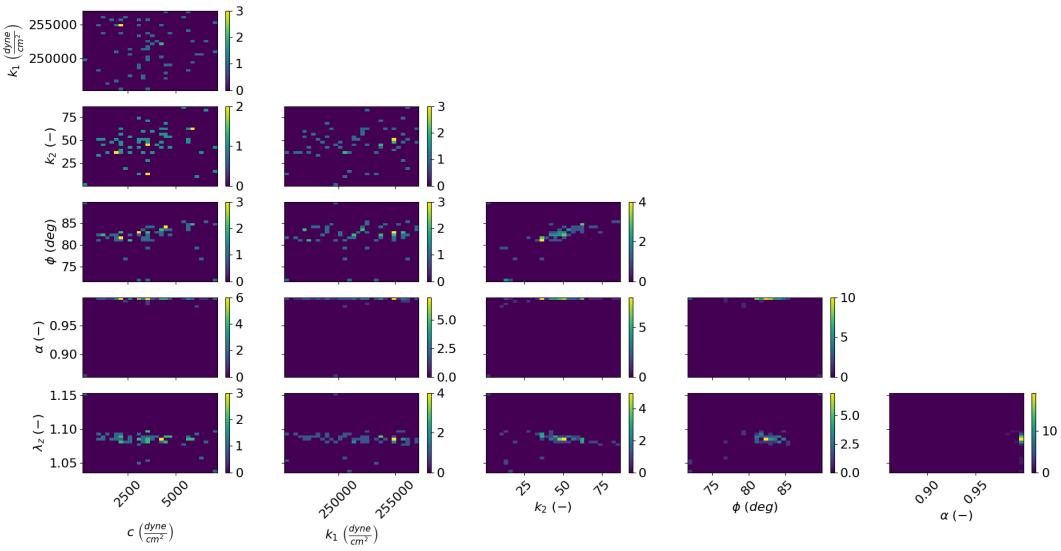

Figure 2.14: Parameter space for the *small* human pial artery. Results presented for $\omega = 80^{\text{o}}$. Number of runs: 50

From the histogram presented (Figure 2.14) it is seen that for the specific fitting there is a much wider spread in the parameter space. To be able to analyse the data, again, the table with the statistical findings of the optimisations is presented.

From Table 2.6 useful information can be obtained. At first, again, the value of the parameter c is highly fluctuating throughout the different optimisations. Next, it is seen the interpolation parameter α is almost equal to 1, which means that the vessel material is mainly characterised by the reinforcement of the fibre. Combining those two, it can be concluded that the value of c, which is an elasticity parameter, does not play a big role in the definition of the material, hence it can vary a lot. Furthermore, the variation of parameters k_1 and k_2 is very similar

to that presented for the previous (human middle cerebral) artery, although here the material behaviour is dominated by the fibres. Finally, the value for the axial stretch implies a very small deformation in the axial direction, which also does not vary in different optimisations.

Table 2.6: Statistical results of the optimisation procedure runs for the *small* human pial artery

Parameter	Mean	Std dev	Geo. mean	Geo. std dev
c (dyn/cm^2)	3551.52	± 1603.87	3084.11	1.87
k_1 (dyn/cm^2)	251783	± 3174	251763	1.01
k_2 $(-)$	45.817	± 16.711	39.269	2.33
ϕ^1 (deg)	82.049	± 3.049	81.991	1.039
α $(-)$	0.993	± 0.017	0.993	1.019
λ_z $(-)$	1.085	± 0.013	1.085	1.012

Similarly to the previous vessel characterisation, the statistical results were imported to the wall model and run, so its behaviour can be evaluated.

Figure 2.15 shows that the results for this vessel diverge more than the previous one, although the fitting is not unacceptable. In general, the values at the low and high pressures are very close to the experiment. Moreover, the geometric mean of the fittings produces a significantly better approach than the average. However, the experimental results for this specific vessel present this bell-like shape, where a typical hyperelastic law is not able to reproduce accurately. Furthermore, the lack of input data could cause this discrepancy.

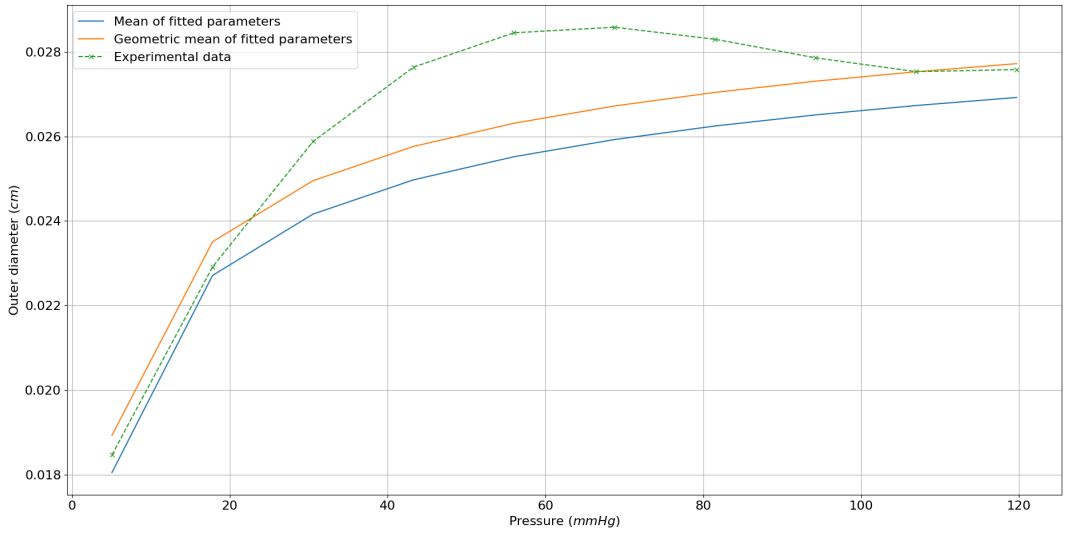

Figure 2.15: Results for diameter for *small* human pial artery using the mean and geometric mean of the optimisation results

Overall, the fibre-reinforced hyperelastic material employed to represent the passive behaviour of vascular wall materials has been shown to be quite accurate

and adaptive. Vessels from different species (human, rabbit), types (basilar, pial), and sizes were tested and the numerical results obtained are very close to the experimental ones. The fitting technique was adaptive to take into account the maximum information available with small implementation changes. It is also rather fast since a small number of parameters are optimised each time. Naturally, the more information is provided from experimental studies, the more accurate the prediction is, as can be seen from the first two cases of the bi-axial experiments. However, the results acquired with limited data are accurate as well.

This framework can be used along with computational solvers that can simulate whole vascular networks by using a material law for each vessel separately, improving the current commonly used laws [149, 97, 107, 165]. Given that implementing a specific material law in such frameworks can increase the computational cost of the solver significantly, it is suggested that the ideal utilisation of the characterisation presented are models that target the vasculature of specific regions, like the Circle of Willis (CoW).

2.6 Conclusive remarks

In this chapter the mathematical background required for the work that follows is presented and discussed.

In the beginning of the chapter, an overview of the 1D fluid solver formulation, and the numerical schemes used are presented. Additionally, a brief overview of the velocity profiles employed in 1D formulations and the connection to lumped-parameter models is reported.

Next, the vascular wall mechanics that are coupled with the fluid model is discussed. The model chosen for the scope of this study is presented, and details on the coupling those models in an FSI framework is discussed.

Finally, a framework to reproduce the passive behaviour measured experimentally of cerebral vessels was developed and presented. This work adjusts the structural model so that it can represent cerebral vessels, which is the aim of this thesis. Through the fitting procedure, it is feasible to approach the response of a number of vessels with the employed constitutive law. The framework fitted experimental data to the parameters of the constitutive law, and a very good agreement was achieved. The process is adaptive to the number of available data, and it was showcased for both uni-axial and bi-axial tests. The work can also be helpful to combine vascular networks with different vessels.

Chapter 3

Intracellular signalling

The active contractile behaviour of a vessel is the result of a combination of multiple and complex biological processes, acting at different levels, as referred in Chapter 1. Modelling this physiological phenomenon requires the identification (supported by experimental evidence) of its main contributors. Vascular Smooth Muscle Cells (SMCs) cover a large part of the media layer and polarised light microscopy has shown that they are mainly aligned in the circumferential direction [6, 5]. These cells constitute the key vascular compartment for short-term contraction/dilation that can be induced through various stimuli such as mechanical or neuro-hormonal, as well as long-term ones where the extracellular matrix is subjected to alterations [166].

This chapter focuses on the description and quantification of the intracellular processes governing SMC contractility, with a particular focus on cerebral vessels. At first, a more detailed background is given regarding the intracellular processes that take place during SMC contractility to highlight the key features that drive this response. Next, two chemical models are presented which describe some of those processes, and their functionality is discussed. Finally, a novel approach developed is presented. The newly developed model aims to identify the pressure-induced intracellular processes in a holistic way by considering the intracellular signalling pathways that occur as a response to pressure.

3.1 Background

It is well accepted that the dynamics governing SMC tone generation can be described through the sliding filament theory [167, 168]. According to this theory, contraction is the result of the relative sliding of two filaments that are within the SMC, the actin (thin) and the myosin (thick). The actomyosin complex constitutes the basic Contractile Unit (CU). All the CUs lie within the cytoplasm

of the SMC which in turn lie within the media layer of the three-layered vessel wall. An llustration of the multitscale vascular wall can be seen in Figure 3.1.

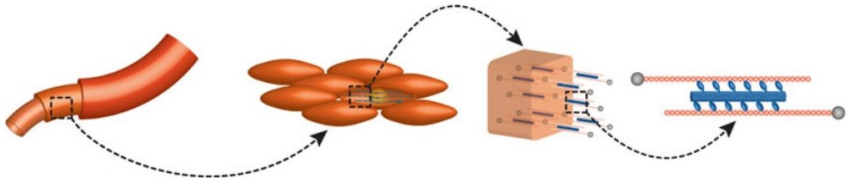

Figure 3.1: Multi-scale Smooth Muscle structure (Image taken from [47], permissions granted from Springer Nature)

The monomer of the motor protein myosin consists of two coiled heavy chains that each has a head and tail part. The head is the part that attaches to the actin protein and form what is known as Cross-Bridges (CBs), while the tail can be attached to other myosin monomers. Underneath the head lie two regulatory light chains, which are responsible for the regulation of the phosphorylation of the heads. This phosphorylation is the key mechanism for the attachment, and thus contraction/dilation, and will be discussed in the next sections. Multiple monomers can be attached and organised in different ways [169] and form the thick myosin filament. The forming and cycling of the CBs which connect the actin and myosin filaments is controlled and dominated by the variation in intracellular calcium concentration $[Ca^{2+}]_i$ [46, 170]. Ultimately, this relative sliding leads to the contraction/dilation of the vessel.

The chemical processes describing the formation and cycling of the CBs have modelled in different previous studies. One of the first models is the Huxley-Simmons [171], which considers two states for the myosin heads, attached and free, that are connected with two rate parameters dependent on the contraction. An extension to the Huxley-Simmons model, is the model developed by Hai and Murphy [85], which is one of the most widely used. It considers four states of the myosin heads, and seven rate parameters. Two of the states described are non-force productive, while the other two are producing force. One of the force productive states is assumed to be the latched state, which is a contradictory state among literature since it is only supported by mechanical and energetic data but not biochemical [47]. Due to their inter-dependency, the cross-bridge kinetics can be coupled with an electrochemical representation of the intracellular calcium dynamics [172, 173, 174].

Yang *et al.* [173, 86] have indeed proposed an electrochemical model coupled with a chemo-mechanical one to simulate the response of rat cerebrovascular arteries to luminal pressure changes. The electrochemical model accounts for the electrical signals that occur within the cell when contraction is stimulated with a change in membrane potential produced by a change in luminal pressure, and produces

the chemical output necessary for the coupled models. The chemo-mechanical compartment makes use of the Hai-Murphy model which is coupled with a three-element Hill model that finally produces the response of the vessel. Murtada *et al.* in their models [47, 175, 144, 88] have also considered a chemo-mechanical model describing the generation of active force within the SMCs in various vessels with a combination of the Hai-Murphy model and a Hill model alteration.

All the above described models assumed that the generation of active tone within the SMC is regulated only by the level of intracellular calcium $[Ca^{2+}]_i$ within the SMC. However, experimental evidence [176, 177, 178, 179, 180] suggests that, besides $[Ca^{2+}]_i$, other intracellular signalling pathways play a key role in the adjustment of cerebral vascular tone (and eventual dilation/contraction). Since the classical/standard methodologies lack of representation for these cellular chemical processes, a new model has been established. In the following the mathematical descriptions for all these models, alongside their simulation results, are reported.

3.2 Classical modelling approach

Here the standard models representing chemical processes behind cerebral SMC active response are reported. These are the Hai-Murphy model for the CB kinematics and the electrochemical model of Yang *et al.* These models, although not used in the computational framework developed in this thesis, provide a very useful insight into the cellular dynamics and its modelling aspects.

3.2.1 Hai and Murphy model

As anticipated earlier, one of the first models to describe the chemical kinematics involved within the SMC is the one proposed by Hai and Murphy [85]. It describes the interaction between the myosin and the actin filaments through the cycling of CB between them.

For this model, it is assumed that the only factor that can affect CBs cycling is the level of intracellular calcium. An increased value of $[Ca^{2+}]_i$ causes more myosin heads to attach to the actin and a lower value causes a lower rate of attachment respectively. The calcium is entering from the extracellular area inside the cell from dedicated channels. These channels are not fully defined in literature and they form a very complex system within the cell [181, 182, 170] with their own dynamics and responses to different stimuli. For the sake of simplicity, within the Hai-Murphy model, they are assumed to be constantly open so they provide instantaneously the Ca^{2+}, and the extracellular amount of calcium, which normally varies and affects the intracellular concentration [183], is assumed to be

infinite.

In the model, the myosin heads behaviour is described, which are assumed to act independently. As already mentioned, there are four possible states for the heads. These states represent their attachment on the actin, and whether their regulatory light chains are phosphorylated or not. Figure 3.2 illustrates these states and their rates at which each state transition is occurring.

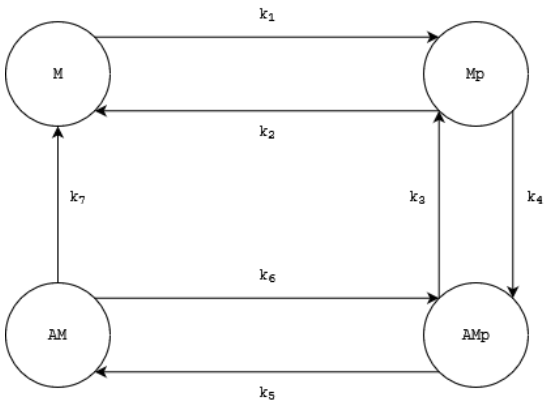

Figure 3.2: Cross-bridge cycling states of Hai-Murphy model and their rate constants

The initial state is M, at which the head is not attached and its light chain is not phosphorylated. Through a complex biological mechanism, free intracellular $[Ca^{2+}]_i$ binds with the protein calmodulin (CaM), which in turn binds to and activates the Myosin Light Chain Kinse (MLCK). The MLCK is then phosphorylated and enables the head to attach to the binding site on the actin filament [184, 185]. This process leads to state M_p in which the heads are phosphorylated but not yet attached. These first two states are the non-force generating ones. Between these two states, the inverse process is also possible, through the activation of the Myosin Light Chain Phosphatase (MLCP), which is de-phosphoryalating and prevents the attachment. The rates for these two processs are k_1 and k_2 respectively and represent the rates that the heads are phosphorylated (MLCK) or de-phosphorylated (MLCP). When the heads are phosphorylated, they are attached to the binding sites on the actin filament through another chemical process. The adenosine triphosphate (ATP) transforms to adenosine disphophate (ADP) and orthophosphate (P_i) and the head is attached to the site forming a CB [186]. This is the first force-generating state, AM_p caused by the release of P_i which in turn causes the attached head to move and produce a power stroke. The rate of this process is described by the parameter k_3. The release of ADP can cause the ATP to bind to the attached head and detach it from the binding site, which then returns to the state M_p, and the rate describing this process is k_4. In time, the attached phosphorylated heads are slowly de-phosphorylated. The rates of de-phosphorylation and phosphorylation are k_5 and k_6 respectively. The

model assumes that some of the de-phosphorylated heads can remain attached and produce force, which is described by state AM. This is the latch state hypothesis, supported by experimental observations of stress that is maintained with reduced levels of myosin phosphorylation [187]. Finally, the latched state heads are de-phosphorylated at an irreversible manner back to state M.

The above processes are describing the kinetics of the CB cycling are modelled with a set of ordinary differential equations (ODEs), which in matrix form are

$$\begin{bmatrix} \dot{n}_M \\ \dot{n}_{Mp} \\ \dot{n}_{AMp} \\ \dot{n}_{AM} \end{bmatrix} = \begin{bmatrix} -k_1 & k_2 & 0 & k_7 \\ k_1 & -(k_2+k_3) & k_4 & 0 \\ 0 & k_3 & -(k_4+k_5) & k_6 \\ 0 & 0 & k_5 & -(k_6+k_7) \end{bmatrix} \begin{bmatrix} n_M \\ n_{Mp} \\ n_{AMp} \\ n_{AM} \end{bmatrix}, \tag{3.1}$$

where k_i are the rate parameters explained above. The variables n of the system are the fraction of the heads that at each state (M, M_p, AM_p, AM). The model is also subjected to the constraint

$$n_M + n_{Mp} + n_{AMp} + n_{AM} = 1. \tag{3.2}$$

This expression represents the mass conservation, and since the variables are fractions it is $n \geq 0$, and they are dimensionless. With this constraint the ODEs reduce to a 3×3 algebraic system. Furthermore, it is assumed that the rates that represent the MLCK and MLCP processes are similar for attached and detached CBs, which translates into $k_1 = k_6$ and $k_2 = k_5$. The fractions are set to start from a state that are all unattached and non-phosphorylated as the initial condition, i.e. $n_M = 1$ and $n_{Mp} = n_{AMp} = n_{AM} = 0$.

As mentioned in the description of the model, the intracellular calcium concentration $[\mathrm{Ca}^{2+}]_i$ is the substance that drives the CB cycling processes. This is imposed through the formulation of rate parameter k_1 with a Hill function dependent on the $[\mathrm{Ca}^{2+}]_i$. Due to the biochemical process of binding CaM with calcium to form the calcium calmodulin complex (CaCaM), an initial consideration is a function of CaCaM that includes calcium indirectly [47, 173]

$$k_1 = \frac{[\mathrm{CaCaM}]^2}{[\mathrm{CaCaM}]^2 + K_{\mathrm{CaCaM}}^2}, \; \mathrm{CaCaM} = \alpha[\mathrm{Ca}^{2+}]_i, \tag{3.3}$$

where the parameters K_{CaCaM} and α are fitted parameters.

In other considerations, the CaCaM dependency can be disregarded and the intracellular calcium concentration can be directly imposed [175, 144] through

$$k_1 = \eta \frac{[\mathrm{Ca}^{2+}]_i^n}{[\mathrm{Ca}^{2+}]_i^n + \mathrm{ED}_{50}^n}, \tag{3.4}$$

where n and η are fitted. This formulation is more useful because it does not refer to the CaCaM, which requires more investigation regarding its formulation. Moreover, on the denominator there is no longer a fitted parameter. Instead, ED_{50}^{n} represents the half activation constant of calcium to MLCK under a constant value of CaM [175, 188].

The calcium concentration increase as a response to pressure elevation in medium and small cerebral arteries is thoroughly examined in experimental studies in steady state conditions [151, 176, 189, 190]. From these studies, the $[Ca^{2+}]_i$ level for different luminal pressure loading are reported. These recordings, although partially differing, represent the reference data used in this thesis and are discussed in later section. It is clear from the aforementioned studies that when the luminal pressure increases, a higher level of intracellular calcium is achieved. This is in line with the mechanism of the active tension generation and the dominating character of $[Ca^{2+}]_i$.

The calcium levels (interpolated) for the different intraluminal pressure values can be seen in Figure 3.3.

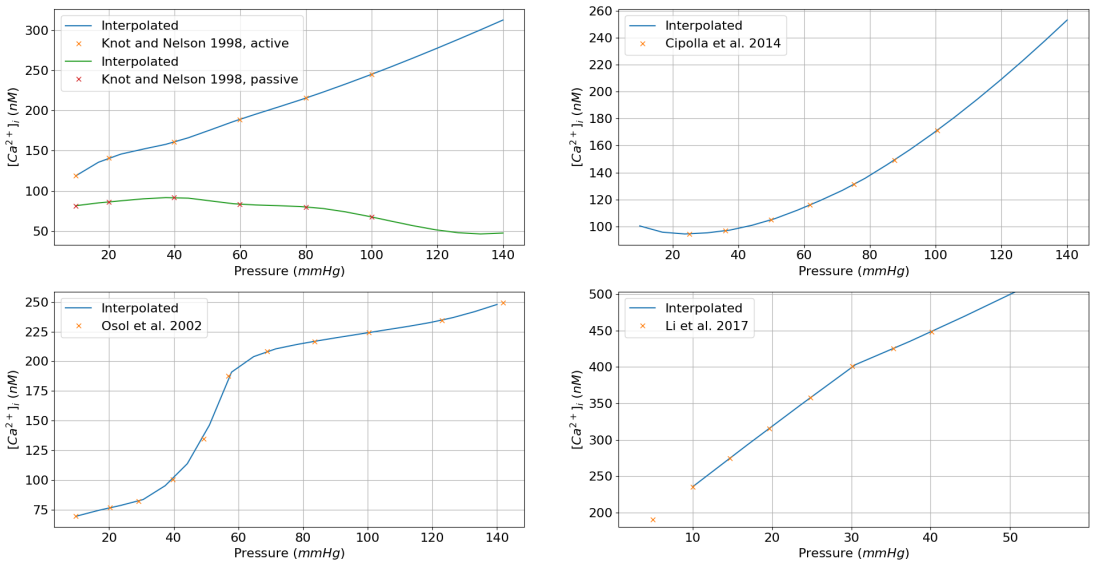

Figure 3.3: Steady state pressure – $[Ca^{2+}]_i$ diagram for different experiments [151, 176, 189, 190]. Interpolated experimental values

In the works [173, 47, 175] three sets of rate parameters, as well as three different formualtions for k_1 are used. These values for the rate parameters are summarised in Table 3.1.

Moreover, in the earlier work of Murtada *et al.* [47], the Equation (3.3) is used to define the input rate parameter, using $\alpha = 35 \cdot 10^{-6}$ and $K_{\text{CaCaM}} = 178\,nM$. In their later works [175, 144], they use the Equation (3.4) with $n = 4$, $\eta = 0.35917\,s^{-1}$ and $\text{ED}_{50} = 370\,nM$, while Yang *et al.* [173] uses the same relationship with $n = 2$, $\eta = 1\,s^{-1}$ and $\text{ED}_{50} = 178\,nM$.

Table 3.1: Summary of the rate parameters used in the works of Murtada *et al.* [47, 175] and Yang *et al.* [173]

	$k_2(s^{-1})$	$k_3(s^{-1})$	$k_4(s^{-1})$	$k_7(s^{-1})$
Murtada 2010	0.5	0.4	0.1	0.01
Murtada 2012	0.16267	0.06667	0.00083	0.00667
Yang 2003	0.4	1.8	0.1	0.045

These two formulations for k_1 that drive the CBs formation were simulated to evaluate the different kinematic states they produce and their dynamic characteristics. At first, the system was simulated at steady-state conditions. This is achieved by setting the transient values of the fractions, i.e. the left hand side of Equation (3.1), equal to zero.

Figure 3.4 presents the results of simulating the different setups of the Hai-Murphy model. What is interesting in these results regarding the scope of this thesis is to identify the level of $[Ca^{2+}]_i$ concentration and the amount of attached myosin filaments it produces. It is clear that the $[Ca^{2+}]_i$ level needed for the first (Murtada *et al.* 2010) model setup is too high compared to the other two. These levels of calcium are not likely to be reached in physiological conditions. About this setup, it is also noted that the maximum level of the force generating states $n_{AMp} + n_{AM}$ differs from the level that the other two setups. It maximises at ~ 0.78 while the other two setups at ~ 0.94. This is because the ratio k_3/k_4 is much lower than the other two setups. This means that the rate at which the attached phosphorylated myosin heads are detaching is much higher than the other two setups, and this does not allow for a higher maximum force-producing fractions to be reached.

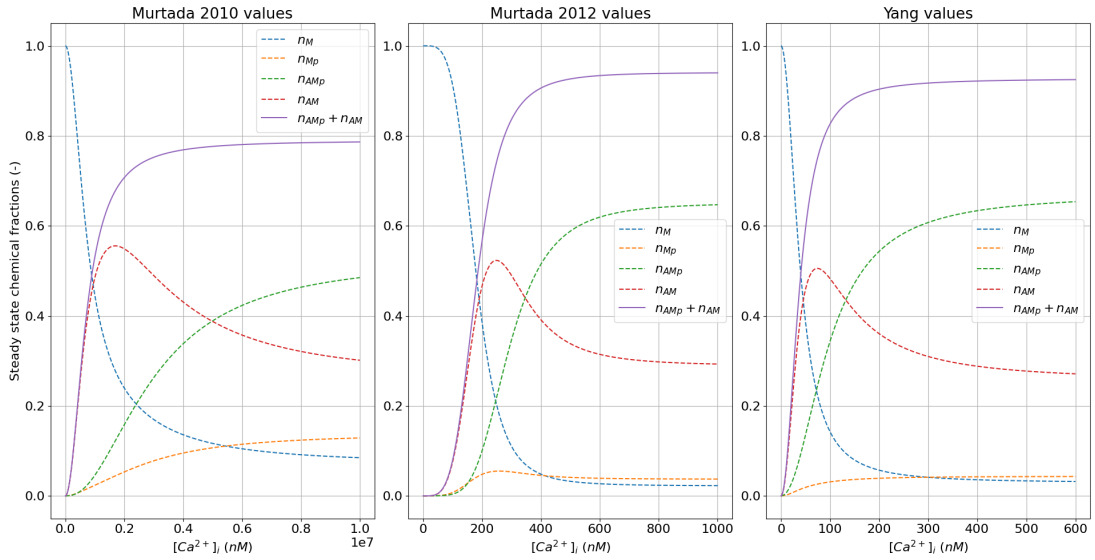

Figure 3.4: Steady state solution of Hai-Murphy model for different setups

For the other two models setups, the only difference is the $[Ca^{2+}]_i$ concentration

at which they converge to their maximum values The trend of the state variables with respect to the $[Ca^{2+}]_i$ is the same in both. Note here that the Yang *et al.* setup [173] aimed to represent cerebral vessels, while the Murtada *et al.* [175, 144] the CCA. This is in line with the physiological explanation of the myogenic response for cerebral vessels, as explained in Chapter 1. Resistant vessels develop more active tone for the preservation of the flow rate.

The second model of Murtada *et al.* and the one of Yang *et al.* were also tested regarding their transient behaviour in order to define their dynamic behaviour and evaluate their differences. At first, The models were tested for a constant value of $[Ca^{2+}]_i$ which corresponds to the calcium value at which $n_{AMp} + n_{AM}$ reaches the maximum value. Figure 3.5 shows the transient results of the Hai-Murphy model for the two setups for a constant calcium concentration. They present a significant difference in terms of the time needed to reach their steady state. The Yang *et al.* setup, which is fitted to simulate cerebral vessels, reaches its steady state very rapidly compared to the Murtada *et al.* setup. This behaviour is related to the choice of rate parameters which define the rate at which the MLCK is phosphorylated and in turn leads to the attachment of the CBs. Furthermore, the setup of the MLCK phosphorylation case does affect the transition.

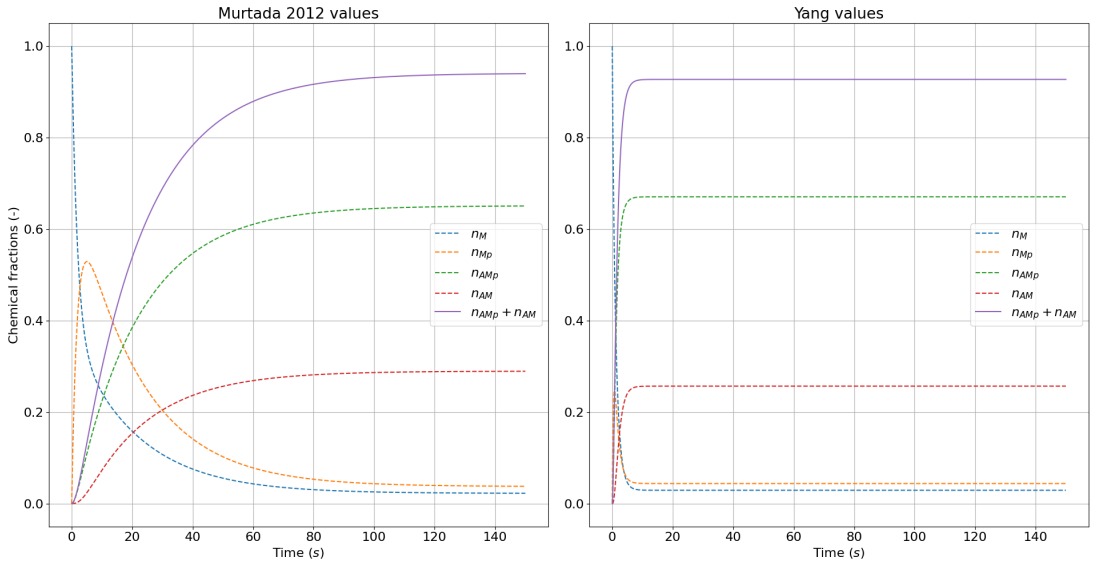

Figure 3.5: Transient solution of the Hai-Murphy model for two different setups for $[Ca^{2+}]_i$ constant and equal to the value that the steady state simulations reached the maximum $n_{AMp} + n_{AM}$ (i.e. $[Ca^{2+}]_i = 800\,nM$ for Murtada 2012 values and $[Ca^{2+}]_i = 600\,nM$ for Yang values)

The last simulation for the Hai-Murphy model was to examine how these two setups behave on a transient intracellular calcium distribution. As a baseline, the distribution presented in Murtada *et al.* work on common carotid artery [144] is used (Figure 3.6 top). To draw some conclusions for this set of simulations it is necessary to plot the fractions for both formulations.

Figure 3.6 shows the transient results of the two setups for a calcium distribution reported in [144]. In these results it is seen that all the transitions from one state to another are occurring in a much quicker manner for the cerebral vessel setup. It is observed that for $t \simeq 100\,s$ to $t \simeq 180\,s$ where $[Ca^{2+}]_i$ is kept almost cosntant, the Yang setup has already reached its steady values and it keeps this value. On the other hand, for the same time span, the Murtada setup has not reached a steady state and follows an increasing trend, before being forced to decrease again due to the decrease in $[Ca^{2+}]_i$. Again, this behaviour also confirms that active tension generation in cerebral arteries, which are resistance arteries, occurs in a rapid manner compared to elastic larger arteries.

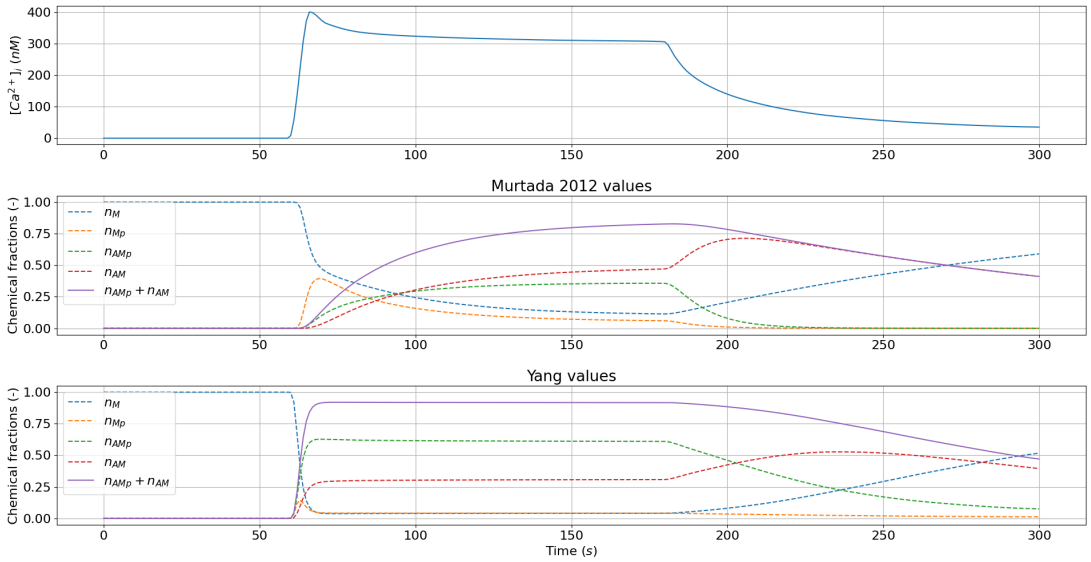

Figure 3.6: Hai-Murphy model solution using a distribution of intracellular calcium concentration

To conclude, the Hai-Murphy model is a versatile modelling representation capable to simulate a wide spectrum of vessels. This is also confirmed by the wide usage of it found in the literature. One drawback of the Hai-Murphy model is that it is designed to tackle only isometric contractions [85], which in some cases can be ignored [47], but alternatives to this drawback have been developed [191, 192].

3.2.2 Yang model

The description of cellular processes regulating active tone development can be enhanced through electrochemical models, such as the one by Yang et al [173]. This approach represents cellular dynamics through electrical analogy to account for all the exchanges of ions between intracellular and extracellular spaces [193]. As explained in previous sections, the focus is on intracellular calcium concentration, as it has been shown to be the main ion responsible for the development of active tone in blood vessels.

In this type of modelling approach a set of ODEs describes the dynamics within the cell that define the rate of change in concentration of quantities of interest, such as intracellular calcium (Ca^{2+}), potassium (K^{+}), sodium (Na^{+}) or chloride (Cl^{-}). These governing ODEs may refer to a change in cell membrane potential or intracellular ion concentration. The membrane potential is altered by ionic influxes and/or effluxes between the intracellular and extracellular space. Ionic fluxes are produced due to the activation/deactivation of certain channels, pumps, or exchangers [194]. It was found that some compartments of electrochemical models found in literature shared some key compartments, which are the most important for these ionic exchanges. These were found to be the following

- the Voltage Operated Calcium Channels (VOCC). VOCCs are calcium channels that allow the entry of calcium ions into cells as a response to changes in membrane potential. The most important VOCC is the L-type, which is are highly selective for calcium ions [195, 196]. These channels open in response to membrane depolarisation, allowing the influx of calcium ions into the intracellular space.
- Na^{+}/Ca^{2+} exchangers. These channels are regulating the exchange of calcium and sodium ions across the cell membrane [197].
- Ca^{2+} pumps. These pumps actively transport calcium ions across cell membranes against their concentration gradient [197].

The exact mechanisms through which the cell detects changes upon luminal pressure alterations, which ultimately leads to the development of active tone, is still unclear. However, it is known that some ionic channels are activated when subjected to mechanical loading, which ultimately lead to membrane depolarization [198, 199]. This process can be modelled in different ways. In most cases, a dedicated stretch/stress-activated channel is used, or alternatively a stretch/stress-activation term is included in one of the calcium channels, often the L-type VOCC.

A variety of models have been developed in the area of electrochemical modelling and in the context of SMC contraction, with various levels of complexity depending on the number of cellular processs modelled. One of the first attempts was the model of Parthimos *et al.* [172] that includes the cytosolic Ca^{2+} oscillation. Calcium oscillations are fluctuations in the concentration of calcium ions within the cell membrane or intracellular compartments. They can be triggered by various stimuli, such as changes in membrane potential, receptor activation, or mechanical signals [200, 201]. This model was used to simulate different pharmacological interventions. The work of Parthimos *et al.* was later modified [202] where the oscillator was eliminated, and an agonist- and calcium-dependent IP3 was added.

The model was used to study SMC synchronisation. Within these models, a minimal number of channels that define dynamic ion exchange are modelled, whereas the ion concentrations variables are also kept to a minimum, accounting only for the Ca^{2+}. In both aforementioned models, the membrane depolarisation resulting from a change in the level of pressure is modelled through an activation term within the L-type VOCC channel.

Alongside these minimal models, more complex models have also been established. These include much more intracellular pathways for the cellular dynamics through more channels and mechanisms that alter the ionic concentration and the membrane potential. One of the first models in this category was the one developed by Yang *et al.* [173, 86], where more transmembrane currents were modelled, whereas the ionic balance of K^+ and Na^+ were also included. The stress activation in this work was introduced through a dedicated channel. The model was then coupled with a chemo-mechanical subsystem in order to study the SMC behaviour of rat cerebrovascular arteries. A model with even more complexity in terms of cellular processes was the model of Kapela *et al.* [183], which also included the ionic balance of Cl^- along with some additional transmembrane currents. The model was used to study the physiology of SMC.

In this thesis, the SMC dynamics model of Yang *et al.* [173] was tested in conjunction with the Hai-Murphy model to get an insight on the intracellular calcium concentration effect on the CB formation. The model is briefly described below, followed by results of the simulations.

Figure 3.7 shows the intracellular and extracellular connection through some basic electric elements that allow a current to flow through them. $I_{Ca,L}$ is the current of the L-type VOCC channel. I_K is the delayed rectifier, which provides an outward current when the membrane is depolarised to limit further depolarisation. $I_{K,Ca}$ is the calcium-activated potassium current, which is activated as a response to large calcium influxes upon depolarisation. I_{Ki} is the inward rectifier. I_M is the stress activated channel and it is $I_M = I_{M,Ca} + I_{M,K} + I_{M,Na}$. Each ionic concentration is assumed to be activated through the stress developed upon the membrane wall. I_B is the background current and similar to the stress activated current, it is defined for each ionic concentration. I_{NaCa} is the Na^+/Ca^{2+} exchanger, I_{NaK} is the Na^+/K^+ exchanger, and I_{CaP} is the calcium pump.

The change in transmembrane potential V_m is given by the Kirchhoff law of currents:

$$\frac{dV_m}{dt} = -\frac{1}{C_m}\left(I_{Ca,L} + I_K + I_{K,Ca} + I_{Ki} + I_M + I_B + I_{NaK} + I_{NaCa} + I_{Ca,P}\right), \tag{3.5}$$

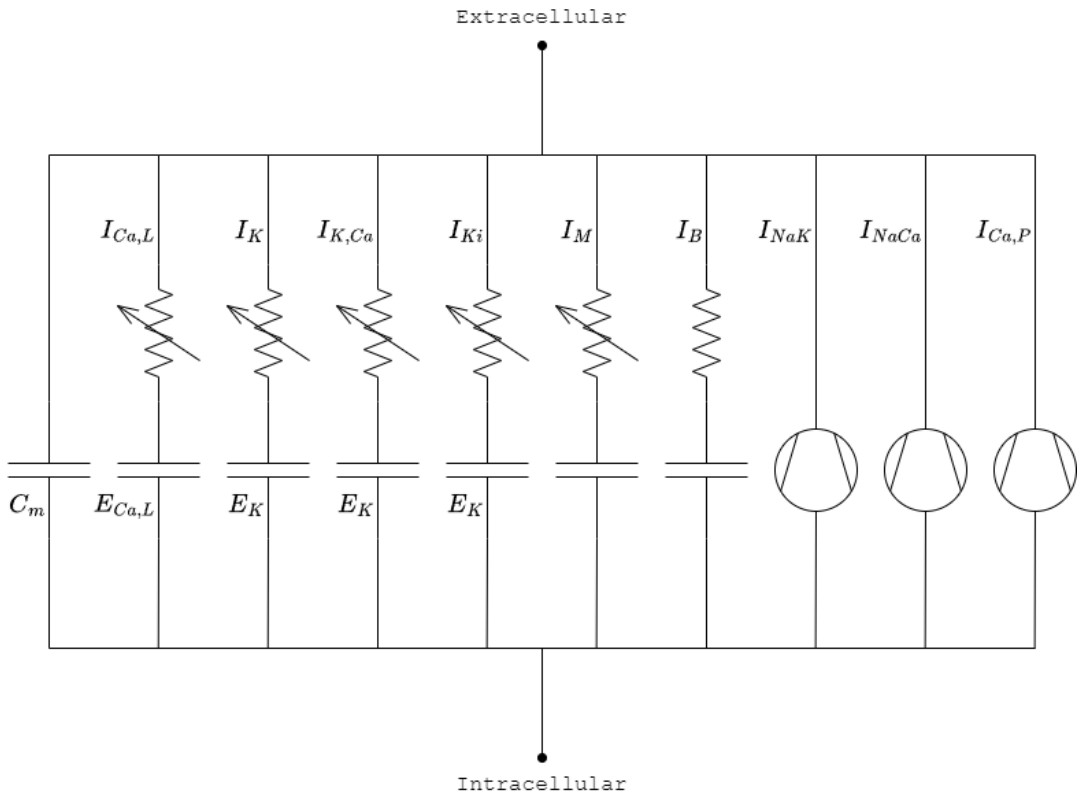

Figure 3.7: Yang *et al.* [173] electrochemical model schamatic. The model consists of variable (and not) resistor, capacitor, and exchanger elements. The variable resistors contain voltage dependent nonlinearities; the last three elements represent pumps or ionic exchangers

where C_m is the membrane capacitance. An intracellular ionic mass balance equation is set for each ion considered and is described by

$$\frac{d[\mathrm{Na}^+]_i}{dt} = -\frac{3I_{NaK} + 3I_{NaCa} + I_{B,Na} + I_{M,Na}}{F \cdot \mathrm{vol}_i}, \tag{3.6}$$

$$\frac{d[\mathrm{K}^+]_i}{dt} = -\frac{I_K + I_{CaK} + I_{Ki} - 2I_{NaK} + I_{B,K} + I_{M,K}}{F \cdot \mathrm{vol}_i}, \tag{3.7}$$

$$\frac{d[\mathrm{Ca}^{2+}]_i}{dt} = -\frac{I_{Ca,L} - 2I_{NaCa} + I_{CaP} + I_{B,Ca} + I_{\mathrm{up}} - I_{\mathrm{rel}}}{2F \cdot \mathrm{vol}_{\mathrm{Ca}}} + \frac{d[\mathrm{S_{CM}}]}{dt} + \frac{d[\mathrm{B_F}]}{dt}, \tag{3.8}$$

where F is the Faraday number, and vol_i is the volume inside the cell. For the calcium concentration, $\mathrm{vol}_{\mathrm{Ca}}$ is the intracellular volume available for calcium. In the calcium balance equation the currents I_{up} and I_{rel} appear. These are currents of the sarcoplasmic reticulum (SR) and the currents are the uptake and release currents respectively. The uptake current refills the SR, while the release current releases calcium into the cytosolic space from the SR. Finally, $[\mathrm{B_F}]$ represents the Ca^{2+} buffering by calmodulin, while $[\mathrm{S_{CM}}]$ represents the concentration of free

calmodulin sites for Ca^{2+} binding.

For validating their model, Yang *et al.* simulated a patch-clamp test, during which the membrane potential is imposed (and treated as a boundary condition). Here the same simulation was setup and the results are presented below.

Figure 3.8 shows the model response for a 1.6 s voltage pulse, transitioning from a holding potential of -60 mV to a depolarised level of 0 mV. The depolarisation pulse produces a rise in the cytosolic calcium concentration, as observed in the top right plot. The bottom plots for the currents illustrate that the initial phase of this calcium transient is primarily attributed the L-type calcium current and, to some extent, the SR release current. The decline in the calcium transient is primarily driven by the rapid reduction in the VOCC, coupled with an increase in SR uptake pump currents.

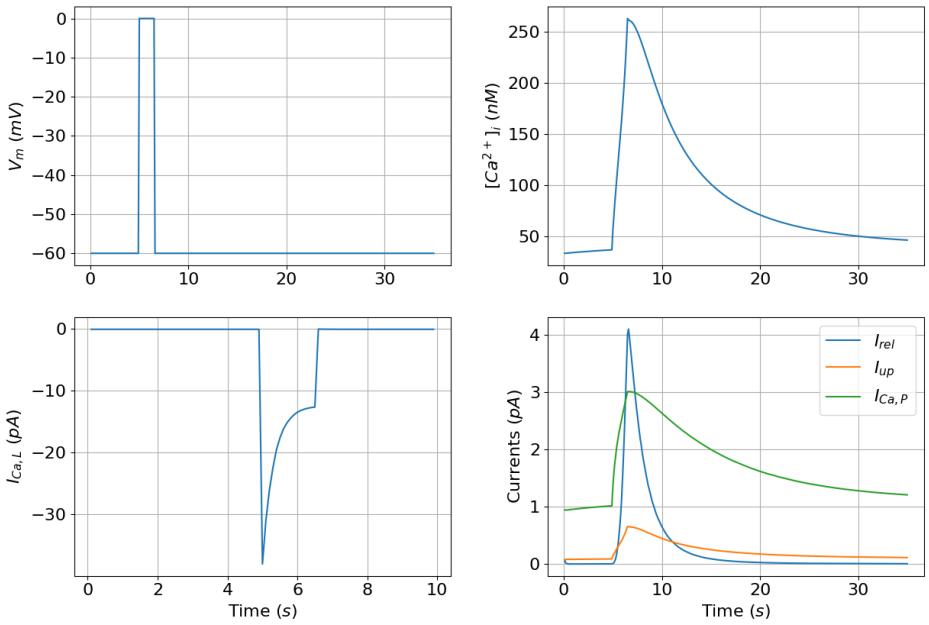

Figure 3.8: Simulation results for the clamp test as setup in [173] fro the validation of the electrochemical model. Top left: membrane potential input for the test; Top right: intracellular calcium concentration output; Bottom left: L-type VOCC channel current; Bottom right: output of channels that directly affect the calcium concentration (calcium pump, SR uptake and release)

Next, the calcium concentration distribution acquired was input to the Hai-Murphy model, with the setup described in the previous section.

Figure 3.9 shows the response of the Hai-Murphy model to the clamp test conditions. The plot shows only the attached cross bridges (including the latched state). Most of the connected cross-bridges at the resting potential of $-60\,mV$ are in a latch state. The phosphorylation of unbound myosin M (not shown)

and the transition from AM to AMp following the Ca^{2+} transient contribute to the rapid rise of the active cycling cross-bridges. With the decrease in Ca^{2+} levels, the dephosphorylation process becomes dominant, causing the connected cross-bridge fraction to shift back toward the latch state.

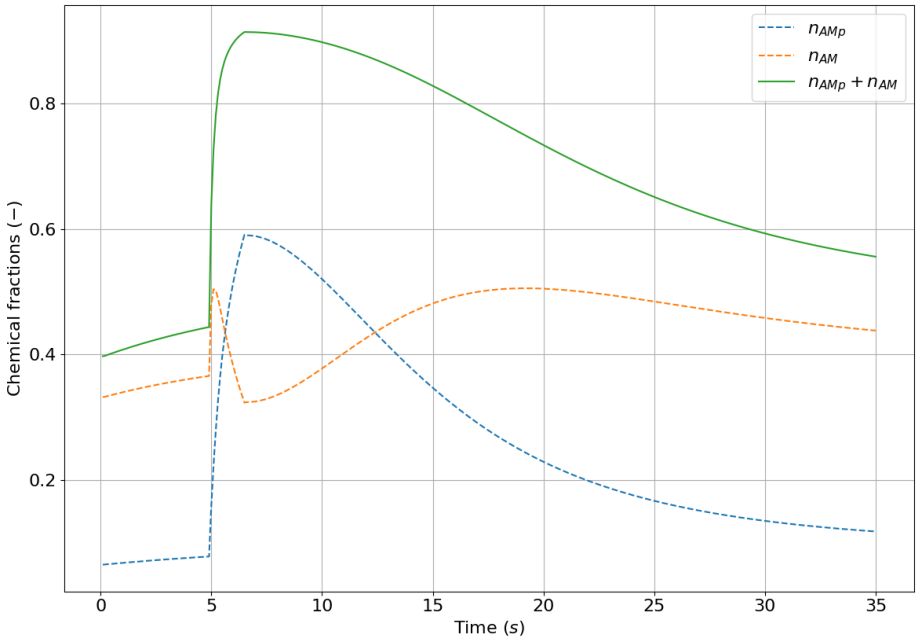

Figure 3.9: Hai-Murphy model results for calcium distribution acquired from the clamp test results

In general, the electrochemical model can provide useful information on the intricate regulatory mechanisms that govern calcium dynamics in smooth muscle cells. Additionally, it is very helpful to better understand how changes in intracellular calcium contribute to smooth muscle contractions. However, electrochemical models require a significant amount of experimental information for their full validation and parameter identification. In the context of cerebral vessels, experimental data concerning various cellular compartments is difficult to obtain. The high number of non-linear equations is also a limitation for their employment. These are some of the reasons that lead to the development of a different approach for modelling intracellular signalling for tone generation, which will be reported in the following section.

3.3 Novel approach

As already discussed, there is enough evidence showing that the pressure-induced intracellular Ca^{2+} concentration increase is mediated through changes in mem-

brane depolarisation level [203, 204]. The process through which this calcium concentration leads to the formation of cross-bridges, and ultimately to active tone generation of the SMC is also well-established. Many computational models of SMCs have been focusing only on this cytosolic Ca^{2+} pathways for describing vascular reactivity [205, 206, 207]. There is, however, sufficient experimental evidence [48, 49] that calcium signalling is not the only pathway through which the SMC contractile behaviour is triggered. This evidence does not dethrone intracellular calcium as the dominant factor, but they can act in parallel. Such mechanisms can make the contractile ability more sensitive to calcium, and thus enhance the contraction. They can also affect the cytoskeleton causing a reorganisation of its structure which ultimately augments the contractile behaviour during myogenic response.

In particular, the cellular pathway of RhoA/Rho-associated kinase (ROK) activates when pressures exceed a threshold ($\sim 40 - 60$mmHg), and it inhibits the MLCP activity, which is the factor that de-phosphorylates the myosin heads. Due to the decrease in de-phosphorylation, the available (phosporylated) myosin head fraction increases, and hence the rate of attachment to actin increases, providing a higher CB fraction, and ultimately generating a higher amount of tone [177, 178, 179, 208].

Higher pressure levels also enhance the polymerisation of actin through Protein Kinase C (PKC) and lead to the re-modelling of the cytoskeleton. This strengthens the connections between the plasma membrane, actin, and extracellular matrix and ultimately enhances the transmission of force generated by the CB cycling process [209, 180, 210, 211].

Although the models reported in the previous section represent a reference framework for computing active tone generation in vascular wall, they also consider only the Ca^{2+} pathway. This motivated the development of a new holistic model [212] that includes all the main cell signalling pathways occurring during the myogenic response. A minimal Cell Signalling (CS) model was developed within this context that, combined with the mechanical model described in the next chapter, provide a multi-scale computational framework that computes the development of pressure-induced tone within the SMCs through all the different signalling pathways.

Another point that needs to be highlighted is that all the referenced models use the Hai-Murphy chemical model for the CB cycling process, which assumes that some of the CBs contributing to active tone generation are in a latched state. However, currently there is no direct experimental evidence supporting this assumption. The new conceived model does not require the existence of a latched state for the CBs.

3.3.1 Cell signalling network

The pressure-induced pathways are assumed to act independently and contribute to the myogenic tone. It is important to state that these pathways are not sequentially activated [213, 214] across a wide range of pressure loads. The model is based on the recent publication of Irons and Humphrey [215] and their logic-based model. According to it, the final cellular signalling network can be described through internal variables connected in terms of activation/inhibition. The processes that define the activation/inhibition are described through activation functions, while their multivariable activity can be described with Boolean algebra operators AND, OR and NOT, as well as their combinations. An illustration of the model is presented in the diagram of Figure 3.10.

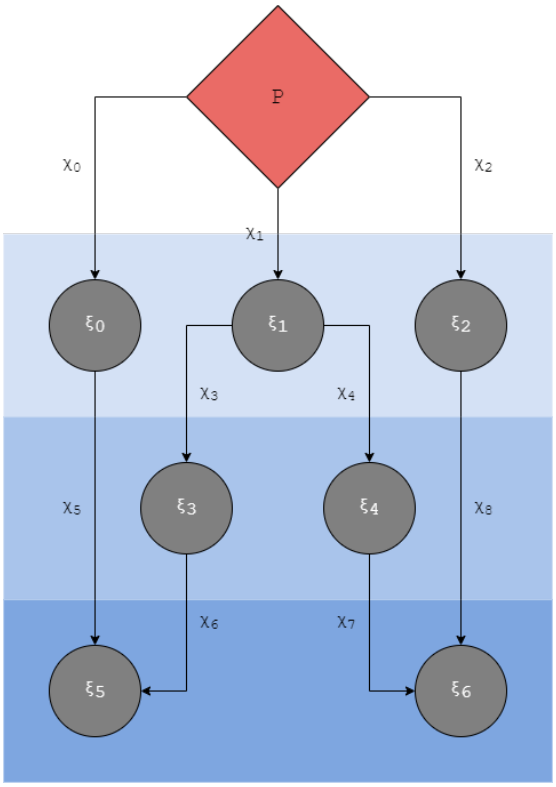

Figure 3.10: Diagram of the cell signalling network

The internal variables ξ_i represent normalised values of ion or protein concentrations or levels of a protein phosphorylation, as described in Table 3.2, and they are by definition between 0 and 1, i.e. $\xi_i \in [0, 1]$. All the processes that activate (or inhibit) these variables are represented by the activation functions χ_i. Each activation function that connects with a variable is defined through

$$\chi(\xi) = \chi_0 + (1 - \chi_0)(1 + K^n)\frac{\xi^n}{\xi^n + K^n}, \tag{3.9}$$

where χ_0 represents the value at basal tone, and n, K are fitted parameters. Some activation functions do not follow the above formulation, but an ad-hoc

expression that is supported from literature evidence. The activation functions are also within the value of 0 and 1, which means either completely inhibiting, or fully activating the pathway. The boundary values for these functions are:

$$\chi(0) = \chi_0,\ \chi(1) = 1. \tag{3.10}$$

The biochemical links assumed within the model are based on the current knowledge of the pressure-induced contraction [177, 178, 180] and thus it is assumed that the pressure stimulus modulates three independent cellular signal pathways: the cytosolic calcium; Rho kinase (ROK); and the protein kinase C. These pathways are distinguished in the first layer of Figure 3.10.

As mentioned earlier, increasing luminal pressure excites a series of calcium-driven or calcium-dependent channels, which in turn influx extracullular calcium inside the cell and increase the intracellular concentration [170, 181, 182]. The intracellular cencentration level is the only one affecting the contractile behaviour, since experiments have shown that changing the concentrations of extracellular calcium does not affect the myogenic response [216, 151]. In this minimal modeling approach, all the complex channel behaviour is unified under one activation function that directly connects the increase in pressure to $[Ca^{2+}]_i$ elevation through the function χ_0. The normalised ranges of intracellular calcium, reported also in Section 3.2.1 are used, which were found in literature [151, 176, 189, 190]. The level of $[Ca^{2+}]_i$ in turn leads to the phosphorylation of the light chain kinase LC_{20} through the CaCaM complex and the MLCK, exactly as described in previous section. All these processes are compressed into the activation function χ_5 and the phosphorylation level of the light chain kinase (pLC_{20}) is represented by ξ_5.

The other two pathways, ROK and PKC, involve a vast and complex system of proteins and messengers, but their contribution is represented by two distinguished variables. Similarly to cytosolic calcium, ROK activity is regulated by the level of pressure via activation function χ_1 and in turn, through the activation functions χ_3 and χ_4, it increases the phosphorylation levels of MLCP and the protein Cofilin which are represented by ξ_3 and ξ_4 respectively. As mentioned earlier in the text, the MLCP activity enhances the de-phosphorylation and thus, prevents the attachment of myosin heads to form CBs. When MLCP is phosphorylated (pMLCP) though, this process is prevented, and hence the LC_{20} de-phosphorylation is inhibited. The level of pLC_{20} is given by variable ξ_5, so the non-phosphorylated level is equal to $1 - \xi_5$. As described above, the MLCK acts on the non-phosphorylated LC_{20}, the balance of phosphorylated light chain, pLC_{20} will thus be described by the following ODE [212]

$$\frac{d\xi_5}{dt} = \frac{1}{\tau_5}\left[\chi_5(1-\xi_5) - (1-\chi_6)\xi_5\right], \tag{3.11}$$

where τ_5 is a time parameter defining how rapid the transition would be. The final branch of the pressure-induced parameter is the PKC pathway. Through this pathway, the alteration in pressure level affects the phosphorylation of HSP27 (pHSP27). This activation is modelled with function χ_2 and the phosphorylation level of pHSP27 is variable ξ_2. This phosphorylation of HSP27 is affecting the G-actin content ξ_6 through the activation function χ_8, which ultimately leads to the promotion of cytoskeleton re-modeling. Moreover, the phosphorylation of Cofilin (pCofilin) is described by ξ_4 and affected, as mentioned, by the ROK activity. It also impacts the re-modeling of the cytoskeleton by downgrading the level of G-actin, and this process is condensed in χ_7. The variables employed and the description on what they represent are summarised in Table 3.2.

Table 3.2: Internal variables description

Variable	Description
ξ_0	$[Ca^{2+}]_i$
ξ_1	ROK
ξ_2	pHSP27
ξ_3	pMLCP
ξ_4	pCofilin
ξ_5	pLC_{20}
ξ_6	G-actin

The mathematical formulation of all these processes of phosphorylation and protein/kinase levels alterations through their activation functions is described by the below set of ODEs [212]

$$\frac{d\xi_0}{dt} = \frac{1}{\tau_0}(\chi_0 - \xi_0), \tag{3.12}$$
$$\frac{d\xi_1}{dt} = \frac{1}{\tau_1}(\chi_1 - \xi_1), \tag{3.13}$$
$$\frac{d\xi_2}{dt} = \frac{1}{\tau_2}(\chi_2 - \xi_2), \tag{3.14}$$
$$\frac{d\xi_3}{dt} = \frac{1}{\tau_3}(\chi_3 - \xi_3), \tag{3.15}$$
$$\frac{d\xi_4}{dt} = \frac{1}{\tau_4}(\chi_4 - \xi_4), \tag{3.16}$$
$$\frac{d\xi_5}{dt} = \frac{1}{\tau_5}\left[\chi_5(1 - \xi_5) - (1 - \chi_6)\xi_5\right], \tag{3.17}$$
$$\frac{d\xi_6}{dt} = \frac{1}{\tau_6}\left[(1 - \chi_7) + (1 - \chi_8) - (1 - \chi_7)(1 - \chi_8) - \xi_6\right], \tag{3.18}$$

where the τ_i in the above have a unit of s (hence $1/\tau_i$ has a unit of s^{-1}) and represent the time parameters that define the transient behaviour of the variables.

3.3.2 Model parameters identification

The model described above presents a set of parameters that need to be identified. These parameters are the $\chi_{0,i}$, n_i and K_i characterising each activation function, as well as the time parameters τ_i. At first, the steady state behaviour of the signalling network is characterised, through the identification of the $\chi_{0,i}$, n_i and K_i. To this end, the predictions of the model (in terms of levels of phosphorylation or concentration of the proteins/kinases) were fitted against data acquired from the works by Cole and colleagues [180, 177] which were conducted on cerebral vasculature of Sprague and Dawley rats. The current model was designed to capture features of the intracellular signalling network under physiological/control conditions and selective pharmacological interventions. Hence the model fitting was carried out by considering these different conditions. An optimisation process was designed (in Python) using the covariance matrix adaptation (CMA) from the open-source library `cma`, which uses of a stochastic optimisation algorithm. With the optimisation process for the steady state case, all the parameters ($\chi_{0,i}$, n_i, K_i) included within the activation functions were acquired according to the experimental target.

To recap, the model to be fitted consists of a set of seven ODEs and nine activation functions as seen in Figure 3.10. All $\chi_{i,0}$, n_i and K_i of the activation functions were optimised in order to reproduce the experimental values of the internal variables ξ_i. This was achieve by minimising the cost function associated to the error e between the predicted value of the model and the experimental value of each variable:

$$e = \sqrt{\sum_{i=1}^{N} \left(\frac{\xi_i^{\text{exp}} - \xi_i}{\xi_i^{\text{exp}}} \right)^2}, \tag{3.19}$$

with ξ_i^{exp} is the experimental value of the concentration or phosphorylation level of any given variable, and ξ_i is the model predictions for the same variable. The number N is the total number of the equations solved. Since the steady state is targeted, the model equations have no transient part, i.e. the left hand side of Equations (3.12) – (3.18) is set to zero and no time parameters are considered. For finding the solution of this linear system of equations, the function `root` of the library `scipy` was used in python environment, which employs the Levenberg–Marquardt algorithm of the least squares method family. The model was optimised by considering two cases of drug intervention and the control case simultaneously, since the objective was to define a model that is able to predict all those cases with one set of parameters.

The optimisation process targeted the identification of 27 parameters (three pa-

rameters for each activation function, and nine activation functions). Finding the global minima of an error function with such a large number of parameters is not trivial and may lead to different outputs. To that end, the optimisation was carried out multiple times and the run with high error values ($e > 0.5$) were discarded. For the remaining, either the minimum error was chosen, or a statistical analysis was carried out that extracted the geometrical average of those cases for each parameters. For the results presented here, the optimised parameters that produced the least error are used. The identification of these parameters enabled the determination of all the activation functions of the intracellular signalling network. Each optimisation was limited in terms of maximum iterations to 1000, while the computational effort needed for each optimisation was $\sim 30\,min$. The experimental data that were used for the fitting procedure can be found in the Appendix B.

Table 3.3 presents the identified coefficients of the nine activation functions obtained by the optimisation procedure.

Table 3.3: Optimised coefficients of the activation functions

	$\chi_0(\bar{P})$	$\chi_1(\bar{P})$	$\chi_2(\bar{P})$	$\chi_3(\xi_1)$	$\chi_4(\xi_1)$	$\chi_5(\xi_0)$	$\chi_6(\xi_3)$	$\chi_7(\xi_4)$	$\chi_8(\xi_2)$
χ_0	0.131	0.181	0.0	0.0	0.419	0.0	0.02	0.187	0.142
K	15.47	6413	0.926	0.512	0.219	0.423	0.332	0.44	4401
n	0.464	3.083	0.558	1.325	15.83	521.5	10.68	88.7	1.408

In Figure 3.11, all the activation functions are presented against the normalized pressure/input variable. The reference pressure level for normalisation is $P_{\text{ref}} = 140 mmHg$ and it was chosen as a maximum value of the reported pressure levels for the experiments considered. It is also a reasonable amount of maximum pressure these cerebral vessels can support before the yielding point [160]. The first three functions that are shown together (top left plot) show the pathways that lead to the increase in intracellular calcium, ROK and PKC respectively. In all three, for lower pressure, the increase is lower than for higher pressures. Especially for the ROK pathway, it is clear that there is a threshold-like point $\sim 0.2P_{\text{ref}}$ that there is no ROK activity. This is in line with previous reports on the pressure-induced ROK pathway findings [208, 177, 210, 178]. This threshold is much lower in terms of pressure for the calcium activity [217, 152] which is reflected in the behaviour of χ_0. Another notable aspect is the behaviour of χ_5 and χ_6. These two functions show how the intracellular calcium elevation and the phosphorylated MLCP affects the phosphorylation of the light chains. It is concluded that for a lower pressure level there is no activity on the formation of CBs, which is also apparent in the Hai-Murphy model, where similarly, for low values of cytosolic calcium, there was no CB formation.

In the following, the capacity of the model to simultaneously fit different experi-

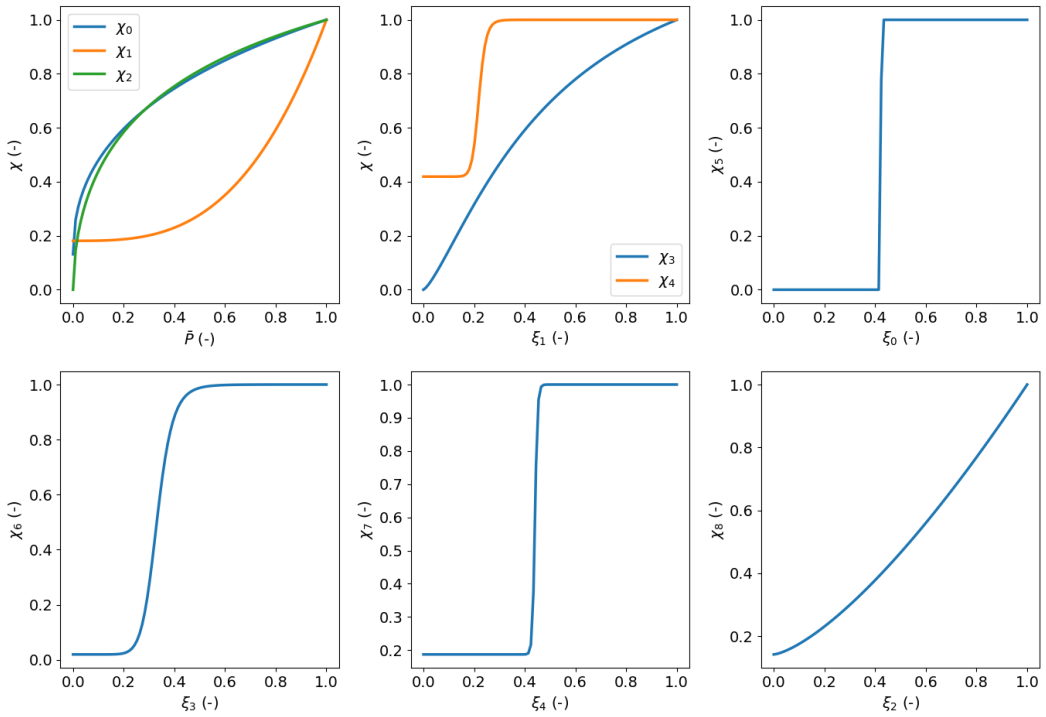

Figure 3.11: Activation functions of the model for a range of normalised pressure levels

mental conditions is reported. Simulation results against the experimental values for the two drug intervention and the control cases for pMLCP and pLC_{20} are first considered.

Figure 3.12 shows how the cell signalling model captures the impact of pressure on pMLCP and pLC_{20} levels in the control case, with $0.3\,\mu M$ H1152, and $3.0\,\mu M$ GF. Normalised pMLCP values are relative to the 10 mmHg control case, while absolute values are provided for pLC_{20} fractions. The experimental pLC_{20} value under $3.0\,\mu M$ GF was adjusted to account for the difference between the two control values at 100 mmHg, as reported [177].

Figure 3.13 presents the impact of pressure on the intracellular pathways responsible for cytoskeleton remodelling. The established chemical model effectively replicates the pressure-induced elevation of pHSP27 in both the control case and under $0.5\,\mu M$ H1152. Similarly, it accurately depicts the associations between pressure and pCofilin, as well as pressure and G-actin levels in the control case, under $0.5\,\mu M$ H1152, and $3.0\,\mu M$ GF.

3.4 Conclusive remarks

To summarise, in this chapter a more detailed description was given regarding the pressure-induced cellular processes that take place during the SMC contraction.

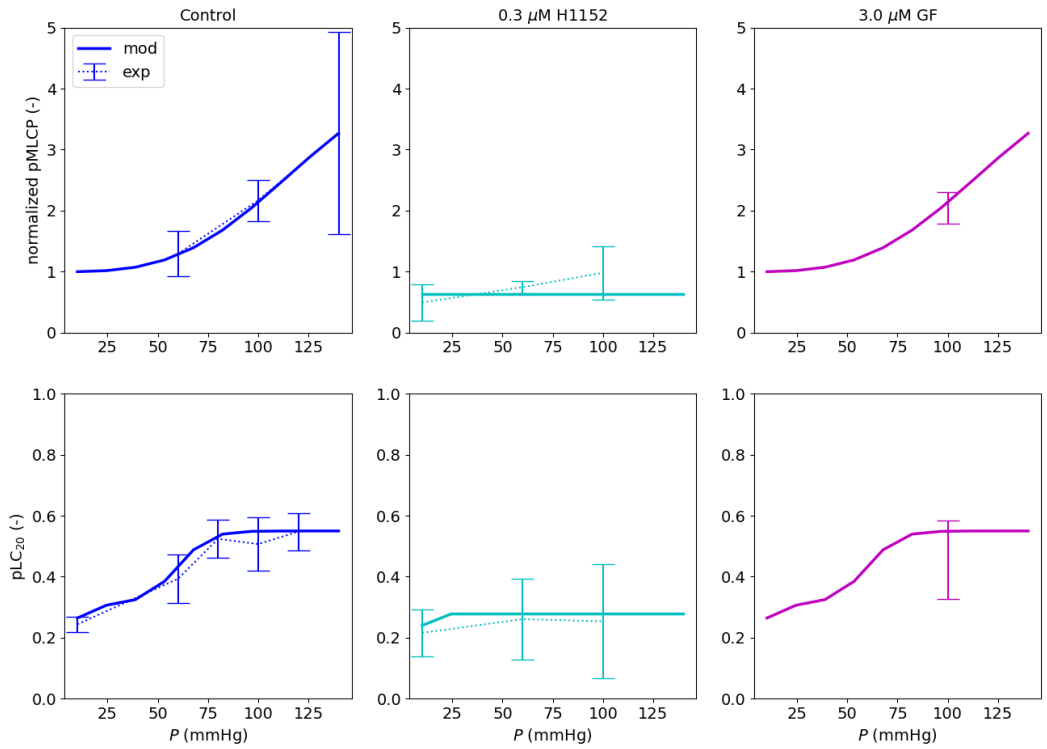

Figure 3.12: Model predictions against experimental evidence for pMLCP and pLC_{20}

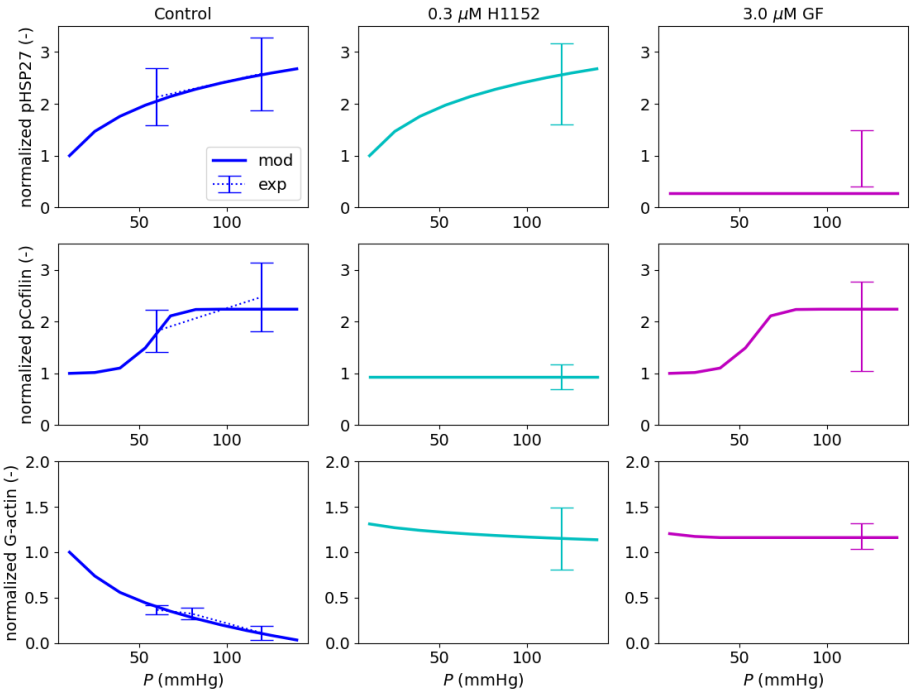

Figure 3.13: Model predictions against experimental evidence for cytoskeleton remodelling variables

An overview was also provided regarding the numerical modelling approach on the topic. Two models were presented that describe different aspects of the cellular dynamics during myogenic response. Finally, the novel model developed in the context of this thesis was introduced.

The proposed model includes all the major pressure-induced intracellular pathways found in literature through a logic-based approach. The simulated behaviour of five different intracellular components well match experimental measurements across a large pressure range, for physiological and drug intervention scenarios.

The limitations of the model lie on the uncertainties associated to some secondary signalling connections between cellular components which have not yet been fully explored. It has been suggested that at intermediate pressure levels, some drug interventions which inhibit or completely prevent actin polymerisation can also affect the influx of calcium within the cell [218]. There is also some preliminary evidence that the calcium waves produced from the sarco-plasmic reticulum can also regulate the MLCP activity [203]. Due to the lack of further experimental evidence, however, these suggested associations were considered of secondary importance. Moreover, the proposed model does not include a detailed link between integrins and calcium sensitisation [219], while it would be a useful addition for the accurate simulation of drugs that have an impact on the signalling between SMC and extracellular matrix. Nevertheless, as per the methodology followed [220, 215], the addition of new components to the framework is something that is easily achieved. Finally, differences in pressure-induced vasoreactivity between the resistance arteries and arterioles seem to exist due to different calcium activity rather than calcium sensitivity [189]. Hence, upon adequate characterisation of the pressure-calcium relationship, the current model could be also extended to arterioles.

Chapter 4

Vascular wall mechanics with active tone generation

In this chapter a methodology for integrating the pressure-induced cellular signalling model presented in Section 3.3 into a vascular wall model is presented and assessed. This is achieved by using a strain energy function component that accounts for the active tone development, connecting the cellular with the continuum scale.

The description of the proposed methodology is followed with identification and validation of model parameters. Its steady-state and transient response is assessed through a number of tests. Furthermore, a sensitivity analysis is conducted on the temporal parameters to evaluate the dynamic character of the model.

4.1 Modelling tissue contractility

The proposed modelling approach follows the works by Murtada *et al.* [47, 175, 144, 88]. These are based on the sliding filament theory, in combination with a Strain-Energy Function (SEF) formulation, as done also in other works [221, 84]. It is worth to mention that there are other reference models describing tone generation that do not consider active tension as a term within the SEF [86, 82, 81]. However, in the former approach the active tone contribution can be integrated in a easy and robust way within a hyperelastic framework.

4.1.1 Background

As mentioned the introduction, the first computational model incorporating the sliding filament theory was introduced by Hill [80] as a three element model, and it referred to the striated muscle mechanical response. The Hill model and

its elements can be seen in Figure 1.3 with an explanation of its elements in the respective chapter. The governing equation is a hyperbolic relationship $(v+b)(P+a) = b(P_0 + a)$ relating the active force P with the velocity v during an isotonic experiment. The muscle is assumed to be initially contracted isometrically to a maximum force P_0, and the parameters a and b are free parameters, fitted to experimental values.

Throughout the years, other models used the three-element Hill model to investigate muscle contraction [222, 223, 224, 225]. The machinery underlying vascular SMC contraction is similar the one regulating striated muscle [47, 226]. Several models have been developed using the sliding filament theory and the three-element Hill model as their mechanical part to simulate the response of the vessel wall during contraction/dilation, as well as an elastic component for the CBs formed. The chemical part, describing CB formation and cycling, is also modeled in the same manner, with Hai-Murphy model and its expansions being the most widely used [227, 192].

4.1.2 Contractile units kinematics

The formulations presented in this section have been puiblished in the work of Murtada *et al.* and repeated here for completeness [88].

The basis for the mechanical model deformation is the three-element Hill model, which appears a common choice for striated and smooth muscles cells. The contractile apparatus responsible for the development of active tone is described as a network of in series contractile units (CUs). The apparatus is considered in two configurations: the reference, which is defined as the *load-free* state, where no loads have been applied, and the current, *loaded*, where loads have been applied. The loads refer to the development of the active tone, which causes a change in length of the CUs. The respective lengths are defined as L_{SMC} for the reference configuration, and l_{SMC} for the current one. As active tone is a response that tends to keep the wall contracted against an increasing tension, the stretch is below the unit for contraction, i.e. $l_{SMC} < L_{SMC}$ during contraction, while the opposite is valid for dilation. Since the SMCs of the vessels are aligned along the circumferential direction [6, 5] this change in length is occurring along the circumference of the wall, and the ratio of lengths is the circumferential stretch, i.e. $\lambda_\theta = l_{SMC}/L_{SMC}$. It is worth noting here that for resistance cerebral vessels the axial stretch does not play a significant role on their pressure-induced vasoreactivity [228]. Figure 4.1 illustrates the connectivity of all the parts constituting a single CU.

Chapter 3 focuses on the biochemical processes that ultimately affect the generation of active tension. There are two main biochemical contributors to the SMC

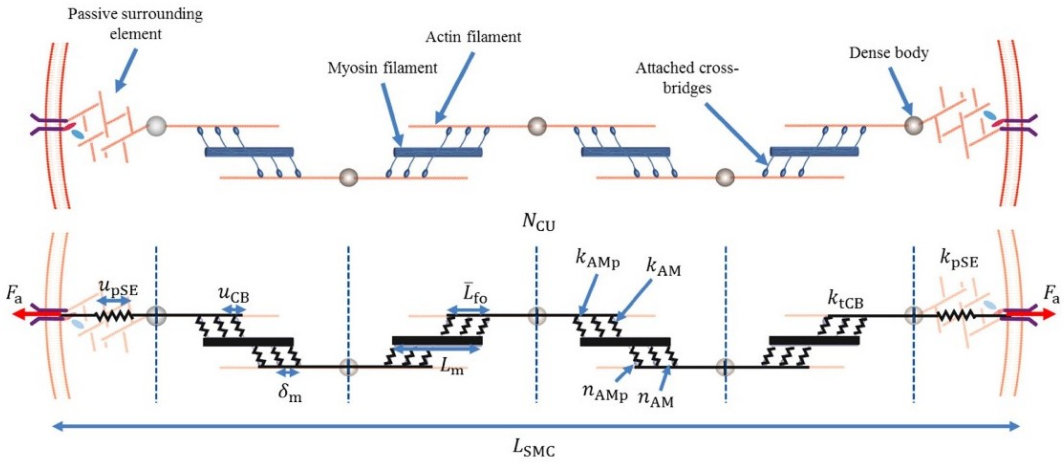

Figure 4.1: Schematic of the cell model (Image taken from [88], permissions granted from Springer Nature)

contractile state: the the number of CBs (shortening the fibre through power stroke) and the cytoskeleton stiffness. Unlike the original formulation [88], in this study only phosphorylated CBs are considered to contribute to force generation, since the latched state is not explicitly modelled, as its role is not supported by biochemical evidence. The CBs are considered as elastic elements contrary to the filaments, which are assumed to be rigid. Therefore, the total stiffness of the CBs is:

$$k_{tCB} = 2\frac{L_m}{\delta_m} n_{AMp} k_{AMp}, \tag{4.1}$$

where L_m and δ_m are the lenth of the myosin and the distance between two myosin heads respectively as can be seen in Figure 4.1. Moreover, n_{AMp} is the population of the attached cross bridges as a fraction of the total myosin heads, and k_{AMp} is the elastic stiffness of the cross-bridges. The stiffness has a multiplier of 2 because it is assumed that the myosin attaches to two actins (up and down, Figure 4.1).

The next step is to formulate the stiffness of all the CUs, but first, it is necessary to define the filament overlap and its function. The actin filament is assumed to be longer than the myosin filament, and the length at which these two overlap is defined as filament overlap L_0. The overlap of those two defines the maximum number of attachments that can be made between them, and thus acts as a regulator of the attached CBs amount. Average filament overlap is defined as a function of the relative sliding between the two filaments u_{fs}. They are also dependent on the optimal relative filament sliding u_{fs}^{opt}, which is the relative sliding for which the distribution is maximised. There are two distributions for the filament overlap reported in literature, a quadratic [175] and a Gaussian [88], which are presented in Figure 4.2.

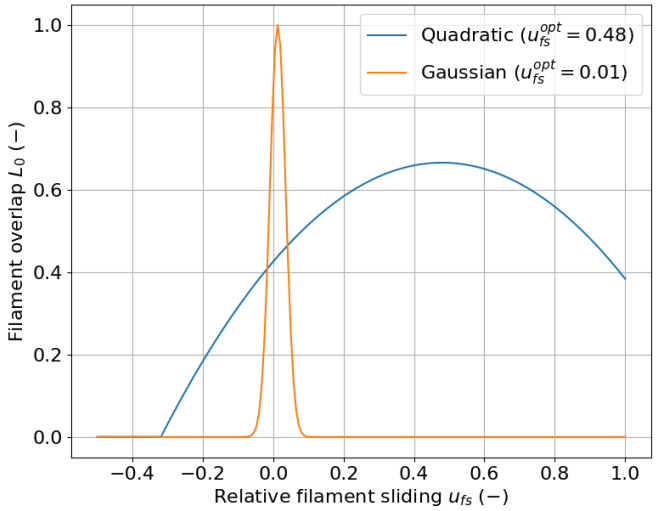

Figure 4.2: Quadratic and Gaussian distribution filament overlap distribution L_0 against relative filament sliding u_{fs}

For the scope of this study, the Gaussian distribution is considered. The overlap and filament sliding are normalised according to the SMC reference length L_{SMC}, and are given by $\bar{L}_0$ and $\bar{u}_{fs}$ respectively. The distribution, as a function of the sliding, is given by the exponential relationship below

$$\bar{L}_0(\bar{u}_{fs}) = \exp\left\{-\frac{(\bar{u}_{fs} - u_{fs}^{opt})^2}{2(s_{f0}/L_m)^2}\right\}, \tag{4.2}$$

where s_{f0} is a fitted parameter. Now, the total stiffness of any number N_{CU} of CUs can be defined as

$$k_{tCU} = \frac{\bar{L}_0}{2N_{CU}} k_{tCB}. \tag{4.3}$$

The total deformation of a single CU depends on two characteristics: the elongation of the attached CBs, u_{CB}, since they are considered elastic; and the deformation of the cytoskeleton, i.e. the passive surrounding element (pSE), u_{pSE}. The pSE is also considered an elastic element and its stiffness is defined as k_{pSE}. Note that the stiffness of the pSE is altered by the F-actin, which is related to G-actin of the chemical model and defined in the next section. The way theF-actin alters the stiffness of the pSE will be discussed in the next section where the coupling of the two models is presented. Finally, the total active force, produced by N_{CU} CUs with their respective pSEs will be

$$F_a = 2\left(u_{CB}N_{CU} + u_{pSE}\right)\frac{k_{tCU}k_{pSE}}{2k_{tCU} + k_{pSE}}. \tag{4.4}$$

For a single cycling CB, an amount of force drives its deformation, the power stroke. If an attached CB with a stiffness of k_{AMp} elongates a distance u_{ps} due to the power stroke, then the total amount of force driving this elongation is

the sum of the products of the stiffness times their elongation. For the scope of this study, the amount of this elongation is assumed to be the same for all CBs. Hence, the total amount of driving force within a CU caused by the cycling CBs would be

$$F_c = \sum k_{AMp} u_{ps} = \bar{L}_0 \frac{L_m}{\delta_m} n_{AMp} k_{AMp} u_{ps}, \tag{4.5}$$

With the elongations of the pSE and the CBs, and the relative filament sliding defined, the length of the SMC at the current configuration is the total elongation with respect to the reference one. For a single CU, the deformation is the sum of two deformations: the elongation of the CB, and the relative sliding between the filaments. The sum of all those CU deformations gives the elongation of the CUs. Finally, the total elongation is extracted if the deformation of the pSE is added to the elongation of the CUs

$$l_{SMC} = L_{SMC} + 2N_{CU} \left(u_{CB} + u_{fs}\right) + 2u_{pSE}. \tag{4.6}$$

At this point, the density of the contractile fibres is introduced. Let N_{CF} be the number of contractile fibres per unit of area. Multiplying it with the active force generated by the CUs, and combining it with Equations (4.3) and (4.6), the first Piola-Kirchhoff stress P_a is obtained

$$P_a = \left(\lambda_\theta - 1 - 2N_{CU}\bar{u}_{fs}\right) L_{SMC} \frac{\bar{L}_0(\bar{u}_{fs}) k_{tCB} k_{pSE}}{2\left(\bar{L}_0 k_{tCB} + N_{CU} k_{pSE}\right)} N_{CF}, \tag{4.7}$$

with the filament sliding $\bar{u}_{fs}$ as a variable. The filaments can slide relative to each other, either because of the cycling of CBs or because of the application of external loading/deformation. Therefore, total sliding can be seen as the addition of these two separate deformations. The first is the chemical part, $\bar{u}_{fs}^{chem}$, related to deformations due to attached CBs and the pSE. The second is the mechanical part, $\bar{u}_{fs}^{mech}$, related to the changes in the circumferential stretch λ_θ. It is assumed that these two deformations are decoupled, and hence the total sliding between the filaments is:

$$\bar{u}_{fs} = \bar{u}_{fs}^{chem} + \bar{u}_{fs}^{mech}. \tag{4.8}$$

For the chemical part of the filament sliding, an evolution law is defined to describe their kinetics. It is, thus

$$\frac{\partial \bar{u}_{fs}^{chem}}{\partial t} = \beta \left(F_a - F_c\right), \tag{4.9}$$

where β is a time parameter which will be analysed in the following sectios. For the mechanical part of the sliding, which is defined to take up any changes in the

stretch, its description in time is

$$\frac{\partial \bar{u}_{fs}^{mech}}{\partial t} = \frac{1}{2N_{CU}} \frac{\partial \lambda_\theta}{\partial t}. \tag{4.10}$$

4.1.3 Constitutive model for tone generation

In Chapter 2 the vascular wall was described as a hyperelastic, fibre-reinforced material. To include the active tone generation, the total SEF is now decomposed into two parts

$$\Psi = \Psi_p + \Psi_a, \tag{4.11}$$

Here, the passive part Ψ_p is formulated according to Equation (2.47) and accounts for the stored energy associated with the passive behaviour of the material. The active part Ψ_a represents the energy accounting for the in-series CUs with their pSE. As mentioned earlier in the thesis, the wall of a cerebral vessel is made mainly by three layers. In the current model only the media layer is considered, which includes the SMCs.

For the CUs (with their pSEs) a unit vector $\mathbf{M}^{CU}$ is introduced that, similar to the wall model, describes the direction that the CUs are placed. This vector will be [13] $\mathbf{M}^{CU} = [0, \sin\phi, \cos\phi]^{-1}$, with ϕ being the angle with respect to the circumferential direction that the CU fibres have. Though, it is already mentioned that the SMCs are aligned along the circumferential direction, thus $\phi = 0^o$, and the unit vector reduces to $\mathbf{M}^{CU} = [0, 0, 1]^{-1}$.

Introducing the deformation gradient $\mathbf{F}$, the right Cauchy-Green is $\mathbf{C} = \mathbf{F}^{\mathrm{T}}\mathbf{F}$ and, subsequently, the fourth strain invariant is $\mathrm{I}_4 = \mathbf{M}^{CU} \cdot \mathbf{C}\mathbf{M}^{CU} = \lambda_\theta^2$. Hence, the relationship between the first Piola-Kirchhoff stress and the SEF is

$$P_a = \frac{\partial \Psi_a}{\partial \lambda_\theta}. \tag{4.12}$$

The Cauchy stress tensor is derived in matrix form as $\boldsymbol{\sigma} = 2\mathbf{F}\frac{\partial \Psi}{\partial \mathbf{C}}\mathbf{F}^{\mathrm{T}} - p\mathbf{I}$, with p being a Lagrange multiplier that enforces incompressibility [142]. Since all contraction is being held at the circumferential direction, the radial and axial components are dropped, and the matrix form reduces to an algebraic one. The final form of the Cauchy stress developed within the wall due to the active component is

$$\sigma_\theta^a = \lambda_\theta \left[\left(\lambda_\theta - 1 - 2N_{CU}\bar{u}_{fs}\right) L_{SMC} \frac{\bar{L}_0 k_{tCB} k_{pSE}}{2\left(\bar{L}_0 k_{tCB} + N_{CU} k_{pSE}\right)} N_{CF} \right]. \tag{4.13}$$

Through the SEF formulation described by equations (4.12) and (4.13) the active

behaviour can be combined with the passive one to calculate the total/resulting response of the vessel.

4.2 Cellular and tissue scales coupling

In this section the coupling of the cell and tissue models is reported, as well as the details of the numerical procedure. As reported above, the cell signalling model is used to evaluate the intracellular biochemical processes, and it is combined with the vascular wall model that includes both passive and active tension development.

Although the chemical model is capable of capturing various drug intervention scenarios, pressure-induced tone generation remains the main scope of this study. This active contractility is pivotal in the vascular wall response to the sudden pressure changes (the myogenic response), as well as in the formation of the basal vascular tone.

4.2.1 Active tone development

The cell signalling network acts independently from the kinematics of the vascular wall. Thus, the chemical model employed to simulate the cell signalling is sequentially coupled with the mechanical one that accounts for the wall response to the pressure stimulus. The cell signalling described in Section 3.3 is stimulated through a pressure level signal, and the variables ξ_5, ξ_6 represent the pLC_{20} and G-actin levels. The pLC_{20} role has already been analysed through the formation of CBs.

The increasing in pressure also leads to increased levels of pCofilin, which down-regulated the level of G-actin content. Moreover, the PKC pathway also regulates the G-actin level through the rise in pHSP27 level. The decrease of G-actin essentially promotes the G-actin to F-actin transition [229], and thus it is defined that F-actin $= 1 -$ G-actin. With F-actin being a key cytoskeletal component by which actin polymerisation is promoted [230] and leads to cytoskeleton re-modeling.

Thus, in terms of mechanical response, these two variables provided by the cell signalling network at cellular level are of crucial importance. Through pLC_{20} the cycling CBs are represented and for its acquisition the new pathways of Ca^{2+} sensitisation is included. Moreover, the F-actin is the variable that promotes cytoskeleton re-modeling, i.e. extracellular matrix (pSE) stiffness alteration.

At first, the response of the chemical model for the steady state was tested for a representative pressure range for cerebral vessels.

The results presented in Figure 4.3 show the steady state response of the chemical model with respect to the level of intraluminal pressure. The variables that are solved for and presented is pLC_{20} and G-actin, while the level of F-actin is extracted from the latter. The values of the variables are normalised with respect to the reference control values. The behaviour of the pLC_{20} follows the trend of the respective Hai-Murphy steady state case with the difference that the sensitisation property makes the calcium level lower for low pressure values, which is in line with the experimental calcium concentrations examined [151, 176, 189, 190]. As can be seen, for lower pressure values, the CB formation has a low value and a low gradient for a range up to $\sim$ 40 mmHg followed by a region where it rapidly increases (from 40 to 80 mmHg) and finally reaches a threshold value where further increase in pressure cannot provide higher CB formation. Moreover, the sensitisation also makes the transition to the maximum value in a smoother manner, which is also seen in the experiments. Regarding the F-actin behaviour, it is observed that as luminal pressure is increasing, it keeps increasing. This is also in line with the experimental observations showing that higher level of polymerisation is observed as a result of higher luminal pressure. The steady state behaviour of the chemical model is of much importance for the coupling with the mechanical model, since the fine tuning of the mechanical parameters was conducted with respect to the steady state response.

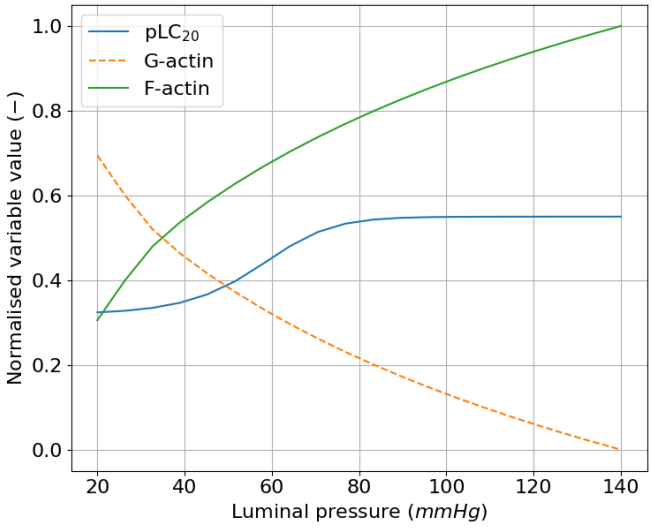

Figure 4.3: Steady state results of the cell signalling model for different pressure inputs

The total mechanical behaviour of the vascular wall is finally computed as a combination between passive and active tone development. These two elements are put together through the proposed SEF, as reported in Equation (4.11).

As described in Chapter 2, only the radial component of the momentum equilibrium equation, since the vessel is considered axysymmetric and the axial stretch is assumed to be fixed. The equilibrium in the radial direction is given by Equation

(2.45), repeated here

$$P - P_{\text{ext}} = \int_{R_i}^{R_i+H} \left(\lambda_\theta \frac{\partial \Psi}{\partial \lambda_\theta} - \lambda_r \frac{\partial \Psi}{\partial \lambda_r} \right) \frac{1}{\lambda_\theta \lambda_z r} \, dR.$$

Employing a SEF description of the active tone development has the advantage that the above equation can be easily manipulated to include the active component. Thus, with the distinction between active and passive components through Equation (4.11), and the set up explained in previous section where the active component only acts in the circumferential direction (i.e. $\partial \Psi_a / \partial \lambda_r = 0$), the equilibrium equation is

$$P - P_{\text{ext}} = \int_{R_i}^{R_i+H} \left(\lambda_\theta \frac{\partial \Psi_p}{\partial \lambda_\theta} + \lambda_\theta \frac{\partial \Psi_a}{\partial \lambda_\theta} - \lambda_r \frac{\partial \Psi_p}{\partial \lambda_r} \right) \frac{1}{\lambda_\theta \lambda_z r} dR. \tag{4.14}$$

It is reminded here that the passive pressure is ultimately a function of several variables as explained in Chapter 2. Equation (2.48) is repeated here

$$P_p = f(A, H, R_i, \lambda_z, \omega, c, k_1, k_2, \alpha, \phi) = \bar{P}(A, \bar{\psi}).$$

Where A is the luminal area and throughout this study it is considered the unknown of the systems set. The thickness H and inner radius of the stress-free configuration R_i, are constant values and part of some examinations that will be discussed later in the text. The axial stretch λ_z is also kept constant, as already mentioned. The opening angle ω, and the parameters referring to the passive wall model c, k_1, k_2, α are variables connected to the constitutive model and the procedure for their characterisation is also discussed later in the text.

For the active part of Equation (4.14), from Equations (4.12) and (4.7) it is clear that Ψ_a is dependent on the circumferential stretch λ_θ and thus on the lumen radius, as described above, as well as the normalised relative filament sliding $\bar{u}_{fs}$. Furthermore, from the definition of the CB elastic stiffness, Equation (4.1), a dependency on the fraction of attached CBs n_{AMp} is apparent, as well as on the extracellular matrix stiffness k_{pSE}. The fraction of the attached CBs n_{AMp} within the CU is the number of the phosphorylated light chains pLC_{20} (ξ_5 of the cell signalling network model) and is directly input from the chemical model solution. The cytoskeleton remodelling, as mentioned in Section 3.3, is affected by the level of F-actin developed within the cell. A Hill function was employed to model the effect of F-actin on the pSE stiffness

$$k_{pSE} = \bar{k}_{pSE} \frac{(1 - \xi_6)^{n_{AC}}}{(1 - \xi_6)^{n_{AC}} + K_{AC}^{n_{AC}}}, \tag{4.15}$$

where the $\bar{k}_{pSE}$ is the mean value of the stiffness, and as explained, since ξ_6 is the level of G-actin, the respective level of F-actin is computed as $1 - \xi_6$. The constants n_{AC}, K_{AC} are fitted parameters, and will be discussed in next sections on the methodology followed for their acquisition. Through this expression, a dependency on the F-actin level is introduced to the behaviour of the extracellular matrix stiffness, which is dictated by the experimental findings [48, 49] and was modelled in the cellular model. Overall, the stress generation due to the active part is a function of another set of parameters.

$$P_a = f(r_i, \bar{u}_{fs}, \xi_5, \xi_6). \tag{4.16}$$

4.2.2 Solution procedure

The chemical and mechanical models are sequentially coupled. This means that the first step of the solution is to solve the chemical model using the pressure input. The output of the chemical model is then passed into the mechanical one. In brief, solving the Equations (3.12) – (3.18) provide the chemical output, and then using its results, computing the luminal area through Equation (4.14), the response in terms of inner diameter can be acquired since a circular cross-sectional area is considered, i.e. $r_i = \sqrt{A/\pi}$.

To find the area using the pressure equation requires the solving of the equation $P = P_{in}$ where P is the pressure integrated along the thickness, and P_{in} is the inner pressure which is a boundary condition for the problem. Note here that the external surface pressure which is in the left-hand side of Equation (4.14) is considered as the reference pressure, and thus set to zero. Essentially, the strategy for the lumen area computation is to find the lumen area for which the pressure developed by the wall is equal to the pressure boundary condition.

For the passive part, this procedure was mentioned in 2.4.4, and is also described in the work of Coccarelli *et al.* [123]. When the active part is considered too, it adds an additional equation to be solved simultaneously for the acquisition of the area (or radius). Consequently, the equations to be solved are given by equations (2.48) and (4.16). Equation (4.16) shows that the active pressure generated is dependent only on the relative sliding $\bar{u}_{fs}$. The equation given for the $\bar{u}_{fs}$ is given by equation 4.8. It is considered that $\bar{u}_{fs}$ is evaluated with an averaged stretch along the thickness, which represents the mean filament sliding across the wall. For the solution, Equation (4.14) is re-arranged, and expressed as a function of the area (or radius)

$$r_i = f(P, \bar{u}_{fs}), \tag{4.17}$$

where the second equation that completes the system is given by the Equation

(4.8), with $\bar{u}_{fs} = f(\bar{u}_{fs}, r_i)$. Note here that $\bar{u}_{fs}$ is also dependent on the chemical part, but chemical and mechanical models are sequentially coupled, the variables ξ_5 and ξ_6 are produced independently to the mechanical system. The procedure is described in more detailed in the next lines.

This is a highly nonlinear problem and is solved again by employment of the Levenberg–Marquardt algorithm of the least squares method family through the non-linear solver `root` included in `scipy` library in Python environment.

In order to compute the filament sliding as the second equation for the system, the time derivative of Equation (4.8) is used with the expressions described in Equations (4.9) and (4.10). To include the differential equation into the system, a temporal discretisation needs to take place. This is achieved with the implicit backward Euler scheme, which is unconditionally stable with respect to the time step employed, and its accuracy is second order. Let t_{n-1} be the previous time step, for which all values are known, and t_n the current one. The integration takes place within this time period $\Delta t = t_n - t_{n-1}$. The backward Euler scheme for the chemical part, based on Taylor series expansion on the neighbourhood of $t = t_n$, will be

$$\begin{aligned} \bar{u}_{fs,n-1}^{chem} \equiv \bar{u}_{fs}^{chem}(t_n - \Delta t) = \bar{u}_{fs}^{chem}(t_n) - \Delta t \frac{\partial \bar{u}_{fs}^{chem}}{\partial t}\Big|_{t=t_n} + \mathrm{O}(\Delta t^2) \\ \bar{u}_{fs,n}^{chem} = \bar{u}_{fs,n-1}^{chem} + \Delta t \cdot \beta(F_{a,n} - F_{c,n}), \end{aligned} \tag{4.18}$$

where the subscripts $n, n-1$ denote the time at which the functions are evaluated. In a similar manner, the temporal discretisation for the circumferential stretch that is included in the mechanical part, as well as the approximation of the mechanical part will be:

$$\frac{\partial \lambda_\theta}{\partial t} \approx \frac{\lambda_{\theta,n} - \lambda_{\theta,n-1}}{\Delta t}, \tag{4.19}$$

$$\bar{u}_{fs,n}^{mech} = \bar{u}_{fs,n-1}^{mech} + \frac{1}{2N_{CU}}(\lambda_{\theta,n} - \lambda_{\theta,n-1}). \tag{4.20}$$

Using the assumption of independence of the two components of the relative sliding, i.e. $\bar{u}_{fs} = \bar{u}_{fs}^{chem} + \bar{u}_{fs}^{mech}$, the final expression for the derivative becomes

$$\bar{u}_{fs,n} = \bar{u}_{fs,n-1} + \Delta t \cdot (F_{a,n} - F_{c,n}) + \frac{1}{2N_{CU}}(\lambda_{\theta,n} - \lambda_{\theta,n-1}). \tag{4.21}$$

Figure 4.4 illustrates the structure of the solver of the system to finally acquire the lumen area and the relative sliding. All formulations in the above equations refer to the general transient case. At first, the solution procedure was employed to test arterial rings for their static solutions. This can be considered by setting

all the transient parts equal to zero.

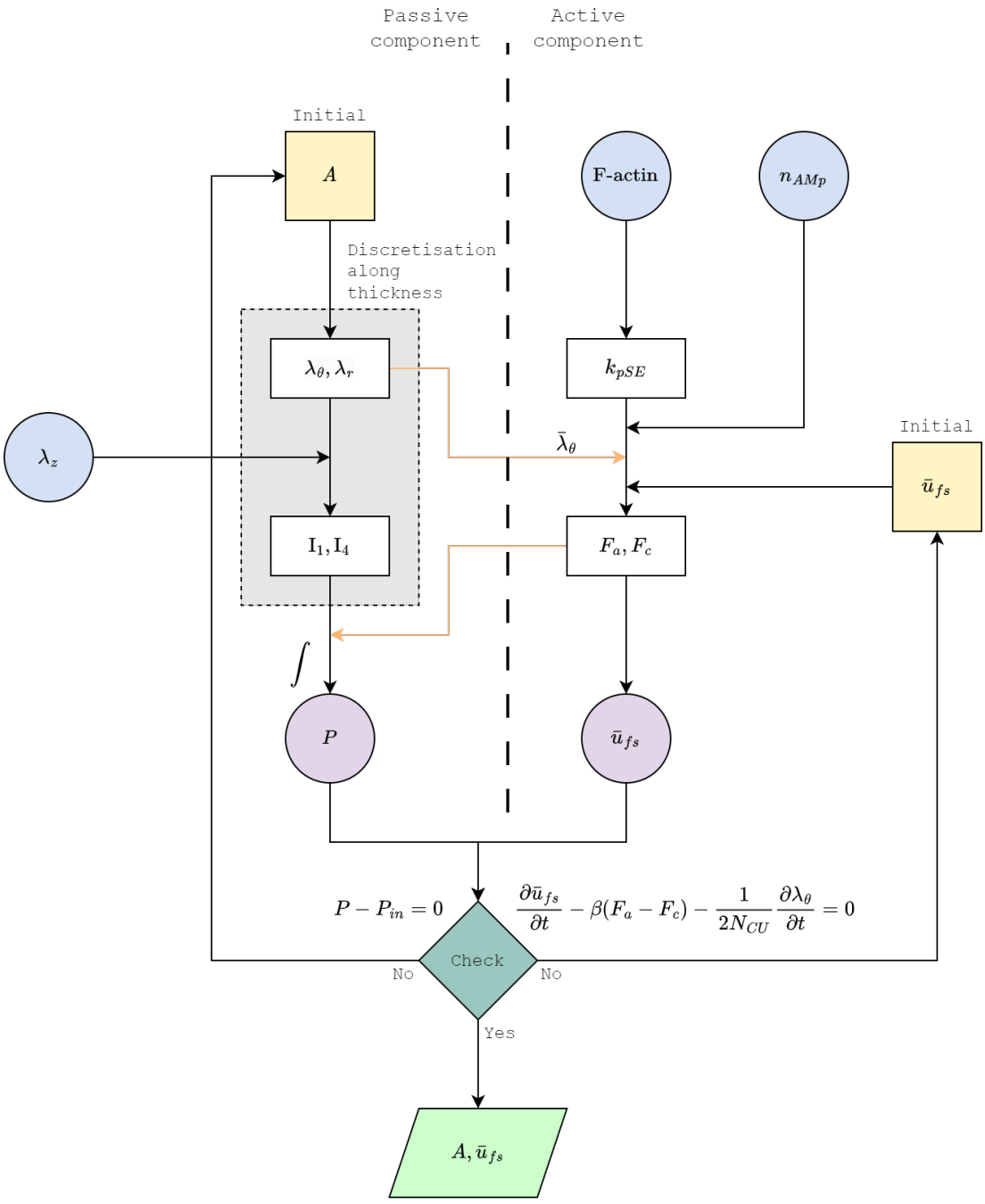

Figure 4.4: Structure of the solver set up to find the lumen area and relative sliding

As an input, the intraluminal pressure is given, and the schematic describes the strategy of the solver after the solution of the chemical part, which are the inputs n_{AMp} (ξ_5) and F-actin (ξ_6). Also, the axial stretch is considered as an input since it is constant for the scope of this study. The procedure is divided into the passive and active components. The system is solved with respect to A and $\bar{u}_{fs}$, and the criteria for convergence is the pressure input and computed values to be equal, and the solution of the relative sliding equation. Every parameter that is omitted

from the schematic is considered constant due to the large number of parameters needed.

In more detail, the solution is initiated by assuming an initial value for the lumen area and the relative sliding. For this study, the lumen area is initiated with the stress-free area $A_{\text{init}} = \pi R_i^2$, and the relative sliding as $\bar{u}_{fs,\text{init}} = 10^{-3}$. Note that for $\bar{u}_{fs}$ a low positive value is set because after some examination, setting an initial value of zero produced some instabilities. The integration of Equation (4.14) is computed by means of Simpson integration rule, dividing the thickness into five equal segments. Through the lumen area, the radial and circumferential stretches $\lambda_r, \lambda_\theta$ are calculated, which allow for the calculation of the strain invariants I_1, I_4, which allow for the integration of the passive part. The active component is input with the level of F-actin and the extracellular matrix stiffness is computed from Equation (4.15). For the calculation of F_a and F_c, apart from k_{pSE}, the fraction of attached heads n_{AMp} is also input. $\bar{u}_{fs}$ is input to the F_a and F_c expressions too. Furthermore, this is the part where the average circumferential stretch is also included in the computations. This way, the value of $\partial\Psi_a/\partial\lambda_\theta$ can be included for the integration, and it is passed as a thickness-averaged value. Finally, the pressure and relative filament sliding are integrated and the area and sliding is updated until convergence.

4.2.3 Strategy for model parameters identification

Also here, the parameters of the mechanical model needed to be identified. This was achieved through an optimisation procedure, in the same manner to the chemical model, through the CMA optimisation algorithm from the `cma` library in Python. Here the parameters of the chemical model that were identified in the previous chapter are considered.

The following parameters were included in the fitting process for the active and passive responses. For the active response these were: the power stroke elongation distance u_{ps}; elastic stiffness of the cross-bridges k_{AMp}; the mean value of the pSE stiffness and the two fitted parameters $\bar{k}_{pSE}, n_{AC}, K_{AC}$; and the optimal filament sliding as well as the fitted parameter for the filament overlap $\bar{u}_{fs}^{opt}, s_{f0}$. The passive response at this stage was optimised by considering the hyperelastic model parameters c and α. For the geometry of the vessel, the LF thickness-medium radius ratio h_w, the axial stretch λ_z, and the κ parameter associated to residual stresses were also optimised. The fibre angles of the collagen fibres were assumed to be zero at this stage for simplicity.

An indicative experimental work that uses both the active response and the drug intervention case is the one conducted by Johnson *et al.* [177]. This work examines rat cerebral vessels which is in line with the values extracted for the chemical

model. The optimising process was set up to minimise an error similar to the chemical model, for a range of luminal pressure inputs:

$$e = \sqrt{\sum_{k=1}^{N} \left(\frac{d_{o,k}^{\text{exp}} - d_{o,k}}{d_{o,k}^{\text{exp}}} \right)^2} \tag{4.22}$$

Here, the outer diameter was set as the target. The error between the experimental measured value d_o^{exp} and the model computed one d_o was minimised for the control, drug intervention, and the extracellular (purely passive) calcium removal cases simultaneously for the range of k pressure values. A summary of all the model parameters, their values and the method of acquisition is shown in Table 4.1.

Table 4.1: Summary of mechanical model parameters used and the method for their acquisition (assumed, found in literature, or fitted).

Parameter	Description	Value
Geometry		
$R'_o\,(cm)$	Load-free outer radius	0.1 (assumed)
$h_w\,(-)$	Load-free thickness-medium radius ratio	0.299 (fitted)
$\lambda_z\,(-)$	Axial stretch	1.179 (fitted)
$\kappa\,(-)$	Circumferential pre-stretch	1.373 (fitted)
Passive response		
$c\,(dyn/cm^2)$	Material constant	$3.38 \cdot 10^4$ (fitted)
$k_1\,(dyn/cm^2)$	Material constant	$3.15 \cdot 10^4$ [144]
$k_2\,(-)$	Material constant	0.262 (fitted)
$\phi\,(\text{deg})$	Fibres orientation angle	0 (assumed)
Active response		
$N_{CF}\,(1/cm^2)$	Number of CF per unit area	$2.44 \cdot 10^{10}$ [88]
$L_{SMC}\,(cm)$	SMC length	0.01 (from [88])
$L_m\,(cm)$	Myosin filament length	$3.0 \cdot 10^{-5}$ [88]
$u_{ps}\,(cm)$	Average elongation caused by power-stroke	$9.398 \cdot 10^{-7}$ (fitted)
$\frac{k_{AMp}}{\delta_m}\,(dyn/cm^2)$	Cross-bridge elastic stiffness per distance between myosin monomers	$9.808 \cdot 10^6$ (fitted)
$\bar{u}_{fs}^{opt}\,(-)$	Normalized optimal filament sliding	$1.19 \cdot 10^{-1}$ (fitted)
$s_{fo}\,(cm)$	Filament overlap scaling factor	$1.732 \cdot 10^{-8}$ (fitted)
$\bar{k}_{pSE}\,(dyn/cm)$	Actin cortex stiffness scaling factor	4.34 (fitted)
$n_{AC}\,(-)$	Actin cortex activation function coefficient	1.876 (fitted)
$K_{AC}\,(-)$	Actin cortex activation function coefficient	5.203 (fitted)

4.3 Pressure-induced wall behaviour

In the previous section, the coupling of the cell signaling model with the chemo-mechanical one was discussed. Both models were fitted independently against experimental data found in the literature. The behaviour of the chemo-mechanical model was compared with experiments in small rat cerebral vessels found in the work of Johnson *et al.* [177]. The fitting of the model was carried out against three cases simultaneously: i) the control case, which is the physiological vessel response; ii) the passive case, for which the extracellular calcium was removed and thus, there was no cross-bridge formation and the vessel responded as a passive material; iii) H1152 drug intervention case, where some specific pathways of the cell signalling model were inhibited, and thus the vessel active response is modulated.

The assessment begins with the evaluation of the steady-state, where the vessel is inflated statically, and then moving to the transient one, where the factors that affect the dynamic character is discussed.

4.3.1 Steady state behaviour

Beginning with the static inflation tests, in this part, the steady-state response produced by the developed models is presented to validate the global methodology. For this tests, a single ring was considered, which was inflated with several pressure values over the physiological range, under fixed axial stretch.

For the study, two groups of vessels were considered, similar to the work of Johnson *et al.* [177]. The vessels differ in diameter, with the second one being larger by 15%. The first vessel was considered to have an LF radius of $0.01\,cm$, and the second $0.0125\,cm$. The first vessel will be the *baseline*, as it is also used later in the thesis. The two arteries were also used to simulate their behaviour in response to addition and removal of vasoactive substances. The results that are presented examine both the validation of the optimised parameter setup as explained in Section 4.2.3, as well as the prediction ability of the (fitted) model. The validation set refers to the *baseline* vessel for the control, calcium-free and H1152 pharmacological intervention cases and is the set that the parameters of the structural model is fitted against. The prediction set refers to the larger vessel ($0.0125\,cm$) for the control, calcium-free, and GF drug intervention case.

The results are separated in three parts. The first part shows the validation set (**baseline** vessel) for the control and calcium-free cases. The second one shows again the control and calcium-free cases, but for the second vessel group (as described above), which evaluates the prediction ability of the model. Finally, the third part includes all the drug intervention cases, whether the model is

fitted against it (H1152) or not (GF). It is noted that the pressure input for the simulations to follow ranges from $P = 10\,\text{mmHg}$ to $P = 100\,\text{mmHg}$ in 6 increments.

Regarding the computational aspects, the time needed to complete all 6 pressure increments in these steady state simulations was $\sim 3\,s$. It is noted that the computational time of the same simulation without considering the active part is $\sim 1\,s$. This indicates that the active part introduces a significant computational effort to the simulations.

Validation results of the model

At first, the *baseline* vessel results are presented, for the passive and active cases. All results were acquired by using the model presented in the previous section, with the optimised parameters for both models (cell-signaling and chemo-mechanical). The passive case is achieved experimentally by removing extracellular calcium, which is the main responsible factor for the formation of cross-bridges in the SMCs. Numerically, this is achieved by inhibiting the pathways that lead to the development of the cross bridges, i.e. χ_1, χ_3, χ_5 in Figure 3.10.

The response acquired by the full model regarding the vascular wall behaviour is shown in Figure 4.5. Since the models were fitted against the experimental results a comparison is shown in the plots. It is seen that the fitted model is approaching very closely the experimental results in both cases. It is reminded here that the objective function to be minimised, was the error between the experimental values and the model prediction, and it was formulated to include both cases (active, passive) seen in Figure 4.5. The experimental results are reported with a standard deviation, which is also present. This deviation is not small, and it shows that the vessel group studied can vary in terms of response. With this deviation considered, the behaviour extracted is very accurate. The diameter of the actively contracted vessel is significantly reduced compared to the passive one. Since the experimental and simulated protocol consists of inflation tests, the response shown by the active model represents the myogenic response. As the pressure takes higher values, the SMCs form the cross bridges, resulting into the development of the active tone in order to maintain the vessel diameter to a lower level.

Prediction ability

The prediction ability of the chemo-mechanical model was also tested. The cell-signaling model was fitted against all three cases: control (active), and two drug intervention cases. The chemo-mechanical model, however, was only fit-

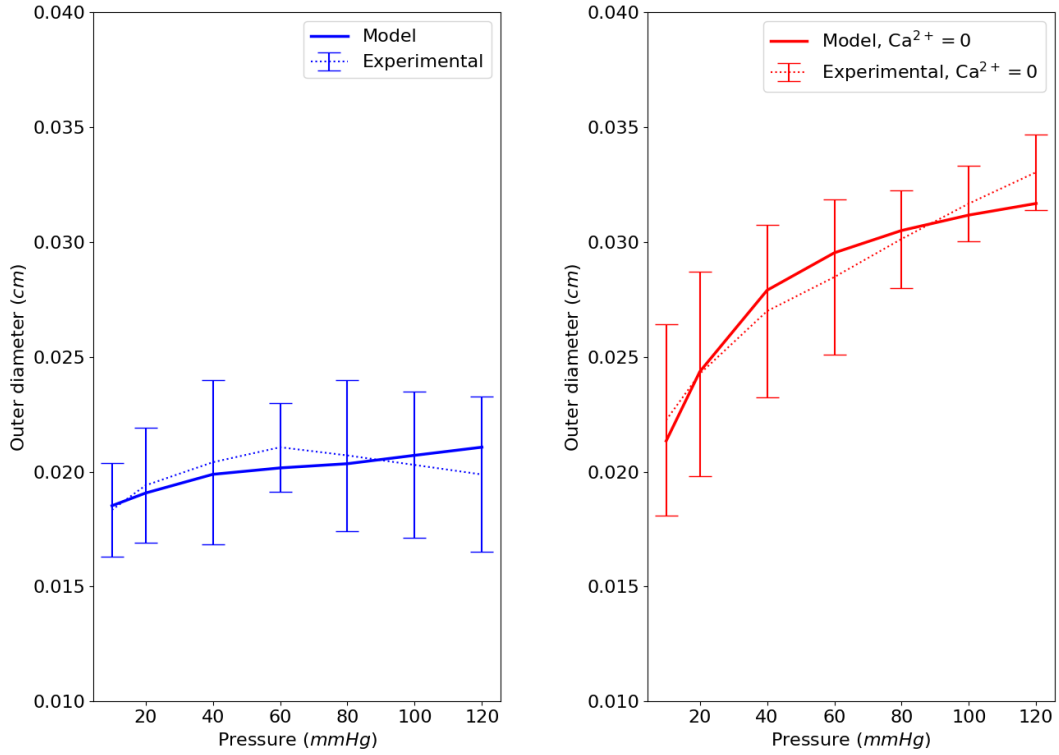

Figure 4.5: Pressure – Diameter results of the developed vascular wall model compared to experimental values from [177]. Left: active response; Right: passive response

ted against the response of the *baseline* vessel for active, passive, and one drug intervention case. To investigate its ability to predict the behaviour of different vessels, the second vessel group is introduced. To that end, all the optimised parameters were kept as fitted for the *baseline*, and only the geometrical characteristics were changed (R_{ref} and H). Similarly to the *baseline*, for this group the active and passive responses are simulated.

The results of the second vessels group is shown in Figure 4.6. It is seen that the active case has a very good agreement with the respective experimental findings. The passive behaviour, however, has a significant error increase. This model results for the passive one can be explained through the larger number of parameters of the active tone development within the SEF, and hence the fitting of those parameters. When the myogenic tone is absent, the material has to be identified through a minimal set of parameters set to describe its properties. This set was even smaller than the sets fitted for the work described in Section 2.5. This minimal set is probably not sufficient enough to describe accurately the passive response isolated. On the other hand, while the active tone development is fitted against the *baseline* vessels group, it is proved sufficient enough to describe the active response of a different sized vessel. This also is an indicator that the myogenic tone development is a dominant mechanism when it comes to vascular

wall characterisation, which affects the wall response much more than its passive (material) properties.

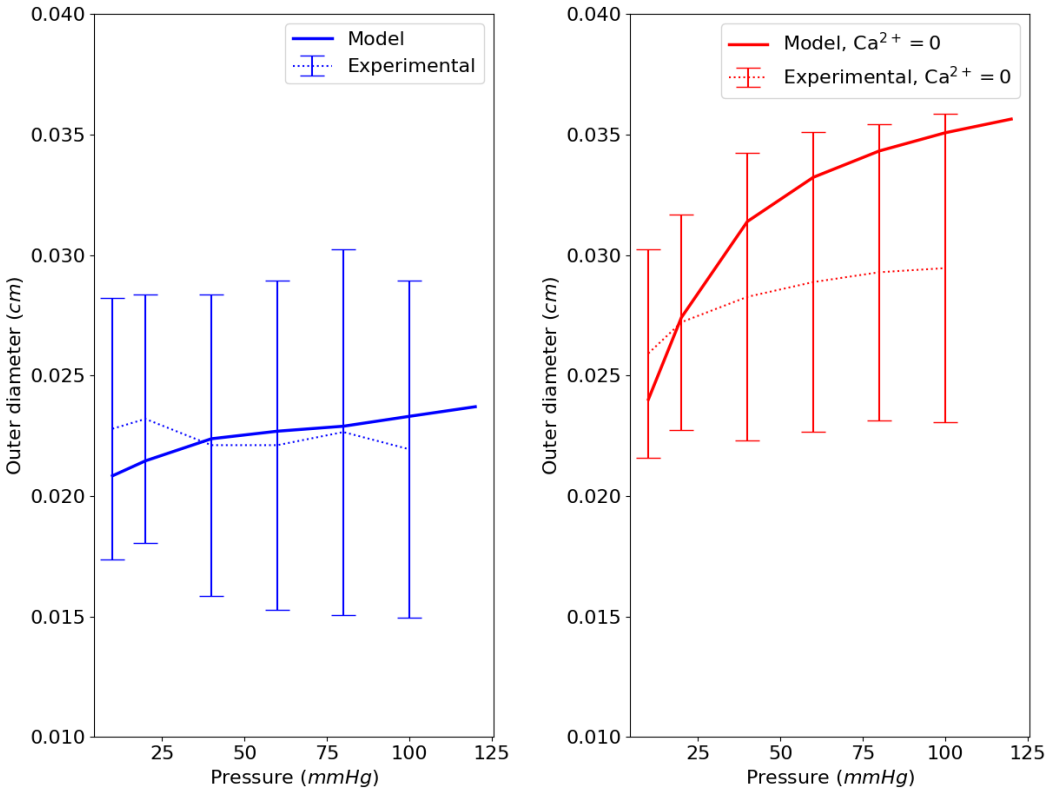

Figure 4.6: Pressure – Diameter results of the developed vascular wall model compared to experimental values from [177]. Second vessel group ($R_{\text{ref}} = 0.0126\,cm$). Left: active response; Right: passive response

Pharmacological intervention cases

In the work of Johnson *et al.* [177], this first (*baseline*) vessels group is also tested by applying a vasodilator, H-1152 dihydrochloride (H1152). This substance causes causes an inhibition of the ROK pathway (ξ_1 in Figure 3.10). As it is already presented in Chapter 3, the inhibition of this pathway affects the cross bridge formation by reducing their fraction through a reduced level of pMLCP. Moreover, the level of pCoffilin is also reduced, leading to a lower G-actin polymerisation. Furthermore, in the study, another vasodialator is applyed on the second vessels group, the PKC inhibitor GF109203X (GF). This substance is expected to inhibit the function of the PKC pathway, and hence prevent the cytoskeleton remodelling.

Numerically, these interventions are modelled by fixing the value of an internal variable. This way, the cellular signalling is manipulated. For the case of H1152 ($0.3\mu M$) the variable ξ_1 is set 0.12, and it affects both the polymerisation and

the cross bridge formation. For the case of GF ($3.0\mu M$), the network variable ξ_2 is set to 0.1.

For simulating the drug intervention cases, the optimised cell-signalling model for each case was employed, as it is described in Chapter 3. The chemical model was then coupled with the chemo-mechanical model. For the chemo-mechanical model, the parameters, again, were the ones optimised for the *baseline* vessels group behaviour and were not altered. Following the experimental work, for the H1152 intervention case, the *baseline* vessels group was used, while for the GF intervention one, the second group was considered.

By applying a vasodilator to the vessel an inhibiting the ROK pathway, a restriction in the active tone development is achieved. This is reflected in Figure 4.7, since the contraction with H1152 is much lower than the active one. The H1152 addition aims to clarify the effect of the specific pathway to the overall contractile behaviour. It is seen that the ROK pathway contribution is a significant one as it affects both the cross-bridge formation level, and the stiffening of the vessel through cytoskeletal remodelling. The developed model was able to approach the response of the H1152 with accuracy too.

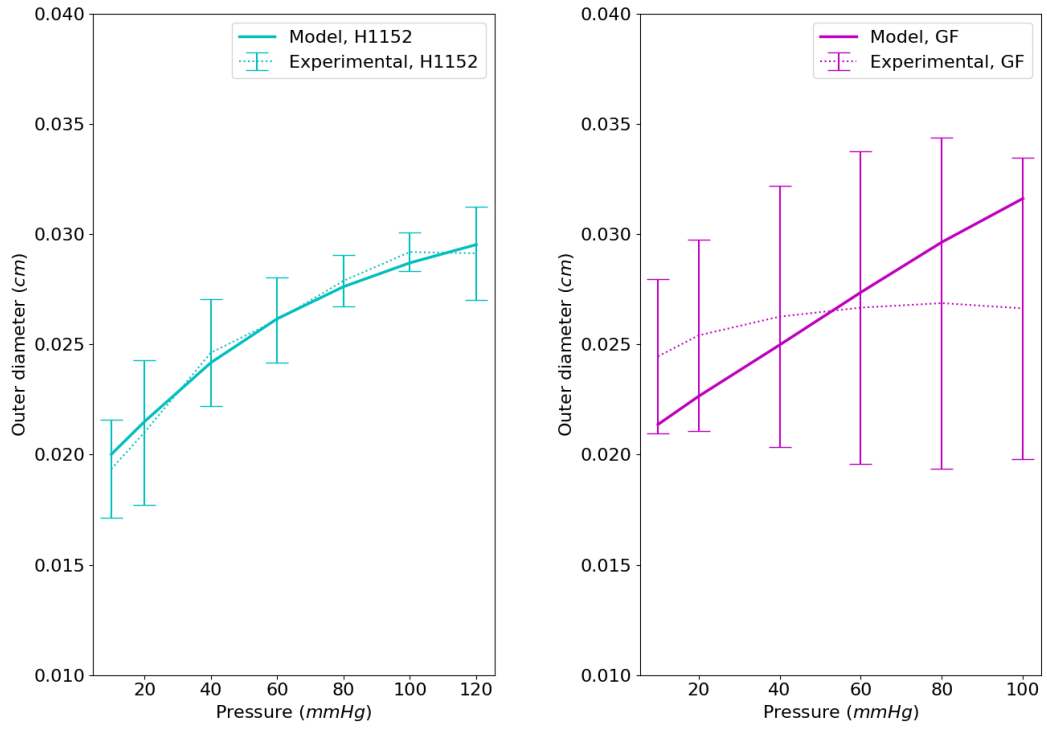

Figure 4.7: Pressure – Diameter results of the developed vascular wall model compared to experimental values from [177]. Drug intervention case. Left: $0.3\,\mu M$ of H1152; Right: $3.0\,\mu M$ of GF

On the other hand, from Figure 4.7 it is also observed that the GF intervention is not captured very accurately by the model. This may be explained by the

fact that the second group of vessels was employed for this intervention. As can be seen from Figure 4.6, the passive response of this group is overestimated by the model. Considering that the GF case is also overestimated for pressure level > 50mmHg, and this intervention is inhibiting the active tone development, thus, what is reflected in this overestimation is this discrepancy of the passive response. Moreover, it is noted that the available experimental data for the GF intervention were much less than those for the H1152 case, which is also an aspect that causes the lack of accuracy. However, the GF case prediction by the model lies within the limits of the statistical error produced by the experiments.

The impact of pressure-induced signaling pathways on the stiffness of CUs and the pSE is further explored in Figure 4.8. As expected, the absence of extracellular calcium has a limiting effect on pressure-induced contractile unit stiffness. Meanwhile, the behavior of the pSE closely mirrors that of the control case. Interestingly, both drug interventions result in an almost complete nullification of pSE stiffness across the entire pressure range.

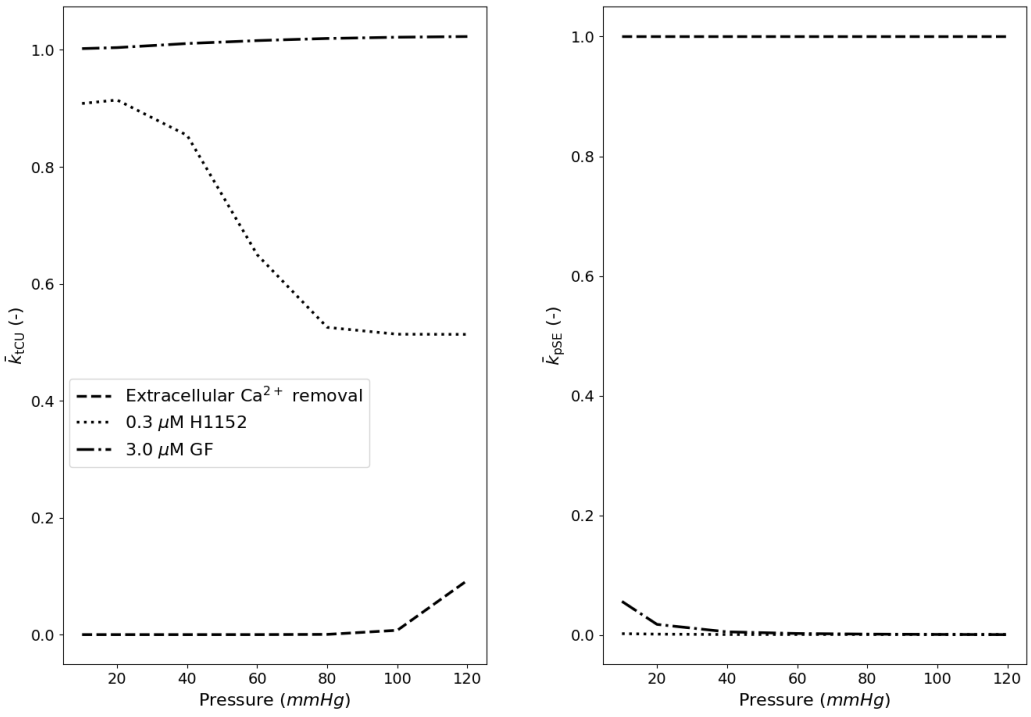

Figure 4.8: Role of luminal pressure on total contractile unit stiffness and passive surrounding element stiffness. All stiffness parameters normalised with respect to the corresponding control value. Left: CU stiffness; Right: pSE stiffness

On the other hand, inhibiting the ROK pathway restricts pressure-induced CU stiffness, but the case of GF exhibits an increase in stiffness under pressure. Surprisingly, this increase is even slightly higher than that observed in the control scenario. This discrepancy may be attributed to the difference in $u_{\text{fs}}^{\text{opt}}$ between

the GF and control cases, highlighting the interaction of factors influencing CU stiffness.

While the numerical findings presented here may offer intuitive insights, it is important that further experimental studies are conducted to validate these observations. The complexity of the interrelationships between pressure, signaling pathways, and cellular structures requires a comprehensive experimental approach for a more holistic understanding of the underlying mechanisms.

4.3.2 Transient behaviour

After studying thoroughly the steady state response, and validating it against experimental data, in this section the transient behaviour is presented.

The total response of a given vessel is the results of the two models which are sequentially coupled, the chemical (cell-signalling) and the chemo-mechanical. From the formulation of those models, there are two parameters related to the transient behaviour, one in the cell signalling model (τ_i) and one in the chemo-mechanical (β). For the studying the transient character, the change of response according to those temporal parameters is necessary, and it is the topic of this section.

It is important to highlight here that due to lack of experimental data defining the dynamic character of the intracellular processes, for this thesis the temporal parameters of the chemical model τ_i are all assumed to be the same and equal to τ.

The interest of this model response is the the pressure-induced active tone development. In order to evaluate the model response along the whole pressure range set for its adjustment, in a transient manner, five pressure increments were chosen, and a time period was allowed with constant pressure. In more detail, the boundary setup starts at $P = 20\,\text{mmHg}$, with an increment step of $20\,\text{mmHg}$. The pressure elevation is occurring as a stepped function, so the experimentally applied pressure is simulated. Finally, a time period of $t = 20\,s$ was chosen for each pressure increment.

Regarding the computational aspects of the simulations, it is reported that for these simulations, as can be seen in the plots that follow, the total simulated time was $100\,s$. Two time steps were used in order to assess the computational time. At first, a $dt = 10^{-2}\,s$ ($10,000$ iterations) was chosen, and the total computational time was $\sim 3.5\,min$. Then the time step was further reduced to $dt = 10^{-3}\,s$ ($100,000$ iterations) which drastically increased the computational time to $\sim 30\,min$. The second time step was chosen because the fluid model, which is presented in the next chapter, requires a significantly low time step. It is reminded

that the following simulations only consider a single arterial ring (equivalent to one node in finite elements). For the solution of the initial time step (here for $P = 20\,\text{mmHg}$), the steady state solution given from the analysis shown in Section 4.3.1 is used. At first, the output of the chemical model is presented with its pressure inlet.

In Figure 4.9 the results of the chemical model are presented, along with the pressure input. For those initial results, the temporal parameter τ was kept to $1\,s^{-1}$. Regarding the cross-bridge formation, It is reminded here that the maximum value for the pLC_{20} is set to 0.55. It is seen that this maximum value, or the saturation point of the cross bridges is almost reached at $P = 80\,\text{mmHg}$. It is also observed by the results, that a smooth transition is occurring with each pressure increment, which takes some seconds until the system reaches to a steady state. The steady state values are the ones presented in Chapter 3. The cell signalling model is undergoing a transition which lasts for about $\sim 5\,s$ after each pressure alteration.

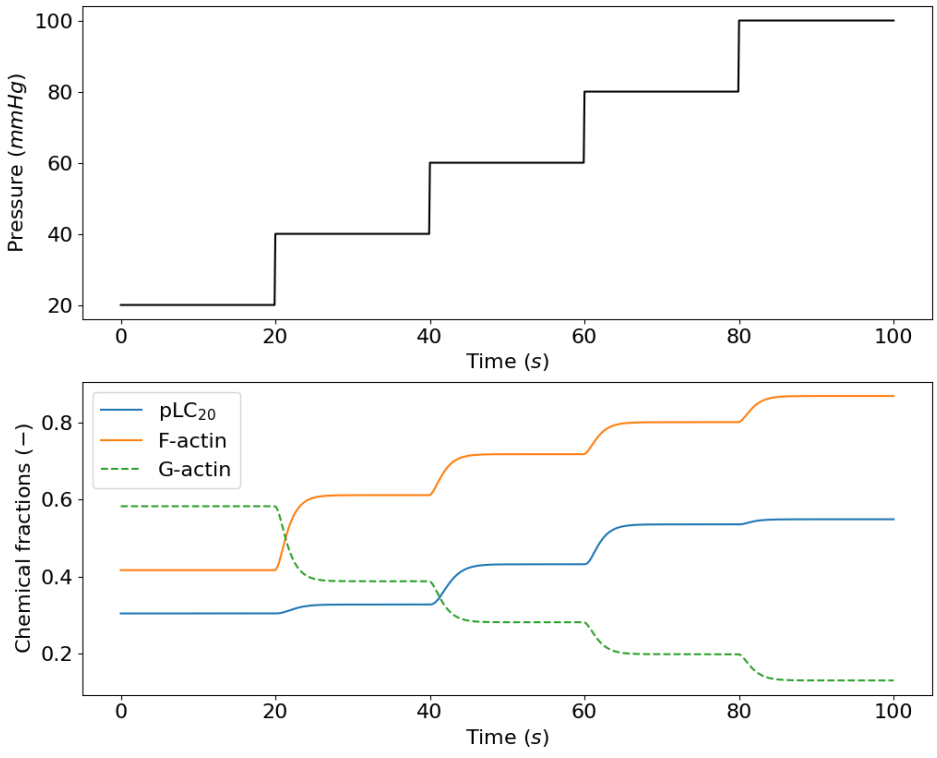

Figure 4.9: Pressure boundary condition setup and output of the chemical model for the transient case. Top: pressure input level; Bottom: output of the chemical model. Only the variables that are input to the chemo-mechanical model presented, i.e. the fraction of cross-bridges formed pLC_{20} and the F-actin (G-actin)

After the cell signalling response, it is feasible to move to the vascular diameter

response with this pressure input.

Figure 4.10 shows the results acquired for the two vessel groups investigated in 4.3.1, which align with the work of Johnson *et al.* [177]. Following the same rationale with the cell signalling model for the temporal parameter, these results are for $\beta = 1.616 \cdot 10^4\, s^{-1}$, which is reported in the work of Murtada *et al.* [88].

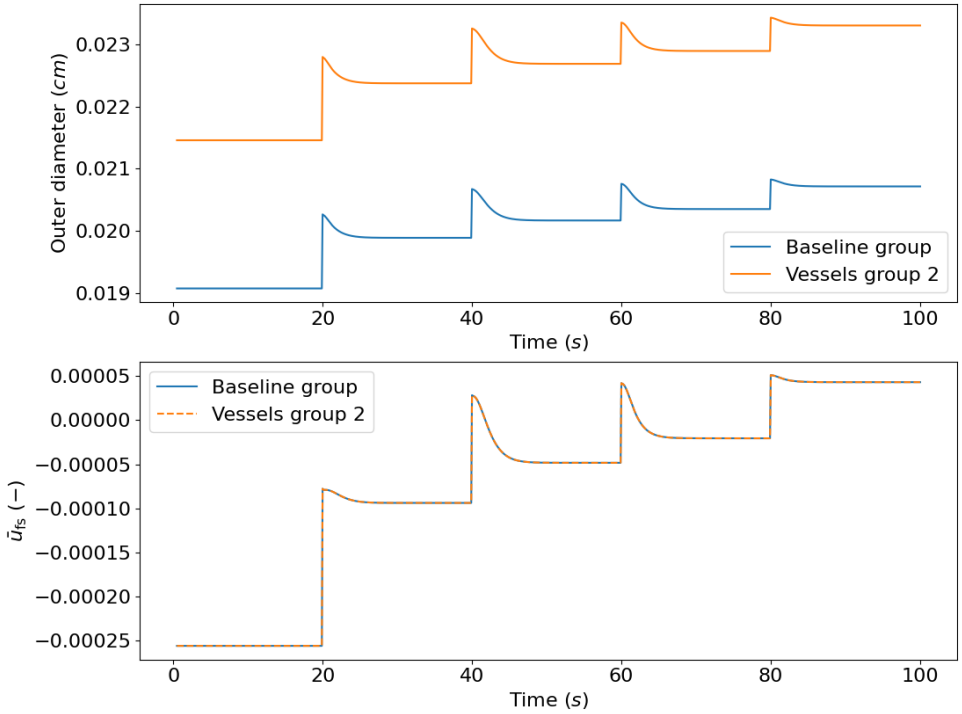

Figure 4.10: Outer diameter and relative filament sliding results for the pressure setup of Fig. 4.9. Results for both vessel groups as they were presented in 4.3.1

A first observation of the results shown in Figure 4.10 top plot, is that the transient character of the actively contracted vessel diameter is dominated by the cell signalling model. This can be seen from the time periods that the vessels need to be contracted to their steady state values. This observation shows that the chemical part of the active tone development is the dominant one, compared to the mechanical one, which is represented by the $u_{\text{fs}}^{\text{mech}}$ term in the relative filament sliding, and is related to the alteration in the circumferential stretch of the vessel. A more detailed comparison of these two terms is presented in the sections to follow.

Another observation can be made about the relative filament sliding u_{fs}, which is the bottom plot of Figure 4.10. As explained in 4.3.1, the parameters of the chemo-mechanical model is not changed for the two vessel groups. With this setup, it is seen from the results, that the difference of those two vessels is only

in terms of value of the diameter, and not to any other qualitative aspect of the transient response. This is proved by the relative sliding those two vessels are presenting. The relative sliding between actin and myosin filaments for these groups is exactly the same. For this relative sliding itself, it is seen that it gradually increases as the pressure level elevates. During a sudden pressure increase, the sliding is similarly suddenly increased, followed by a decrease. This sliding is defined by the difference in forces acting on the tissue, and initially it follows the elongation caused by the sudden increase in pressure. In time, the cross bridges starting to form, with the contribution of the chemical model, and the driving force of the bridges resists the force of the tissue deformation. In a similar manner, the force of the cross bridges becomes greater, until the system is balancing to the steady state value. This change of balance is ultimately responsible for the diameter behaviour seen in the top plot of Figure 4.10.

Next, both vessel groups were compared to the respective passive cases in order to assess the effect of myogenic response in the constriction of arterial wall.

Figure 4.11 shows a comparison for both vessel groups against their passive behaviours. The passive response was achieved as presented in the previous section. The plot above clearly shows that the pressure-induced tone manages to constrict the vessel as a response to elevation of pressure. It is seen that a vessel without considering the active mechanism just follows the pressure increase. In contrast, when myogenic response is introduced, there is an active reaction of the vessel.

Overall, it is observed that the transient behaviour of the model is indeed approaching the functioning of a vessel responding to a sudden increase in pressure with the myogenic tone activation.

Impact of cellular signalling temporal parameter on model dynamics

Since the scope of this thesis is the qualitative assessment of the pressure-induced active tone development, following the initial transient results acquired from the model, it is necessary to investigate the dynamic characteristics produced by the developed models. The tone activation, and ultimately the constriction of the tissue is a process that is occurring within few seconds [37, 34], but the exact timing is not defined in a deterministic way, and varies along different vessels and conditions [231].

In this section, the effect of the temporal parameters of the cell signalling model to the tissue mechanics response is evaluated. This is achieved through keeping every other parameter of the model constant, as shown in Table 4.1, and varying the parameters τ of the cell signalling model. The maximum variation is one order of magnitude higher and lower. This variation proved to cover all the range

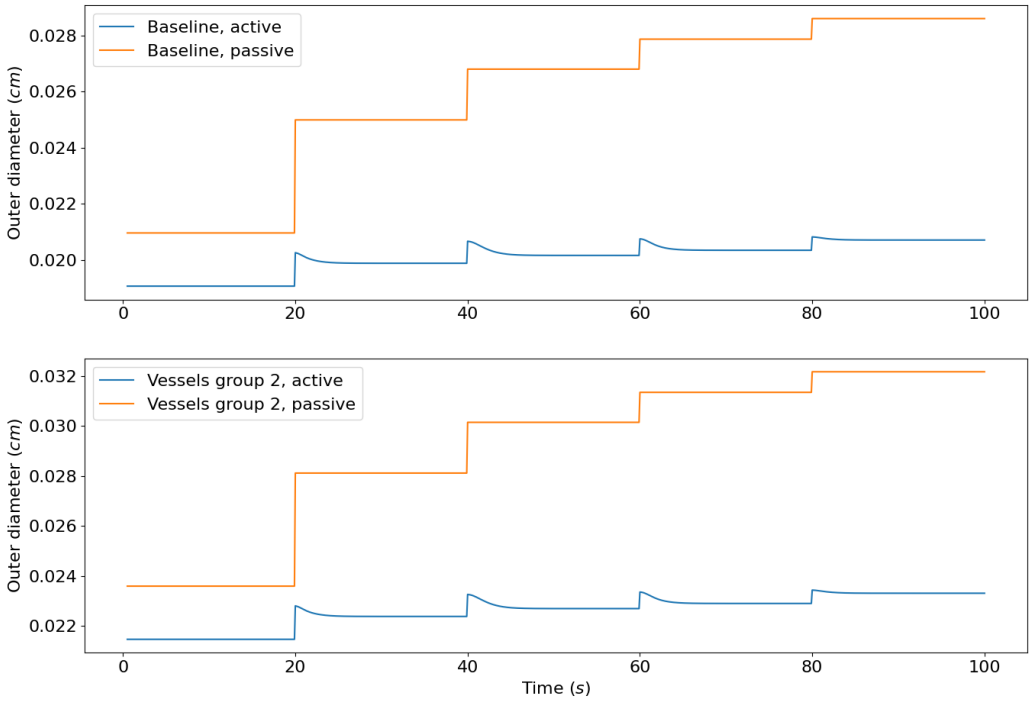

Figure 4.11: Outer diameter results for active and passive vessels. Both vessels (*baseline* and group 2). Pressure setup of Fig. 4.9.

of the dynamic responses.

As already explained, for the analysis it is assumed that τ is the same for Equations (3.12) – (3.18). In reality this is not true, because the time required for each (de)phosphorylation, or increase/decrease in concentration due to the intracellular signalling may vary. There are different times for all the signalling pathways that may depend of the medium of the signal transition and the complexity of the mechanism. However, there was no available data that would support such a temporal separation of each internal process, and hence, the simplest approach was chosen. At first, the different responses of the cell signalling model alone is presented.

Figure 4.12 shows the transient response of the cell signalling model with respect to different values for the temporal parameter τ, and all other parameters kept constant. It is reminded that the temporal term is $1/\tau\,(s^{-1})$. It is observed from the plot that as τ is increased, and thus the temporal term decreases, the transition between the steady state values takes longer to occur. On the other hand, as τ decreases, and thus the temporal term decreases, the transitions occur more rapidly. It is also seen that for $\tau = 10\,s$ the transition is occurring slow, and the time period of $20\,s$ is not enough for the model to reach the steady state value. Contrary, when $\tau = 10^{-1}\,s$ the transition is happening almost simultaneously. This parameter to describe the dynamic character, as well as the consideration

of a single τ for all the ODEs is the most simplistic approach that could be considered, given the lack of data.

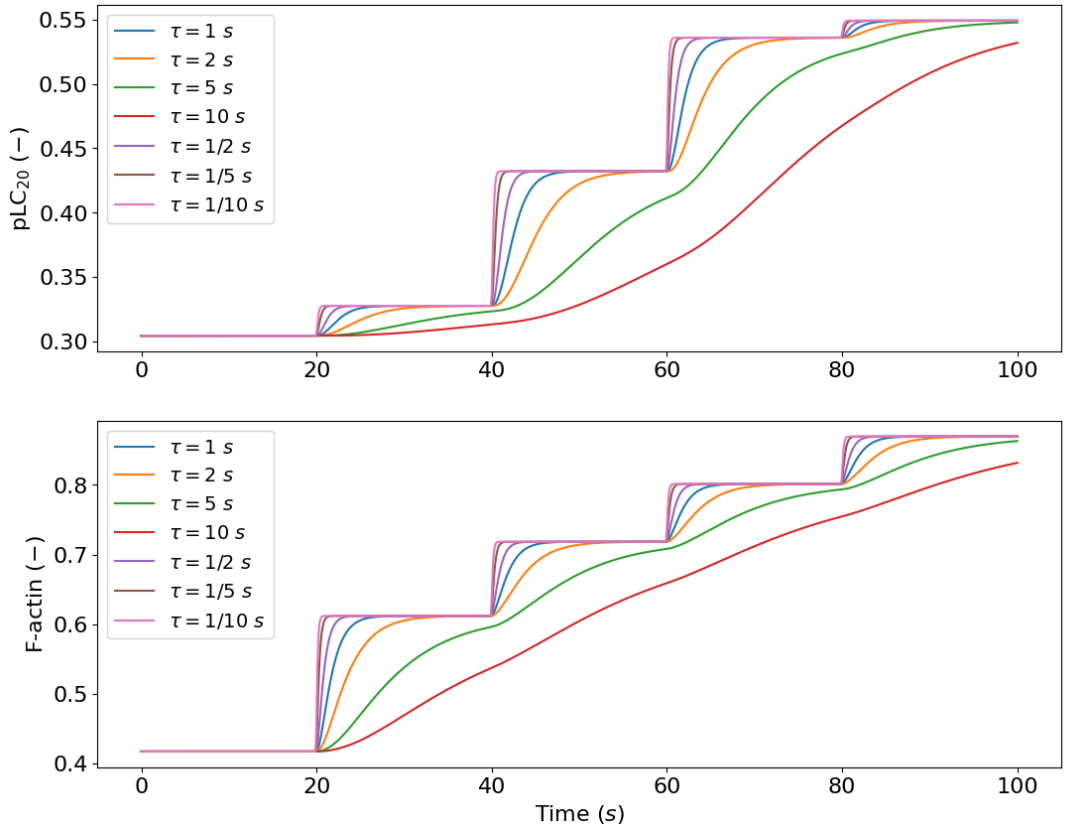

Figure 4.12: Transient results of cell signalling model. Investigation of response for different temporal parameter τ

The range of τ of Figure 4.12 were then imposed to the chemo-mechanical (*baseline*) model in order to assess its effect on the dynamic response of the mechanical part.

In Figure 4.13 this response of the mechanical model with respect to all the τ range is presented. Again, it is observed that as the cell signalling temporal term tends to lower values, the transition is occurring more slowly, and at the most extreme case (for this range), the diameter has not converged to its respective state value before the pressure is elevated again. In contrast, when the temporal term tends to higher values, the contraction of the vascular wall occurs in a rapid time frame.

This temporal parameter investigation provided very useful insight in terms of timing of the active tone development. Even with this approach of $1/\tau$ it is the control parameter for the quickness of the tone development and is able to provide intuitive insights on the vessel response.

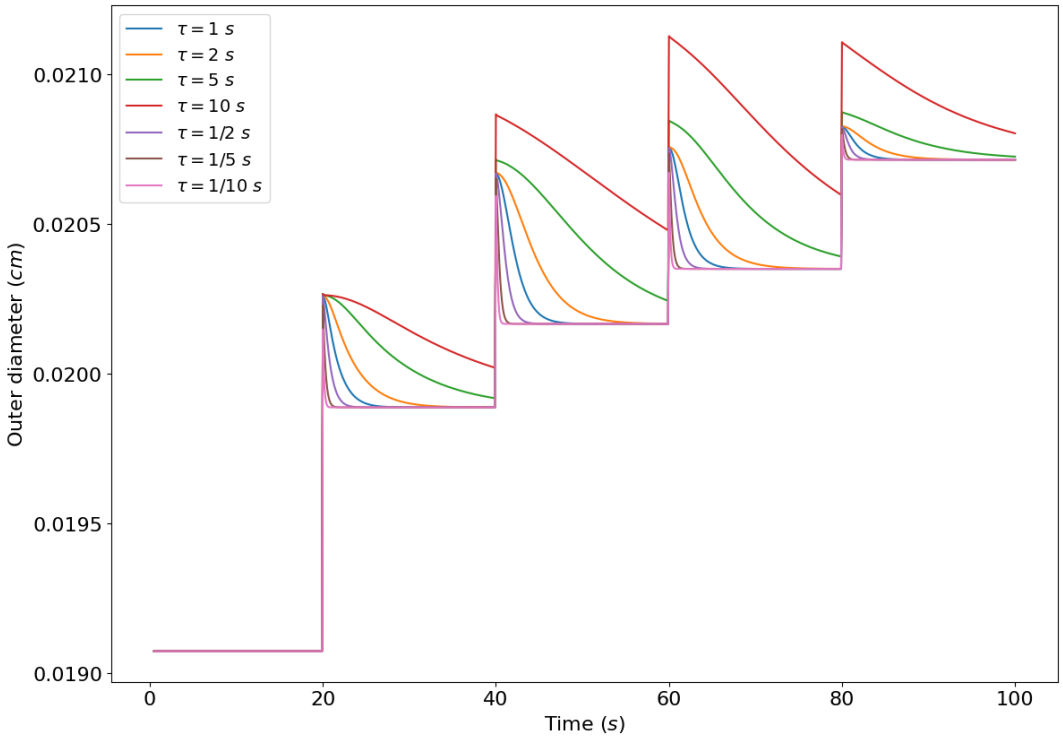

Figure 4.13: Model results on vessel diameter for different τ parameter of the cell signalling model

Impact of chemo-mechanical model temporal parameter on model dynamics

After assessing the effect of the temporal parameter of the cell signalling, the temporal parameter incorporated within the chemo-mechanical model needs to be investigated.

The temporal parameter of the chemo-mechanical model β is incorporated in the evolution law employed for the chemical part of the relative filament sliding, i.e. Equation (4.9). From the formulation $\partial \bar{u}_{fs}^{chem}/\partial t = \beta(F_a - F_c)$, it is seen that it is incorporated in the same manner as the τ for the cell signalling model, as a constant that defines a dynamic response. In a similar rationale as the cell signalling model, to identify its effect on the dynamics of the overall response, a range was given at this temporal parameter β. The variation was carried out around the baseline value of $\beta = 1.616 \cdot 10^4\, s^{-1}$, which is the value found in the work of Murtada [88].

Figure 4.14 shows all the different dynamic responses acquired by varying the β parameter of the chemo-mechanical model. The variation here was made by decreasing an order of magnitude for each different case, since it was found that changes of this level have visible differences. Furthermore, by experimenting with the values of the investigation, it was shown that further increase in the β term has

minimal effect on the response, so they were omitted from the plot. Furthermore, from Equation (4.8), the relative filament sliding is composed by two component, the *chemical* and the *mechanical*. As first results, since the temporal parameter is present only in the *chemical* part, the response acquired by considering only that component is shown in Figure 4.14. Moreover, in order to showcase the differences in the response, the plot is focused on two pressure changes.

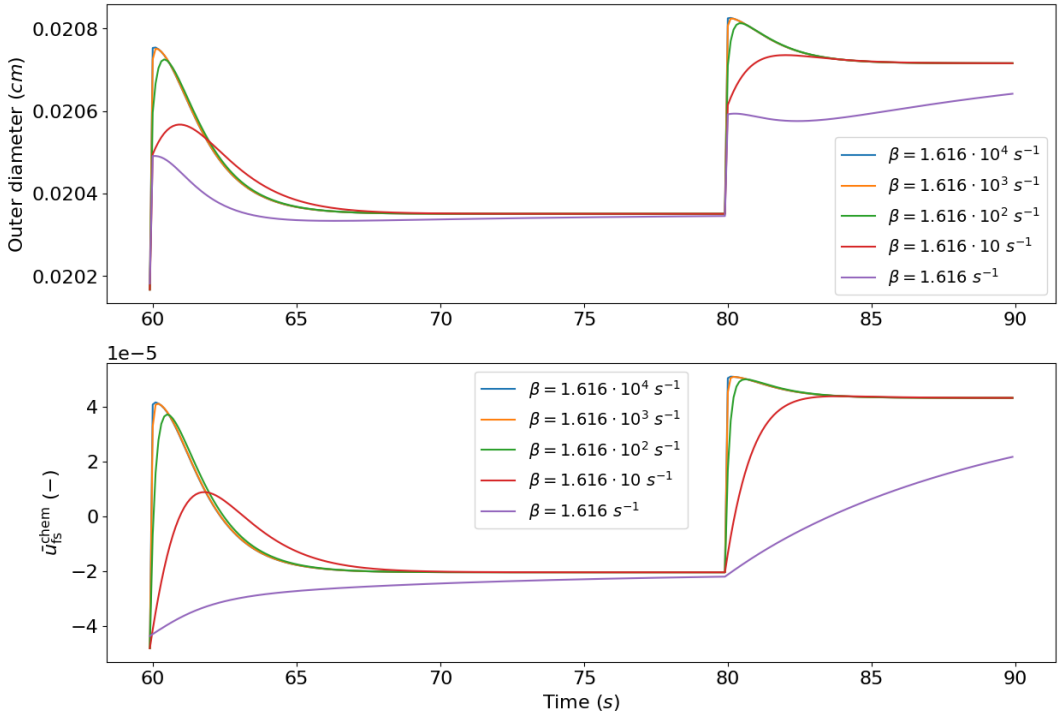

Figure 4.14: Investigation of temporal parameter β of the chemical model. Focus on the transition from $P = 60\,\text{mmHg}$ to $P = 80\,\text{mmHg}$ ($t = 60\,s$ to $t = 80\,s$) and $P = 80\,\text{mmHg}$ to $P = 100\,\text{mmHg}$ ($t = 80\,s$ to $t = 100\,s$). Only $\bar{u}_{fs}^{chem}$ considered. Top: diameter results; Bottom: relative filament sliding results (chemical component)

It is observed that as β is decreased, the vessel tends to dilate less before it contracts. This is justified by the $\bar{u}_{\text{fs}}^{\text{chem}}$ plot for the relative sliding, where the sliding is less for lower temporal parameter values. However, the time needed to converge to the steady state value does not seem to change much for different β values.

Chemical and mechanical contributors to the contraction

Next, the effect of the combined mechanical and chemical part is assessed, as computed from Equation (4.8). The mechanical part is added to account for the deformations produced by the change of the circumferential stretch, and it is expected to alter the total response of the vessel.

To assess this effect, the same cases for the β parameter was set, so a direct comparison is feasible.

In Figure 4.15, the setup is exactly the same as Figure 4.14, but the relative filament sliding is calculated as the sum of *chemical* and *mechanical* terms. Quite interestingly, the opposite behaviour than the one with only the *chemical* component is observed. It is seen that as the temporal constant β decreases, now the total response is dilating more before it contracts. This is also reflected from the $\bar{u}_{\text{fs}}^{\text{chem}} + \bar{u}_{\text{fs}}^{\text{mech}}$ term in the bottom plot of the Figure. Unlike the respective sliding of the *chemical* part, now the sliding tends to higher values as the temporal parameter β tends to lower values. This behaviour implies that the *mechanical* part is significantly contributing to the overall active response of the vessel.

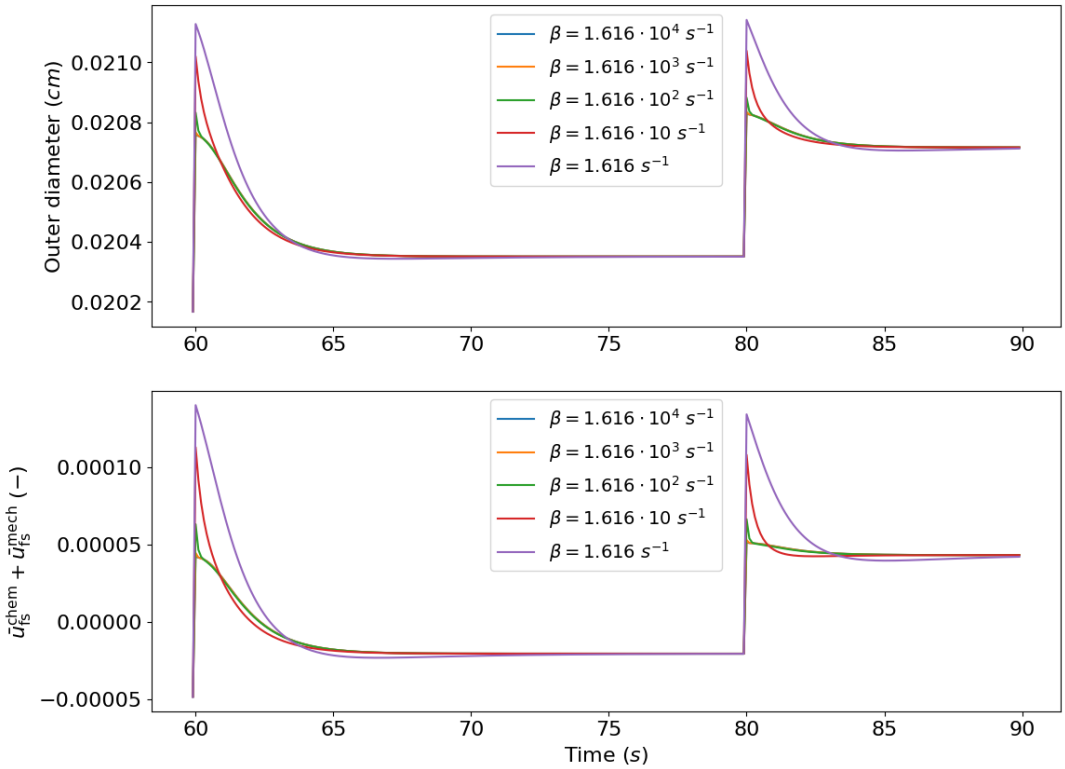

Figure 4.15: Investigation of temporal parameter β for the chemical and mechanical parts. Focus on the transition from $P = 60\,\text{mmHg}$ to $P = 80\,\text{mmHg}$ ($t = 60\,s$ to $t = 80\,s$) and $P = 80\,\text{mmHg}$ to $P = 100\,\text{mmHg}$ ($t = 80\,s$ to $t = 100\,s$). Top: diameter results; Bottom: relative filament sliding results (chemical component)

From the investigation of the temporal parameters, it can be extracted that the two terms of the two sub-models (chemical, chemo-mechanical) control the dynamic behaviour of the response. On the one hand, the cell signalling model can define the time needed for the vessel to reach its steady state value, while the chemo-mechanical model defines the amount of dilation of the vessel until it contracts. Furthermore, the characterisation through analysing the temporal parameters of the employed models can capture the dynamics of physiologically

interpretable parameters, like the CB formation, the extracellular stiffening or the filament sliding.

4.4 Conclusive remarks

In this chapter, the mechanics of the vascular wall of a cerebral vessel were examined. The analysis considered both the passive and active material behaviours.

The static and dynamic response of the newly developed cell signalling and chemomechanical model were presented. At first, the steady state response was presented for the control and passive cases, as well as for two drug intervention cases, for two vessel groups. The results showed a very good agreement with the respective experimental ones, especially for the optimised vessel.

The inclusion of additional signalling pathways (via the signalling network reported in the previous chapter) that ultimately affect the CB formation, as well as the cytoskeleton re-modeling process which affects the passive matrix of the cell have a significant impact on the final response of a vessel in terms of active tone development.

Finally, the dynamic response of the vessel was assessed, and the temporal parameters that define the dynamic characteristics of the response were investigated. It was found that with a combination of adjustments of the chemical and chemomechanical model temporal parameters, the exact dynamic response of the vessel can be achieved.

Chapter 5

Blood flow in self-regulated vessels

As discussed in previous chapters, the vessels of interest in this work are medium and small cerebral arteries. In particular, the focus of this thesis lies in the vascular region between the middle cerebral artery (MCA) downstream and the capillary level. The cerebral vascular network terminates in the capillaries, where the organs receive oxygen and nutrients through microcirculation. Microcirculation is highly affected by upstream haemodynamic conditions and therefore cerebral blood flow through small and medium vessels is of critical importance for brain function and viability [37]. Both developed models (chemical and chemo-mechanical) [212] described in the previous chapters aimed to describe and evaluate pressure-induced vascular tone generation in cerebral vessels, which has a significant effect on the distribution of blood flow across the vasculature [231, 232].

This chapter focuses on the blood flow control achieved through myogenic mechanism. The vascular wall model described in Chapter 4 is combined with the 1D fluid solver introduced in Chapter 2 into an FSI framework.

The interest here lies on the impact on blood flow development due to changes in systemic/upstream pressure and the constriction/dilation produced during myogenic response. To that end, three pressure boundary configurations were set. The first is to assess the flow development under a fixed pressure drop across the vessel. The second one fixes the outlet to a certain pressure and varies the inlet. These two configurations are aiming to simulate in-vitro conditions, this allows the isolation of the vessel from any upstream/downstream effects. The final one aims to vary both inlet and outlet, which better represents in-vivo conditions, which will include the effect of downstream vasculature.

In the first part, the strategy for coupling the structural model with the fluid solver, and the solution procedure are reported. Next, the results for steady state

conditions are presented, which examine the first two pressure boundary condition configurations described. Next, an examination of the effect of geometrical features on the solution is carried out. Finally, the transient conditions are investigated and discussed, followed by the inclusion of the downstream circulation.

5.1 Coupling the fluid and structural domains

As reported in Chapter 2, the fluid solver used in this thesis is a reduced order model using a 1D representation for blood vessels with a PQ formulation of the Navier-Stokes equations. The system produced by the linearised equations has both pressure and flow fields as unknowns. To evaluate these, an iterative procedure needs to be used. The final form of the system solved is the following

$$\mathbf{K}\mathbf{P}^{n+1} = \mathbf{f}^n + \mathbf{Q}^{n+1}, \tag{5.1}$$

here, to be consistent with equation (2.70), $\mathbf{K} = [-\mathbf{G}^{-1}\mathbf{F}]$ and $\mathbf{f} = [-\mathbf{G}^{-1}\mathbf{h}^n]$.

The interest of this thesis lies in the definition of the flow response in changes in pressure, so the myogenic response can be examined. This requires a control over the pressure applied on the vessels. Implicit pressure boundary conditions are achieved by applying Dirichlet boundary conditions to the system, unlike the original formulation [149]. To demonstrate the application of pressure boundary conditions, a four-node vessel is assumed, for which the equation (5.1) in matrix form would be

$$\begin{bmatrix} k_{11} & k_{12} & k_{13} & k_{14} \\ k_{21} & k_{22} & k_{23} & k_{24} \\ k_{31} & k_{32} & k_{33} & k_{34} \\ k_{41} & k_{42} & k_{43} & k_{44} \end{bmatrix} \begin{bmatrix} P_1 \\ P_2 \\ P_3 \\ P_4 \end{bmatrix}^{n+1} = \begin{bmatrix} f_1 \\ f_2 \\ f_3 \\ f_4 \end{bmatrix}^{n} + \begin{bmatrix} Q_1 \\ Q_2 \\ Q_3 \\ Q_4 \end{bmatrix}^{n+1}. \tag{5.2}$$

If the pressure is prescribed at the beginning and end points of the vessel, that would mean that the values of the boundaries are $P_1 = P_{\text{in}}$ and $P_4 = P_{\text{out}}$. Moreover, as explained in Chapter 2, all internal flow values cancel each other, as they represent mass conservation. In this way, when the pressure is prescribed at the inlet and outlet, the flow vector would ultimately be a zero vector for the internal nodes. With Dirichlet boundary condition elimination, the values of the internal pressure nodes will be given by

$$\begin{bmatrix} k_{22} & k_{23} \\ k_{32} & k_{33} \end{bmatrix} \begin{bmatrix} P_2 \\ P_3 \end{bmatrix}^{n+1} = \begin{bmatrix} f_2 \\ f_3 \end{bmatrix}^{n} - \begin{bmatrix} k_{21}P_{\text{in}} + k_{24}P_{\text{out}} \\ k_{41}P_{\text{in}} + k_{44}P_{\text{out}} \end{bmatrix}^{n+1}. \tag{5.3}$$

The above, again transformed into vector form, means that the solution does not involve any flow rate value of the current time step, and is given by

$$\mathbf{K}\mathbf{P}^{n+1} = \mathbf{f}^{n}. \tag{5.4}$$

Once the pressure field is computed, the flow field is extracted by again solving (5.1) for the flow vector, which would be

$$\mathbf{Q}^{n+1} = \mathbf{K}\mathbf{P}^{n+1} - \mathbf{f}^{n}. \tag{5.5}$$

The vessels are considered compliant [149, 97]. The computation of the vessel compliance is carried out through equation (2.75) proposed by Carson [125], as presented in the relevant chapter. The equation is repeated here for completeness

$$C_A = \frac{2\epsilon}{P(A+\epsilon) - P(A-\epsilon)}, \tag{5.6}$$

where $\epsilon = 10^{-6}$ is in line with previous work [123].

For the studies that follow, the active tone is evaluated at vessel level (and not at nodal level) by considering the pressure at the inlet of the vessel. This choice was made for reducing the computational cost, which was significantly increased with the implementation of the active part. This choice is also discussed in the conclusive section of this chapter.

5.2 Steady state flow conditions

In this section the behaviour of the coupled fluid-solid system in steady-state conditions is analysed. At first, two pressure boundary condition configurations are set and the resulting flow is evaluated. Next, the geometrical features of the vessels are examined regarding their effect on the overall solution. Finally, a comparison is carried out between the computed solution and the analytical one, provided by the Poiseuille law.

It is important to note that for the studies that follow, the time step was limited for reasons associated with stability and accuracy. To that end, a time step of $\Delta t = 5 \cdot 10^{-4}\, s$ was considered. For reaching the steady state solution, the transient problem is simulated for 50 iterations with a constant pressure at the boundaries. This means that a total simulated time of $0.005\, s$ is sufficient for the solver to converge to the steady state. The computational time required for each pressure increment (the 50 iterations) was less than $10\, s$.

5.2.1 Behaviour for different pressure setups

In this section, two configurations of pressure boundary conditions are set to assess behaviour of an isolated vessel. These configurations are tested under different luminal pressure levels, and under variable pressure difference between inlet and outlet. The details for these configurations are described in their respective sections.

Constant pressure drop across the vessel

The first case aims to evaluate the behaviour of the vessel for different luminal pressure levels, as mentioned previously. To that end, a range of pressure levels was chosen that started at 20 mmHg up to 100 mmHg, which is the expected operational range of the cerebral vessels [37, 231, 233]. Each pressure value was imposed at the inlet of the vessel as P_{in}. In order to impose the outlet boundary condition P_{out}, the pressure drop ΔP across the length is kept constant, and therefore $P_{\text{out}} = P_{\text{in}} - \Delta P$. Several values of ΔP were considered to characterise the vessel behaviour across various conditions.

The vessel considered has a reference (LF) radius of $R_{\text{LF}} = 0.01\,cm = 100\,\mu m$, and a wall thickness of $H = 0.0026\,cm = 26\,\mu m$. Moreover, a length of $L = 0.1\,cm = 1000\,\mu m$ is considered with the rationale of $L \approx 10 \cdot R$. This geometrical setup is the *baseline* case. The spatial discretisation was considered to be with $\Delta x = 0.01\,cm = 100\,\mu m$, which produces 10 elements across the length. This spatial and temporal discretisation is maintained throughout the present section, and it only changes when the effect of the vessel length is evaluated (where the new discretisation is reported).

For these cases, five increments for the input pressure were considered for each case (20, 40, 60, 80 and 100 mmHg). To demonstrate the effect of active contraction, in many cases the corresponding passive case is also shown, which is achieved by setting pLC_{20} fraction equal to 0, which corresponds to no active cross bridges attached. For the first case, a pressure drop of $\Delta P = 0.1$ mmHg is chosen.

Figure 5.1 shows the simulation results for $\Delta P = 0.1$ mmHg. It presents the flow development in the *baseline* vessel for different pressure levels (top). The actively contracted vessel is seen to almost maintain the flow despite the pressure level, which coincides with the action of the resistance vessels. This behaviour of the actively contracted vessel is what is expected based on physiology.

For a closer examination, the middle plot of Figure 5.1 shows the active case alone. It is seen that the flow gradient in the active case changes across the pressure range. It shows a relatively high increase rate for $P_{\text{in}} = 20$ mmHg until $P_{\text{in}} \sim 40$ mmHg, followed by a significantly lower increase rate for the range

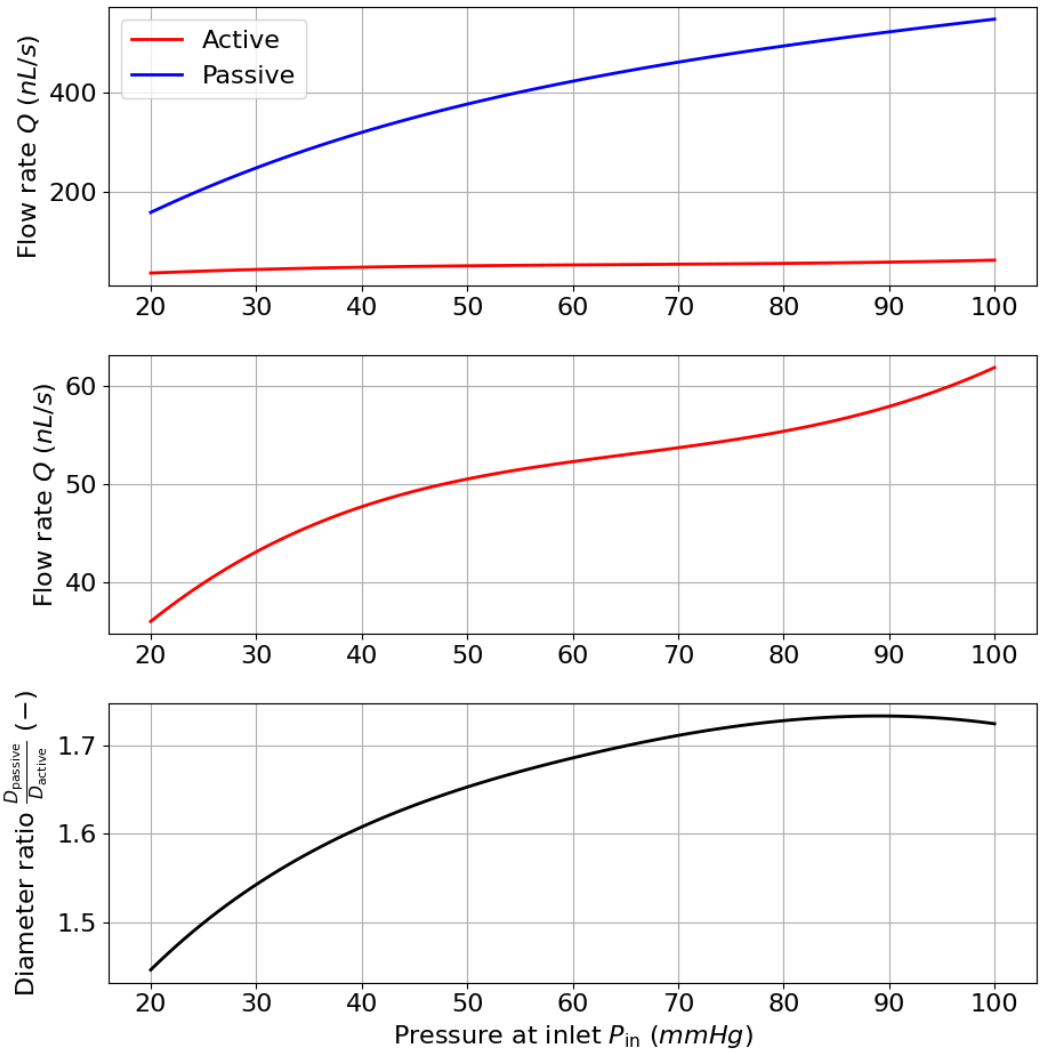

Figure 5.1: Simulation results of *baseline* vessel for different pressure levels with constant $\Delta P = 0.1\,\text{mmHg}$. Top: active and passive case comparison; Middle: flow developed with the active model only; Bottom: luminal diameter ratio $D_{\text{passive}}/D_{\text{active}}$ for the simulated pressure range.

between $\sim$ 40 and $\sim$ 80 mmHg, and then the gradient increases again. This is in line with the cerebral blood flow regulation curves [34], and indicates a pressure range at which the myogenic response has the most significant impact on maintaining blood supply. Moreover, it is also observed that the absolute values of the flow rate with active tone, is much less than the passive case, which indicates the presence of myogenic tone within the vessel.

The passive behaviour is slightly tending to lower flow gradients (with respect to pressure) as pressure increases. However, compared to the gradient of the flow in the active case, it is much higher. This happens due to the hyperelastic constitutive law for the material of the vascular wall. It indicates a point beyond which further increase in pressure will produce much less deformation to the

vascular wall, and the flow developed is affected accordingly.

The bottom plot of Figure 5.1 shows the diameter ratio for the two considered cases (active and passive). The ratio has an increasing tendency for almost the whole pressure range, which indicates that the diameter of the passive vessel is expanding with a much higher rate with respect to pressure, than the active one. This behaviour is in line with the adjustment (contraction or dilation) of the lumen diameter as a response to pressure change during myogenic response [39, 234].

Next, the imposed pressure drop ΔP is increased and decreased by an order of magnitude in order to assess its impact on the flow, for the whole pressure range.

Figure 5.2 presents the active and passive flow results of *baseline* vessel for $\Delta P = 0.01\,\text{mmHg}$ and $\Delta P = 1\,\text{mmHg}$ (left and right respectively). The flow development is seen to follow the change in pressure drop. That is, when ΔP is decreased by an order of magnitude, the flow within the vessel decreases by an order of magnitude too, and the same behaviour occurs for the increase of ΔP. This behaviour is reasonable, since the active tone in all cases is the same, and the flow is driven by the pressure gradient. Although different in terms of values, the trends and features of the flow–pressure curve for higher and lower ΔP is the same as Figure 5.1.

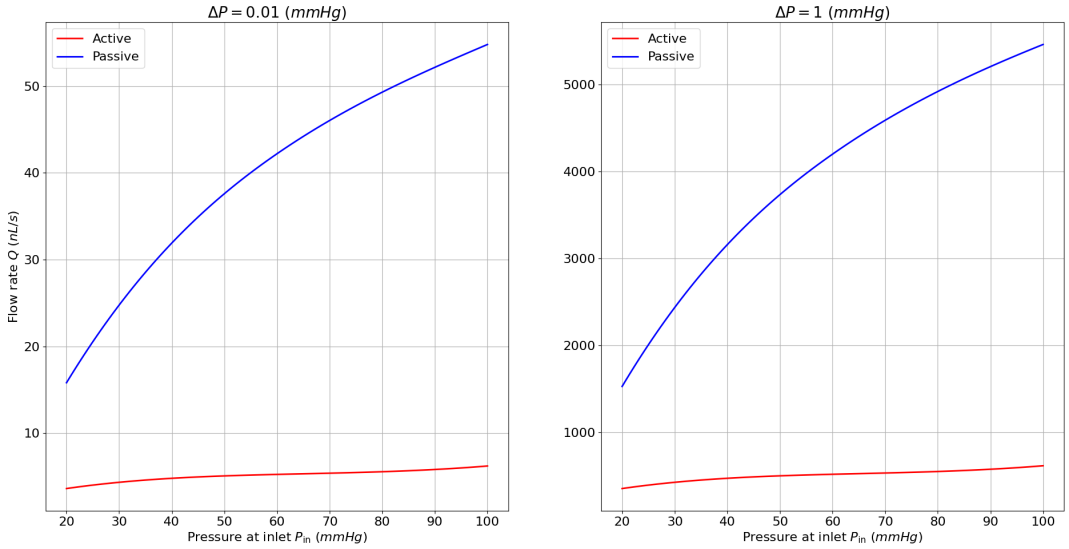

Figure 5.2: Simulation results of *baseline* vessel for two cases of constant ΔP across the pressure range. Left: $\Delta P = 0.01\,\text{mmHg}$; Right: $\Delta P = 1\,\text{mmHg}$.

Further insight to this behaviour can be provided if one considers the friction term of the governing equations given by equation (2.22). For the chosen velocity profile, the resistance to the flow R_f is inversely proportional to the area on the second power according to

$$R_f = \frac{8\mu L\pi}{A^2}. \tag{5.7}$$

Figure 5.3 shows the change in R_f and diameter in the given pressure range. In the top plot, the values of the resistance are shown, in the middle plot is the ratio of $R_{f,\text{passive}}/R_{f,\text{active}}$, while in the bottom one are the diameters of the vessels. At first, the resistance developed in the vessel with active tone is much higher than the passive one across the pressure range. This is due to the difference on the diameters of the vessels, which can be seen in the bottom plot of the figure. The ratio distribution of the resistance follows the inverse trend of the diameter ratio shown in Figure 5.1, which is dictated by equation (5.7). This behaviour of resistance to flow is justified by the presence of the active tone. With the vessel contracting/dilating by the active tone, the resistance to flow is altered (increased/decreased) through the diameter change in order to regulate the flow.

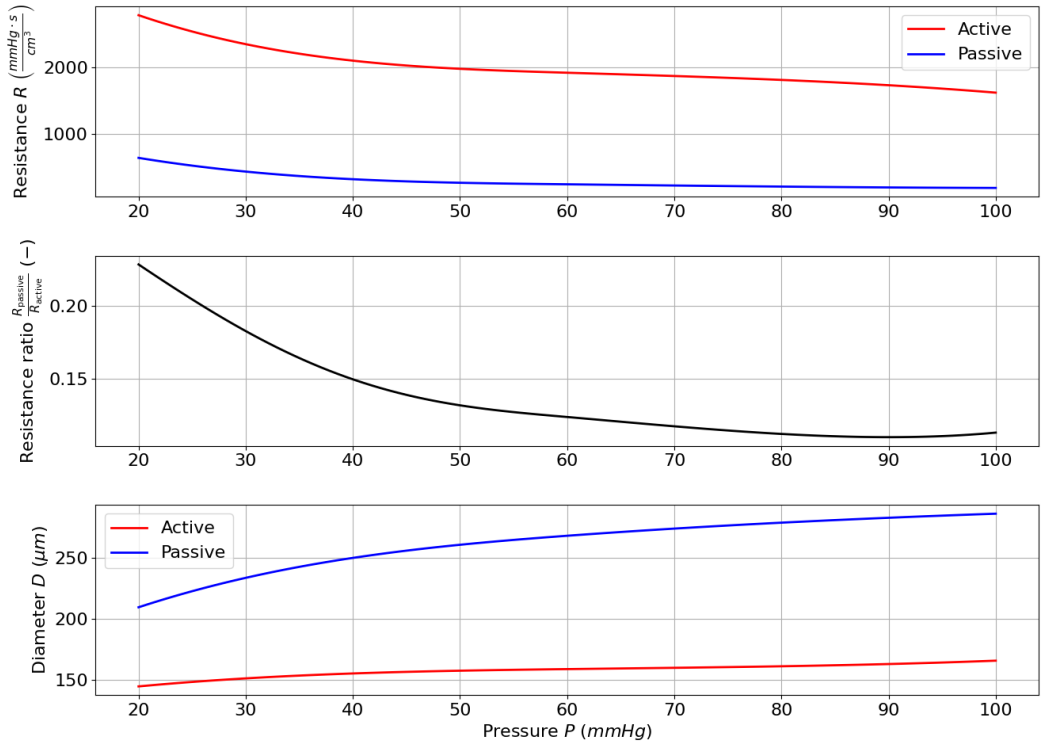

Figure 5.3: Simulation results of *baseline* vessel for resistance to flow and diameter across the pressure range. Top: R_f for the active and passive cases; Middle: ratio $R_{f,\text{passive}}/R_{f,\text{active}}$; Bottom: diameter results for active and passive cases.

The resistance and diameter distribution with respect to the luminal pressure is the same for every case considered in this section (each ΔP case). This is because the geometrical characteristics of the vessel are not changing.

Variable pressure drop across the vessel

The next aspect that is investigated is the effect that the pressure drop within the vessel has on the flow development. To achieve that, another pressure boundary

condition configuration was set. Two indicative pressure values were chosen, and the outlet of the vessel was fixed to those values. The values chosen are $P_{\text{out}} = 40\,\text{mmHg}$ and $P_{\text{out}} = 80\,\text{mmHg}$. Then, the pressure at the inlet was gradually increased, so that $\Delta P = P_{\text{in}} - P_{\text{out}}$ increased. The range of ΔP tested is starting at $\Delta P = 0.01\,\text{mmHg}$ and goes up to $\Delta P = 10\,\text{mmHg}$.

For this study again the *baseline* vessel is used for the sake of consistency, as reported in the previous section. Also in here, the discretisation aspects are: $\Delta x = 0.01\,cm = 100\,\mu m$, which means 10 elements across the length. The time step again is set to $\Delta t = 5 \cdot 10^{-4}\,s$.

Figure 5.4 shows the results for the boundary condition setup of this section. Both cases of outlet pressure ($P_{\text{out}} = 40\,\text{mmHg}$ and $P_{\text{out}} = 80\,\text{mmHg}$), and both vessels (active and passive) are presented simultaneously. In the left plot, the flow rate results obtained, with respect to ΔP, for both cases and vessels are shown. It is observed that the flow development for all four cases has a linear dependency on ΔP. However, the active vessels develop significantly lower flow rates, which is due to the lower diameter of the contracted vessel. Moreover, for the case with higher outlet pressure ($P_{\text{out}} = 80\,\text{mmHg}$), the gradient of the flow with respect to pressure drop is also higher. In the right plot of the figure, the flow rate ratios ($Q_{\text{passive}}/Q_{\text{active}}$) are shown for both outlets pressure cases with respect to ΔP. It is observed that for the higher outlet pressure ($P_{\text{out}} = 80\,\text{mmHg}$), the flow ratio is significantly higher.

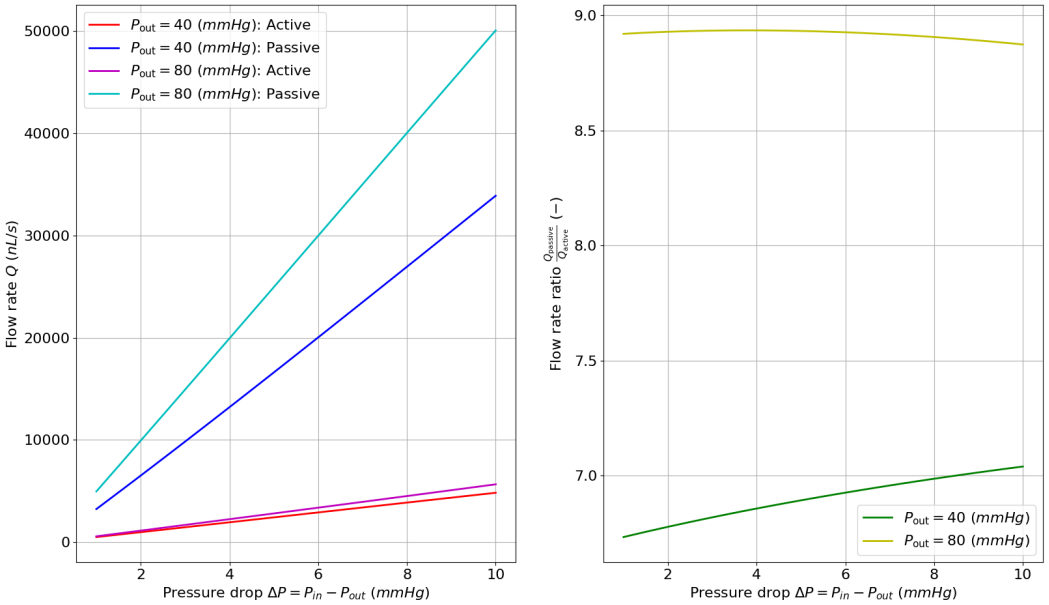

Figure 5.4: Simulation results for flow rate using constant pressure at the outlet and variable ΔP. Cases of outlet pressure $P_{\text{out}} = 40\,\text{mmHg}$ and $P_{\text{out}} = 80\,\text{mmHg}$. Left: active and passive vessel flow development; Right: $Q_{\text{passive}}/Q_{\text{active}}$ ratios

The aforementioned observations from Figure 5.4 can be explained when com-

bined with the resistance to flow that was presented in the previous section. For each of the pressure outlet cases, the pressure range at which the vessel is functioning does not show a high variation. As it was stated, the maximum difference is $\Delta P = 10\,\text{mmHg}$, hence the vessels are functioning within a range of 10 mmHg. This change does not produce significant changes to the diameter of the vessel. Therefore, the resistance to the flow does not undergo high alterations too. Given the above, the flow development is driven by the pressure drop in a linear fashion.

5.2.2 Difference with Poiseuille law case

Similar to the Ohm law for electric circuits, the flow rate would theoretically be governed by a pressure (potential) difference between the start and end points and a resistance element, which in the case of blood vessels represents the friction within the vessel that resists the flow. The value of the flow rate, hence, would be

$$Q = \frac{\Delta P}{R} = \Delta P \frac{A^2}{8\mu L \pi}. \tag{5.8}$$

The above equation, the Poiseuille law, is an analytical solution assuming the fluid to flow within a rigid tube. In the context of this thesis, the area A was updated at each time step, and therefore it is a semi-analytical form. The resistance element in equation (5.8) is the same as the friction term considered in the previous sections since, as reported in Section 2.1.2, a Poiseuille profile was chosen. In this section, a comparison between the obtained results and the Poiseuille law is examined.

One case from each configuration presented in Sections 5.2.1 and 5.2.1 was chosen to be simulated from each configuration. The flow was computed through equation (5.8) for the comparison. The cases chosen were $\Delta P = 0.1\,\text{mmHg}$ the first configuration, and constant $P_{\text{out}} = 40\,\text{mmHg}$ from the second one. The vessel used for this comparison was the *baseline*. The flow produced with Poiseuille law is hereby mentioned as Q_{P}.

Figure 5.5 presents the difference between the computed flow and the Q_{P} for the active and passive case. In the top plot the comparison of the first pressure configuration (Section 5.2.1) is shown, and on the bottom the comparison for the second one (Section 5.2.1). As seen in the figure, the difference associated with the two setups has different behaviors. In the case of constant pressure drop (top plot), for both active and passive cases the difference goes to lower values as the pressure increases. For the constant outlet pressure (bottom plot), the difference increases as ΔP increases. In addition, it is clear that vessels with an actively contracting wall have lower difference with the Poiseuille law than passive ones.

Furthermore, Table 5.1 presents a summary of the second pressure configuration,

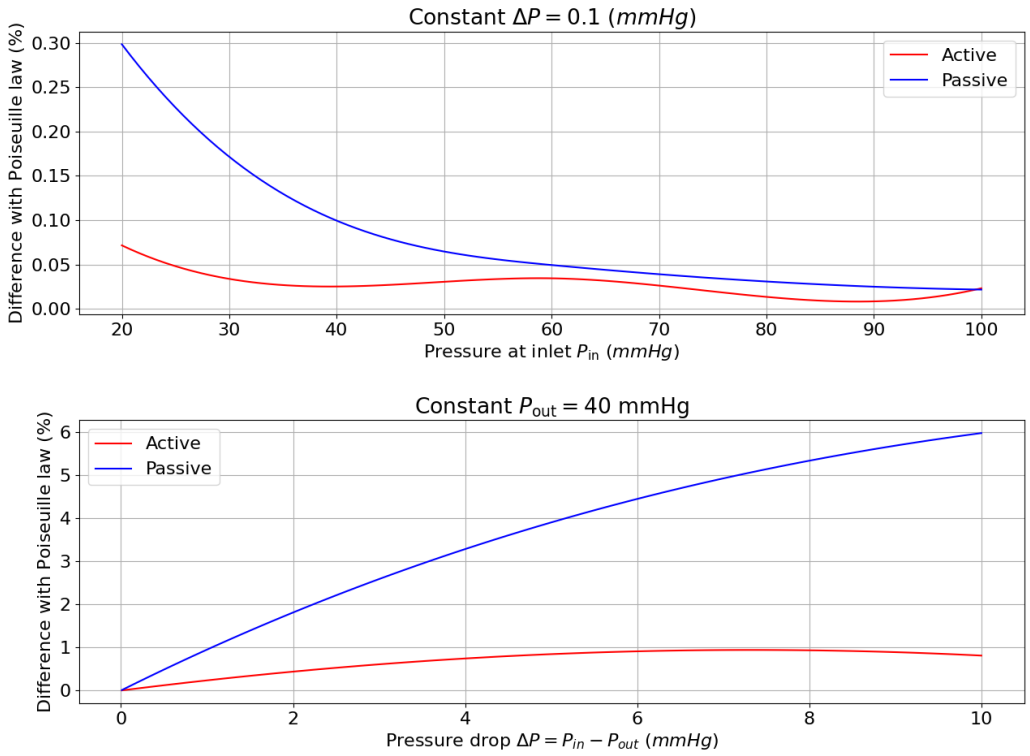

Figure 5.5: Difference between computed solution and Poiseuille law computed for the two pressure setup cases. Top: constant $\Delta P = 0.1$ mmHg; Bottom: constant $P_{\text{out}} = 40$ mmHg

with the constant outlet pressure and the variable ΔP for the case of $P_{\text{out}} = 40$ mmHg. The table is useful because it shows that the Poiseuille law always underestimates the values of the flow rate.

Table 5.1: Summary of results for the case with constant pressure outlet $P_{\text{out}} = 40$ mmHg and variable pressure gradient across the vessel ΔP

	Active			Passive		
ΔP	$Q\,(nL/s)$	$Q_{\text{P}}\,(nL/s)$	Diff. (%)	$Q\,(nL/s)$	$Q_{\text{P}}\,(nL/s)$	Diff. (%)
0.01	4.776	4.776	0.002505	31.930	31.926	0.009948
0.1	47.775	47.763	0.024912	319.581	319.265	0.099066
1	478.756	477.632	0.235034	3223.121	3192.648	0.949947
2	959.457	955.264	0.438013	6502.033	6385.296	1.811654
3	1441.632	1432.896	0.607854	9829.146	9577.944	2.588763
4	1924.788	1910.528	0.743619	13197.115	12770.592	3.285025
5	2408.413	2388.160	0.844484	16598.896	15963.240	3.904265
10	4815.212	4776.319	0.810979	33894.494	31926.481	5.979897

The behaviours described can be explained by considering the compliance of these vessels. When the flow rate is approximated with the Poiseuille law, its compliance is not taken into consideration. The vessels implemented in this framework are compliant, which means that they can store some amount of fluid within them. This is the reason in every case the Q_{P} value is always underestimating

the computed flow. For the same pressure drop and area, the compliant vessel allows less flow passing.

Figure 5.6 presents the compliance for the two pressure configurations (both for active and passive vessel). It is observed and expected that the myogenic tone does not only adjust the diameter but also reduces the compliance making the vessel stiffer in both configurations presented.

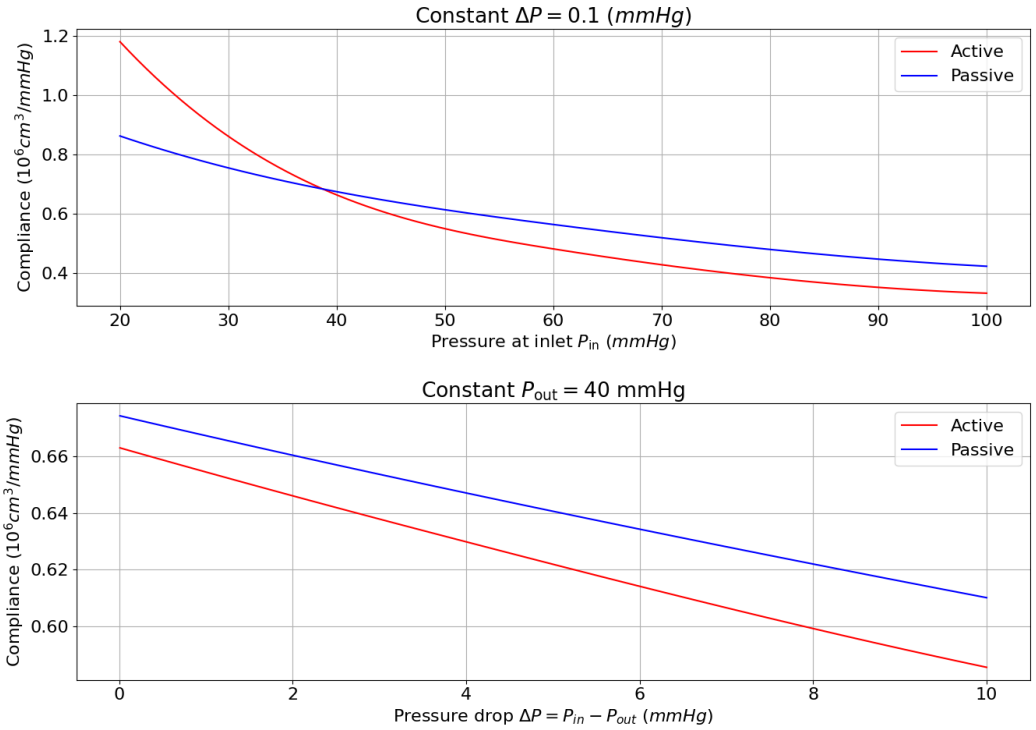

Figure 5.6: Compliance of the vessel for the two pressure setup cases. Top: constant $\Delta P = 0.1\,\text{mmHg}$; Bottom: constant $P_{\text{out}} = 40\,\text{mmHg}$

It is noted that the Poiseuille law for flow within a rigid tube is useful to verify that the results acquired from the 1D model are valid. However, a Poiseuille law is not practical for adaptation to 1D networks or transient conditions. Physiologically, vessels are compliant as they expand significantly due to pressure variations, and to a lesser degree, vessel axial and circumferential stretching. In compliant vessels, the elastic properties allow the vessel walls to expand and contract, influencing the characteristics of the pulse propagation. A compliant vessel can account for these wave reflections and interactions.

5.2.3 Role of geometry in the vessel flow dynamics

So far, the investigations presented referred to changes in the pressure settings for a given vessel geometry. In this section, changes in geometrical features and their effect on vessel flow under steady state are examined. The geometrical

features that are altered are the reference luminal radius and the length of the vessel, whilst the same pressure boundary conditions configurations as before are considered.

Reference radius sensitivity

At first, an investigation of the effect of reference radius is evaluated. The reference radius of the *load-free* configuration is changed by ±12.5% while the rest of the parameters of the vascular wall model are kept unchanged.

For consistency, the pressure boundary configuration setups of Section 5.2.1 and 5.2.1 are used here. The first set of results is set according to the first configuration. The three vessels are examined for the flow development across a certain pressure range, and with a fixed pressure drop ΔP. $\Delta P = 0.1\,\text{mmHg}$ is chosen to be simulated and the results are presented below.

As can be seen in the left plot of Figure 5.7, the flow rate increases as the reference radius increases, maintaining the same trend. The trend of the flow curves with respect to inlet pressure is exactly the same as the diameter trends, presented in the right plot of the figure. This is in line with the flow rate results presented in Section 5.2.1.

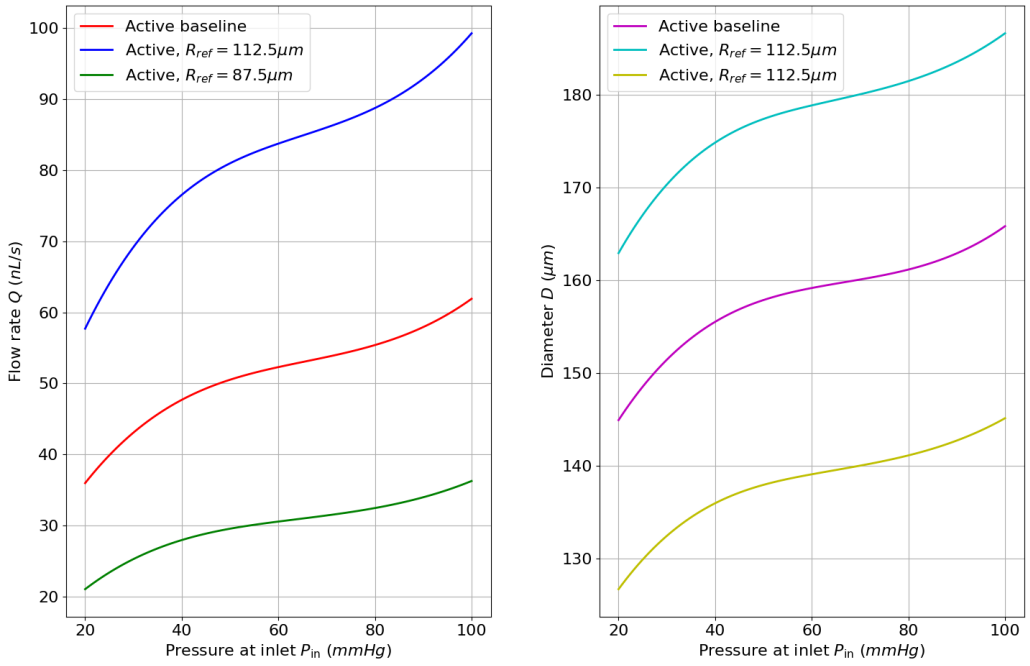

Figure 5.7: Simulation results of sensitivity analysis for the flow rate with respect to reference radius alteration. Constant pressure drop $\Delta P = 0.1\,\text{mmHg}$. Left: flow rate results; Right: diameter of the vessels.

The increase/decrease in vessel size results in a shift upwards/downwards

of the baseline curve. It should be noted that when the reference radius is increased/decreased for the same amount (±12.5%), the amount of increase/decrease in flow is not the same. In more detail, when the reference radius is increased, the flow rate is 46.3% higher with respect to the *baseline*, while when the reference radius is decreased the flow rate is 52.2% lower (with respect to the *baseline*). Another feature that can be observed from the plot is that while the trend of the line is the same in all three radius cases, as the reference radius increases, the absolute change in flow (from minimum to maximum) is higher. This happens because, for smaller radii, the active constriction becomes greater, and hence it dominates the response.

The next set of results refers to the second pressure configuration. The outlet pressure of the vessels is kept constant and their inlet is varied. Here the indicative case of $P_{\text{out}} = 40\,\text{mmHg}$ is considered.

In Figure 5.8 it is observed that the percentage change with respect to the *baseline* is almost the same as in the previous case, i.e. 46.3% increase for the larger radius and 52.1% lower for the smaller radius. It is seen that as the radius increases, not only the flow amount is increased, but also its gradient. This is indicating that when the reference radius is decreased, the vessel is becoming more stiff due to the active component presence, and hence the restriction to the flow is much higher.

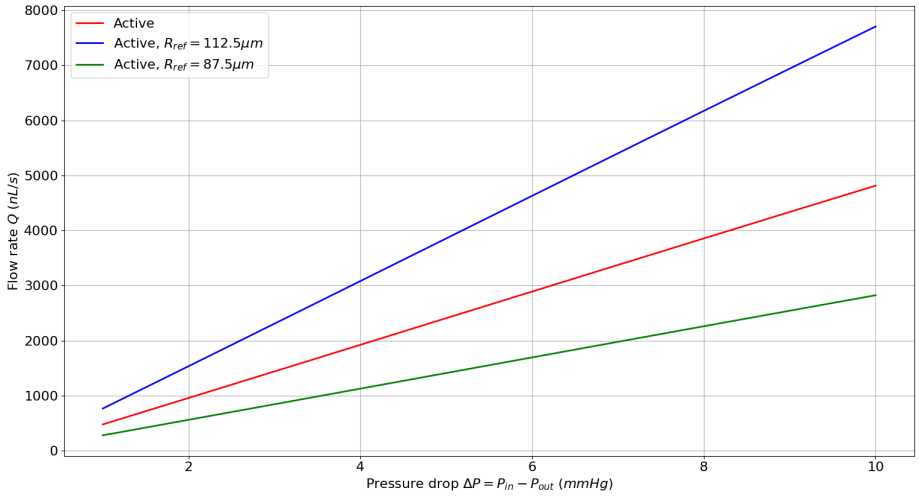

Figure 5.8: Simulation results of sensitivity analysis for the flow rate with respect to reference radius alteration. Constant outlet pressure $P_{\text{out}} = 40\,\text{mmHg}$

Figure 5.9 presents the compliance of the three vessels, for the two pressure configurations. The first thing to notice in these figures is that the compliance is decreasing for the smaller vessel for both pressure configurations. This is in line

with what reported before that for smaller radius, the vessels are stiffer and more resistant to flow.

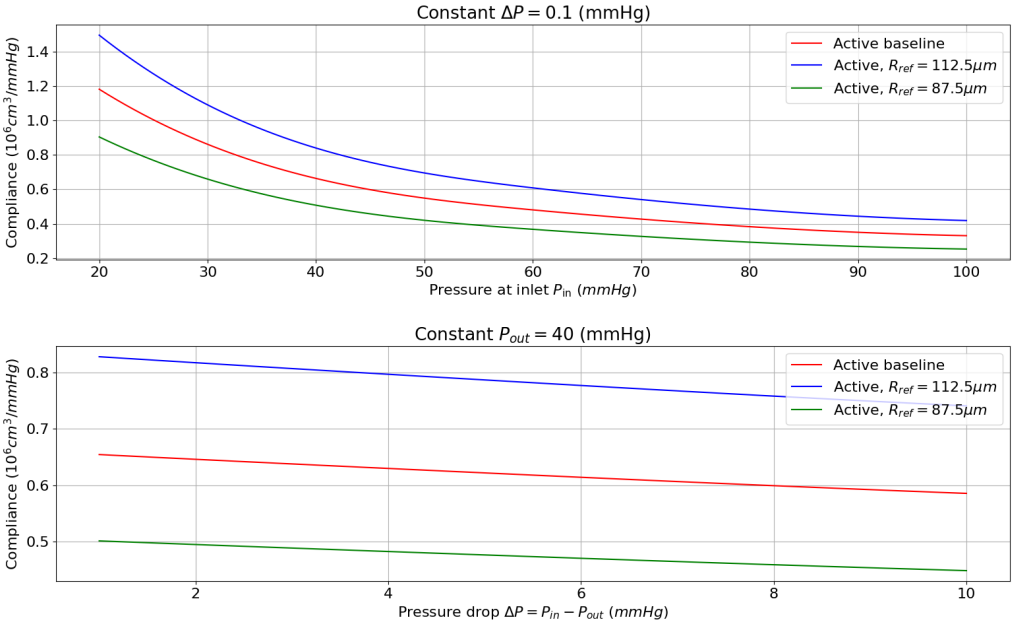

Figure 5.9: Simulation results of sensitivity analysis for the compliance with respect to reference radius alteration. Results for both pressure setup cases

It is also seen that the compliance plot seems equidistant for the case where the outlet pressure is constant and the inlet is increasing (bottom plot), while it shows a linear dependency on the pressure drop. When the reference radius increases the compliance gets 23.4% higher, while when it is decreased the compliance is 26.5% lower with respect to the *baseline*.

On the other hand, when the pressure drop across the vessel remains constant and the whole pressurisation of the vessel changes (top plot), the compliance does not have a linear distribution with respect to the inlet pressure. This non-linearity is explained by considering the pressure-area relationship employed. The pressure-area relationship of the active model shows a higher gradient in the area between 20 mmHg and 40 mmHg. Furthermore, the difference in compliance with respect to the baseline case for this pressure setup is the same with the previous one (+23.4% for an increase and −26.5% for a decrease).

Finally, when the compliance is calculated for a constant outlet pressure and variable ΔP, it means that within each element of the vessel the pressure drop will be higher. When the pressure drop is constant, the pressure difference within each element is the same. This means that the area computed for each element would be much different between the two cases, and the same applies for the gradient $\partial A/\partial P$.

In general, the dependence of the flow rate on the changes of the reference radius

is in line with the expectations. The flow rate appears to be smaller for lower reference radius and vice versa.

Vessel length sensitivity

Here the effect of vessel length on the pressure-flow relationship is investigated. For the examination, the length was increased tenfold, i.e. $L = 1\,cm$, and the *baseline* reference radius was employed. Note that the length was only increased (and not decreased). Also, for the higher length case, the discretisation level was kept the same, i.e. 10 elements total within the vessel ($\Delta x = 0.1\,cm$).

Again, two pressure configurations were examined. For the first configuration (ΔP = constant) the value selected for this study was $\Delta P = 1\,\text{mmHg}$. For the second configuration P_{out} = constant, the value of $P_{\text{out}} = 40\,\text{mmHg}$ was chosen.

As can be seen in Figure 5.10 for both cases, for the same pressure conditions, a longer vessel exhibits a smaller flow. This is natural and expected because the resistance to the flow R_f is proportional to the length. The flow computed within the vessel with $L = 1\,cm$ is roughly $1/10^{\text{th}}$ of the one with $L = 0.1\,cm$. This occurs for both cases of pressure setup. The length of the vessel is, hence, another important factor in defining the flow rate, and depending on the network the type of vessel it tends to vary a lot.

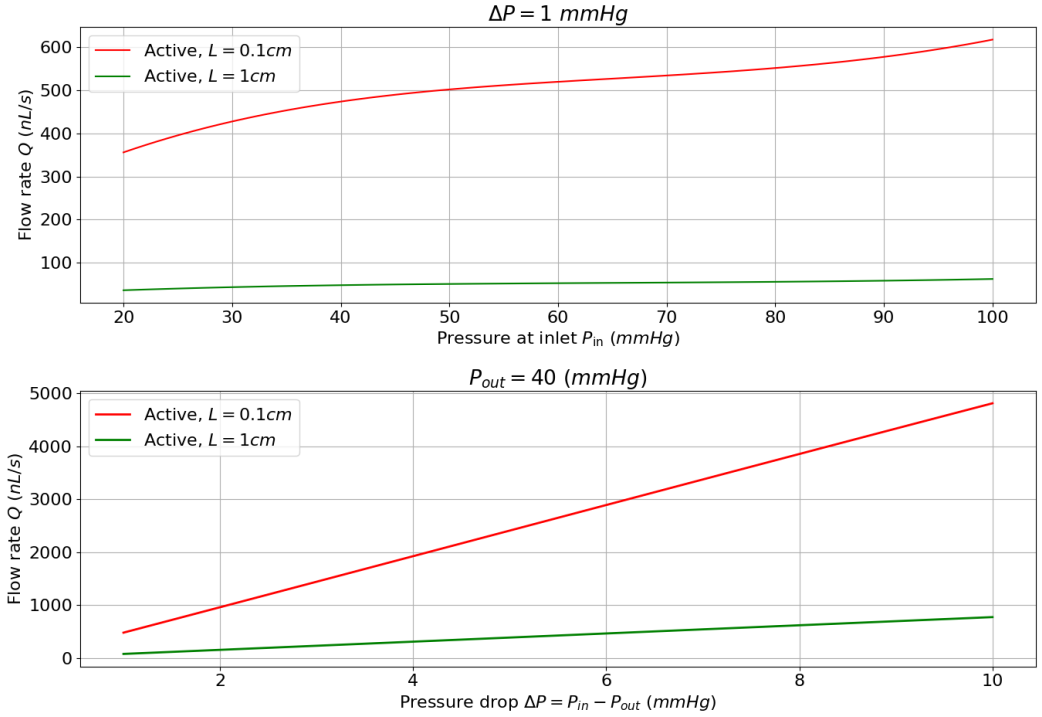

Figure 5.10: Simulation results of sensitivity analysis for the flow rate with respect to length alteration. Results for both pressure setups. Top: $\Delta P = 1\,\text{mmHg}$; Bottom: $P_{\text{out}} = 40\,\text{mmHg}$

5.3 Transient behaviour

After investigating the steady-state behavior of the coupled solid-fluid flow system, the next step is to assess the transient behaviour of the vessel with the active tone development. This section aims to identify the dynamic characteristics of the flow development during the active contraction.

To that end, the behaviour of the vessel under sudden changes in luminal pressures is evaluated. Both cases of increased and decreased pressure are examined in several scenarios. Furthermore, an investigation of the effect of the vessel reference radius on the flow development is assessed.

5.3.1 Response for different pressure configurations

Since myogenic response is a mechanism that tries to maintain a constant flow rate during pressure fluctuations, the dynamic phenomena occurring due to those pressure changes are an aspect that needs to be addressed. The first study of the transient examination investigates this dynamic behaviour of a vessel with active tone under sudden luminal pressure changes.

Sudden pressure changes are used widely in experimental tests to study the active behaviour of resistance vessels [177, 151, 235, 236, 237, 176]. In these experimental studies, the vessels were subjected to inflation/deflation tests with increments of sudden pressure change.

Pressure increase

The study begins by examining a scenario of sudden increase in pressure. This change is introduced by applying a ramp that rapidly elevates the inlet pressure. To explore the dynamic impact of active tone development on blood flow, two cases are established. The first case involves a single pressure increase, whereas the second case incorporates three successive pressure increases.

The vessel used is the *baseline*. It is initialised with the steady state conditions for the initial pressure and then the increase is applied. In the case of multiple pressure increases, each one lasts $12.5\,s$. The ramp used to apply the increase has a duration of $0.5\,s$ in order to simulate a sudden increase. The time step used in all cases again is $dt = 5 \cdot 10^{-4}\,s$. With this time step, the total number of iterations was $25,000$ for each of these simulations. The computational time was at the order of one hour. Similar to the steady state study, the spatial discretisation is 10 elements across the vessel.

For this study, the pressure boundary conditions are set with the configuration

described in Section 5.2.1. That is, the pressure level at the inlet P_{in} is imposed, with a fixed ΔP between inlet and outlet. For the cases in this section, $\Delta P = 1\,\text{mmHg}$ is chosen.

For the first investigation scenario, the pressure is raised in a single step. It rises from $P_{\text{in}} = 60\,\text{mmHg}$ to $P_{\text{in}} = 80\,\text{mmHg}$ according to the ramp set. After elevation, the inlet pressure is kept constant to allow the flow to reach a steady state.

Figure 5.11 presents the simulation results for an incremental pressure change. On the top right and bottom left plots, the results of the flow rate are presented, for the active and the passive vessels (top right). The active case is also presented alone (bottom left) so the dynamics of the flow regulations are visible. Finally, in the bottom right plot, the compliances of those two vessels are compared.

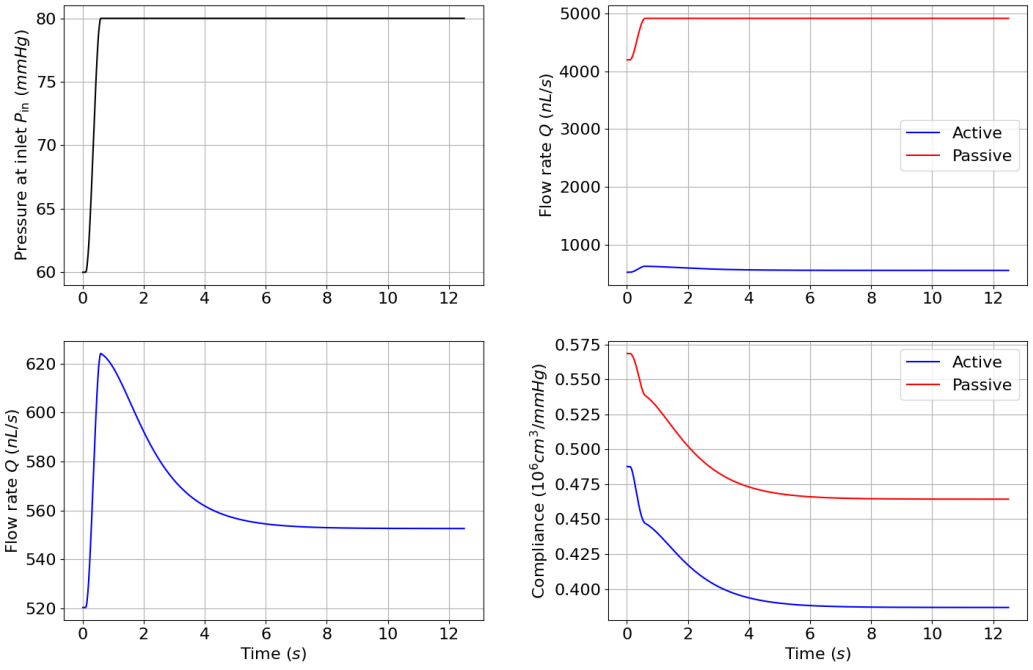

Figure 5.11: Simulation results for flow rate and compliance of the active and passive vessel cases. Pressure increase from $P_{\text{in}} = 60\,\text{mmHg}$ to $P_{\text{in}} = 80\,\text{mmHg}$. Constant pressure drop $\Delta P = 1\,\text{mmHg}$ between inlet and outlet. Top left: inlet pressure imposed; Top right: active and passive flow results; Bottom left: active case flow results; Bottom right: active and passive case compliance results

As can be seen in Figure 5.11, when the vessel is actively contracted, the flow rate initially increases, but the active tone development gradually reduces the flow. As expected from the pressure-area relationships, the flow rate is drastically reduced with the contribution of myogenic control. On the other hand, when the vessel response is dictated only by the material (passive) properties, the flow increase upon pressure elevation is maintained. Furthermore, the compliance shown in the

same figure indicates that the actively contracted vessel is less compliant, in line with pressure-area relationships reported in the previous chapters. Note here that the time needed for active contraction is controlled through the time parameters of the implemented chemical and chemo-mechanical model, as examined in Section 4.3.2.

Next, the fluid-structure interaction is evaluated for multiple pressure steps. The same configuration of pressure boundary conditions is kept ($\Delta P = 1\,\text{mmHg}$), and three increments of pressure increase are simulated in a range from $P_{\text{in}} = 40\,\text{mmHg}$ to $P_{\text{in}} = 100\,\text{mmHg}$. The multiple pressure steps are increasing the total iterations needed for the complete simulation to $75,000$ and the computational time is similarly increase to ~ 3 hours. For validation, the total pressure increase is also simulated using one step.

Figure 5.12 shows the increase from $P_{\text{in}} = 40\,\text{mmHg}$ to $P_{\text{in}} = 100\,\text{mmHg}$ with one and three steps (left and right columns). For the three-step increase, the pressure is at first increased by $10\,\text{mmHg}$, then by another $30\,\text{mmHg}$, and finally by $20\,\text{mmHg}$. For the single-step increase, the pressure directly goes from $P_{\text{in}} = 40\,\text{mmHg}$ to $P_{\text{in}} = 100\,\text{mmHg}$. Moreover, the middle row shows the flow developed for each case for the active and passive responding behaviour. Finally, in the bottom row, the diameter ratio of the active and passive vessels is shown.

At first, both active and passive cases end up in the same flow rate, which shows that the final pressure increase across the vessel produces a unique flow rate development. The final solution of flow rate is independent on the path of the pressure increase. Moreover, the development of active tone manages to regulate the flow rate and prevents it from having high variability for the whole pressure range simulated. From the diameter ratio, it is seen that the amount of increase in the passive vessel is much higher than the increase in the actively contracted vessel.

Moreover, another interesting aspect observed is that there is a difference in the diameter ratio transition between the one-step and the three-step pressure increase. More specifically, the one-step increase tends to higher values than the three-stepped one. This can be explained through the level of myogenic tone within the vessel. The myogenic tone refers to the baseline level of smooth muscle contraction that vessels maintain, which influences their resting diameter. With the intermediate steps, the myogenic tone within the vessel is higher, and hence already contracted more.

These simulations resemble the procedure followed by experimental protocols in terms of how the pressure is increased or decreased. In many experimental studies the inflation of the vessel is achieved by applying multiple pressure steps, allowing some time under constant pressure [176, 177]. The results obtained quantify the

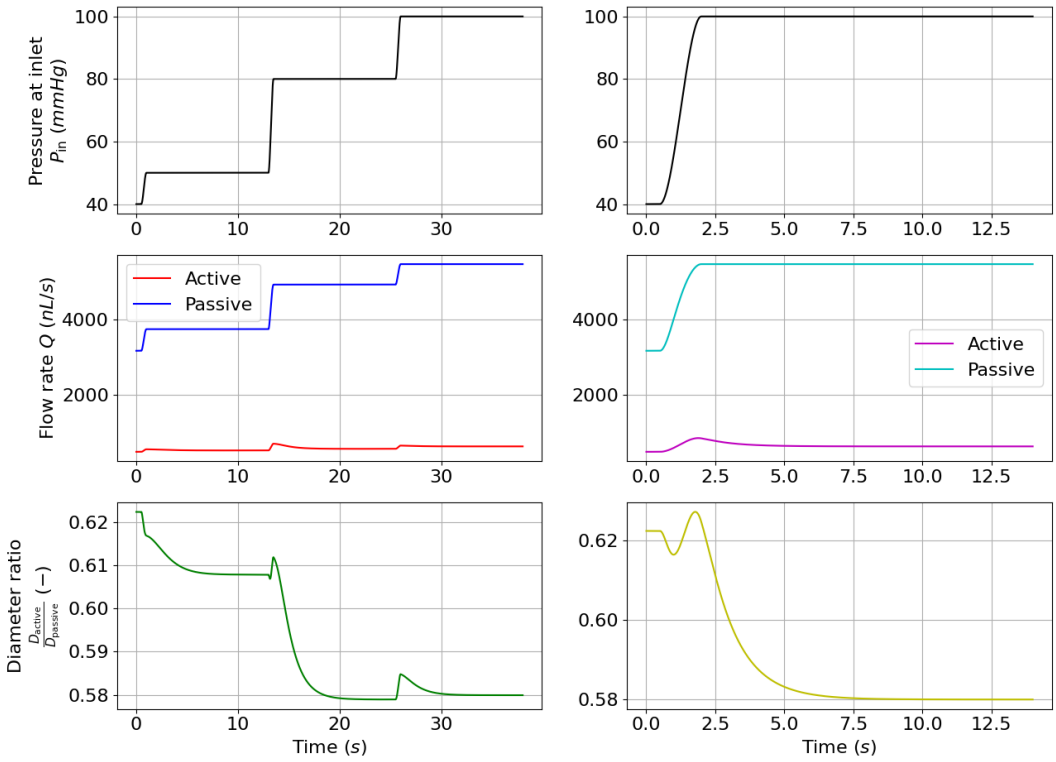

Figure 5.12: Simulation results for flow rate and diameter ratio of vessel for active and passive case. Pressure increase from $P_{\text{in}} = 40\,\text{mmHg}$ to $P_{\text{in}} = 100\,\text{mmHg}$ in one and three steps (constant $\Delta P = 1\,\text{mmHg}$). Left column: three pressure steps; Right column: one pressure step. Top row: inlet pressure; Middle row: flow rate; Bottom row: diameter ratio ($D_{\text{active}}/D_{\text{passive}}$).

impact of the myogenic mechanism on the blood flow control. In general, it is observed that when the inlet pressure is increased, initially the vessel does not contract but follows this increase (although lower than it would have if it was a purely passive). The myogenic response then decreases the area and therefore the flow rate.

Pressure decrease

To complete the examination of the dynamic characteristics of the flow development due to myogenic response, the scenario of luminal pressure decrease is examined. Here, the fluid-structure behaviour of the vessel is assessed by considering a pressure reduction. For consistency, the same setup as in 5.3.1 is used. That is, a single-step pressure decrease and a three-step one.

The *baseline* vessel is used also here. The vessel is initialised with the initial pressure level and the pressure decrease is imposed by a ramp of duration $0.5\,s$. After each decrease in pressure, it remains constant for $12.5\,s$ to allow the flow rate to reach a steady state. The time step used is $dt = 5 \cdot 10^{-4}\,s$. Note also that

the constant pressure drop within the vessel is $\Delta P = 1\,\text{mmHg}$.

The first scenario is the single-step pressure decrease. The inlet pressure is initially set to $P_{\text{in}} = 100\,\text{mmHg}$ and after a short time it decreases to $P_{\text{in}} = 80\,\text{mmHg}$.

The results presented in Figure 5.13 show the flow rate developed and the compliance within actively contracted and passive vessels for the case where the pressure decreases by 20 mmHg. The flow in this test has the opposite behaviour with respect to the contraction case, which means that the vessel dilates to allow more flow to pass through it. This occurs because the myogenic response is a mechanism that helps maintain stable blood flow. Therefore, a decrease in pressure would cause relaxation, leading to vasodilation. As expected, the time requested by dilation is the same with that required by vessel contraction upon pressure increase.

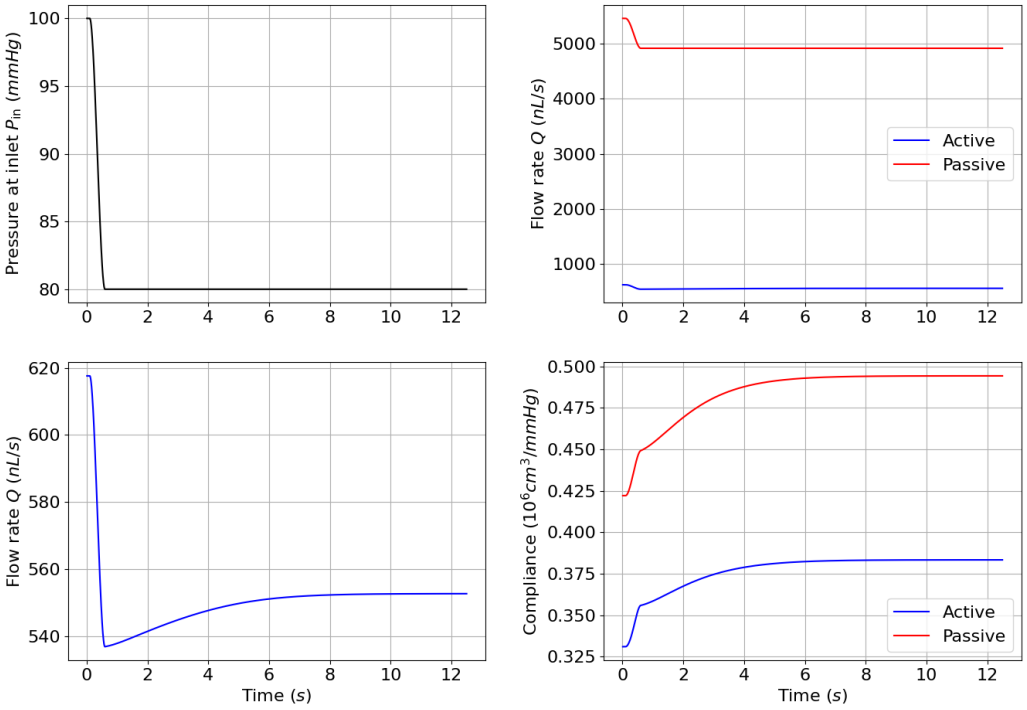

Figure 5.13: Simulation results for flow rate and compliance of the active and passive vessel cases. Pressure increase from $P_{\text{in}} = 100\,\text{mmHg}$ to $P_{\text{in}} = 80\,\text{mmHg}$. Constant pressure drop $\Delta P = 1\,\text{mmHg}$ between inlet and outlet. Top left: inlet pressure imposed; Top right: active and passive flow results; Bottom left: active case flow results; Bottom right: active and passive case compliance results

Regarding the compliance of the vessels, it is seen that when the vessels are dilating, the compliance is increased. However, the value of the actively dilated vessel is always lower than the passive one.

Subsequently, the fluid-structure interaction across multiple pressure decreases is

assessed, maintaining consistent pressure boundary conditions ($\Delta P = 1\,\text{mmHg}$). Simulations involve three decreases in pressure within the range of $P_{\text{in}} = 100\,\text{mmHg}$ to $P_{\text{in}} = 40\,\text{mmHg}$, as well as the single-step approach for comparison.

Figure 5.14 shows the flow rate and diameter ratio results of actively dilated and passive vessels for two scenarios of pressure reduction. In these scenarios, the pressure is decreased in three-steps and in one step. For the three-step scenario, it begins from 100 mmHg, then decreases to 80 mmHg, then to 50 mmHg and finally ends up at 40 mmHg. The second scenario is a direct decrease from 100mmHg to 40 mmHg in a single step.

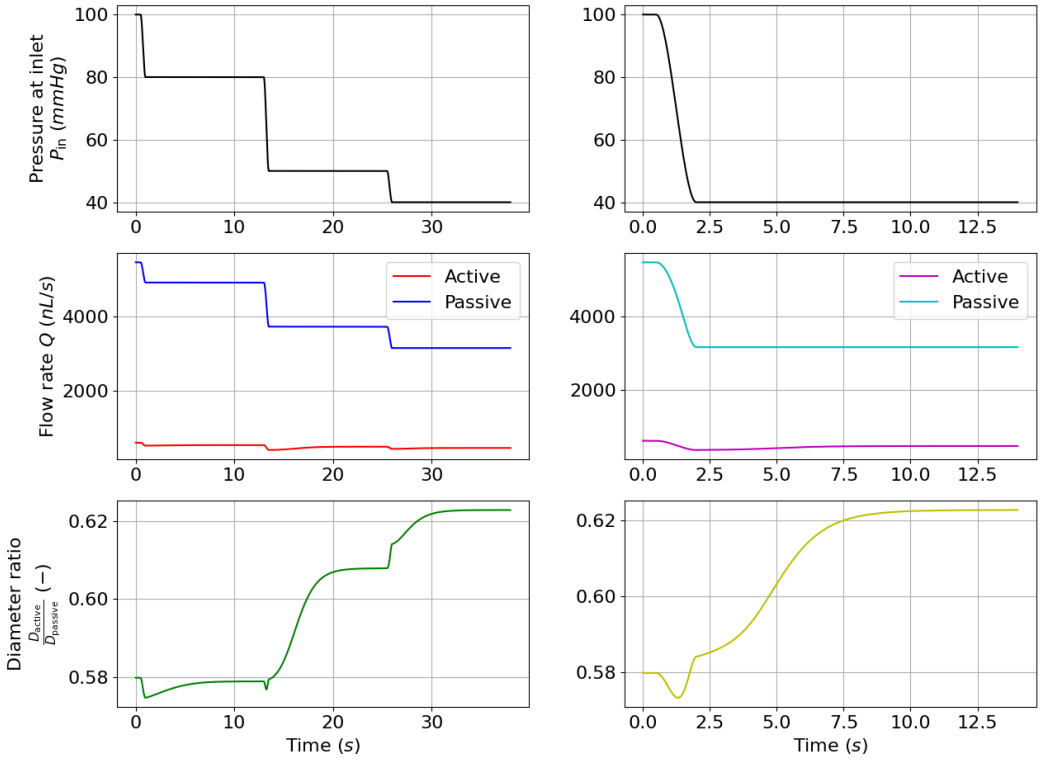

Figure 5.14: Simulation results for flow rate and diameter ratio of vessel for active and passive case. Pressure decrease from $P_{\text{in}} = 100\,\text{mmHg}$ to $P_{\text{in}} = 40\,\text{mmHg}$ in one and three steps (constant $\Delta P = 1\,\text{mmHg}$). Left column: three pressure steps; Right column: one pressure step. Top row: inlet pressure; Middle row: flow rate; Bottom row: diameter ratio ($D_{\text{active}}/D_{\text{passive}}$).

Here, the effect of vessel dilation is clearly seen. When the pressure suddenly drops, the vessel initially decreases its radius, following the diameter increase. After this decrease, the myogenic response actively dilates the vessel in order to maintain the flow rate. Furthermore, the diameter ratio ($D_{\text{active}}/D_{\text{passive}}$) increases in both scenarios. This means that actively dilated vessel is going to values closer to the passive one. This is explained by the very high diameter decrease of the passive vessel compared to the dilation of the vessel with the active

tone.

As discussed in Chapter 1 myogenic response is a mechanism that acts as a counterbalance to sudden pressure change, altering the diameter of the vessel to ensure the proper level of blood perfusion. The cases tested the effect of a sudden change (increase and decrease) in pressure on the flow development with the proposed framework, and were found to reproduce this effect.

5.3.2 Reference radius sensitivity

Similar to the Section 5.2.3, the reference radius was altered to see how it affects the flow rate development. For this investigation, the reference radius was increased at a rate of 12.5%.

For this investigation, the one-step pressure increase setup was used, as it was introduced in Section 5.3.1. The pressure is elevated from $P_{\text{in}} = 60\text{mmHg}$ to $P_{\text{in}} = 80\text{mmHg}$.

Figure 5.15 shows the two flow rate responses to pressure changes for the two considered reference radii. It is observed that both flow rates as well as the compliance of the vessels have the same trends and features. The only difference is in magnitude. This is in line with the study of Section 5.2.3 regarding the reference radius. Furthermore, the increase in flow rate for the different reference radii is also higher. Specifically, for the actively contracted vessel, with the *baseline* vessel the flow rate is increased by $32.2\,nl/s$, while with the larger vessel $51.5\,nl/s$. For the passive vessels, the respective increases are $719.5\,nl/s$ with the *baseline*, and $1152.6\,nl/s$ with the larger vessel.

Moreover, the larger vessel is more compliant, which is seen from the right hand side plots. Both results can be explained through the vascular wall model. For the case examined, only the reference radius is altered, and all the other parameters are kept constant. This means that the pressure-area relationship will not be altered, just scaled. Therefore, the flow development will also be scaled accordingly.

Overall, it is seen that an alteration in the reference radius, and keeping all other wall parameters constant has an impact on the flow development. However, the produced flow rate and compliance will only differ in magnitude, scaled either up or down.

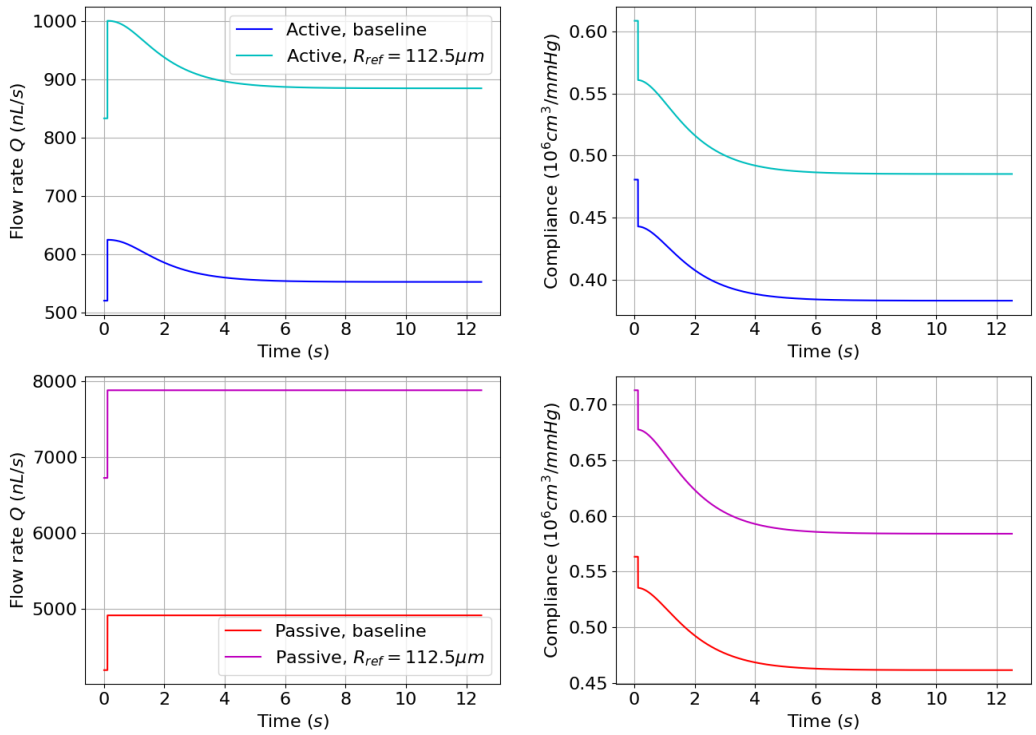

Figure 5.15: Simulation results for flow rate results and compliance of the vessel for different reference radii. Pressure increase from $P_{\text{in}} = 60\,\text{mmHg}$ to $P_{\text{in}} = 80\,\text{mmHg}$ and constant pressure drop $\Delta P = 1\,\text{mmHg}$. Top row: active responses; Bottom row: passive responses

5.4 Considering the downstream circulation

The final part of this chapter concerns the assessment of the pressure stabilisation effect operated by a self-regulated vessel on the downstream circulation. This is achieved by connecting a self-regulated vessel to a lumped parameter model representing the downstream circulation, as already done in several works [104, 146, 25] modelling cerebrovascular flow across the Circle of Willis (CoW). The dowsntream circulation (or vascular bed) is represented through a three-element Windkessel (WK) model in this work. The aim of this chapter is to investigate how a self-regulated vessel interacts with a WK model when it is attached to one.

In Chapter 2, the three-element WK model is presented, and a summary is repeated here. Figure 5.16 illustrates the WK model components: resistance Z_{art} signifies the characteristic impedance of the vessel, R_{VB} represents the resistance of downstream circulation, and together they constitute the total peripheral resistance $R_{\text{p}} = Z_{\text{art}} + R_{\text{VB}}$. The compliance element C reflects the total compliance of the downstream circulation which is much higher than the vessel compliance. The node after R_{VB} can represent several points in the vasculature. In this work it is considered to represent the capillary level, i.e. the cerebral vasculature region

upstream the venous system.

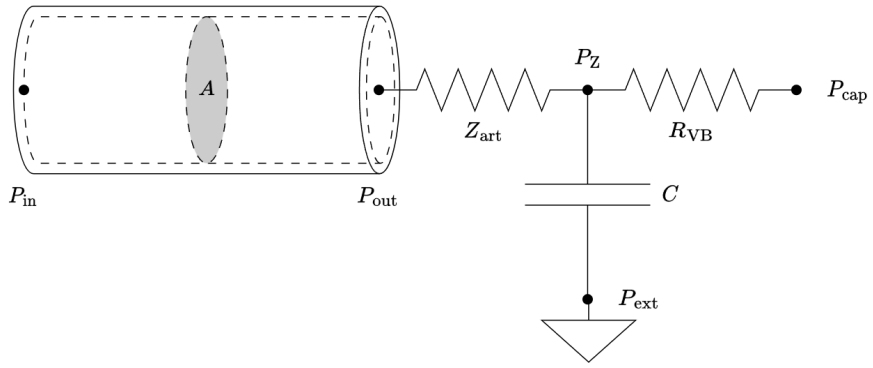

Figure 5.16: Windkessel model attached to a vessel. Z_{art}: characteristic impedance. R_{VB}: vascular bed resistance. C: vascular bed compliance

5.4.1 Strategy for flow within physiological range

There is no source available on the parameters of the WK model to represent the circulation downstream of the vessels used in this chapter. In this section, a strategy for identifying the resistances of the WK model was followed. The target is to find a set of values for Z_{art} and R_{VB} that produce a flow rate based on physiological data for the *baseline* vessel.

Studies on cerebral flow within rat and mouse arterioles and cerebral vessels show that blood flow within can vary considerably depending on its size and type. The study of Sweeney *et al.* [238] shows that mice arterioles diametered $\sim 40\,\mu m$ develop a flow rate of $2.5\,nl/s$. The study of Hoshikawa *et al.* [239] on rat and mice cerebral vessels shows that the velocity within these vessels may range from $\sim 0.1\,cm/s$ up to $\sim 1\,cm/s$ for both mice and rats. The corresponding flow rate for these velocities depends also on the diameter of the vessel, which varies from $\sim 50\,\mu m$ to $\sim 270\,\mu m$.

The size of the *baseline* vessel which is used in this thesis is within the diameter range reported in the latter work ([239]). Furthermore, the vascular wall model used in this thesis is fitted against experimental data from [177] which are from experiments on rat cerebral arteries. This is convenient since in [239] rat cerebral vessels are considered too. Therefore, only data that refer to the cerebral arteries of rats are considered from [239]. The minimum and maximum values were obtained in terms of flow rate. The smallest diameter with the lowest velocity would give a flow rate of $Q_{min} \approx 5.2\,nl/s$ ($d = 74 \pm 5\,\mu m, u = 2.4 \pm 1\,mm/s$), while the largest vessel would give $Q_{max} \approx 125\,nl/s$ ($d = 231 \pm 36\,\mu m, u = 1.5 \pm 0.7\,mm/s$).

Now, the 1D/0D system of vessel and WK models is considered, with the connectivity shown in Figure 5.16. As already mentioned, its resistances need to be adjusted in order the flow within the vessel produced is within the aforementioned

range. As a baseline parameter setup, the model of Alastruey *et al.* is used [107]. For the new system, the prescribed pressure boundary conditions will be P_{in}, P_{ext} and P_{cap}.

Since the aim of this study is the assessment of the interaction between the vessel and WK models, the impact of the downstream network on wave reflections are investigated. In order to vary the resistance imposed by the downstream network, the impedance Z_{art} is scaled. The criterion for terminating this adjustment is the flow development within the vessel. The impedance was scaled until the flow rate reaches a steady state condition whilst being within the defined range.

5.4.2 Obtained results

The external pressure is set to $P_{\text{ext}} = 0\,\text{mmHg}$, while at the capillary level $P_{\text{cap}} = 10\,\text{mmHg}$ [240]. The inlet pressure is set with a value within the physiological range of cerebral arteries $P_{\text{in}} = 60\,\text{mmHg}$ [233], and kept constant to acquire a steady state solution. It was found that for an up-scale of the impedance in the order of 10^4, the flow developed is within the range defined, and the results of this investigation are presented.

Regarding the computational aspects of this study, it was found that with the attachment of the WK model, the time step could be increased, so for the results to follow it was set to $dt = 0.1\,s$ which also drastically decreased the computational time needed to the order of minutes. This behaviour indicates that the time step limitation is related to the effect of backward waves on the single vessel.

Figure 5.17 shows the obtained results for flow rate and velocity for both actively contracted and passive vessels. As can be seen, the flow rate achieved with the setup is $Q = 123.1\,nl/s$ which is within the desired range. Moreover, the axial velocity of the flow acquired is $U = 0.81\,cm/s$, which also within the range presented in [239]. However, it is observed here that the flow developed in the passive vessel is only slightly higher than the active case. The velocity of the active case is significantly larger than the passive case, which is explained by the difference in the diameter shown next.

In Figure 5.18 the diameter and compliance spatial distribution of both vessels is shown. The results are plotted for the last time step of the simulation. It is seen that the diameter of the passive vessel is much higher than the actively contracted vessel. Moreover, the passive vessel is much more compliant than the active. These two features are explained through the constitutive law, as already discussed in previous sections. Under steady state condition, the compliance of the system has less of an effect on the solutions on flow and pressure. The compliance has a greater impact on the system upon dynamic changes in the

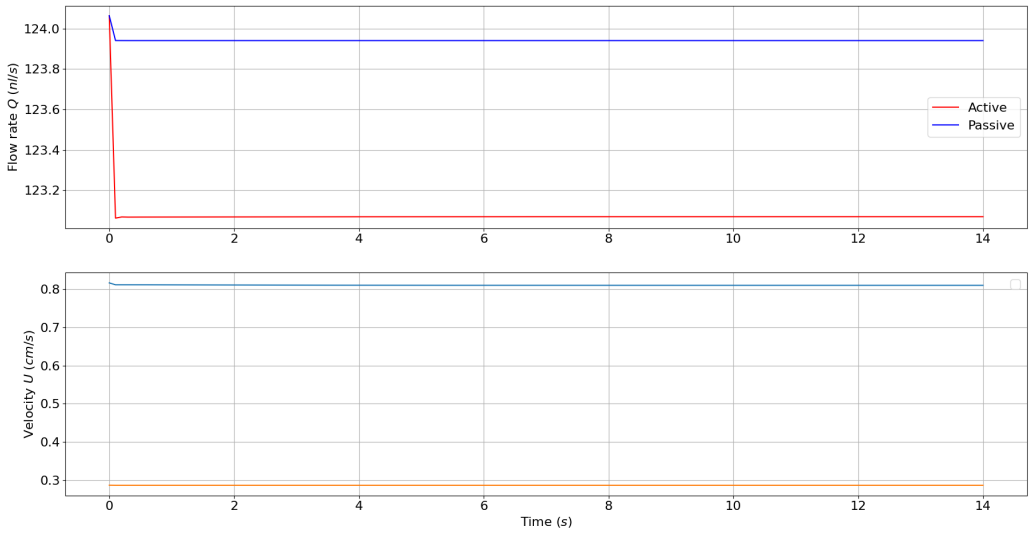

Figure 5.17: Simulation results of flow rate and velocity in time for actively contracted and passive vessels. Vessels attached to the WK model. Top: flow rate development; Bottom: axial velocity within the vessel.

diameter.

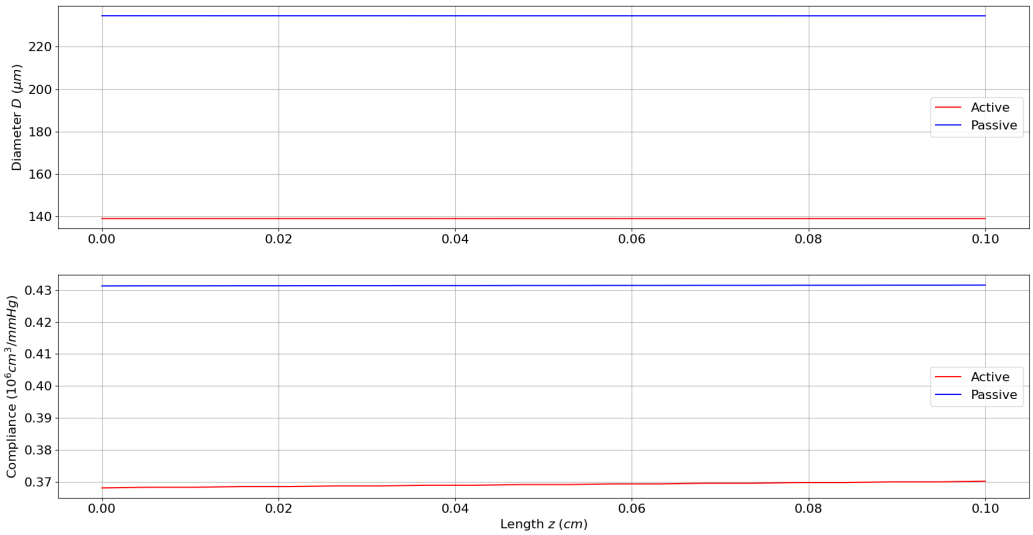

Figure 5.18: Simulation results of diameter and compliance in space for actively contracted and passive vessels. Vessels attached to the WK model. Top: luminal diameter spatial distribution; Bottom: compliance spatial distribution.

Continuing with the examination of the system, the pressure distribution needs to be inspected. One thing that is different compared to the cases without a WK model is the boundary conditions and where those are set. With the WK model included, there is no longer a Dirichlet boundary condition at the outlet of the vessel, so the pressure at the vessel outlet is solved with the rest of the nodes, as well as the middle node of the WK (node with pressure P_Z in Figure

5.16). The pressure at the outlet of the vessel is dependent on the WK setup, and its boundary conditions. For the next test, the inlet of the vessel was set to $P_{\text{in}} = 60\text{mmHg}$, and the two nodes of the WK model as $P_{\text{cap}} = 10\text{mmHg}$ and $P_{\text{ext}} = 0\text{mmHg}$.

In Figure 5.19 the spatial distribution of the pressure is shown. The schematic of the WK shows the pressure at the nodes of the WK model. As explained above, with the WK model attached, the pressures P_{out} and P_{Z} are part of the solution, and not boundary condition nodes. For this setup it is observed that the actively contracted vessel has a pressure drop of $\Delta P = 0.4\,\text{mmHg}$ between the inlet and the outlet. Interestingly, the pressure drop within the passive vessel is much lower with a value of $\Delta P = 0.02\,\text{mmHg}$. Moreover, it is observed that the intermediate node of the WK model (the one connecting all 3 elements) has the same pressure for both vessels $P_{\text{Z}} = 10.01\,\text{mmHg}$.

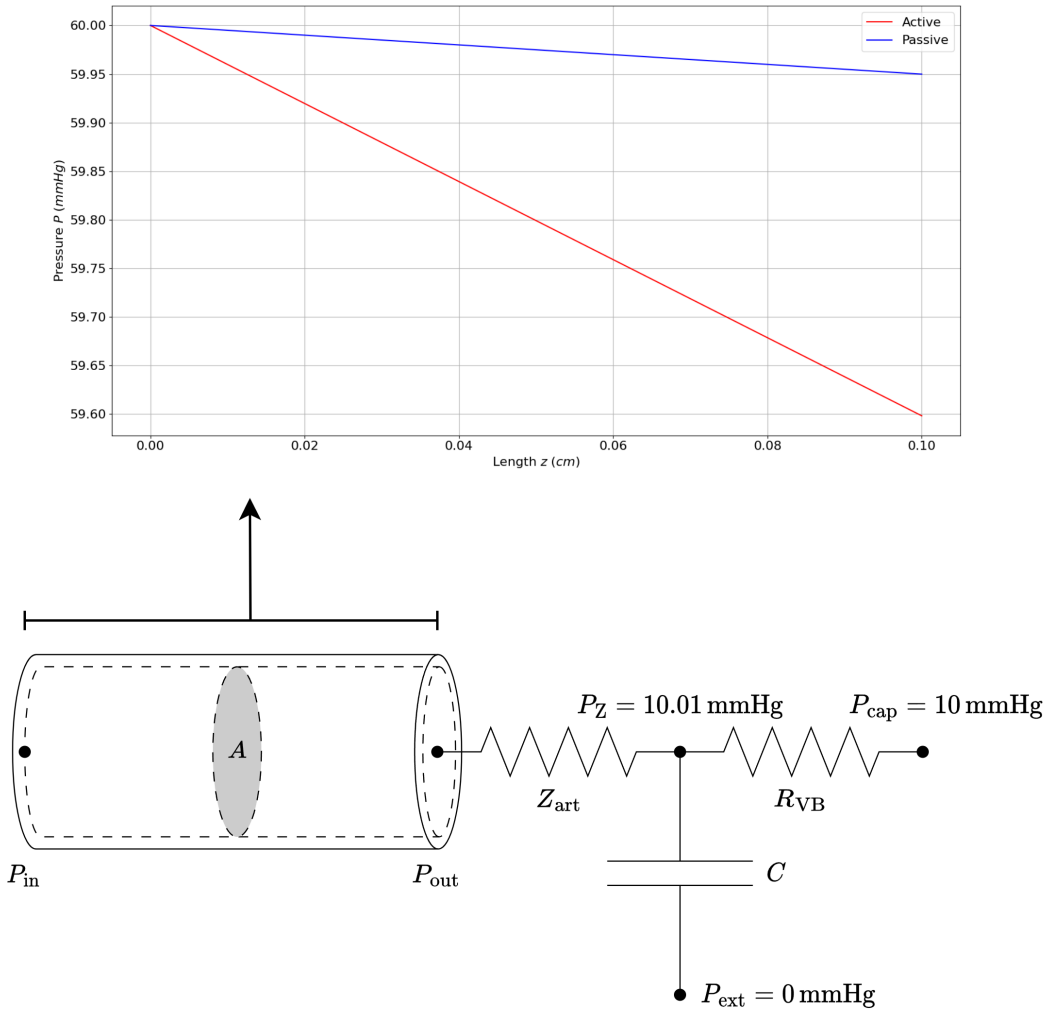

Figure 5.19: Simulation results of the pressure spatial distribution in the system. Steady state results for active and passive vessels attached to the WK model.

The pressure drop across the actively contracted vessel is significantly higher than the drop in the passive one. This occurs due to the increased resistance of the vessel caused by the decreased diameter due to the active contraction. However, the resistance of the total system is dominated by the WK Z_{art}, which means that the majority of the pressure drop in the system occurs across the impedance.

It is thus seen that for a given resistance of the downstream circulation, the actively contracted vessel presents a higher pressure drop than the passive one. If the vessel behaviour is isolated within a fixed system, it is seen that the active mechanism is maintaining a specific perfusion level by adjusting the pressure drop within that vessel.

For the sake of completeness, the vessel attached to the Windkessel model was run for the case of multiple increase levels. Again, the increase through multiple steps was simulated for the vessel-WK system. In the same way as in the work done in Section 5.3.1, the inlet pressure was increased from $P_{\text{in}} = 40\,\text{mmHg}$ to $P_{\text{in}} = 100\,\text{mmHg}$ through multiple steps, and through one step for comparison.

From Figure 5.20, the flow does not show the fluctuating behaviour when the pressure is initially increased, rather it rapidly converges to its steady-state value. That can be explained by the WK model dominating the total resistance of the system. It is observed that the diameter of the active vessel initially increases and then actively contracts having negligible effects on the flow rate. Finally, it is seen that the diameter and flow rate are converging to the same solution regardless of the pathway taken to reach the same pressure drop.

Next, an examination is taking place regarding the level of pressure drop with respect to the inlet pressure for the actively contracted vessel and the passive one.

Figure 5.21 shows the pressure drop ΔP in both active and passive vessels for different levels of pressure at the inlet when the vessel is attached to the WK model. Interestingly, it is seen that as the pressure at the inlet is taking higher values, the pressure drop within a passive vessel has a slight increase. On the other hand, it is observed that the pressure drop between the inlet and outlet of a vessel with a myogenic tone development is tending to higher values for the same WK configuration. As the pressure of the inlet increases, the active contraction also increases, which causes the resistance of the vessel to increase. This leads to the larger pressure drop observed in the active case compared to the passive.

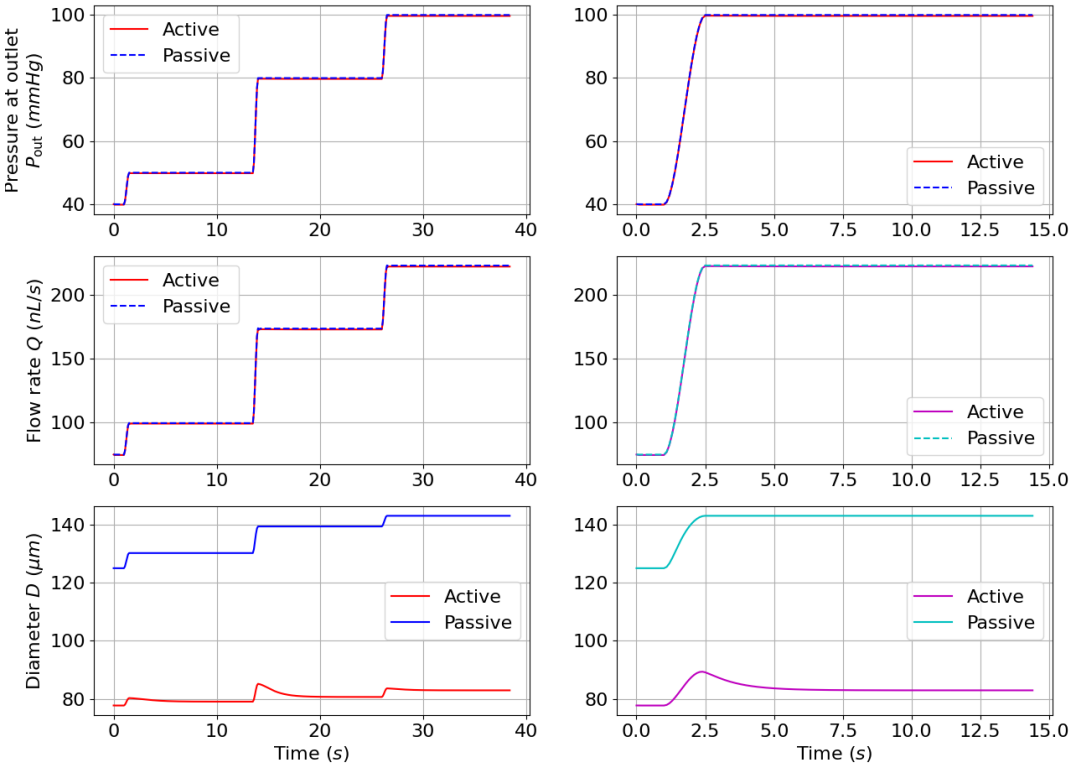

Figure 5.20: Simulation results for flow rate and diameter ratio with several increasing pressure steps. Vessels attached to WK model. Left column: three-step pressure increase, flow rate, and diameter; Right column: one-step pressure increase, flow rate, and diameter

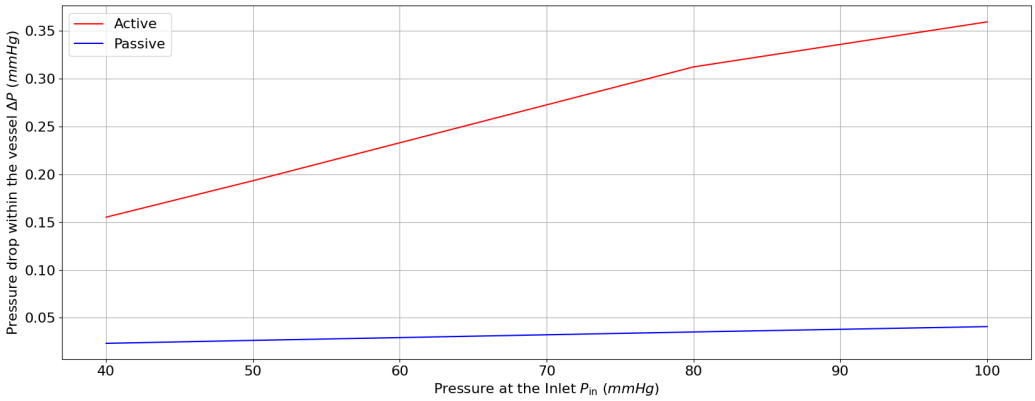

Figure 5.21: Comparison of pressure drop in actively contracted and passive vessel for different inlet pressures when they are attached to the WK model.

5.5 Conclusive remarks

Concluding this chapter, a thorough investigation was carried out regarding the flow development within self-regulated cerebral vessels. At first, the vessel was studied under steady state and transient conditions considering both cases of ac-

tive and passive response. The model indicated that the flow rate developed as a response to an increase or decrease in pressure follows the pressure-area relationship given by the implemented constitutive law. It is in line with the experimental findings as shown in previous chapters, and is the reason the myogenic response is present in vessels, to ensure the perfusion of the brain.

Furthermore, an investigation regarding the effect of geometrical features of the vessel was carried out under both steady-state and transient conditions. It was found that both vessel length and reference radius have a significant impact on the flow magnitude. An increase/decrease of 12.5% of the reference radius can cause increase/decrease up to $\sim 40\%$ to the flow rate within the vessel, while the length/flow relationship was proved to be linear.

Finally, the vessel model was connected to a WK model aiming to assess the interaction of the system. The results suggested that when the vessel is attached to a WK model which dominates the flow development, the active contraction causes a larger pressure drop to occur across the vessel which may aid in regulating blood flow in the region. The complete picture though would require further investigation within a network structure in order to assess the interactions between multiple actively contracted vessels and the downstream components.

Chapter 6

Conclusions and future work

This chapter provides a summary of the findings of the previous chapters, as well as general conclusions. In addition, potential paths for further research related to this work are suggested and discussed.

6.1 Summary of work

A computational tool was developed to analyse the impact of the myogenic mechanism on blood flow within a cerebral artery. This was done by taking a multi-scale approach, which considered the fluid and structural mechanics of the vessel, as well as the chemical processes that occur in the smooth muscle cells that line the vascular wall. The entire process was reproduced through distinct interconnected models that operate at different scales. The preceding chapters of the thesis provided a comprehensive description of the sub-models, either developed or adapted from existing literature, and their connection, in order to evaluate the effect of intraluminal pressure changes on the blood flow of a small cerebral artery.

In Chapter 2, the FSI framework employed is outlined. In this context, the constitutive law that outlines the pressure-area relationship of the vascular wall is discussed, which was initially designed to represent the carotid artery. As this work is intended to characterise cerebral arteries, the material parameters of the constitutive law had to be adjusted to reflect the arteries of the cerebral vasculature. Hence, an optimisation procedure was set to identify the material parameters of the constitutive law to represent the cerebral arteries. The aim was to be able to cover a wide range of arteries in terms of passive (material) response. Furthermore, since the constitutive relationship introduced anisotropy to the response, it is able to approach the response in more than one direction.

To that end, experimental data from cerebral arteries was collected from literature

and the material parameters were identified to replicate the observed behaviour. The vessels chosen for this purpose were a rabbit basilar artery, three human middle cerebral arteries, and three human pial arteries. Two of the studies were bi-axial tests, while the third was uni-axial. The optimisation process was designed to minimise the difference between the experimental measurement of the response and the model output. For bi-axial tests, only minor modifications were made to the objective function. The results obtained were in close agreement with the experimental data. The selection of species, vessel type, and experiment type was intended to demonstrate the capacity of the constitutive model to represent a wide range of responses. The identification of the parameter space for the material properties showed relatively increased deviations regarding the parameter that defined the elastic part, most probably due to the fact that the collagen fibres are dominating the response.

A novel, holistic model was developed to account for the intracellular processes that take place as a response to pressure changes in the lumen of the artery. All the details regarding the development and implementation are presented in Chapter 3, as well as its validation. Apart from the dominant calcium effect of the cross-bridge formation, the sensitisation to calcium, as well as the cytoskeletal remodelling were added to this model. This model uses a logical approach to include all the major signalling pathways involved in the myogenic mechanism, in a minimalistic manner. Experimental data were used to identify the internal model parameters through an optimisation procedure for control and two drug intervention cases in steady state conditions.

The parameter fitting yielded results that were in line with the experimental ones for the scenarios studied, despite the limited experimental data available. There was a limitation regarding the amount of available experimental data, particularly for the drug intervention cases. The model has certain restrictions due to the interconnection between secondary signalling pathways that have not been completely identified yet. However, its structural simplicity makes it easy to incorporate more pathways and extra connections.

In Chapter 4 the output of the cellular model is incorporated in a chemo-mechanical model that connects the cellular scale to the continuum one. This way, the processes that take place within the cell are translated into active vascular tone development. The vascular tone is included into the constitutive model of the first chapter as an active component in the strain-energy function, which is decoupled into active and passive parts. The wall model is then fitted against experimental data in order to represent the vessel under study.

The complete response (passive and active) to intraluminal pressure loading is then assessed under both steady state and transient conditions. The proposed

model is able to capture very well experimental data obtained under different conditions. The wall model is validated by using a vessel that is different from the one used for model parameters fitting. The model presents a very good response regarding the control case and one drug case, showing a close agreement with the experimentally measured response. There are some discrepancies regarding the second drug, and the passive case which may be related to the minimal parameters used for the material characterisation. Next, the results of the transient behaviour of the model are shown, which are in line with the expectations. Furthermore, the impact of model temporal parameters on the response is assessed. Overall, the behaviour of the vascular wall model was in line with the experimentally observed myogenic response.

Finally, in Chapter 5 all the aforementioned models are coupled with the fluid solver to assess the effect of the myogenic response on blood flow regulation. The aim was to test the model under different pressure configurations. Started with investigation the solution for an isolated vessel unaffected by upstream/downstream vasculature. The vessel model was then coupled with a Windkessel model representing the downstream circulation to assess the interaction of the system.

The model results reproduced the expected behaviour, which was similar to the cerebral blood flow regulation curves found in literature. The actively contracted vessel kept the flow level much lower than the passive one, and it managed to keep the flow fluctuations low across the whole pressure range. A qualitative validation of the flow development was conducted. The model also captures the dynamic features observed in the flow rate and lumen area changes during myogenic response. Finally, it was demonstrated that when considering downstream circulation, the myogenic response is regulating the pressure drop across the vessel so a level of perfusion is maintained.

6.2 Main limitations and future work directions

The inclusion of the autoregulation mechanisms within the cerebral circulation using multi-physics approach into an 1D haemodynamics framework could be used to provide insights into both healthy and pathological conditions. The work presented in this thesis could form the basis for a more complete representation of the cerebral arterial network towards that aim. In this final part of the thesis some future directions will be discussed, highlighting the main limitations of the proposed framework.

Regarding the cell signalling model, its main limitation is associated with the potential existence of secondary pathways that were not included in the model. Further experimental findings and evidence could guide extensions of the pro-

posed model. Furthermore, a more complete identification of intracellular concentration and phosphorylation levels, especially during drug intervention, would improve the accuracy and prediction ability of the model, shedding more light on the cell signaling during the myogenic response.

Another point that needs further investigation concerns the cell signalling and chemo-mechanical models and under transient conditions. At first, regarding the formulation of the cell signalling model, currently a single temporal parameter defines every internal variable ODE. This approach was adapted for simplicity and due to lack of data regarding the temporal response of those processes. The formulation of a single temporal parameter proved to be sufficient for the current study, providing control over the temporal scale of the contraction. However, it would be more physiologically realistic if each intracellular process was characterized by a distinct time constant. Because the model parameters are optimised against experimental data under steady state at different pressure levels, this classification would require temporal experimental evidence for these processes. Identification of the time constants of multiple intracellular processes will reduce the discrepancy between the experimentally observed transient behaviours and the simulated results.

Regarding the material model itself, there are some future directions that would provide a more accurate representation of the vascular wall. At first, it would be an interesting study to characterise the material regarding its 3D compressible behaviour. Anisotropy is introduced to the material with the consideration of the fibres. The different fibre families are altering the Poisson ratios of the model. It would be an interesting direction for the framework to assess the different Poisson ratios that are computed for different fibre families. However, this direction would also require experimental evidence for the material too. Another interesting addition to the model would be the consideration of the adventitia layer. This would be possible by considering a multi-layered structural wall. This augmentation will provide a more accurate representation of the wall since the histological analysis has shown this multi-layered structure. It is noted here that the endothelial layer has no significant contribution structural, hence it can be omitted.

Moving to the integration of the active tone to the structural mechanics of the whole vessel, the pressure-induced tone is considered uniform across the vessel. In the current formulation, the pressure at the inlet drives the development of active tone. This approach was taken for simplicity and reducing the computational cost. Moreover, for the cases tested, the node-to-node pressure difference was small. However, it could be extended to a node-wise formulation, where the pressure of each node determines the vascular tone at that location. This would be more important when considering larger vessels, increasing the accuracy.

On the fluid solver, it is reminded that the Newtonian fluid assumption was made in the context of this thesis. Although this is a suitable assumption for the scope of this thesis in terms of vessel sizes, if the intention is to study the capillary or arteriole level flow, this assumption is not valid. Hence, the employment of non-Newtonian fluid would be an interesting pathway to follow in order to study that scale and its effect on the cerebral blood flow development.

Regarding the FSI model, a more comprehensive implementation of the capillary network through lumped-parameter modelling would provide insight on how the flow regulation through myogenic response affects the flow across the capillary bed. This direction has its limitations, though, due to lack of experimental data which makes it more difficult identify the downstream vascular parameters.

After evaluating the myogenic mechanism and its effect on blood flow on a single vessel, it is natural that this could be extended to a vascular network. One of the benefits of the considered 1D flow methodology is that they can be used for studying the haemodynamics across large vascular networks. This would provide valuable insights on how the myogenic mechanism modulate each network vessel for various upstream/downstream configurations, under healthy and pathological conditions.

Bibliography

[1] M. S. Olufsen, "Structured tree outflow condition for blood flow in larger systemic arteries," *American Journal of Physiology*, vol. 276, pp. H257–H268, 1999.

[2] H. H. Lipowsky, "Microvascular rheology and hemodynamics," *Microcirculation*, vol. 12, no. 1, pp. 5–15, 2005.

[3] C. G. Caro, T. J. Pedley, R. C. Schroter, W. A. Seed, and K. H. Parker, *The Mechanics of the Circulation*. Cambridge University Press, 2nd ed., 12 2011.

[4] W. D. Tucker, Y. Arora, and K. Mahajan, *Anatomy, Blood Vessels*. StarPearls Publishing, 1 2023.

[5] P. B. Canham, H. M. Finlay, J. G. Dixon, D. R. Boughner, and A. Chen, "Measurements from light and polarised light microscopy of human coronary arteries fixed at distending pressure," *Cardiovascular Research*, vol. 23, pp. 973–982, 11 1989.

[6] H. M. Finlay, L. McCullough, and P. B. Canham, "Three-dimensional collagen organization of human brain arteries at different transmural pressures," *Journal of Vascular Research*, vol. 32, pp. 301–312, 1995.

[7] B. Alberts, A. Johnson, J. Lewis, M. Raff, K. Roberts, and P. Walter., *Molecular Biology of the Cell*. Garland Science, New York, 4th ed., 2002.

[8] J. E. Wagenseil and R. P. Mecham, "Vascular extracellular matrix and arterial mechanics," *Physiological Reviews*, vol. 89, pp. 759–1078, 2009.

[9] C. E. Gilkes and P. C. Whitfield, "Intracranial pressure and cerebral blood flow," *Surgery (Oxford)*, vol. 25, pp. 530–535, 2007.

[10] J. G. Walmsley, "Vascular smooth muscle orientation in straight portions of human cerebral arteries," *Journal of Microscopy*, vol. 131, pp. 361–375, 1983.

[11] P. B. Canham, "Orientation of cerebral vascular smooth muscle, mathematically modelled," *Journal of Biomechanics*, vol. 10, pp. 241–251, 1977.

[12] C. A. Taylor and J. D. Humphrey, "Open problems in computational vascular biomechanics: Hemodynamics and arterial wall mechanics," *Computer Methods in Applied Mechanics and Engineering*, vol. 198, pp. 3514–3523, 9 2009.

[13] G. A. Holzapfel, T. C. Gasser, and R. W. Ogden, "A new constitutive framework for arterial wall mechanics and a comparative study of material models," *Journal of Elasticity*, vol. 61, pp. 1–48, 2000.

[14] C. A. Schulze-Bauer, C. Mörth, and G. A. Holzapfel, "Passive biaxial mechanical response of aged human iliac arteries," *Journal of Biomechanical Engineering*, vol. 125, pp. 395–406, 6 2003.

[15] G. A. Holzapfel, T. C. Gasser, and M. Stadler, "A structural model for the viscoelastic behavior of arterial walls: Continuum formulation and finite element analysis," *European Journal of Mechanics - A/Solids*, vol. 21, pp. 441–463, 2002.

[16] B. M. Learoyd and M. G. Taylor, "Alterations with age in the viscoelastic properties of human arterial walls," *Circulation Research*, vol. 18, pp. 278–292, 1966.

[17] R. H. Cox, "Regional variation of series elasticity in canine arterial smooth muscles," *American Journal of Physiology-Heart and Circulatory Physiology*, vol. 234, pp. H542–H551, 1978.

[18] M. R. Roach and A. C. Burton, "The reason for the shape of the distensibility curves of arteries.," *Canadian journal of biochemistry and physiology*, vol. 35, pp. 681–690, 1957.

[19] K. Hayashi, "Experimental approaches on measuring the mechanical properties and constitutive laws of arterial walls," *Journal of Biomechanical Engineering*, vol. 115, pp. 481–488, 1993.

[20] C. J. Chuong and Y. C. Fung, "Three-dimensional stress distribution in arteries," *Journal of Biomechanical Engineering*, vol. 105, pp. 268–274, 8 1983.

[21] T. E. Carew, R. N. Vaishnav, and D. J. Patel, "Compressibility of the arterial wall," *Circulation Research*, vol. 23, pp. 61–68, 7 1968.

[22] Y.-C. Fung, *Biomechanics*. Springer New York, 2nd ed., 1993.

[23] S. E. Greenwald, E. Moore, A. Rachev, T. P. C. Kane, and J.-J. Meister, "Experimental investigation of the distribution of residual strains in the artery wall," *Journal of Biomechanical Engineering*, vol. 119, pp. 438–444, 1997.

[24] A. P. Avolio, "Multi-branched model of the human arterial system," *Biol. Eng. & Comput*, vol. 18, p. 718, 1980.

[25] J. Alastruey, K. H. Parker, J. Peiró, S. M. Byrd, and S. J. Sherwin, "Modelling the circle of willis to assess the effects of anatomical variations and occlusions on cerebral flows," *Journal of Biomechanics*, vol. 40, pp. 1794–1805, 2007.

[26] J. P. Mynard and J. J. Smolich, "One-dimensional haemodynamic modeling and wave dynamics in the entire adult circulation," *Annals of Biomedical Engineering*, vol. 43, pp. 1443–1460, 6 2015.

[27] C. Mimata, M. Kitaoka, S. Nagahiro, K.-I. Iyama, H. Hori, H. Yoshioka, and Y. Ushio, "Differential distribution and expressions of collagens in the cerebral aneurysmal wall," *Acta Neuropathologica*, vol. 94, pp. 197–206, 1997.

[28] R. M. K. W. Lee, "Morphology of cerebral arteries," *Pharmacology and Therapeutics*, vol. 66, pp. 149–173, 1995.

[29] H. M. Finlay, P. Whittaker, and P. B. Canham, "Collagen organization in the branching region of human brain arteries," *Stroke*, vol. 29, pp. 1595–1601, 1998.

[30] T. Kulik, Y. Kusano, S. Aronhime, A. L. Sandler, and H. R. Winn, "Regulation of cerebral vasculature in normal and ischemic brain," *Neuropharmacology*, vol. 55, pp. 281–288, 9 2008.

[31] A. J. Rowe, H. M. Finlay, and P. B. Canham, "Collagen biomechanics in cerebral arteries and bifurcations assessed by polarizing microscopy," *Journal of Vascular Research*, vol. 40, pp. 406–415, 2003.

[32] F. . B. Canham, E. A. Talman, H. M. Finlay, and J. G. Dixon, "Medial collagen organization in human arteries of the heart and brain by polarized light microscopy," *Connective Tissue Research*, vol. 26, pp. 121–134, 1991.

[33] K. Hayashi, H. Handa, S. Nagasawa, A. Okumura, and K. Moritake, "Stiffness and elastic behavior of human intracranial and extracranial arteries," *Journal of Biomechanics*, vol. 13, pp. 175–184, 1980.

[34] J. A. Claassen, D. H. Thijssen, R. B. Panerai, and F. M. Faraci, "Regulation of cerebral blood flowin humans: Physiology and clinical implications of autoregulation," *Physiological Reviews*, vol. 101, pp. 1487–1559, 10 2021.

[35] J. A. H. R. Claassen, R. Zhang, Q. Fu, S. Witkowski, and B. D. Levine, "Transcranial doppler estimation of cerebral blood flow and cerebrovascular conductance during modified rebreathing," *Journal of Applied Physiology*, vol. 102, pp. 870–877, 3 2007.

[36] H. Girouard and C. Iadecola, "Neurovascular coupling in the normal brain and in hypertension, stroke, and alzheimer disease," *Journal of Applied Physiology*, vol. 100, pp. 328–335, 1 2006.

[37] S. Fantini, A. Sassaroli, K. T. Tgavalekos, and J. Kornbluth, "Cerebral blood flow and autoregulation: current measurement techniques and prospects for noninvasive optical methods," *Neurophotonics*, vol. 3, p. 031411, 6 2016.

[38] Y. C. Tzeng and P. N. Ainslie, "Blood pressure regulation ix: Cerebral autoregulation under blood pressure challenges," *European Journal of Applied Physiology*, vol. 114, pp. 545–559, 3 2014.

[39] R. B. Panerai, "Assessment of cerebral pressure autoregulation in humans - a review of measurement methods," *Physiological Measurement*, vol. 19, pp. 305–338, 1998.

[40] H. A. Kontos, "Regulation of the cerebral circulation," *Annual Review of Physiology*, vol. 43, pp. 397–407, 10 1981.

[41] C. Iadecola, "Neurovascular regulation in the normal brain and in alzheimer's disease," *Nature Reviews Neuroscience*, vol. 5, pp. 347–360, 5 2004.

[42] N. Herring and D. J. Paterson, *Levick's Introduction Cardiovascular Physiology*. CRC Press, 6th ed., 2018.

[43] M. Mederos Y Schnitzler, U. Storch, S. Meibers, P. Nurwakagari, A. Breit, K. Essin, M. Gollasch, and T. Gudermann, "Gq-coupled receptors as mechanosensors mediating myogenic vasoconstriction," *EMBO Journal*, vol. 27, pp. 3092–3103, 12 2008.

[44] P. W. Pires, E. A. Ko, H. A. Pritchard, M. Rudokas, E. Yamasaki, and S. Earley, "The angiotensin ii receptor type 1b is the primary sensor of intraluminal pressure in cerebral artery smooth muscle cells," *Journal of Physiology*, vol. 595, pp. 4735–4753, 7 2017.

[45] Y. Cui, M. Kassmann, S. Nickel, C. Zhang, N. Alenina, Y. M. Anistan, J. Schleifenbaum, M. Bader, D. G. Welsh, Y. Huang, and M. Gollasch, "Myogenic vasoconstriction requires canonical gq/11 signaling of the angiotensin ii type 1 receptor," *Journal of the American Heart Association*, vol. 11, 2 2022.

[46] A. Horowitz, C. B. Menice, and K. G. Morgan, "Mechanisms of smooth muscle contraction," *Physiological Reviews*, vol. 76, pp. 967–1003, 1996.

[47] S. I. Murtada, M. Kroon, and G. A. Holzapfel, "A calcium-driven mechanochemical model for prediction of force generation in smooth muscle," *Biomechanics and Modeling in Mechanobiology*, vol. 9, pp. 749–762, 12 2010.

[48] S. Chrissobolis and C. G. Sobey, "Evidence that rho-kinase activity contributes to cerebral vascular tone in vivo and is enhanced during chronic hypertension comparison with protein kinase c," *Circulation Research*, vol. 88, pp. 774–779, 2001.

[49] M. J. Cipolla, N. I. Gokina, and G. Osol, "Pressure-induced actin polymerization in vascular smooth muscle as a mechanism underlying myogenic behavior," *The FASEB Journal*, vol. 16, pp. 72–76, 1 2002.

[50] Y. C. Fung, K. Fronek, and P. Patitucci, "Pseudoelasticity of arteries and of its mathematical expression the choice," *American Journal of Physiology-Heart and Circulatory Physiology*, vol. 237, pp. H620–H631, 1979.

[51] J. D. Humphrey, "Mechanics of the arterial wall: Review and directions," *Critical Reviews in Biomedical Engineering*, vol. 23, pp. 1–162, 1995.

[52] V. A. Kas'yanov and A. Rachev, "Deformation of blood vessels upon stretching, internal pressure, and torsion," *Mechanics of Composite Materials*, vol. 16, pp. 76–80, 1980.

[53] S. X. Deng, J. Tomioka, J. C. Debes, and Y. C. Fung, "New experiments on shear modulus of elasticity of arteries," *American Journal of Physiology*, vol. 266, pp. H1–H10, 1994.

[54] G. A. Holzapfel, G. Sommer, C. T. Gasser, and P. Regitnig, "Determination of layer-specific mechanical properties of human coronary arteries with nonatherosclerotic intimal thickening and related constitutive modeling," *Am J Physiol Heart Circ Physiol*, vol. 289, pp. 2048–2058, 2005.

[55] V. Alastrué, E. Peña, M. A. Martínez, and M. Doblaré, "Experimental study and constitutive modelling of the passive mechanical properties of

the ovine infrarenal vena cava tissue," *Journal of Biomechanics*, vol. 41, pp. 3038–3045, 10 2008.

[56] P. Ciarletta, P. Dario, F. Tendick, and S. Micera, "Hyperelastic model of anisotropic fiber reinforcements within intestinal walls for applications in medical robotics," *International Journal of Robotics Research*, vol. 28, pp. 1279–1288, 2009.

[57] R. Eberlein, G. A. Holzapfel, and M. Fröhlich, "Multi-segment fea of the human lumbar spine including the heterogeneity of the annulus fibrosus," *Computational Mechanics*, vol. 34, 7 2004.

[58] G. A. Holzapfel and R. W. Ogden, "Constitutive modelling of passive myocardium: A structurally based framework for material characterization," *Philosophical Transactions of the Royal Society A: Mathematical, Physical and Engineering Sciences*, vol. 367, pp. 3445–3475, 9 2009.

[59] I. Karšaj, C. Sansour, and J. Sorić, "The modelling of fibre reorientation in soft tissue," *Biomechanics and Modeling in Mechanobiology*, vol. 8, pp. 359–370, 10 2009.

[60] T. C. Gasser and G. A. Holzapfel, "A rate-independent elastoplastic constitutive model for biological fiber-reinforced composites at finite strains: Continuum basis, algorithmic formulation and finite element implementation," *Computational Mechanics*, vol. 29, pp. 340–360, 2002.

[61] E. Peña, B. Calvo, M. A. Martínez, and M. Doblaré, "On finite-strain damage of viscoelastic-fibred materials. application to soft biological tissues," *International Journal for Numerical Methods in Engineering*, vol. 74, pp. 1198–1218, 5 2008.

[62] E. Peña, M. A. Martínez, B. Calvo, and M. Doblaré, "Application of the natural element method to finite deformation inelastic problems in isotropic and fiber-reinforced biological soft tissues," *Computer Methods in Applied Mechanics and Engineering*, vol. 197, pp. 1983–1996, 4 2008.

[63] J. Stålhand, "Determination of human arterial wall parameters from clinical data," *Biomechanics and Modeling in Mechanobiology*, vol. 8, pp. 141–148, 4 2009.

[64] I. Masson, P. Boutouyrie, S. Laurent, J. D. Humphrey, and M. Zidi, "Characterization of arterial wall mechanical behavior and stresses from human clinical data," *Journal of Biomechanics*, vol. 41, pp. 2618–2627, 8 2008.

[65] S. Baek, R. L. Gleason, K. R. Rajagopal, and J. D. Humphrey, "Theory of small on large: Potential utility in computations of fluid-solid interactions in arteries," *Computer Methods in Applied Mechanics and Engineering*, vol. 196, pp. 3070–3078, 6 2007.

[66] S. Zeinali-Davarani, J. Choi, and S. Baek, "On parameter estimation for biaxial mechanical behavior of arteries," *Journal of Biomechanics*, vol. 42, pp. 524–530, 3 2009.

[67] H. P. Wagner and J. D. Humphrey, "Differential passive and active biaxial mechanical behaviors of muscular and elastic arteries: Basilar versus common carotid," *Journal of Biomechanical Engineering*, vol. 133, pp. 1–11, 2011.

[68] H. Y. Chen, J. A. Navia, and G. S. Kassab, "A simulation of vessel-clamp interaction: Transient closure dynamics," *Annals of Biomedical Engineering*, vol. 37, pp. 1772–1780, 9 2009.

[69] G. A. Holzapfel, M. Stadler, and C. A. Schulze-Bauer, "A layer-specific three-dimensional model for the simulation of balloon angioplasty using magnetic resonance imaging and mechanical testing," *Annals of Biomedical Engineering*, vol. 30, pp. 753–767, 2002.

[70] D. E. Kiousis, T. C. Gasser, and G. A. Holzapfel, "A numerical model to study the interaction of vascular stents with human atherosclerotic lesions," *Annals of Biomedical Engineering*, vol. 35, pp. 1857–1869, 11 2007.

[71] T. C. Gasser and G. A. Holzapfel, "Finite element modeling of balloon angioplasty by considering overstretch of remnant non-diseased tissues in lesions," *Computational Mechanics*, vol. 40, pp. 47–60, 2007.

[72] J. F. Rodríguez, V. Alastrue, and M. Doblare, "Finite element implementation of a stochastic three dimensional finite-strain damage model for fibrous soft tissue," *Computer Methods in Applied Mechanics and Engineering*, vol. 197, pp. 946–958, 2 2008.

[73] M. Kroon and G. A. Holzapfel, "Modeling of saccular aneurysm growth in a human middle cerebral artery," *Journal of Biomechanical Engineering*, vol. 130, 10 2008.

[74] J. Lu, X. Zhou, and M. L. Raghavan, "Computational method of inverse elastostatics for anisotropic hyperelastic solids," *International Journal for Numerical Methods in Engineering*, vol. 69, pp. 1239–1261, 2 2007.

[75] J. F. Rodríguez, G. Martufi, M. Doblaré, and E. A. Finol, "The effect of material model formulation in the stress analysis of abdominal aortic aneurysms," *Annals of Biomedical Engineering*, vol. 37, pp. 2218–2221, 11 2009.

[76] I. Hariton, G. deBotton, T. C. Gasser, and G. A. Holzapfel, "Stress-modulated collagen fiber remodeling in a human carotid bifurcation," *Journal of Theoretical Biology*, vol. 248, pp. 460–470, 10 2007.

[77] I. Hariton, G. DeBotton, T. C. Gasser, and G. A. Holzapfel, "Stress-driven collagen fiber remodeling in arterial walls," *Biomechanics and Modeling in Mechanobiology*, vol. 6, pp. 163–175, 4 2007.

[78] P. W. Alford, J. D. Humphrey, and L. A. Taber, "Growth and remodeling in a thick-walled artery model: Effects of spatial variations in wall constituents," *Biomechanics and Modeling in Mechanobiology*, vol. 7, pp. 245–262, 8 2008.

[79] A. Valentín and J. D. Humphrey, "Parameter sensitivity study of a constrained mixture model of arterial growth and remodeling," *Journal of Biomechanical Engineering*, vol. 131, 10 2009.

[80] A. V. Hill, "The heat of shortening and the dynamic constants of muscle," *Proceedings of the Royal Society B*, vol. 126, pp. 136–195, 1938.

[81] S. Gestrelius and P. Borgström, "A dynamic model of smooth muscle contraction," *Biophysical Journal*, vol. 50, pp. 157–169, 1986.

[82] B. E. Carlson and T. W. Secomb, "A theoretical model for the myogenic response based on the length-tension characteristics of vascular smooth muscle," *Microcirculation*, vol. 12, pp. 327–338, 6 2005.

[83] A. Rachev and K. Hayashi, "Theoretical study of the effects of vascular smooth muscle contraction on strain and stress distributions in arteries," *Annals of Biomedical Engineering*, vol. 27, pp. 459–468, 1999.

[84] M. A. Zulliger, A. Rachev, and N. Stergiopulos, "A constitutive formulation of arterial mechanics including vascular smooth muscle tone," *Am J Physiol Heart Circ Physiol*, vol. 287, pp. 1335–1343, 2004.

[85] C. M. Hai and R. A. Murphy, "Cross-bridge phosphorylation and regulation of latch state in smooth muscle," *American Journal of Physiology*, vol. 254, pp. 99–106, 1988.

[86] J. Yang, J. W. Clark, R. M. Bryan, and C. S. Robertson, "The myogenic response in isolated rat cerebrovascular arteries: Vessel model," *Medical Engineering and Physics*, vol. 25, pp. 711–717, 2003.

[87] A. Schmitz and M. Böl, "On a phenomenological model for active smooth muscle contraction," *Journal of Biomechanics*, vol. 44, pp. 2090–2095, 7 2011.

[88] S. I. Murtada, S. Lewin, A. Arner, and J. D. Humphrey, "Adaptation of active tone in the mouse descending thoracic aorta under acute changes in loading," *Biomechanics and Modeling in Mechanobiology*, vol. 15, pp. 579–592, 6 2016.

[89] A. Quarteroni, M. Tuveri, and A. Veneziani, "Computing and visualization in science computational vascular fluid dynamics: problems, models and methods," *Comput Visual Sci*, vol. 2, pp. 163–197, 2000.

[90] J. F. Gerbeau, M. Vidrascu, and P. Frey, "Fluid-structure interaction in blood flows on geometries based on medical imaging," *Computers and Structures*, vol. 83, pp. 155–165, 2005.

[91] R. Torii, N. B. Wood, N. Hadjiloizou, A. W. Dowsey, A. R. Wright, A. D. Hughes, J. Davies, D. P. Francis, J. Mayet, G. Z. Yang, S. A. G. Thom, and X. Y. Xu, "Fluid-structure interaction analysis of a patient-specific right coronary artery with physiological velocity and pressure waveforms," *Communications in Numerical Methods in Engineering*, vol. 25, pp. 565–580, 2009.

[92] A. Valencia, P. Burdiles, M. Ignat, J. Mura, E. Bravo, R. Rivera, and J. Sordo, "Fluid structural analysis of human cerebral aneurysm using their own wall mechanical properties," *Computational and Mathematical Methods in Medicine*, vol. 2013, 2013.

[93] S. Miyazaki, K. Itatani, T. Furusawa, T. Nishino, M. Sugiyama, Y. Takehara, and S. Yasukochi, "Validation of numerical simulation methods in aortic arch using 4d flow mri," *Heart and Vessels*, vol. 32, pp. 1032–1044, 8 2017.

[94] R. J. van der Geest and P. Garg, "Advanced analysis techniques for intracardiac flow evaluation from 4d flow mri," *Current Radiology Reports*, vol. 4, 7 2016.

[95] J. Luo and E. E. Konofagou, "Imaging of wall motion coupled with blood flow velocity in the heart and vessels in vivo: A feasibility study," *Ultrasound in Medicine and Biology*, vol. 37, pp. 980–995, 6 2011.

[96] J. Alastruey, N. Xiao, H. Fok, T. Schaeffter, and C. A. Figueroa, "On the impact of modelling assumptions in multi-scale, subject-specific models of aortic haemodynamics," *Journal of the Royal Society Interface*, vol. 13, 6 2016.

[97] J. P. Mynard and P. Nithiarasu, "A 1d arterial blood flow model incorporating ventricular pressure, aortic valve and regional coronary flow using the locally conservative galerkin (lcg) method," *Communications in Numerical Methods in Engineering*, vol. 24, pp. 367–417, 5 2008.

[98] J. P. Mynard and J. J. Smolich, "Influence of anatomical dominance and hypertension on coronary conduit arterial and microcirculatory flow patterns: a multiscale modeling study," *Am J Physiol Heart Circ Physiol*, vol. 311, pp. 11–23, 2016.

[99] A. Coccarelli, E. Boileau, D. Parthimos, and P. Nithiarasu, "An advanced computational bioheat transfer model for a human body with an embedded systemic circulation," *Biomechanics and Modeling in Mechanobiology*, vol. 15, pp. 1173–1190, 10 2016.

[100] J. M. Carson, M. Lewis, D. Rassi, and R. Van Loon, "A data-driven model to study utero-ovarian blood flow physiology during pregnancy," *Biomechanics and Modeling in Mechanobiology*, vol. 18, pp. 1155–1176, 8 2019.

[101] P. J. Blanco, S. M. Watanabe, M. A. R. Passos, P. A. Lemos, and R. A. Feijóo, "An anatomically detailed arterial network model for one-dimensional computational hemodynamics," *IEEE Transactions on Biomedical Engineering*, vol. 62, pp. 736–753, 2 2015.

[102] T. J. R. Hughes and J. Lubliner, "On the one-dimensional theory of blood flow in the larger vessels," *Mathematical Biosciences*, vol. 18, pp. 161–170, 1973.

[103] N. Stergiopulos, D. F. Young, and T. R. Rowe, "Computer simulation of arterial flow with applications to arterial and aortic stenoses," *Journal of Biomechanics*, vol. 25, pp. 1477–1488, 1992.

[104] P. Reymond, Y. Bohraus, F. Perren, F. Lazeyras, and N. Stergiopulos, "Validation of a patient-specific one-dimensional model of the systemic arterial tree," *Am J Physiol Heart Circ Physiol*, vol. 301, pp. 1173–1182, 2011.

[105] L. Formaggia, D. Lamponi, and A. Quarteroni, "One-dimensional models for blood flow in arteries," *Journal of Engineering Mathematics*, vol. 47, pp. 251–276, 2003.

[106] S. J. Sherwin, V. Franke, J. Peiró, and K. Parker, "One-dimensional modelling of a vascular network in space-time variables," *Journal of Engineering Mathematics*, vol. 47, pp. 217–250, 2003.

[107] J. Alastruey, A. W. Khir, K. S. Matthys, P. Segers, S. J. Sherwin, P. R. Verdonck, K. H. Parker, and J. Peiró, "Pulse wave propagation in a model human arterial network: Assessment of 1-d visco-elastic simulations against in vitro measurements," *Journal of Biomechanics*, vol. 44, pp. 2250–2258, 8 2011.

[108] L. R. Hellevik, J. Vierendeels, T. Kiserud, N. Stergiopulos, F. Irgens, E. Dick, K. Riemslagh, and P. Verdonck, "An assessment of ductus venosus tapering and wave transmission from the fetal heart," *Biomechanics and Modeling in Mechanobiology*, vol. 8, pp. 509–517, 12 2009.

[109] S. J. Sherwin, L. Formaggia, J. Peiró, and V. Franke, "Computational modelling of 1d blood flow with variable mechanical properties and its application to the simulation of wave propagation in the human arterial system," *International Journal for Numerical Methods in Fluids*, vol. 43, pp. 673–700, 10 2003.

[110] L. O. Müller and E. F. Toro, "Well-balanced high-order solver for blood flow in networks of vessels with variable properties," *International Journal for Numerical Methods in Biomedical Engineering*, vol. 29, pp. 1388–1411, 12 2013.

[111] M. S. Olufsen, C. S. Peskin, W. Y. Kim, E. M. Pedersen, A. Nadim, and J. Larsen, "Numerical simulation and experimental validation of blood flow in arteries with structured-tree outflow conditions," *Annals of Biomedical Engineering*, vol. 28, pp. 1281–1299, 2000.

[112] M. Saito, Y. Ikenaga, M. Matsukawa, Y. Watanabe, T. Asada, and P. Y. Lagrée, "One-dimensional model for propagation of a pressure wave in a model of the human arterial network: Comparison of theoretical and experimental results," *Journal of Biomechanical Engineering*, vol. 133, 2011.

[113] A. Caiazzo, G. Montecinos, L. O. Müller, E. M. Haacke, and E. F. Toro, "Computational haemodynamics in stenotic internal jugular veins," *Journal of Mathematical Biology*, vol. 70, pp. 745–772, 3 2015.

[114] A. Quarteroni, A. Manzoni, and C. Vergara, "The cardiovascular system: Mathematical modelling, numerical algorithms and clinical applications," *Acta Numerica*, vol. 26, pp. 365–590, 5 2017.

[115] D. Valdez-Jasso, M. A. Haider, H. T. Banks, D. B. Santana, Y. Z. Germán, R. L. Armentano, and M. S. Olufsen, "Analysis of viscoelastic wall properties in ovine arteries," *IEEE Transactions on Biomedical Engineering*, vol. 56, pp. 210–219, 2 2009.

[116] D. Bessems, C. G. Giannopapa, M. C. Rutten, and F. N. van de Vosse, "Experimental validation of a time-domain-based wave propagation model of blood flow in viscoelastic vessels," *Journal of Biomechanics*, vol. 41, pp. 284–291, 2008.

[117] P. Reymond, F. Merenda, F. Perren, D. Rü, and N. Stergiopulos, "Validation of a one-dimensional model of the systemic arterial tree," *Am J Physiol Heart Circ Physiol*, vol. 297, pp. 208–222, 2009.

[118] S. Čanić, J. Tambača, G. Guidoboni, A. Mikelić, C. J. Hartley, and D. Rosenstrauch, "Modeling viscoelastic behavior of arterial walls and their interaction with pulsatile blood flow," *SIAM Journal on Applied Mathematics*, vol. 67, no. 1, pp. 164–193, 2006.

[119] G. Bertaglia, V. Caleffi, and A. Valiani, "Modeling blood flow in viscoelastic vessels: the 1d augmented fluid–structure interaction system," *Computer Methods in Applied Mechanics and Engineering*, vol. 360, 3 2020.

[120] Y. S. Vahedein and A. S. Liberson, "Cardiofan: open source platform for noninvasive assessment of pulse transit time and pulsatile flow in hyperelastic vascular networks," *Biomechanics and Modeling in Mechanobiology*, vol. 18, pp. 1529–1548, 10 2019.

[121] A. R. Ghigo, X. F. Wang, R. Armentano, J. M. Fullana, and P. Y. Lagrée, "Linear and nonlinear viscoelastic arterial wall models: Application on animals," *Journal of Biomechanical Engineering*, vol. 139, 1 2017.

[122] G. I. Montecinos, L. O. Müller, and E. F. Toro, "Hyperbolic reformulation of a 1d viscoelastic blood flow model and ader finite volume schemes," *Journal of Computational Physics*, vol. 266, pp. 101–123, 6 2014.

[123] A. Coccarelli, J. M. Carson, A. Aggarwal, and S. Pant, "A framework for incorporating 3d hyperelastic vascular wall models in 1d blood flow simulations," *Biomechanics and Modeling in Mechanobiology*, vol. 20, pp. 1231–1249, 8 2021.

[124] K. Uhlmann and D. Balzani, "Chemo-mechanical modeling of smooth muscle cell activation for the simulation of arterial walls under changing blood pressure," *Biomechanics and Modeling in Mechanobiology*, vol. 22, pp. 1049–1065, 6 2023.

[125] J. M. Carson, *Development of a cardiovascular and lymphatic network model during human pregnancy.* PhD thesis, Swansea Universsity, 2019.

[126] T. Omori, Y. Imai, K. Kikuchi, T. Ishikawa, and T. Yamaguchi, "Hemodynamics in the microcirculation and in microfluidics," *Annals of Biomedical Engineering*, vol. 43, no. 1, pp. 238–257, 2014.

[127] S. A. Urquiza, P. J. Blanco, M. J. Vénere, and R. A. Feijóo, "Multidimensional modelling for the carotid artery blood flow," *Computer Methods in Applied Mechanics and Engineering*, vol. 195, pp. 4002–4017, 7 2006.

[128] L. O. Müller and E. F. Toro, "A global multiscale mathematical model for the human circulation with emphasis on the venous system," *International Journal for Numerical Methods in Biomedical Engineering*, vol. 30, pp. 681–725, 2014.

[129] W. Kroon, W. Huberts, M. Bosboom, and F. V. D. Vosse, "A numerical method of reduced complexity for simulating vascular hemodynamics using coupled 0d lumped and 1d wave propagation models," *Computational and Mathematical Methods in Medicine*, vol. 2012, 2012.

[130] D. Bessems, M. Rutten, and F. Van De Vosse, "A wave propagation model of blood flow in large vessels using an approximate velocity profile function," *Journal of Fluid Mechanics*, vol. 580, p. 145–168, 2007.

[131] J. Alastruey, T. Passerini, L. Formaggia, and J. Peiró, "Physical determining factors of the arterial pulse waveform: Theoretical analysis and calculation using the 1-d formulation," *Journal of Engineering Mathematics*, vol. 77, pp. 19–37, 12 2012.

[132] E. Boileau, P. Nithiarasu, P. J. Blanco, L. O. Müller, F. E. Fossan, L. R. Hellevik, W. P. Donders, W. Huberts, M. Willemet, and J. Alastruey, "A benchmark study of numerical schemes for one-dimensional arterial blood flow modelling," *International Journal for Numerical Methods in Biomedical Engineering*, vol. 31, pp. 1–33, 10 2015.

[133] N. P. Smith, A. J. Pullan, and P. J. Hunter, "An anatomically based model of transient coronary blood flow in the heart," *SIAM Journal on Applied Mathematics*, vol. 62, pp. 990–1018, 2002.

[134] S. Čanić, "Blood flow through compliant vessels after endovascular repair: wall deformations induced by the discontinuous wall properties," *Computing and Visualization in Science*, vol. 4, pp. 147–155, 2002.

[135] N. Westerhof, N. Stergiopulos, and M. I. Noble, *Snapshots of Hemodynamics.* Springer US, 2010.

[136] G. Sommer, P. Regitnig, L. Költringer, and G. A. Holzapfel, "Biaxial mechanical properties of intact and layer-dissected human carotid arteries at physiological and supraphysiological loadings," *Am J Physiol Heart Circ Physiol*, vol. 298, pp. 898–912, 2010.

[137] G. Sommer and G. A. Holzapfel, "3d constitutive modeling of the biaxial mechanical response of intact and layer-dissected human carotid arteries," *Journal of the Mechanical Behavior of Biomedical Materials*, vol. 5, pp. 116–128, 1 2012.

[138] K. L. Monson, N. M. Barbaro, and G. T. Manley, "Biaxial response of passive human cerebral arteries," *Annals of Biomedical Engineering*, vol. 36, pp. 2028–2041, 12 2008.

[139] H. P. Wagner, *Mechanical Characterization, Modeling, and Examination of a Muscular Intercranial and Elastic Extracranial Artery with an Emphasis in Microstructure, Residual Stress, and Smooth Muscle Cell Activation.* PhD thesis, Texas A&M University, 2011.

[140] T. C. Gasser, R. W. Ogden, and G. A. Holzapfel, "Hyperelastic modelling of arterial layers with distributed collagen fibre orientations," *Journal of the Royal Society Interface*, vol. 3, pp. 15–35, 2 2006.

[141] G. A. Holzapfel and T. C. Gasser, "Computational stress-deformation analysis of arterial walls including high-pressure response," *International Journal of Cardiology*, vol. 116, pp. 78–85, 3 2007.

[142] F. Auricchio, M. Conti, and A. Ferrara, "How constitutive model complexity can affect the capability to fit experimental data: A focus on human carotid arteries and extension/inflation data," *Archives of Computational Methods in Engineering*, vol. 21, pp. 273–292, 2014.

[143] G. A. Holzapfel and R. W. Ogden, "Constitutive modelling of arteries," *Proceedings of the Royal Society A: Mathematical, Physical and Engineering Sciences*, vol. 466, pp. 1551–1597, 6 2010.

[144] S. I. Murtada and G. A. Holzapfel, "Investigating the role of smooth muscle cells in large elastic arteries: A finite element analysis," *Journal of Theoretical Biology*, vol. 358, pp. 1–10, 10 2014.

[145] X. Liu, Z. Gao, H. Xiong, D. Ghista, L. Ren, H. Zhang, W. Wu, W. Huang, and W. K. Hau, "Three-dimensional hemodynamics analysis of the circle of willis in the patient-specific nonintegral arterial structures," *Biomechanics and Modeling in Mechanobiology*, vol. 15, pp. 1439–1456, 12 2016.

[146] A. Melis, F. Moura, I. Larrabide, K. Janot, R. H. Clayton, A. P. Narata, and A. Marzo, "Improved biomechanical metrics of cerebral vasospasm identified via sensitivity analysis of a 1d cerebral circulation model," *Journal of Biomechanics*, vol. 90, pp. 24–32, 6 2019.

[147] N. Westerhof, P. Sipkema, G. C. V. D. Bos, and G. Elzinga, "Forward and backward waves in the arterial system," *Cardiovascular Research*, vol. 6, pp. 648–656, 1972.

[148] N. Westerhof, F. Bosman, C. J. D. Vries, and A. Noordergraaf, "Analog studies of the human systemic arterial tree," *Journal of Biomechanics*, vol. 2, pp. 121–143, 1969.

[149] J. M. Carson and R. Van Loon, "An implicit solver for 1d arterial network models," *International Journal for Numerical Methods in Biomedical Engineering*, vol. 33, pp. 1–16, 2017.

[150] N. Thorin-Trescases, T. Bartolotta, N. Hyman, P. L. Penar, C. L. Walters, R. D. Bevan, and J. A. Bevan, "Diameter dependence of myogenic tone of human pial arteries: Possible relation to distensibility," *Stroke*, vol. 28, pp. 2486–2492, 1997.

[151] H. J. Knot and M. T. Nelson, "Regulation of arterial diameter and wall [ca2+] in cerebral arteries of rat by membrane potential and intravascular pressure," *Journal of Physiology*, vol. 501, pp. 199–209, 1998.

[152] H. J. Knot, N. B. Standen, and M. T. Nelson, "Ryanodine receptors regulate arterial diameter and wall [ca2+] in cerebral arteries of rat via ca2+-dependent k+ channels," *Journal of Physiology*, vol. 508, pp. 211–221, 1998.

[153] J. A. Bevan, J. Dodge, C. L. Walters, T. Wellman, and R. D. Bevan, "As human pial arteries (internal diameter 200-1000μm) get smaller, their wall thickness and capacity to develop tension relative to their diameter increase," *Life Sciences*, vol. 65, pp. 1153–1161, 1999.

[154] D. Nakagawa, M. Shojima, M. Yoshino, T. Kin, H. Imai, S. Nomura, T. Saito, H. Nakatomi, H. Oyama, and N. Saito, "Wall-to-lumen ratio of intracranial arteries measured by indocyanine green angiography," *Asian Journal of Neurosurgery*, vol. 11, pp. 361–364, 12 2016.

[155] C. J. Chuong and Y. C. Fung, "On residual stresses in arteries," *Journal of Biomechanical Engineering*, vol. 108, pp. 189–192, 1986.

[156] J. H. Cheng, L. F. Zhang, F. Gao, Y. G. Bai, M. Boscolo, X. F. Huang, and X. Zhang, "Mechanics and composition of middle cerebral arteries from

simulated microgravity rats with and without 1-h/d -gx gravitation," *PLoS ONE*, vol. 9, 5 2014.

[157] J. M. Diaz-Otero, H. Garver, G. D. Fink, W. F. Jackson, and A. M. Dorrance, "Aging is associated with changes to the biomechanical properties of the posterior cerebral artery and parenchymal arterioles," *Am J Physiol Heart Circ Physiol*, vol. 310, pp. 365–375, 2016.

[158] M. Mandalà, A. L. Pedatella, S. M. Palomares, M. J. Cipolla, and G. Osol, "Maturation is associated with changes in rat cerebral artery structure, biomechanical properties and tone," *Acta Physiologica*, vol. 205, pp. 363–371, 7 2012.

[159] T. Tropea and M. Mandalà, "Caloric restriction enhances vascular tone of cerebral and mesenteric resistance arteries in aged rats," *Mechanisms of Ageing and Development*, vol. 197, 7 2021.

[160] E. D. Bell, R. S. Kunjir, and K. L. Monson, "Biaxial and failure properties of passive rat middle cerebral arteries," *Journal of Biomechanics*, vol. 46, pp. 91–96, 1 2013.

[161] R. L. Gleason, E. Wilson, and J. D. Humphrey, "Biaxial biomechanical adaptations of mouse carotid arteries cultured at altered axial extension," *Journal of Biomechanics*, vol. 40, pp. 766–776, 2007.

[162] K. Takamizawa and K. Hayashi, "Strain energy density function and uniform strain hypothesis for arterial mechanics," *Journal of Biomechanics*, vol. 20, no. 1, pp. 7–17, 1987.

[163] J. K. Farrar and M. R. Roach, "The effects of increased intracranial pressure on flow through major cerebral arteries in vitro," *Stroke*, vol. 4, pp. 795–806, 1973.

[164] A. A. Harteveld, N. P. Denswil, W. V. Hecke, H. J. Kuijf, A. Vink, W. G. Spliet, M. J. Daemen, P. R. Luijten, J. J. Zwanenburg, J. Hendrikse, and A. G. van der Kolk, "Data on vessel wall thickness measurements of intracranial arteries derived from human circle of willis specimens," *Data in Brief*, vol. 19, pp. 6–12, 8 2018.

[165] L. O. Müller, S. M. Watanabe, E. F. Toro, R. A. Feijóo, and P. J. Blanco, "An anatomically detailed arterial-venous network model. cerebral and coronary circulation," *Frontiers in Physiology*, vol. 14, 2023.

[166] Q. Li, Y. Muragaki, I. Hatamura, H. Ueno, and A. Ooshima, "Stretch-induced collagen synthesis in cultured smooth muscle cells from rabbit aortic media and a possible involvement of angiotensin ii and transforming

growth factor-beta," *Journal of vascular research*, vol. 35, no. 2, p. 93—103, 1998.

[167] H. Huxley and J. Hanson, "Changes in the cross-striations of muscle during contraction and stretch and their structural interpretation," *Nature*, vol. 173, pp. 973–976, 1954.

[168] A. F. Huxley and R. Niedergerke, "Interference microscopy of living muscle fibres," *Nature*, vol. 173, pp. 971–973, 1954.

[169] A. M. Herrera, B. E. McParland, A. Bienkowska, R. Tait, P. D. Paré, and C. Y. Seow, "'sarcomeres' of smooth muscle: Functional characteristics and ultrastructural evidence," *Journal of Cell Science*, vol. 118, pp. 2381–2392, 6 2005.

[170] W. F. Jackson, "Calcium-dependent ion channels and the regulation of arteriolar myogenic tone," *Frontiers in Physiology*, vol. 12, 11 2021.

[171] A. Huxley and R. M. Simmons, "Proposed mechanism of force generation in striated muscle," *Nature*, vol. 233, pp. 533–538, 1971.

[172] D. Parthimos, D. H. Edwards, and T. M. Griffith, "Minimal model of arterial chaos generated by coupledintracellular and membrane ca2+ oscillators," *Heart Circ. Physiol*, vol. 46, pp. 1119–1144, 1999.

[173] J. Yang, J. W. Clark, R. M. Bryan, and C. S. Robertson, "The myogenic response in isolated rat cerebrovascular arteries: Smooth muscle cell model," *Medical Engineering and Physics*, vol. 25, pp. 691–709, 2003.

[174] A. Coccarelli, D. H. Edwards, A. Aggarwal, P. Nithiarasu, and D. Parthimos, "A multiscale active structural model of the arterial wall accounting for smooth muscle dynamics," *Journal of the Royal Society Interface*, vol. 15, 2018.

[175] S. C. Murtada, A. Arner, and G. A. Holzapfel, "Experiments and mechanochemical modeling of smooth muscle contraction: Significance of filament overlap," *Journal of Theoretical Biology*, vol. 297, pp. 176–186, 3 2012.

[176] G. Osol, J. F. Brekke, K. Mcelroy-Yaggy, and N. I. Gokina, "Myogenic tone, reactivity, and forced dilatation: a three-phase model of in vitro arterial myogenic behavior," *Am J Physiol Heart Circ Physiol*, vol. 283, pp. 2260–2267, 2002.

[177] R. P. Johnson, A. F. El-yazbi, K. Takeya, E. J. Walsh, M. P. Walsh, and W. C. Cole, "Ca2+ sensitization via phosphorylation of myosin phosphatase

targeting subunit at threonine-855 by rho kinase contributes to the arterial myogenic response," *Journal of Physiology*, vol. 587, pp. 2537–2553, 2009.

[178] W. C. Cole and D. G. Welsh, "Role of myosin light chain kinase and myosin light chain phosphatase in the resistance arterial myogenic response to intravascular pressure," *Archives of Biochemistry and Biophysics*, vol. 510, pp. 160–173, 6 2011.

[179] A. F. El-Yazbi, R. P. Johnson, E. J. Walsh, K. Takeya, M. P. Walsh, and W. C. Cole, "Pressure-dependent contribution of rho kinase-mediated calcium sensitization in serotonin-evoked vasoconstriction of rat cerebral arteries," *Journal of Physiology*, vol. 588, pp. 1747–1762, 5 2010.

[180] A. Moreno-Domínguez, A. F. El-Yazbi, H. L. Zhu, O. Colinas, X. Z. Zhong, E. J. Walsh, D. M. Cole, G. J. Kargacin, M. P. Walsh, and W. C. Cole, "Cytoskeletal reorganization evoked by rho-associated kinase- and protein kinase c-catalyzed phosphorylation of cofilin and heat shock protein 27, respectively, contributes to myogenic constriction of rat cerebral arteries," *Journal of Biological Chemistry*, vol. 289, pp. 20939–20952, 7 2014.

[181] R. Schubert and M. J. Mulvany, "The myogenic response: established facts and attractive hypotheses," *Clinical science*, vol. 96, pp. 313–326, 1999.

[182] V. N. Shah, B. Chagot, and W. J. Chazin, "Calcium-dependent regulation of ion channels," *Calcium Bind Proteins*, vol. 1, pp. 203–212, 2006.

[183] A. Kapela, A. Bezerianos, and N. M. Tsoukias, "A mathematical model of ca2+ dynamics in rat mesenteric smooth muscle cell: Agonist and no stimulation," *Journal of Theoretical Biology*, vol. 253, pp. 238–260, 7 2008.

[184] D. K. Blumenthal and J. T. Stull, "Activation of skeletal muscle myosin light chain kinase by calcium(2+) and calmodulin," *Biochemistry*, vol. 19, pp. 5608–14, 11 1980.

[185] P. F. Dillon, M. O. Aksoy, S. P. Driska, and R. A. Murphy, "Myosin phosphorylation and the cross-bridge cycle in arterial smooth muscle," *Science*, vol. 211, pp. 495–497, 1981.

[186] S. B. Marston, "The regulation of smooth muscle contractile proteins," *Progress in Biophysics and Molecular Biology*, vol. 41, pp. 1–41, 1982.

[187] K. E. Kamm and J. T. Stull, "The function of myosin and myosin light chain kinase phosphorylation in smooth muscle," *Annual Review of Pharmacology and Toxicology*, vol. 25, pp. 593–620, 1985.

[188] C. M. Rembold, "Modulation of the [ca2+] sensitivity of myosin phosphorylation in intact swine arterial smooth muscle," *Journal of Physiology*, vol. 429, pp. 77–94, 1990.

[189] M. J. Cipolla, J. Sweet, S.-L. Chan, M. J. Tavares, N. Gokina, and J. E. Brayden, "Increased pressure-induced tone in rat parenchymal arterioles vs. middle cerebral arteries: role of ion channels and calcium sensitivity," *J Appl Physiol*, vol. 117, pp. 53–59, 2014.

[190] Y. Li and J. E. Brayden, "Rho kinase activity governs arteriolar myogenic depolarization," *Journal of Cerebral Blood Flow and Metabolism*, vol. 37, pp. 140–152, 1 2017.

[191] S. I. Murtada, J. D. Humphrey, and G. A. Holzapfel, "Multiscale and multiaxial mechanics of vascular smooth muscle," *Biophysical Journal*, vol. 113, pp. 714–727, 8 2017.

[192] C. D. Maggio, S. R. Jennings, J. L. Robichaux, P. C. Stapor, and J. M. Hyman, "A modified hai-murphy model of uterine smooth muscle contraction," *Bulletin of Mathematical Biology*, vol. 74, pp. 143–158, 1 2012.

[193] N. M. Tsoukias, "Calcium dynamics and signaling in vascular regulation: Computational models," *Wiley interdisciplinary reviews. Systems biology and medicine*, vol. 3, pp. 93–106, 1 2011.

[194] D. Ghosh, A. U. Syed, M. P. Prada, M. A. Nystoriak, L. F. Santana, M. Nieves-Cintrón, and M. F. Navedo, *Calcium Channels in Vascular Smooth Muscle*, vol. 78. Academic Press Inc., 2017.

[195] M. T. Nelson, J. B. Patlak, J. F. Worley, and N. B. Standen, "Calcium channels, potassium channels, and voltage dependence of arterial smooth muscle tone," *Journal of Physiology*, vol. 259, pp. 3–18, 1990.

[196] J. R. Martens and C. H. Gelband, "Ion channels in vascular smooth muscle: Alterations in essential hypertension," *Experimental Biology and Medicine*, vol. 218, pp. 192–203, 1998.

[197] M. E. O'Donnell and N. E. Owen, "Regulation of ion pumps and carriers in vascular smooth muscle," *Physiological reviews*, vol. 74, pp. 683–721, 1994.

[198] W. F. Jackson, "Myogenic tone in peripheral resistance arteries and arterioles: The pressure is on!," *Frontiers in Physiology*, vol. 12, 7 2021.

[199] M. J. Davis and M. A. Hill, "Signaling mechanisms underlying the vascular myogenic response," *Physiological reviews*, vol. 79, pp. 387–423, 1999.

[200] G. Dupont, L. Combettes, G. S. Bird, and J. W. Putney, "Calcium oscillations," *Cold Spring Harbor Perspectives in Biology*, vol. 3, pp. 1–18, 2011.

[201] J. Sneyd, K. Tsaneva-Atanasova, D. I. Yule, J. L. Thompson, and T. J. Shuttleworth, "Control of calcium oscillations by membrane fluxes," *Proceedings of the National Academy of Sciences*, vol. 101, pp. 1392–1396, 2004.

[202] M. Koenigsberger, R. Sauser, D. Seppey, J. L. Bény, and J. J. Meister, "Calcium dynamics and vasomotion in arteries subject to isometric, isobaric, and isotonic conditions," *Biophysical Journal*, vol. 95, pp. 2728–2738, 9 2008.

[203] R. E. Mufti, S. E. Brett, C. H. T. Tran, R. AbdEl-Rahman, Y. Anfinogenova, A. El-Yazbi, W. C. Cole, P. P. Jones, S. R. Chen, and D. G. Welsh, "Intravascular pressure augments cerebral arterial constriction by inducing voltage-insensitive ca2+ waves," *Journal of Physiology*, vol. 588, pp. 3983–4005, 10 2010.

[204] D. R. Harder, "Pressure-dependent membrane depolarization in cat middle cerebral artery," *Circulation Research*, vol. 55, pp. 197–202, 1984.

[205] A. Kapela, A. Bezerianos, and N. M. Tsoukias, "A mathematical model of vasoreactivity in rat mesenteric arterioles: I. myoendothelial communication," *Microcirculation*, vol. 16, pp. 694–713, 2009.

[206] A. Kapela, S. Nagaraja, and N. M. Tsoukias, "A mathematical model of vasoreactivity in rat mesenteric arterioles. ii. conducted vasoreactivity," *Am J Physiol Heart Circ Physiol*, vol. 298, pp. 52–65, 2010.

[207] A. Karlin, "Membrane potential and ca2+ concentration dependence on pressure and vasoactive agents in arterial smooth muscle: A model," *Journal of General Physiology*, vol. 146, pp. 79–96, 2015.

[208] N. I. Gokina, K. M. Park, K. McElroy-Yaggy, and G. Osol, "Effects of rho kinase inhibition on cerebral artery myogenic tone and reactivity," *Journal of Applied Physiology*, vol. 98, pp. 1940–1948, 5 2005.

[209] M. P. Walsh and W. C. Cole, "The role of actin filament dynamics in the myogenic response of cerebral resistance arteries," *Journal of Cerebral Blood Flow and Metabolism*, vol. 33, pp. 1–12, 1 2013.

[210] A. F. El-Yazbi, K. S. Abd-Elrahman, and A. Moreno-Dominguez, "Pkc-mediated cerebral vasoconstriction: Role of myosin light chain phosphoryla-

tion versus actin cytoskeleton reorganization," *Biochemical Pharmacology*, vol. 95, pp. 263–278, 5 2015.

[211] S. J. Gunst and W. Zhang, "Actin cytoskeletal dynamics in smooth muscle: a new paradigm for the regulation of smooth muscle contraction," *Am J Physiol Cell Physiol*, vol. 295, pp. 576–587, 2008.

[212] A. Coccarelli, S. Pant, I. Polydoros, and O. F. Harraz, "A new model for evaluating pressure-induced vascular tone in small cerebral arteries," *Biomechanics and Modeling in Mechanobiology*, 11 2023.

[213] G. Lagaud, N. Gaudreault, E. D. W. Moore, C. V. Breemen, and I. Laher, "Pressure-dependent myogenic constriction of cerebral arteries occurs independently of voltage-dependent activation," *Am J Physiol Heart Circ Physiol*, vol. 283, pp. 2187–2195, 2002.

[214] D. Lidington, R. Schubert, and S. S. Bolz, "Capitalizing on diversity: An integrative approach towards the multiplicity of cellular mechanisms underlying myogenic responsiveness," *Cardiovascular Research*, vol. 97, pp. 404–412, 3 2013.

[215] L. Irons and J. D. Humphrey, "Cell signaling model for arterial mechanobiology," *PLoS Computational Biology*, vol. 16, 8 2020.

[216] R. Schubert, D. Lidington, and S. S. Bolz, "The emerging role of ca2+ sensitivity regulation in promoting myogenic vasoconstriction," *Cardiovascular Research*, vol. 77, pp. 8–18, 1 2008.

[217] J. F. Brekke, W. F. Jackson, and S. S. Segal, "Arteriolar smooth muscle ca2+ dynamics during blood flow control in hamster cheek pouch," *J Appl Physiol*, vol. 101, pp. 307–315, 2006.

[218] N. I. Gokina and G. Osol, "Actin cytoskeletal modulation of pressure-induced depolarization and ca(2+) influx in cerebral arteries," *The American Journal of Physiology-Heart and Circulatory Physiology*, vol. 282, pp. 1410–1420, 2002.

[219] O. Colinas, A. Moreno-Domínguez, H. L. Zhu, E. J. Walsh, M. T. Pérez-García, M. P. Walsh, and W. C. Cole, "α5-integrin-mediated cellular signaling contributes to the myogenic response of cerebral resistance arteries," *Biochemical Pharmacology*, vol. 97, pp. 281–291, 10 2015.

[220] L. Irons, M. Latorre, and J. D. Humphrey, "From transcript to tissue: Multiscale modeling from cell signaling to matrix remodeling," *Annals of Biomedical Engineering*, vol. 49, pp. 1701–1715, 7 2021.

[221] J. Stålhand, A. Klarbring, and G. A. Holzapfel, "Smooth muscle contraction: Mechanochemical formulation for homogeneous finite strains," *Progress in Biophysics and Molecular Biology*, vol. 96, pp. 465–481, 1 2008.

[222] A. S. Wexler, J. Ding, and S. A. Binder-Macleod, "A mathematical model that predicts skeletal muscle force," *IEEE Transactions on Biomedical Engineering*, vol. 44, p. 337, 1997.

[223] G. J. C. Ettema and K. Meijer, "Muscle contraction history: modified hill versus an exponential decay model," *Biological Cybernetics*, vol. 83, pp. 491–500, 2000.

[224] D. G. Lloyd and T. F. Besier, "An emg-driven musculoskeletal model to estimate muscle forces and knee joint moments in vivo," *Journal of Biomechanics*, vol. 36, pp. 765–776, 6 2003.

[225] G. A. Lichtwark and A. M. Wilson, "A modified hill muscle model that predicts muscle power output and efficiency during sinusoidal length changes," *Journal of Experimental Biology*, vol. 208, pp. 2831–2843, 8 2005.

[226] L. Luo, L. Wang, P. D. Paré, C. Y. Seow, and P. Chitano, "The huxley crossbridge model as the basic mechanism for airway smooth muscle contraction," *Am J Physiol Lung Cell Mol Physiol*, vol. 317, pp. 235–246, 2019.

[227] C.-M. Hai and H. R. Kim, "An expanded latch-bridge model of protein kinase c-mediated smooth muscle contraction the inclusion of mlcp inhibition in the four-state model also," *Journal of Applied Physiology*, vol. 98, pp. 1356–1365, 2005.

[228] P. Coats and C. Hillier, "Determination of an optimal axial-length tension for the study of isolated resistance arteries on a pressure myograph," *Experimental Physiology*, vol. 84, pp. 1085–1094, 1999.

[229] R. Dominguez and K. C. Holmes, "Actin structure and function," *Annual Review of Biophysics*, vol. 40, pp. 169–186, 6 2011.

[230] C. Viney, "Natural protein fibers," in *Encyclopedia of Materials: Science and Technology* (K. J. Buschow, R. W. Cahn, M. C. Flemings, B. Ilschner, E. J. Kramer, S. Mahajan, and P. Veyssière, eds.), pp. 5948–5956, Oxford: Elsevier, 2001.

[231] C. O. Tan, J. W. Hamner, and J. A. Taylor, "The role of myogenic mechanisms in human cerebrovascular regulation," *Journal of Physiology*, vol. 591, pp. 5095–5105, 10 2013.

[232] E. C. Peterson, Z. Wang, and G. Britz, "Regulation of cerebral blood flow," *International Journal of Vascular Medicine*, vol. 2011, 2011.

[233] W. M. Armstead, "Cerebral blood flow autoregulation and dysautoregulation," *Anesthesiology Clinics*, vol. 34, pp. 465–477, 9 2016.

[234] N. A. Lassen, "Cerebral blood flow and oxygen consumption in man," *Physiological Reviews*, vol. 39, pp. 183–238, 1959.

[235] E. VanBavel, J. P. M. Wesselman, and J. A. E. Spaan, "Myogenic activation and calcium sensitivity of cannulated rat mesenteric small arteries," *Circulation Research*, vol. 82, pp. 210–220, 1998.

[236] J. G. Mccarron, C. A. Crichton, P. D. Langton, A. Mackenzie, and G. L. Smith, "Myogenic contraction by modulation of voltage-dependent calcium currents in isolated rat cerebral arteries," *Journal of Physiology*, vol. 498, pp. 371–379, 1997.

[237] S. J. Bund, "Spontaneously hypertensive rat resistance artery structure related to myogenic and mechanical properties," *Clinical Science*, vol. 101, pp. 385–393, 2001.

[238] P. W. Sweeney, S. Walker-Samuel, and R. J. Shipley, "Insights into cerebral haemodynamics and oxygenation utilising in vivo mural cell imaging and mathematical modelling," *Scientific Reports*, vol. 8, 12 2018.

[239] R. Hoshikawa, H. Kawaguchi, H. Takuwa, Y. Ikoma, Y. Tomita, M. Unekawa, N. Suzuki, I. Kanno, and K. Masamoto, "Dynamic flow velocity mapping from fluorescent dye transit times in the brain surface microcirculation of anesthetized rats and mice," *Microcirculation*, vol. 23, pp. 416–425, 8 2016.

[240] S. Maxwell, D. Webb, and A. C. Shore, "Capillaroscopy and the measurement of capillary pressure," *British Journal of Clinical Pharmacology*, vol. 50, pp. 501–513, 2000.

Appendix A

Extra simulations

A.1 Passive model parameter identification

In this section the results of the material parameters presented in Section 2.5 for the extra vessels regarding the studies of Monson *et al.* [138] and Thorin *et al.* [150] are presented. The methodology for the identification is discussed in Section 2.5 and is exactly the same for these two groups.

A.1.1 Human cerebral arteries

This section includes the results regarding the work of Monson *et al.* [138]. The vessels are the ones noted as "A6" and "A9" in their work.

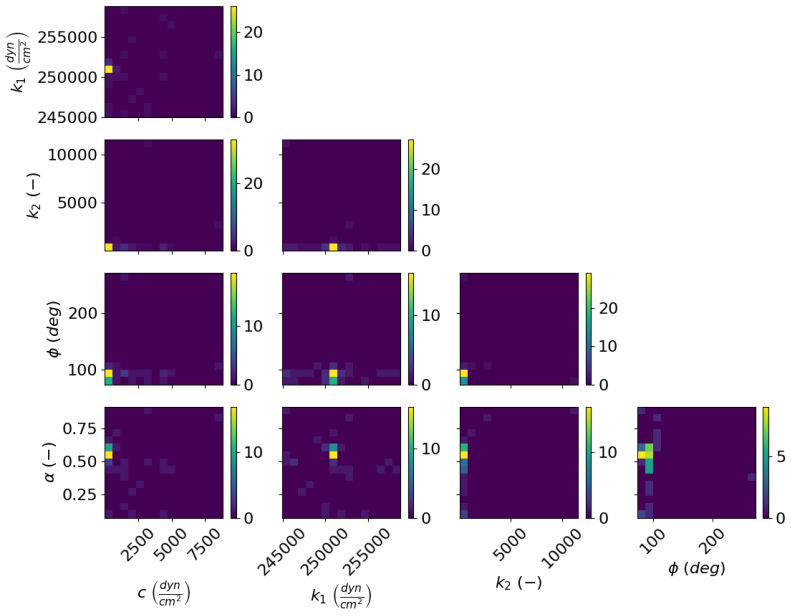

Figure A.1: Parameter space for A6 human cerebral artery. Number of runs: 50

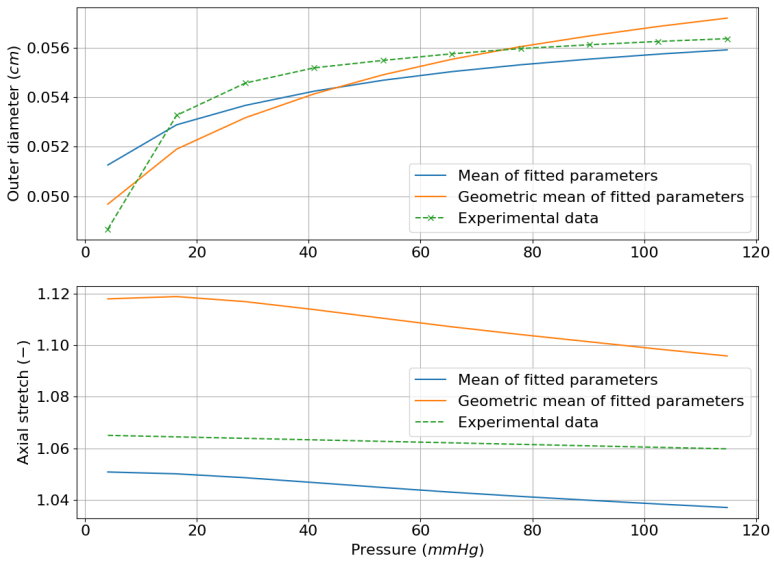

Figure A.2: Results for diameter and axial stretch for A6 human cerebral artery using the mean and geometric mean of the optimisation results

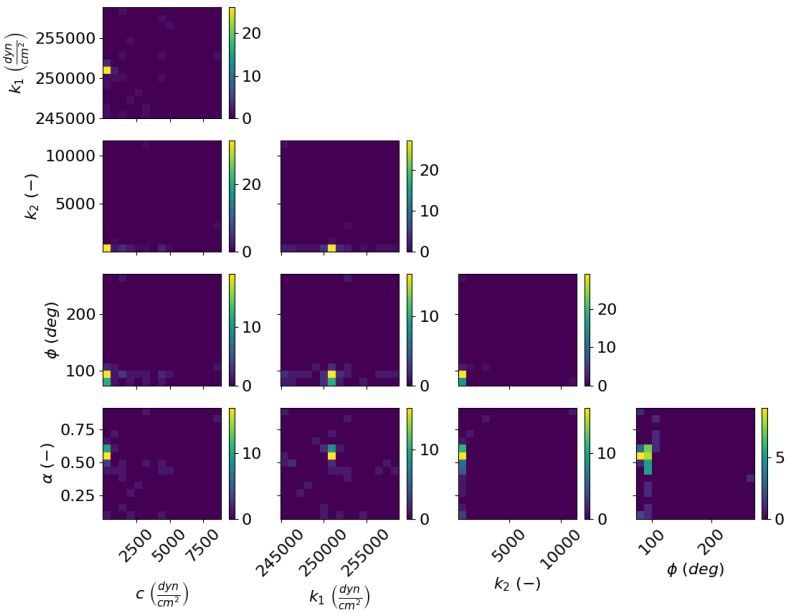

Figure A.3: Parameter space for A9 human cerebral artery. Number of runs: 50

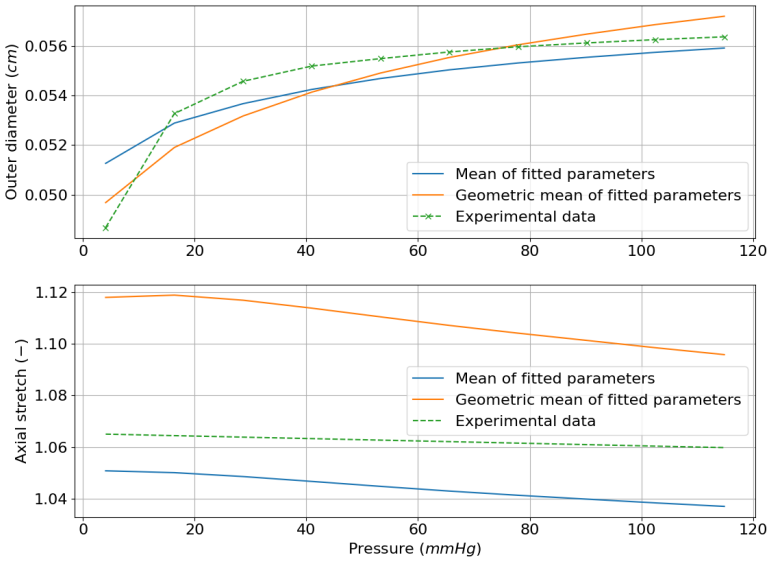

Figure A.4: Results for diameter and axial stretch for A9 human cerebral artery using the mean and geometric mean of the optimisation results

A.1.2 Human pial arteries

This section includes the results regarding the work of Thorin *et al.* [150]. The vessels are the ones noted as "medium" and "large" in their work.

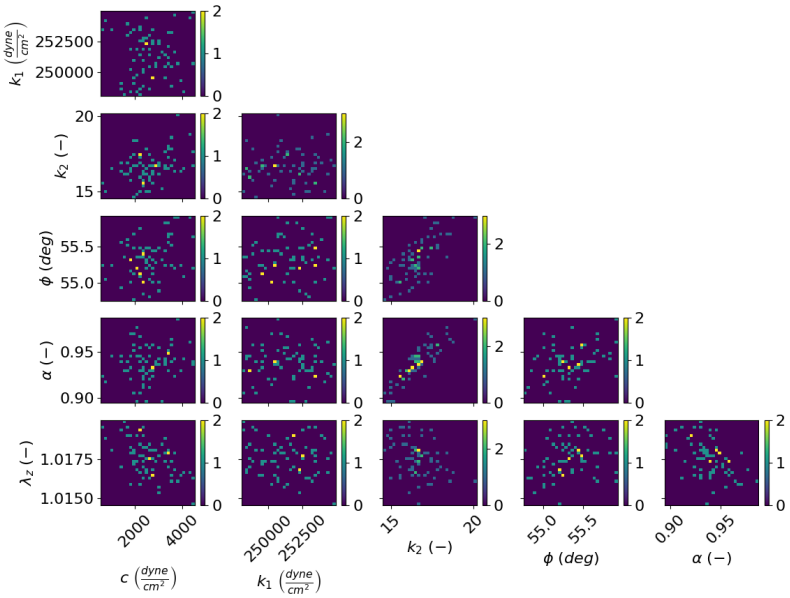

Figure A.5: Parameter space for the *medium* human pial artery. Results presented for $\omega = 80^{o}$. Number of runs: 50

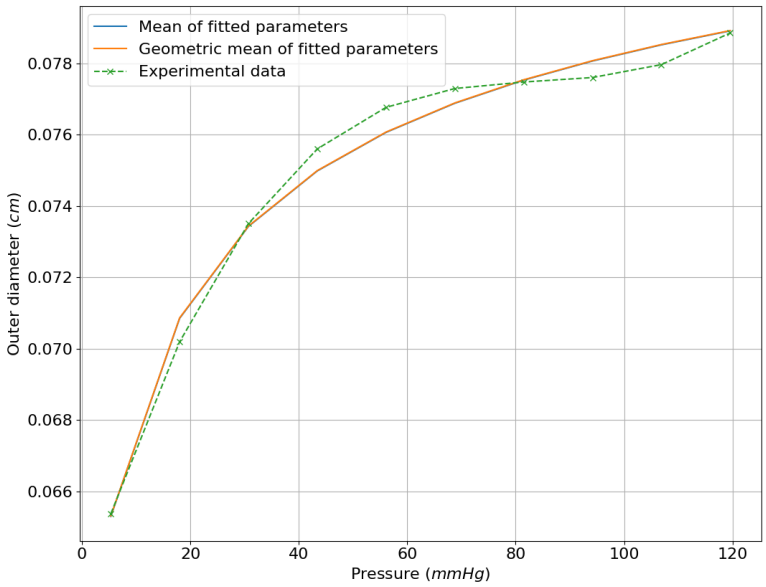

Figure A.6: Results for diameter for *medium* human pial artery with $\omega = 80^{o}$ using the mean and geometric mean of the optimisation results

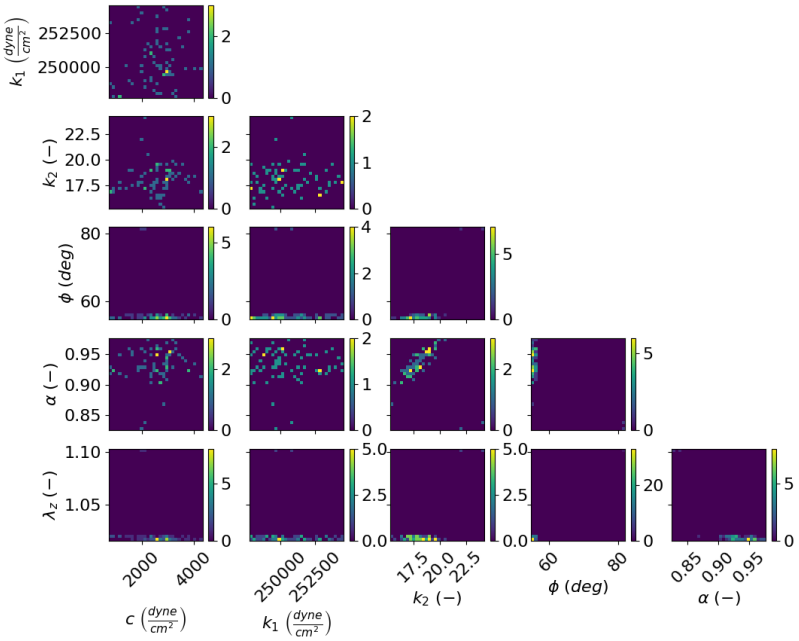

Figure A.7: Parameter space for the *medium* human pial artery. Results presented for $\omega = 120^{o}$. Number of runs: 50

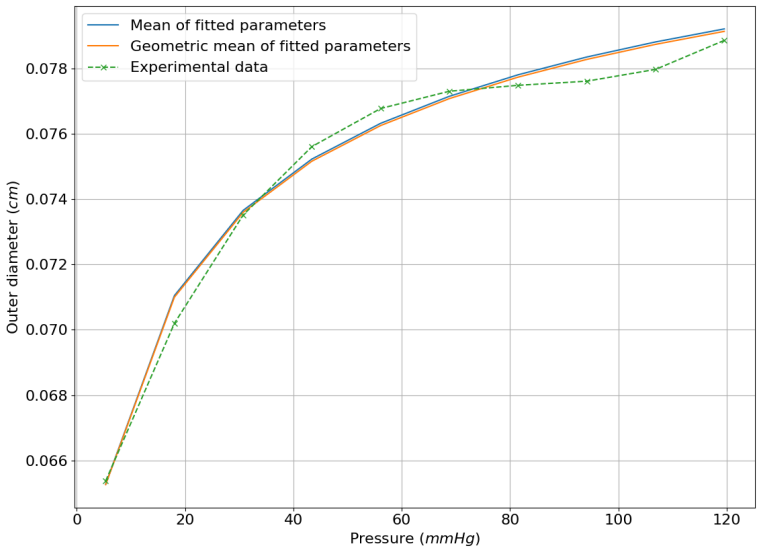

Figure A.8: Results for diameter for *medium* human pial artery with $\omega = 120^{o}$ using the mean and geometric mean of the optimisation results

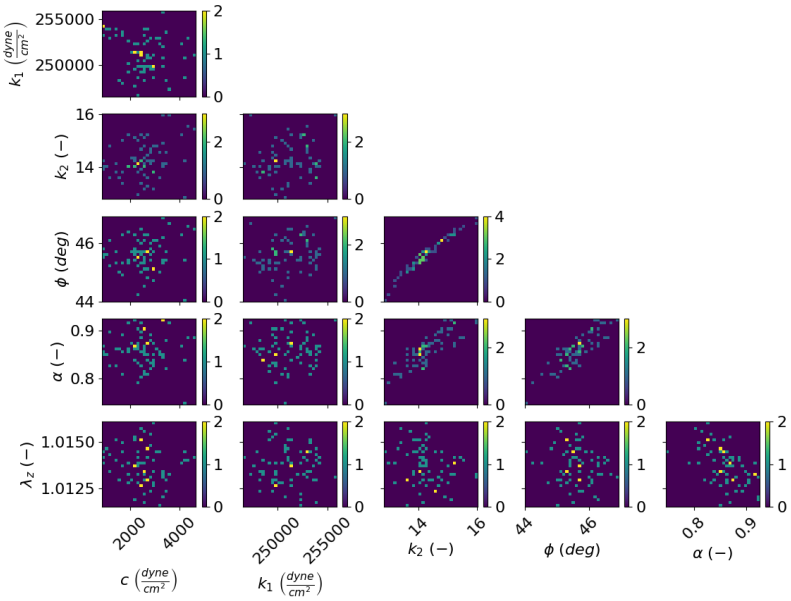

Figure A.9: Parameter space for the *medium* human pial artery. Results presented for $\omega = 80^{o}$. Number of runs: 50

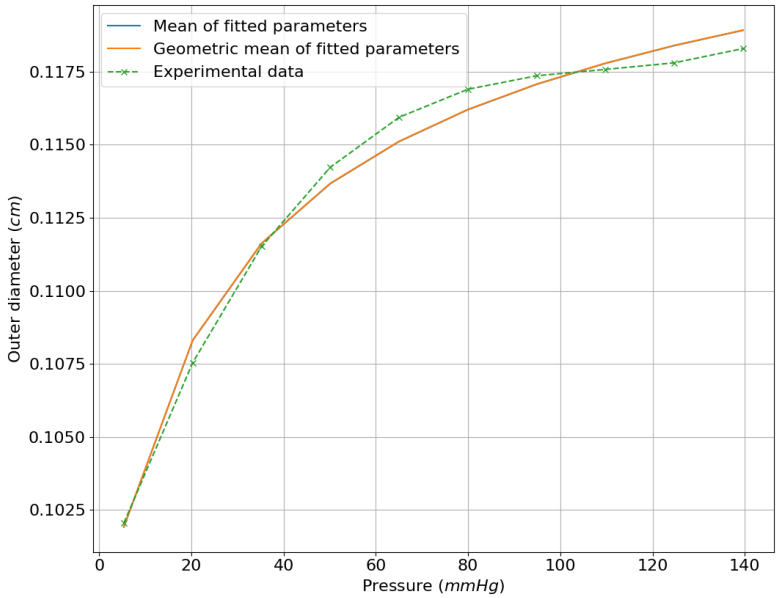

Figure A.10: Results for diameter for *medium* human pial artery with $\omega = 80^{o}$ using the mean and geometric mean of the optimisation results

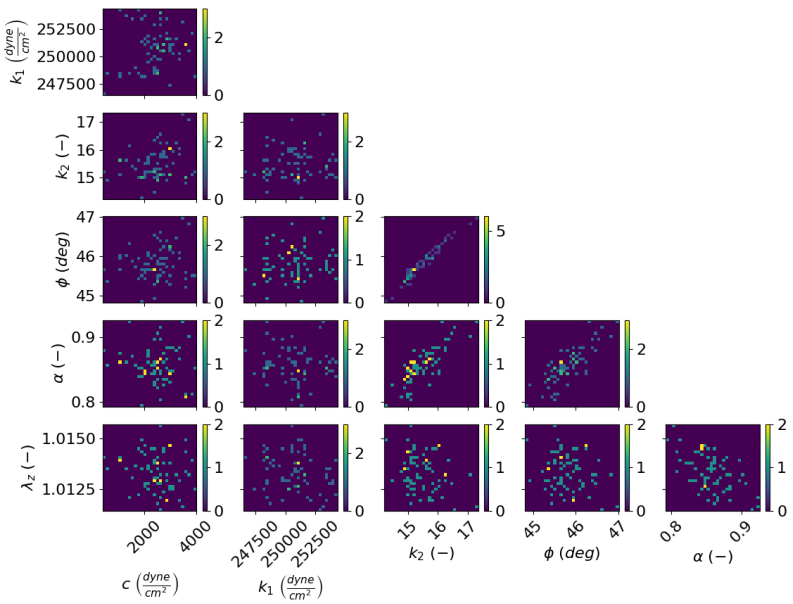

Figure A.11: Parameter space for the *medium* human pial artery. Results presented for $\omega = 120^{o}$. Number of runs: 50

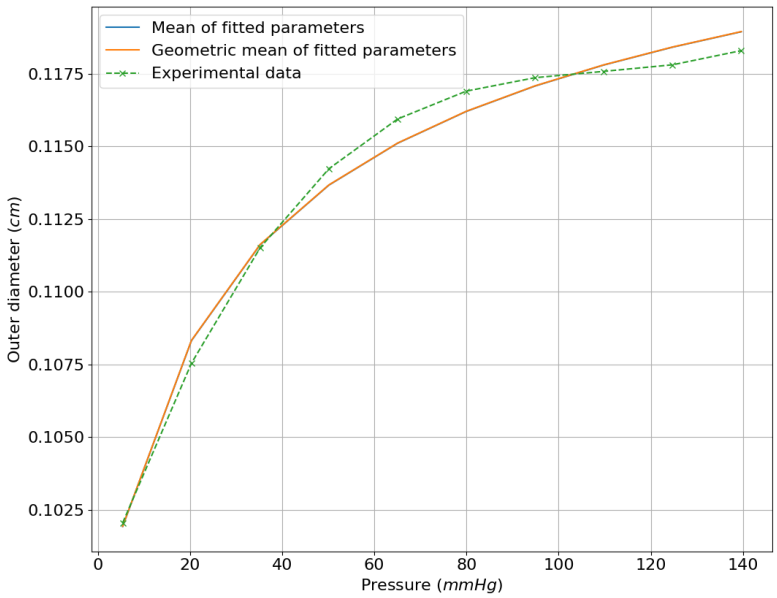

Figure A.12: Results for diameter for *medium* human pial artery with $\omega = 120^{o}$ using the mean and geometric mean of the optimisation results

Appendix B

Tables for the cell signalling model experimentally recorded values

In this section all the experimentally recorded values for the fitting of the cell-signalling model of Section 3.3 are reported.

Table B.1: Experimentally recorded normalised (with respect to the $P = 10\,(\text{mmHg})$ control case) values of the control case for pHSP27, pMLCP, pCofilin, pLC_20 and G-actin

$P\,(\text{mmHg})$	$\bar{\xi}_1$	$\bar{\xi}_3$	$\bar{\xi}_4$	$\bar{\xi}_5$	$\bar{\xi}_6$
60	2.134 [180]	1.292 [177]	1.821 [180]	1.611 [177]	0.365 [180]
80	-	-	-	2.148 [180]	0.322 [180]
100	-	2.169 [177]	-	2.078 [177]	-
120	2.582 [180]	-	2.476 [180]	2.246 [180]	0.110 [180]
140	-	3.272 [179]	-	-	-

Table B.2: Experimentally recorded normalised (with respect to the $P = 10\,(\text{mmHg})$ control case) values for pHSP27, pMLCP, pCofilin, pLC_20 and G-actin under $0.3\,\mu M$ H1152

$P\,(\text{mmHg})$	$\bar{\xi}_1$	$\bar{\xi}_3$	$\bar{\xi}_4$	$\bar{\xi}_5$	$\bar{\xi}_6$
60	-	0.494 [177]	-	1.208 [177]	-
100	-	0.981 [177]	-	1.176 [177]	-
120	2.387 [180]	-	0.938 [180]	-	1.151 [180]

Table B.3: Experimentally recorded normalised (with respect to the $P = 10\,(\text{mmHg})$ control case) values for pHSP27, pMLCP, pCofilin, pLC_20 and G-actin under $3.0\,\mu M$ GF. *Obtained by re-normalising the original experimental data with respect to ξ_2 at $10\,mmHg$ control case. **obtained by re-scaling the original experimental data with respect to the reference ξ_5 at $100\,mmHg$ control case (scaling factor ≈ 1.1)

$P\,(\text{mmHg})$	$\bar{\xi}_1$	$\bar{\xi}_3$	$\bar{\xi}_4$	$\bar{\xi}_5$	$\bar{\xi}_6$
100	-	2.045* [177]	-	0.456** [177]	-
120	0.942 [180]	-	1.907 [180]	-	1.175 [180]

Appendix C

Numerical investigations

In this section, some instabilities that were recognised during the model development and testing are presented. The instabilities are both on numerical issues that were identified.

At first, so far a pressure ramp is employed to introduce sudden increase or decrease of luminal pressure. Here, this elevation is assumed to occur instantaneously. Computationally, this means that the pressure is changing within one time step.

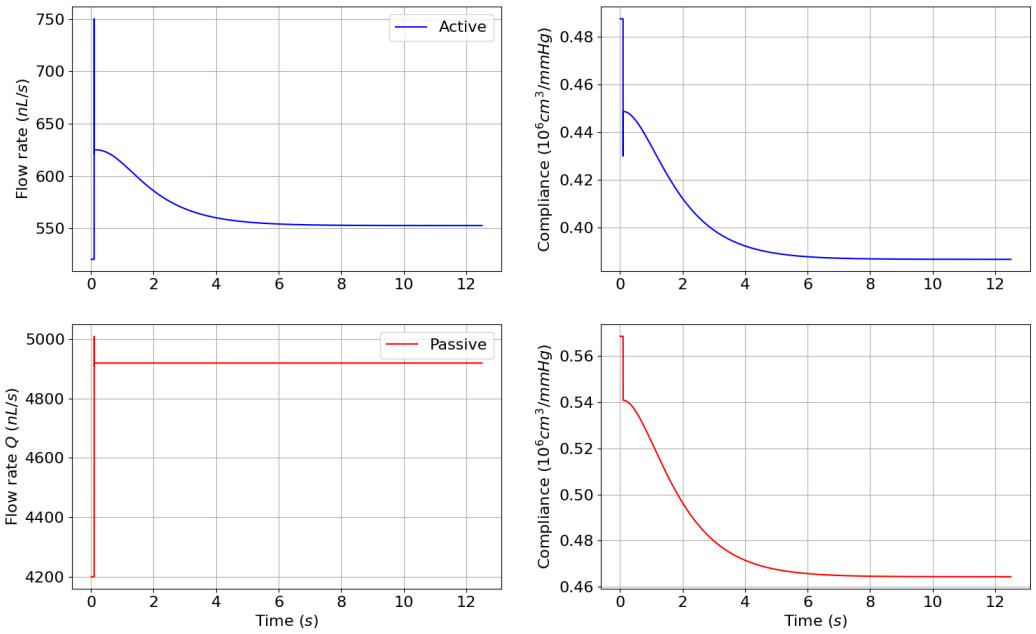

Figure C.1: Transient results for flow rate and compliance of the vessel for active and passive cases. Pressure increases instantaneously from $P_{\text{in}} = 60\,\text{mmHg}$ to $P_{\text{in}} = 80\,\text{mmHg}$. Constant pressure drop $\Delta P = 1\,\text{mmHg}$ across the vessel. Top row: actively contracted vessel; Bottom row: passive vessel

Figure C.1 presents the results for flow rate and compliance for this instantaneous

pressure boundary condition. The results for both vessels show a spike in flow rate when the pressure is changed, while the actively contracted vessel shows this spike in compliance too. The flow is seen to increase immediately very high before convergence.

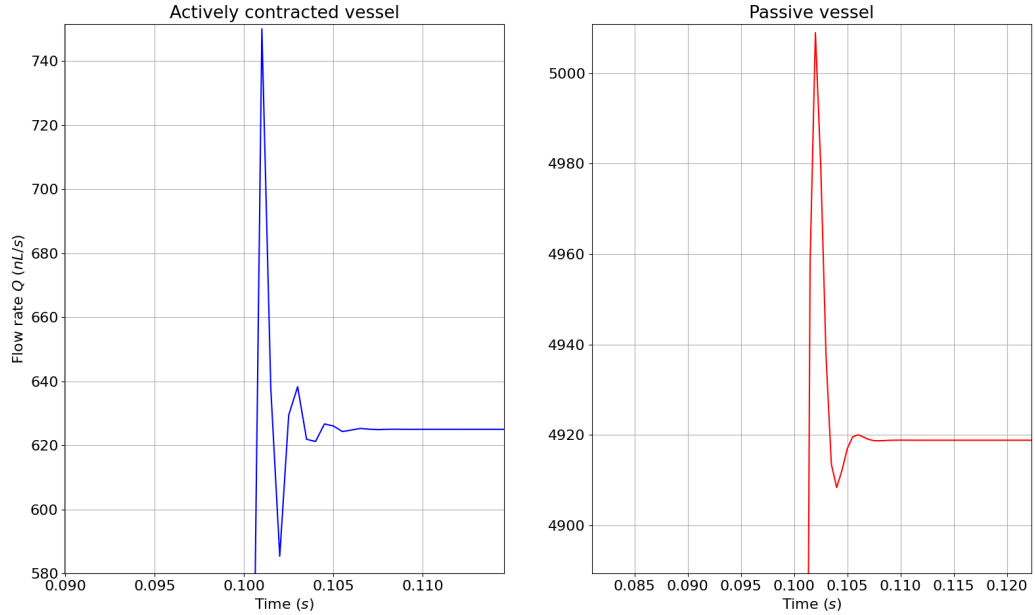

Figure C.2: Results focused on the point of pressure change for flow rate. Stepped pressure increase from $P_{\text{in}} = 60\,\text{mmHg}$ to $P_{\text{in}} = 80\,\text{mmHg}$ instantaneously, and constant pressure drop $\Delta P = 1\,\text{mmHg}$ across the vessel. Left: active response; Right: passive response

Figure C.2 is a zoomed-in plot showing the exact region where the pressure is increased. The flow rate is oscillating for some time steps around the value that should take. This is a numerical oscillation caused by the sudden change in pressure. According to the second order time discretisation scheme, for solving the n^{th} time step, the values of the $n-1$ and $n-2$ are used. When the pressure is changing radically within a single time step, the scheme may present a lag regarding the value that it should converge to, and hence these oscillations are produced. This oscillation is present in both active and passive vessels, however, it takes less steps to converge in the passive case.